

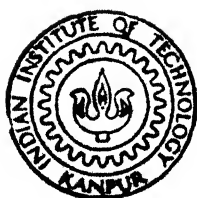
ELECTRON PARAMAGNETIC RESONANCE AND LOW-FIELD DEPENDENT MICROWAVE ABSORPTION IN HIGH T_c CUPRATE SUPERCONDUCTORS

by

MOHAMMAD SHAHABUDDIN

PHY
1992
D
SHA
ELE

TH
PHY/1992/D
Sh 13c



DEPARTMENT OF PHYSICS
INDIAN INSTITUTE OF TECHNOLOGY KANPUR
FEBRUARY, 1992

ELECTRON PARAMAGNETIC RESONANCE AND LOW-FIELD DEPENDENT MICROWAVE ABSORPTION IN HIGH T_c CUPRATE SUPERCONDUCTORS

*A Thesis Submitted
In Partial Fulfilment of the Requirements
for the Degree of
DOCTOR OF PHILOSOPHY*

by
MOHAMMAD SHAHABUDDIN

to the
DEPARTMENT OF PHYSICS
INDIAN INSTITUTE OF TECHNOLOGY KANPUR
FEBRUARY, 1992

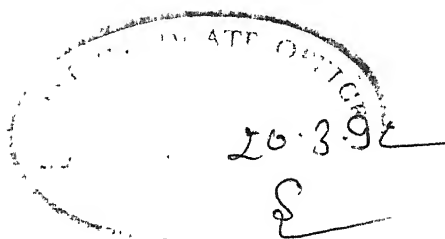
Th
537623
Sh13e

- 3 FEB 1994 / Phy

CENTRAL LIBRARIES
IIT, KANPUR

No. A.I.17203

PHY - 1995-D-SHA-ELE



CERTIFICATE

It is certified that the work contained in the thesis entitled "ELECTRON PARAMAGNETIC RESONANCE AND LOW FIELD DEPENDENT MICROWAVE ABSORPTION IN HIGH T_c CUPRATE SUPERCONDUCTORS" has been carried out under my supervision and that this work has not been submitted elsewhere for a degree.

March 1992

(H.D. BIST)

Professor
Department of Physics
I.I.T. Kanpur

SYNOPSIS

NAME OF THE STUDENT : MOHAMMAD SHAHABUDDIN
 ROLL NO. : 8610969
 DEGREE FOR WHICH SUBMITTED : Ph.D.
 DEPARTMENT : Physics
 THESIS TITLE : ELECTRON PARAMAGNETIC RESONANCE AND LOW-FIELD
 DEPENDENT MICROWAVE ABSORPTION IN HIGH T_c CUPRATE
 SUPERCONDUCTORS

NAME OF THESIS SUPERVISOR : Prof. H.D. Bist

MONTH AND YEAR OF THESIS SUBMISSION : March 1992

The discovery of superconductivity with transition temperature above 30 K in $\text{La}_{2-x}\text{Ba}_x\text{CuO}_4$, system by Bednorz and Müller triggered a flood of research in the field of high temperature superconductivity. Since the discovery of earliest $\text{La}_{2-x}(\text{Sr},\text{Ba})_x\text{CuO}_4$ system with transition temperature around 30 to 40 K, many new such systems have been discovered, with the highest reproducibly acknowledged T_c 125 K. Although each of these new materials has its own individual characteristics, they exhibit common phenomenological characters. The presence of anisotropy, granular structure and unusual range of the characteristic parameters like the coherence length ξ_o and penetration depth λ etc. lead to some novel features not observed in classic superconductors. The BCS coherence length $\xi_o = 0.2 \frac{\hbar v_F}{kT_c}$ is very small for high T_c materials. A representative value for ξ_o is 10 Å (averaged over crystal axes) which is the order of a unit cell dimension. The coherence length ξ_o sets the length scale for variation of the superconducting order parameter. The small value

implies that the superconductivity in these superconductors will be much more sensitive to small scale structural or chemical imperfections than that in a classic superconductor where $\xi_0 = 10^2$ to 10^4 \AA . Small coherence length gives a coherence volume which is so small that it contains only a few Cooper-pairs inside it. This implies that fluctuations will play a more significant role in these materials than in a classical superconductor.

One of the novel features in high T_c superconductors is low magnetic field dependent microwave absorption below the superconducting transition temperature. The origin of the microwave losses in the copper oxide superconductors is of interest for both scientific and technical reasons. In particular, the sensitivity of microwave losses to small magnetic fields has been attributed to the suppression of superconductivity in weak link structure between or within superconductors. Low frequency resistance measurements have also been interpreted in terms of weak links. These losses must be reduced if the material is to be useful for many applications. As a probe of the material properties, a microwave measurement is a useful complement to low frequency susceptibility and resistivity measurements for at least two reasons. Firstly, it is contactless measurement. Secondly, it permits the study of the resistive behavior below superconducting transition temperature T_c . Additionally, the changes in the microstructure of the materials are reflected in the low field microwave absorption.

This thesis is primarily concerned with the low magnetic field dependent microwave absorption in high T_c superconductors, $\text{YBa}_2\text{Cu}_3\text{O}_{7-\delta}$ and $\text{Tl}_2\text{Ba}_2\text{CaCu}_2\text{O}_{8+\delta}$ in polycrystalline form. It has been divided into seven chapters. Each chapter is self contained.

▼

Chapter I briefly outlines the general introduction to the low field dependent microwave absorption and Electron Paramagnetic Resonance (EPR) in high T_c superconductors. Relevant properties such as granularity, glassy effect, critical state, flux flow and flux creep etc. and the fundamentals of EPR have also been discussed.

Chapter II contains the brief description of EPR spectrometer. The design of Helmholtz coils and current source have been discussed. This combination provides the scan of the magnetic field in the range -130 to +130 G in the low field region. Thus the sample could be placed in the resonant cavity outside the electromagnet. Low temperature cell design has also been discussed. Sample preparation by different methods and set up of the resistance measurement have been briefly summarised. Iodometric titration method for the estimation of oxygen content in $\text{YBa}_2\text{Cu}_3\text{O}_{7-\delta}$ has been discussed.

Chapter III discusses the characterization of the samples ($\text{YBa}_2\text{Cu}_3\text{O}_{7-\delta}$ and $\text{Tl}_2\text{Ba}_2\text{CaCu}_2\text{O}_{2.8+\delta}$ systems) by resistance measurement, X-ray powder diffraction and scanning electron microscopy. EPR of $\text{YBa}_2\text{Cu}_3\text{O}_{7-\delta}$ (having different oxygen content) and $\text{Tl}_2\text{Ba}_2\text{CaCu}_2\text{O}_{2.8+\delta}$ at room temperature has been studied. It has been concluded that all pure high T_c superconductors are EPR silent; whatever weak signal of Cu^{2+} is seen is due to other impurity phases which are formed at the grain-boundary during the synthesis of the samples. Various possibilities for the absence of EPR signal have been discussed.

Chapter IV presents the studies of the low field dependent microwave absorption in pure $\text{YBa}_2\text{Cu}_3\text{O}_{7-\delta}$ (prepared by different methods having different particle sizes), Hf-doped $\text{YBa}_2\text{Cu}_3\text{O}_{7-\delta}$ and $\text{Tl}_2\text{Ba}_2\text{CaCu}_2\text{O}_{2.8+\delta}$. The temperature dependence of the

samples is also presented. The parameter, peak position H_m , of the derivative of the low field dependent microwave absorption (DLFDMA) shifts towards lower fields as the grain size of the sample increases. This parameter H_m in fact related to the H_{cij} of the intergranular junction. The temperature dependence of the DLFDMA near T_c shows very interesting behavior. The peak height grows very rapidly as we go few degrees below T_c . The peak position does not show any shift near the transition temperature while the hysteresis area decreases with increasing temperature and vanishes at T_c . The peak height and hysteresis areas vary as $(T_c - T)^\alpha$, where α varies from sample to sample in the range 0.5 to 3.5. The results have been explained in terms of the model proposed by Dulcic et al. This model assumes that there exists a large number of random intergranular Josephson junctions which can be represented by a single representative Josephson junction. The exposition of the magnetic field induces a current I_o on the surface of the sample. This transport current I_o is limited by the critical current of the junction I_c . Expression for the microwave absorption in the junction has been obtained analytically which explains most of our observations.

In Chapter V effect of modulation amplitude and microwave power on the DLFDMA of pure $\text{YBa}_2\text{Cu}_3\text{O}_{6.85}$, Hf-doped $\text{YBa}_2\text{Cu}_3\text{O}_{7-\delta}$ and $\text{Tl}_2\text{Ba}_2\text{CaCu}_2\text{O}_{8+\delta}$ have been presented. The peak height and hysteresis area show nonlinear behavior in certain range of modulation amplitude. As the doping concentration of Hf increases in $\text{YBa}_2\text{Cu}_3\text{O}_{7-\delta}$, the threshold of the modulation amplitude (at which nonlinear behavior appears) is lowered. These observations have also been explained in terms of the model discussed in the above paragraph.

Chapter VI contains the field cooling (FC) effect and the effect of field exposure (FE) on the DLFDMA of the zero field cooled samples, $\text{YBa}_2\text{Cu}_3\text{O}_{7-\delta}$ and $\text{Tl}_2\text{Ba}_2\text{CaCu}_2\text{O}_{8+\delta}$. The field cooled FC (Meissner effect) and the FE to the zero field cooled (shielding effect) show different behavior. Upto a certain low value of the magnetic field exposure (H_{c1j}) the DLFDMA does not show hysteresis. As this value is surpassed it shows hysteresis (i.e. the field penetrates into the junction of the sample) which increases rapidly and gets saturated. On further increasing the magnitude of the exposure field hysteresis area increases. The sample contains a large number of random intergranular Josephson junctions having different H_{c1j} . The magnitude of exposure field at which the hysteresis appears is the lowest H_{c1j} among them. The field at which hysteresis area gets saturated is the critical field H_j^* at which all junctions are in critical state. The higher exposing field at which the hysteresis area starts to increase is H_{c1g} which is the lower critical field of the grains. Field cooling effect is very interesting. The parameters, peak height and hysteresis area, increase initially and attain a maximum. The peak occurs at the H_{c1j} of the samples. They decrease very fast as the cooling field is increased further. The peak position of the DLFDMA increases towards higher field in both cases of FC and FE. But the rate of increase of peak position in the FC case is higher than that in the case of the FE. In all the cases the peak position shifts towards higher field and gets saturated at larger value of cooling and exposing fields. All these observations have been explained in terms of the critical state model of random intergranular Josephson junctions.

It is concluded from the present study that the low field dependent microwave absorption and EPR studies are very important

tools to characterize the quality of the high T_c superconductors. The EPR can detect the impurity phase well beyond the detection limit of the X-ray powder diffraction. Low field microwave absorption study is very sensitive tool to find out the superconducting phase inside the mixed phases of nonsuperconducting materials. The microwave studies show that the intergranular Josephson junctions or weak-links play an effective role in limiting the critical current of the polycrystalline samples.

LIST OF PUBLICATIONS RESULTING FROM THE WORK PRESENTED IN THE
THESIS (HAVE BEEN CITED FULLY INSIDE AT APPROPRIATE PLACES)

1. EPR AND RAMAN SPECTROSCOPY OF HIGH T_c SUPERCONDUCTOR
 $\text{YBa}_2\text{Cu}_3\text{O}_{7-\delta}$;
Solid State Commun. 65, 899 (1988).
2. EPR AND LOW MAGNETIC FIELD MICROWAVE ABSORPTION IN HAFNIUM DOPED $\text{YBa}_2\text{Cu}_3\text{O}_{7-\delta}$;
Physica C 158, 385 (1989).
3. TEMPERATURE DEPENDENCE OF MICROWAVE LOSS SIGNAL IN HAFNIUM DOPED YBaCuO;
Phys. Lett. A 139, 415 (1989).
4. EFFECT OF MODULATION AMPLITUDE ON LOW FIELD MICROWAVE ABSORPTION IN HAFNIUM DOPED YBaCuO;
Bull. Mater. Sci. 14, 789 (1991).
5. MICROWAVE ABSORPTION STUDIES IN FIELD COOLED HAFNIUM DOPED YBaCuO;
Bull. Mater. Sci. 14, 777 (1991).

ACKNOWLEDGEMENT

I have great pleasure in expressing my gratitude to Professor H.D. Bist for introducing me to this interesting field, his many lessons and giving me the confidence to engage myself in this fast developing highly competitive area.

I would like to thank Professor J.K. Bhattacharya, for valuable discussions on theoretical aspect of superconductivity and Professor A.V. Narlikar to provide the high T_c superconducting samples. I would also like to thank Dr. Prem Chand for giving me valuable suggestion and full cooperation in carrying out experimental work.

I am very much thankful to Dr. S.S.A. Razee for his critical reading of this thesis and giving good suggestion. I thank Renu Tripathi, Abul Hossain, Mansoor Ahmed and P.K. Khulbe helping me in proof reading.

I thank Mr. K.N. Islam for typing the manuscript, Mr. G.S. Thapa for tracing the figures and D.K. Kanaujia for helping in recording the EPR spectrum. I thank to all my colleagues for their timely help.

I take this opportunity to express my deep sense of gratitude to all my family members especially my mother and wife who showed great patience and encouraged me during the entire period of my research.

Mohammad Shahabuddin

CONTENTS

	Page
LIST OF FIGURES	xy-xix
CHAPTER I	
INTRODUCTION	1
Abstract	1
1.1 GENERAL	2
1.2 MAGNETIC PROPERTIES OF ISOTROPIC SUPERCONDUCTOR	3
1.3 STRUCTURE OF VORTEX	4
1.4 FLUX FLOW	5
1.5 VORTEX PINNING	8
1.6 BEAN'S CRITICAL STATE MODEL	9
1.7 FLUX CREEP	12
1.8 GRANULARITY	14
1.9 EFFECTIVE MEDIUM PARAMETERS OF A GRANULAR SUPERCONDUCTOR	14
1.9.1 Model of Granular Superconductor	14
1.9.2 Critical Current	15
1.9.3 Penetration Depth	16
1.9.4 Coherence Length	16
1.9.5 Thermodynamic Critical Field	17
1.9.6 Ginzburg-Landau Parameter	18
1.9.7 Lower Critical Field H_{c1J}	18
1.9.8 Upper Critical Field H_{c2J}	19
1.10 SUPERCONDUCTING GLASS AND RELATED MODELS	19
1.10.1 What is a Glass	19
1.10.2 The Spin Glass	22
1.10.3 The Superconducting Phase Glass-Granular System and Arrays	24
1.11 ELECTRON PARAMAGNETIC RESONANCE	28
1.11.1 The Resonance Condition	28
1.11.2 Thermal Equilibrium and Saturation	28
1.11.3 Spin Lattice Relaxation	29

1.11.4 Crystal Field	30
1.11.5 Fine Structure	32
References	34
CHAPTER II	
EXPERIMENTAL	40
Abstract	40
2.1 EXPERIMENTAL APPARATUS	41
2.1.1 EPR Spectrometer	41
2.1.2 Helmholtz Coils	43
2.1.3 Current Source	44
2.1.4 Low Temperature Cell	46
2.2 SYNTHESIS OF $\text{YBa}_2\text{Cu}_3\text{O}_{7-\delta}$	46
2.2.1 Solid State Reaction Method	47
2.2.2 Co-Precipitation Method	49
2.2.3 Chemical Precursor Method	49
2.2.4 Sol-Gel	50
2.3 RESISTANCE MEASUREMENT	51
2.4 ESTIMATION OF OXYGEN IN $\text{YBa}_2\text{Cu}_3\text{O}_{7-\delta}$	52
References	55
CHAPTER III	
ELECTRON PARAMAGNETIC RESONANCE IN HIGH T_c SUPERCONDUCTORS	65
Abstract	65
3.1 INTRODUCTION	66
3.2 SAMPLE PREPARATION	66
3.3 RESISTANCE MEASUREMENT	68
3.4 POWDER X-RAY DIFFRACTION	69
3.5 SCANNING ELECTRON MICROPHOTOGRAPH STUDIES	69
3.6 ELECTRON PARAMAGNETIC RESONANCE	71
3.7 DISCUSSION	74
References	79

CHAPTER IV

DERIVATIVE OF LOW FIELD DEPENDENT MICROWAVE ABSORPTION IN $\text{YBa}_2\text{Cu}_3\text{O}_{6.85}$, Hf-doped $\text{YBa}_2\text{Cu}_3\text{O}_{7-\delta}$ and $\text{Tl}_2\text{Ba}_2\text{CaCu}_2\text{O}_{8+\delta}$	88
AND ITS TEMPERATURE DEPENDENCE	
Abstract	89
4.1 INTRODUCTION	89
4.2 EXPERIMENT	90
4.3 LOW FIELD DEPENDENT MICROWAVE ABSORPTION	91
4.3.1 Conventional Superconductors Pb and Nb	92
4.3.2 High T_c Superconductors	93
4.4 TEMPERATURE DEPENDENCE OF THE DERIVATIVE OF THE LOW FIELD DEPENDENT MICROWAVE ABSORPTION	96
4.4.1 $\text{YBa}_2\text{Cu}_3\text{O}_{7-\delta}$	97
4.4.2 $\text{Tl}_2\text{Ba}_2\text{CaCu}_2\text{O}_{8+\delta}$	99
4.4.3 Hysteresis Area	101
4.5 DISCUSSION	105
References	111

CHAPTER V

EFFECT OF MODULATION FIELD AMPLITUDE AND MICROWAVE POWER ON THE DERIVATIVE OF THE LOW FIELD DEPENDENT MICROWAVE ABSORPTION IN $\text{YBa}_2\text{Cu}_3\text{O}_{6.85}$, Hf-DOPED $\text{YBa}_2\text{Cu}_3\text{O}_{7-\delta}$ AND $\text{Tl}_2\text{Ba}_2\text{CaCu}_2\text{O}_{8+\delta}$	129
Abstract	129
5.1 INTRODUCTION	130
5.2 EXPERIMENT	131
5.3 RESULTS	132
5.4 DISCUSSION	134
References	137

CHAPTER VI**EFFECT OF FIELD EXPOSURE AND FIELD COOLING ON DERIVATIVE OF
LOW FIELD DEPENDENT MICROWAVE ABSORPTION IN $\text{YBa}_2\text{Cu}_3\text{O}_{6.85}$** **Hf-DOPED $\text{YBa}_2\text{Cu}_3\text{O}_{7-\delta}$ AND $\text{Tl}_2\text{Ba}_2\text{CaCu}_2\text{O}_{8+\delta}$** 143**Abstract** 143**6.1 INTRODUCTION** 144**6.2 EXPERIMENT** 145**6.3 RESULTS** 147**6.3.1 Field Exposure Effect on DLFDMA of $\text{YBa}_2\text{Cu}_3\text{O}_{6.85}$
and $\text{Tl}_2\text{Ba}_2\text{CaCu}_2\text{O}_{8+\delta}$** 147**6.3.2 Field Cooling Effect on DLFDMA of $\text{YBa}_2\text{Cu}_3\text{O}_{6.85}$
and $\text{Tl}_2\text{Ba}_2\text{CaCu}_2\text{O}_{8+\delta}$** 149**6.3.3 Negative Field Exposure Effect on DLFDMA of Field
Exposed and Field Cooled Samples $\text{YBa}_2\text{Cu}_3\text{O}_{6.85}$ and
 $\text{Tl}_2\text{Ba}_2\text{CaCu}_2\text{O}_{8+\delta}$** 150**6.4 DISCUSSION** 153**References** 161**CHAPTER VII****CONCLUSIONS** 176

LIST OF FIGURES

Figures	Page
1.1 The magnetization curve for an ideal Type-II superconductors.	36
1.2 The structure of an isolated vortex in a Type-II superconductor in the Abrikosov picture.	36
1.3 A schematic representation of the magnetization of a Type-II superconductor with and without pinning.	37
1.4 Schematic representation of flux bundles hopping over barriers between pinning sites.	37
1.5 A schematic plot of the configurational space of a glass.	38
1.6 Static susceptibilities of CuMn spin glasses versus temperature in a 5.9G field.	38
1.7 The physical picture of superconducting phase glass.	38
1.8 Schematic diagram for microwave field and spin lattice interaction.	39
1.9 Schematic energy levels for $S = 3/2$.	39
2.1 Block diagram of an EPR spectrometer.	58
2.2 Block diagram of an automatic frequency control (AFC).	59
2.3 Output voltage from cavity as a result of AFC modulation.	60
2.4 The field distribution of Helmholtz coils along axis.	60
2.5 Circuit diagram for current source.	61
2.6 Circuit diagram for dual power supply.	61
2.7 Low temperature cell for EPR study.	62
2.8 Low temperature cell for EPR study upto freezing temperature of liquid nitrogen.	63
2.9 Schematic diagram for resistance measurement by four probe technique.	64
2.10 A set up to vary the sample temperature from room to liquid nitrogen temperature for resistance measurement.	64
3.1 Resistance of $Tl_2Ba_2CaCu_2O_{8+\delta}$ and $YBa_2Cu_3O_{7-\delta}$ (Sample NPL) as a function of temperature.	81
3.2 Variation of resistance of 0.5% Hf-doped $YBa_2Cu_3O_{7-\delta}$ as a function of temperature.	81
3.3 Resistance of Sample A and Sample C as a function of temperature.	82
3.4 Powder X-ray diffraction of three different $YBa_2Cu_3O_{7-\delta}$ Sample A, Sample B and Sample C.	83

LIST OF FIGURES (Contd.)

Figures	Page
3.5 SEM micrograph of 0.5% and 2% Hf-doped $\text{YBa}_2\text{Cu}_3\text{O}_{7-\delta}$.	84
3.6 SEM micrograph of Sample A, Sample B and Sample C.	84
3.7 SEM micrograph of $\text{Tl}_2\text{Ba}_2\text{CaCu}_2\text{O}_{2.8+\delta}$ and Sample D.	85
3.8 X-band EPR spectrum of $\text{YBa}_2\text{Cu}_3\text{O}_{7-\delta}$ (Sample NPL) at room temperature.	85
3.9 Temperature dependence of X-band EPR signal in $\text{YBa}_2\text{Cu}_3\text{O}_{7-\delta}$, Sample NPL.	85
3.10 Room temperature X-band EPR spectra of $\text{YBa}_2\text{Cu}_3\text{O}_{7-\delta}$ with different oxygen content.	86
3.11 Room temperature X-band EPR spectra of another batch of $\text{YBa}_2\text{Cu}_3\text{O}_{7-\delta}$ with different oxygen content.	86
3.12 X-band EPR signal at RT and LNT of Hf-doped $\text{YBa}_2\text{Cu}_3\text{O}_{7-\delta}$.	87
3.13 EPR powder spectra of Y_2BaCuO_5 and $\text{BaCaO}_{2.02}$ at X and Q-band	87
4.1 DLFDMA of Pb and Nb with oxidised surface at 4.3K.	114
4.2 DLFDMA of $\text{YBa}_2\text{Cu}_3\text{O}_{7-\delta}$ at 82.4K.	114
4.3 DLFDMA of ZFC $\text{YBa}_2\text{Cu}_3\text{O}_{7-\delta}$ and $\text{Tl}_2\text{Ba}_2\text{CaCu}_2\text{O}_{2.8+\delta}$ with different average grain size at LNT.	115
4.4 Variation of peak positions of DLFDMA as a function of grain size.	115
4.5 DLFDMA Hf-doped samples at LNT.	116
4.6 DLFDMA of Sample A at different temperatures.	117
4.7 DLFDMA of Sample B at different temperatures.	118
4.8 Variation of peak height of DLFDMA of Samples A and B as a function of temperature T and $(T_c - T)$.	119
4.9 DLFDMA of ZFC $\text{YBa}_2\text{Cu}_3\text{O}_{6.85}$ (Sample C) at different temperatures.	120
4.10 DLFDMA of 40G field exposed Sample C at different temperatures.	121
4.11 DLFDMA of ZFC Sample D at different temperatures.	122
4.12 DLFDMA of 60G field exposed $\text{Tl}_2\text{Ba}_2\text{CaCu}_2\text{O}_{2.8+\delta}$ at differnt temperatures.	123

LIST OF FIGURES (Contd.)

Figures	Page
4.13 Variation of $\log(h_p)$ of DLFDMA of $\text{YBa}_2\text{Cu}_3\text{O}_{6.85}$ and $\text{Tl}_2\text{Ba}_2\text{CaCu}_2\text{O}_{2.8+\delta}$ as a function of temperature.	124
4.14 Variation of peak height of DLFDMA of $\text{YBa}_2\text{Cu}_3\text{O}_{7-\delta}$ and $\text{Tl}_2\text{Ba}_2\text{CaCu}_2\text{O}_{2.8+\delta}$ as a function of $(T_c - T)$.	125
4.15 Variation of \log (hysteresis area) of DLFDMA of $\text{YBa}_2\text{Cu}_3\text{O}_{7-\delta}$ and $\text{Tl}_2\text{Ba}_2\text{CaCu}_2\text{O}_{2.8+\delta}$.	126
4.16 Variation of \log (hysteresis area) of DLFDMA of $\text{YBa}_2\text{Cu}_3\text{O}_{7-\delta}$ and $\text{Tl}_2\text{Ba}_2\text{CaCu}_2\text{O}_{2.8+\delta}$ as a function of $(T_c - T)$.	127
4.17 Normalized transport critical current density of $\text{YBa}_2\text{Cu}_3\text{O}_{7-\delta}$ Vs applied field normalized to a characteristic field H_0 .	128
4.18 (a) The diffraction pattern and its envelope $F(H)$ as the reduction factor for the critical current in Josephson junctions. (b) Calculated microwave absorption signal for different values of η_0 .	128
5.1 DLFDMA of $\text{YBa}_2\text{Cu}_3\text{O}_{6.85}$ at different modulation amplitude.	139
5.2 Variation of peak height (h_p) of DLFDMA of $\text{YBa}_2\text{Cu}_3\text{O}_{6.85}$ and $\text{Tl}_2\text{Ba}_2\text{CaCu}_2\text{O}_{2.8+\delta}$ as a function of modulation amplitude (A_m).	140
5.3 Variation of peak position (H_m) of DLFDMA of $\text{YBa}_2\text{Cu}_3\text{O}_{6.85}$ and $\text{Tl}_2\text{Ba}_2\text{CaCu}_2\text{O}_{2.8+\delta}$ as a function of modulation amplitude (A_m).	140
5.4 Variation of hysteresis area (ΔA) of DLFDMA of $\text{YBa}_2\text{Cu}_3\text{O}_{6.85}$ and $\text{Tl}_2\text{Ba}_2\text{CaCu}_2\text{O}_{2.8+\delta}$ as a function of modulation amplitude A_m	140

LIST OF FIGURES (Contd.)

Figures	Page
5.5 Log-log plot of h_p of DLFDMA of Hf-doped $\text{YBa}_2\text{Cu}_3\text{O}_{7-\delta}$ versus modulation amplitude.	141
5.6 Variation of $\log (H_m)$ of Hf-doped $\text{YBa}_2\text{Cu}_3\text{O}_{6.85}$ as a function of $\log A_m$.	141
5.7 Variation of $\log (\Delta A)$ of Hf-doped $\text{YBa}_2\text{Cu}_3\text{O}_{6.85}$ as a function of $\log A_m$.	141
5.8 Variation of h_p , H_m and ΔA of DLFDMA of $\text{YBa}_2\text{Cu}_3\text{O}_{6.85}$ and $\text{Tl}_2\text{BaCaCu}_2\text{O}_{8+\delta}$ as a function of microwave power.	142
6.1 DLFDMA of ZFC $\text{YBa}_2\text{Cu}_3\text{O}_{6.85}$ for different field scan.	163
6.2 DLFDMA of ZFC $\text{Tl}_2\text{Ba}_2\text{CaCu}_2\text{O}_{8+\delta}$ for different field scan.	164
6.3 Hysteresis area of first and second scan of DLFDMA of $\text{YBa}_2\text{Cu}_3\text{O}_{6.85}$ as a function of field exposed and field cooled.	165
6.4 Hysteresis area of first and second scan of DLFDMA of $\text{Tl}_2\text{Ba}_2\text{CaCu}_2\text{O}_{8+\delta}$ as a function of field exposed and field cooled.	165
6.5 Variation of H_m of DLFDMA of $\text{YBa}_2\text{Cu}_3\text{O}_{6.85}$ as a function of field exposure and field cooling.	166
6.6 Variation of H_m of DLFDMA of $\text{Tl}_2\text{Ba}_2\text{CaCu}_2\text{O}_{8+\delta}$ as a function of field exposure and field cooling.	166
6.7 Variation of h_p of DLFDMA of $\text{YBa}_2\text{Cu}_3\text{O}_{6.85}$ as a function of field exposure and field cooling.	167
6.8 Variation of h_p of DLFDMA of $\text{Tl}_2\text{Ba}_2\text{CaCu}_2\text{O}_{8+\delta}$ as a function of field exposure	167
6.9 DLFDMA of $\text{YBa}_2\text{Cu}_3\text{O}_{6.85}$ at different cooling field.	168
6.10 DLFDMA of $\text{Tl}_2\text{Ba}_2\text{CaCu}_2\text{O}_{8+\delta}$ at different cooling field.	169
6.11 Hysteresis area of DLFDMA of 1% Hf-doped $\text{YBa}_2\text{Cu}_3\text{O}_{7-\delta}$ as a function of cooling field.	170
6.12 h_p and H_m of DLFDMA 1% Hf-doped $\text{YBa}_2\text{Cu}_3\text{O}_{7-\delta}$ as a function of cooling field.	170

LIST OF FIGURES (Contd.)

Figures	Page
6.13 DLFDMA of positive field exposed $\text{YBa}_2\text{Cu}_3\text{O}_{6.85}$ at different negative field exposure.	171
6.14 DLFDMA of positive field exposed $\text{Tl}_2\text{Ba}_2\text{CaCu}_2\text{O}_{8+\delta}$ at different negative field exposure.	172
6.15 Hysteresis area of DLFDMA of positive field exposed $\text{YBa}_2\text{Cu}_3\text{O}_{6.85}$ and $\text{Tl}_2\text{Ba}_2\text{CaCu}_2\text{O}_{8+\delta}$ at different negative field exposure.	173
6.16 Peak height of DLFDMA of positive field exposed $\text{YBa}_2\text{Cu}_3\text{O}_{6.85}$ and $\text{Tl}_2\text{Ba}_2\text{CaCu}_2\text{O}_{8+\delta}$ at different negative field exposure.	173
6.17 Peak position of DLFDMA of positive field exposed $\text{YBa}_2\text{Cu}_3\text{O}_{6.85}$ and $\text{Tl}_2\text{Ba}_2\text{CaCu}_2\text{O}_{8+\delta}$ at different negative field exposure.	173
6.18 DLFDMA of positive field cooled $\text{YBa}_2\text{Cu}_3\text{O}_{6.85}$ at different negative field exposure.	174
6.19 Hysteresis area of DLFDMA of positive field cooled $\text{YBa}_2\text{Cu}_3\text{O}_{6.85}$ and $\text{Tl}_2\text{Ba}_2\text{CaCu}_2\text{O}_{8+\delta}$ as a function of negative field exposure.	175
6.20 Peak height of DLFDMA of positive field cooled $\text{YBa}_2\text{Cu}_3\text{O}_{6.85}$ and $\text{Tl}_2\text{Ba}_2\text{CaCu}_2\text{O}_{8+\delta}$ as a function of negative field exposure.	175
6.21 Peak position of DLFDMA of positive field cooled $\text{YBa}_2\text{Cu}_3\text{O}_{6.85}$ and $\text{Tl}_2\text{Ba}_2\text{CaCu}_2\text{O}_{8+\delta}$ as a function of negative field exposure.	175

CHAPTER I

INTRODUCTION

Abstract

This chapter gives a general introduction to the low field magnetic properties of high T_c superconductors. Magnetic properties of Type-I, ideal Type-II and hard superconductors are presented. The other relevant properties like flux flow, vortex pinning, critical state, granularity, superconducting glass and spin glass are also discussed. In addition, fundamentals of electron paramagnetic resonance are outlined.

1.1 GENERAL

The CuO based high transition temperature superconductors exhibit a number of interesting features. Among these are the magnetic properties. The exclusion of the flux is one of the hall marks of superconductivity. However, the high T_c materials are found to be extreme Type II superconductors, which means that there is a large field region, $H_{c1} < H < H_{c2}$, where Abrikosov flux vortices reside in the material. Due to the granular nature [1] of high T_c superconductors, the magnetic field penetrates into the sample much less than the thermodynamical critical field H_{c1} . In a polycrystalline sample the grains are oriented randomly and connected via Josephson junctions or weak links. These weak links or the Josephson junctions limit the critical current in the polycrystalline samples and give a number of interesting features in the low field region. Among these one of the interesting feature is that of low field dependent microwave absorption. Microwave absorption studies in normal metals and conventional superconductors have been used [2-4] to get information about the superconducting state below T_c ($\rho = 0$). For Phonon-mediated Type-II superconductors, the microwave surface resistance provides a well established method for studying the flux flow surface losses in bulk planar samples above H_{c1} . All high T_c superconductors give large field dependent microwave absorption when these are cooled below T_c . The experimental method used by the most of the workers is centered around conventional Electron Paramagnetic Resonance (EPR) spectrometer operating at the X-band frequencies 8.5 to 9.5 GHz. In our studies we also used the conventional EPR spectrometer operating at X-band. All high T_c superconductors have Cu atoms. Replacing Cu by any other transition metal, decreases the T_c very fast [5-6]. It is expected that the Cu-O planes play major role in these high T_c superconductors. EPR is

a powerful tool to find the state of the Cu atoms. But all high T_c superconductors are EPR silent. This thesis is mainly concerned with the low field dependent microwave absorption and EPR of Cu^{2+} signs in pure $\text{YBa}_2\text{Cu}_3\text{O}_{7-\delta}$, Hf-doped $\text{YBa}_2\text{Cu}_3\text{O}_{7-\delta}$ and $\text{Tl}_2\text{Ba}_2\text{CaCu}_2\text{O}_{8+\delta}$.

1.2 MAGNETIC PROPERTIES OF ISOTROPIC SUPERCONDUCTORS

The equilibrium behavior of a superconductor in a magnetic field is ultimately determined by two length scale parameters : the penetration depth, $\lambda(T)$ and the coherence length, $\xi(T)$. Their ratio, $= \lambda(T)/\xi(T)$, is the essential parameter used in the Ginzburg-Landau (GL) [7] theory of superconductivity. The value of this parameter is material dependent and divide the superconductors into two classes: Type I ($K < 1/\gamma^2$) and Type II ($K > 1/\gamma^2$). In equilibrium, a superconductor tries to stay in the lowest energy configuration. The response of a superconductor to the magnetic field reflects the competition between the condensation and field energies. The system tries to keep the favorable (negative) condensation energy of superconductivity (occurs over a length scale ξ) by not allowing the order parameter to vary. But as the field is increased, it becomes increasingly difficult to keep the field out. There is a surface energy involved with the boundary between the normal (where the field can penetrate) and the superconducting regions. The GL K parameter characterizes the surface energy by considering the competition of energies. For $K > 1/\gamma^2$, the surface energy is negative. In other words, a Type II superconductors finds it favorable energetically to allow some field into its interior.

The response of a Type-I superconductor to an applied magnetic field is that the superconductor almost completely excludes field from the interior ($B = 0$ inside; the Meissner effect) by setting up the shielding currents in a surface sheath. These currents and the local field fall proportional to $\exp(-x/\lambda)$ going inward from

the surface. This shielding remains perfect ($B = 0$ everywhere inside) till the thermodynamical critical field value, H_c , is reached at the surface. At this point superconductor becomes normal (if the demagnetization factor is zero), and the field inside is equal to the applied field value. If the demagnetization effects are not negligible, the internal field exceeds H_c before the applied field reaches a value H_c . An intermediate state exists where the system is composed of both normal field regions and superconducting regions. Once the applied field reaches a value H_c , all the superconductivity is destroyed.

Fig. 1.1 shows the magnetization for an ideal (no vertex pinning) Type II superconductors as a function of thermodynamic field strength. Type II superconductor excludes the field completely when the magnitude of the field is less than the lower critical field H_{c1} . As soon as the field is increased above H_{c1} , it becomes favorable to have a fraction of the field in the interior of the sample. This region is called the mixed state, since there exists a mixture of superconducting and normal regions in the interior of the sample in this case. Abrikosov [8] showed that the magnetic flux inside the sample is broken up into singly quantized flux vortices. Each vortex represents a fluxoid of value $\phi_0 (2 \times 10^{-7} \text{ G-cm}^2)$, the flux quantum for a superconductor. As the field is increased further, the number-density of vortices increases, thus increasing B (flux density) in the sample. Finally, at the value of upper critical field, H_{c2} , there is no superconducting region left inside the sample, and B in the sample becomes equal to the applied field (plus whatever normal state magnetism is present).

1.3 STRUCTURE OF VORTEX

The structure of a vortex in an isotropic superconductor

can be calculated directly for a material with a large K using the GL theory and a modified London theory. It is found that the order parameter goes to zero in the center of the vortex over a characteristic length ξ . The field is maximum in the center and falls off over a length λ as shown in Fig.1.2.

The currents associated with the local field lie in a plane perpendicular to the vortex direction. The field and the magnitude of the normalized order parameter have the following radial dependence.

$$f = \tan h \frac{\nu r}{\xi} \quad (1.1)$$

$$h(r) = \frac{\phi_0}{2\pi\lambda^2} K_0(r/\lambda) \quad (1.2)$$

Here ν is a constant of the order 1 and K_0 is the zero order Hankel function of imaginary argument. In the large limit, the vortex line energy density (linear density) can be calculated using the London formulation. This approach takes care of only field energy and kinetic energy contributions of the electrons to the total energy.

$$\epsilon_1 = \frac{1}{8\pi} \int (h^2 + \lambda^2 |\nabla \times h|^2) dS \quad (1.3)$$

Using the field distribution results the line energy per unit length is approximately given by

$$\epsilon_1 = \left(\frac{\phi_0}{4\pi\lambda} \right)^2 \ln K = \frac{H_c^2}{8\pi} \frac{4\pi\xi^2}{\lambda} \ln K \quad (1.4)$$

1.4 FLUX FLOW

Flux flow is a concept that is used in the discussions of both the magnetization and electronic transport. For an ideal Type-II superconductor (that is one with no pinning) there is always

finite resistance for any value of applied current in the mixed state. This does not mean that the superconducting order parameter is lost. It is still finite. The resistance is due to the flux flow; that is, the motion of vortices in response to the applied current.

An applied current produces a Lorentz force on each of the vortices,

$$f_L = J_S \times \frac{\Phi_0}{C} \quad (1.5)$$

causing them to move. The quantity J_S is the net supercurrent at the vortex. The force is at right angle to the supercurrent direction and so the vortex will accelerate in this direction. Bardeen and Stephen [9] showed that the motion of a vortex across this current flow will produce dissipation, with a net space averaged electric field in the same direction as the current flow.

$$E = \frac{B \times v}{C} \quad (\text{In C.G.S.}) \quad (1.6)$$

The $J \cdot E$ product is the power dissipated. The velocity of the vortex line in response to the Lorentz force will reach a terminal value when the viscous damping forces of the dissipation balance the Lorentz force,

$$J \frac{\Phi_0}{C} = \eta v_L \quad (1.7)$$

Hence η is the effective viscosity, equation 1.7 represents the steady state situation. The vortices pass right out from one edge of the sample and new ones are created at the other edge, giving rise to a continuous flux flow which results in resistance. By using equations (1.6) and (1.7) the resistivity can be written in terms of the viscosity,

$$\rho_f = \frac{E}{J} = B \frac{\phi_0}{\eta c^2} \quad (1.8)$$

Bardeen and Stephen calculated the viscosity

$$\begin{aligned} \eta &= \frac{\phi_0^2}{(2\pi a^2 c^2 \rho_n)} \\ &\simeq \frac{\phi_0 H_{c2}}{\rho_n c^2} \end{aligned} \quad (1.9)$$

and determined the flux flow resistivity,

$$\rho_f = \rho_n \left[\frac{a}{\xi} \right]^2 \frac{B}{H_{c2}} \quad (1.10)$$

This resistance is linear in the induction, B.

A complete description of the vortex motion will now be given. Before the vortex moves, the force is directed exactly perpendicular to the current direction. However, once it moves, there is a component of the total supercurrent interacting with the vortex which is perpendicular to the applied current flow. Now the total has a component parallel to the applied current direction,

$$f_m = \left[\frac{Ne}{c} \right] v_L \times \phi_0 \quad (1.11)$$

If the vortex velocity is high, this component of force, known as the Magnus force can be quite substantial Nozieres and Vinen [10] pointed out that the condition for dynamical equilibrium is given by

$$f_m + f_L = \eta v_L$$

$$\left[\frac{Ne}{c} \right] (v_L - v_T) \times \phi_0 = \eta v_L \quad (1.12)$$

where v_T is the velocity of the superelectrons due to the applied transport current. The result of these equations is that the vortex velocity will be directed at an angle from the perpendicular direction. This produces a transverse voltage in addition to the longitudinal one. As the viscosity becomes smaller (v_L can become larger), v_L becomes closer to being parallel with v_T . If a case exists, where η was zero, then the vortex will flow along the transport current. In most actual samples, η is large (mostly due to pinning), v_L is consequently small, and thus the Magnus force is small compare with the Lorentz force.

1.5 VORTEX PINNING

An ideal Type-II superconductor is one which remains always in thermodynamic equilibrium. In such a system the flux density changes without any hindrance when the applied field is changed. Most real Type-II superconductors have defects which tend to pin vortices. The flux cannot easily move around within the sample, as is the case with an ideal Type-II superconductor.

There are several different types of pinning. A list of the various types will not be given here. However, in general one may say that a pinning site locally produces a potential well for the vortex. the lowest energy situation corresponds to the vortex residing in the bottom of this well. One type of pinning involves the presence of a region with defects in which the electronic mean free path, ℓ , is short compared to its value in defect free material. The coherence length will be reduced in this region according to the typical behavior of a dirty superconductor $1/\xi = 1/\xi_0 + 1/\ell$ [10]. A vortex is a topological excitation in which the order parameter falls to zero in the core region. The order parameter recovers its bulk value in a distance equal to the coherence length. Thus, the vortex

core removes an amount of condensation energy approximately equal to $(H_c^2/8\pi)(\xi^2 l)$, where l is the length of the vortex line. If the coherence length is reduced locally in a defect region, the core will destroy less superconducting condensation energy by residing in this region than if it resides in a defect free region. Thus, a pinning potential well is effected.

Consider the following simple cases: first, a single vortex pinned to a defect site in a superconductor. It sits in the bottom of the potential well. If a current is applied, the vortex will tend to move in response to the Lorentz force. If the Lorentz force is less than the maximum pinning force, $f_L < f_p$, ($f_p = \text{grad } V$) then the vortex will stay pinned. When the current is raised to a level so high that the pinning force can't compensate for the Lorentz force, $f_L > f_p$, then the vortex will become free to move. This vortex may encounter other pinning sites in which it may become retrapped. The current at which the vortex just becomes unpinned, $f_L = f_p$, is defined as the critical current for a Type-II superconductor. Generally speaking, critical current is the current at which resistivity begins to appear. For a Type-II superconductor, this is defined as the current at which vortices start to move, since dissipation occurs once vortices move. It should be noted that the critical current defined in this way is not the same as the GL depairing current.

1.6 BEAN'S CRITICAL STATE MODEL

Early in the history of the field, it was discovered that most Type-II superconductors exhibited magnetic properties that were labelled as "irreversible" and "hysteretic". In analogy with ferromagnetics, these were called "hard" superconductors. Today we know that this behavior is due to vortex pinning. Bean [11] used a

simple model to describe the magnetization of a Type-II superconductor with pinning, the "critical state" model. In this model, the pinning force is uniform in the material and can be described in terms of the critical current through the relation $f_p = J_c \times \Phi_0 / c$. To understand this, we consider a cylindrical sample initially in zero field and with no flux inside. When the field is raised from zero but is still less than H_{c1} , all flux is kept outside the sample just like the case for the ideal Type-II superconductor (Meissner effect). As H is increased above H_{c1} it is thermodynamically favorable for flux to enter the sample. However, because of the pinning force, flux does not distribute to a uniform density. Instead the flux density is highest at the edge of the sample and lower further inside. When the vortices first enter, the gradient of B is large (B is the local flux line density). A large current is present because of this gradient ($\text{grad } B = 4\pi J/c$ for cylindrical geometry). It produces a Lorentz force which pushes the vortices further inside. Equivalently, it can be said that the vortices exert forces on each other, and the net pressure tends to push the vortices towards the interior of the sample. (Recall that the field and current are related by one of Maxwell's equations.) As the vortices move inward, the gradient of B decreases, reducing the Lorentz force. Vortices continue to move inside until the Lorentz force equals the pinning force. At this point, the flux will cease to move inward since the Lorentz force is no longer sufficient to overcome the pinning force. The flux density gradient is said to be at the critical state. The circulating currents due to the gradient in B flow at a value of J_c . For example as discussed just now it is important to note that the total amount of flux in the sample is less than for the equilibrium case with no pinning. Therefore, the resulting magnetization is larger than for the case with no pinning. The difference between the magnetizations for the two cases is

referred to as the *irreversible magnetization*. This picture can be used to predict the magnetization as a function of field.

The magnetization can be computed from

$$4\pi M = \frac{\int h_i dV}{\int dV} - H \quad (1.13)$$

where h_i is the local value of the internal magnetic field and H is the thermodynamic field. For a cylindrical sample the magnetization as a function of increasing field is given by

$$4\pi M \quad 0 < H < H_{c1} \quad (1.14)$$

$$4\pi M = -H + \frac{H^2 - H_{c1}^2}{H^*} + \frac{H_{c1}^2(3H - 2H_{c1}) - H^3}{3H^*^2} \quad H_{c1} < H < H^* + H_{c1} \quad (1.15)$$

$$4\pi M = -\frac{H^*}{3} \quad H^* + H_{c1} < H \quad (1.16)$$

where H^* is given by $4\pi J_c R / 10$ ($[J_c] = \text{amp/cm}^2$, $[R] = \text{cm}$), the lowest field at which the sample is in the critical state. The large field relation can be rewritten in terms of J_c to give $M = J_c R / 30$. Within the context of this model, this is a useful relation in the sense that the critical current can be estimated by measuring the irreversible magnetization. This is often done to estimate the critical current (called the Bean critical current) for a sample. Due to the hysteretic nature of this model, if the field is swept up to a high value and then back to zero, flux will remain trapped in the sample. Like the case of the glass system, this trapped magnetization can be called the remanent magnetization. The Bean model is somewhat naive because it assumes a field independent pinning (i.e. J_c is not a function of field). Nevertheless, it is a

useful tool in understanding the irreversible magnetization.

The magnetizations of superconductors in the cases without pinning and with pinning are depicted in Fig. 1.3. Better critical state models have recently been proposed, where the critical current is taken to be field dependent [12,13].

It should be noted that the Bean critical state model does not include the effect of temperature other than in $J_c(T)$. In this model, once the flux distribution moves to the critical state, it does not change any further. In other words, once the critical state has been achieved, the magnetization is stable and doesn't change with time. However, experiments shows that the irreversible magnetization of a Type-II superconductor does change with time. The concept of flux creep is introduced to allow thermally activated flux motion at and below the critical state gradient.

1.7 FLUX CREEP

The idea of flux creep as the origin of a relaxing magnetization is actually a straightforward extension of the ideas introduced in the critical state model. In Bean's critical state model, once grad B has reached the critical state value, it doesn't change any more. The flux remains pinned. However, with flux creep the gradient can be reduced further by the thermal activation of the vortices out of their pinning wells. Work by Anderson and Kim, et al [14-16] first laid down these phenomenological ideas. Consider a superconductor having pinning sites of well depth U_0 . For the present we will consider the case where all of the pinning sites have the same characteristic well depth, i.e., a single activation energy model. The amount of flux which moves in a thermally activated hopping event may involve one or more vortices. This is a consequence of the mutual repulsion between vortices of the same

helicity. The flux that moves in a thermally activated event will be referred to as a *flux bundle* to make the argument general. The probability for a flux bundle to hop out a pinning well is given by a Boltzman factor. By having a net current flowing in the system (due to ∇B or an applied current), the effective well depth is reduced by a term which represents the tipping of the potential well structure, $U = U(U_0, J)$. This term is given by the Lorentz force times the distance the vortex bundle moves. To describe the effective well depth, Anderson and Kim used the linear relation $U_{\pm} = U_0 \pm f_L VL = U_0 \pm JBVL/c$, where U_- is for the vortex bundle to hop down the potential hill and U_+ is for the bundle to hop up the hill as in Fig. 1.4. The quantity V is the effective volume of the flux bundle, and L is the hopping length. Defining $J_{co} = (U_{oc}/BVL)$, the effective well depth can be rewritten as $U_{\pm} = U_0 (1 - J/J_{co})$. J_{co} is the current at which, in the absence of thermal activation, the vortices will move because the potential is tipped far enough. In the Arrhenius fashion, the hopping rate is given by

$$\nu = \nu'_0 \exp[-U_{\pm}/k_B T] = \nu'_0 \exp[-U_0/k_B T] \sinh \left[\frac{JU_0}{J_{co} k_B T} \right] \quad (1.17)$$

To short the notation a bit let $\gamma_0 = U_0/k_B T$ and write

$$\nu = \nu'_0 \exp[-\gamma_0] \sinh \left[\gamma_0 \frac{J}{J_{co}} \right] \quad (1.18)$$

One can use this relation in various circumstances. The decay of flux in a sample in which the field has been changed is of present concern.

1.8 GRANULARITY

A granular superconductor contains many grains or islands connected to their neighbors by tunnel junctions or by normal metal proximity-effect weak links. Such systems typically show the two stage transition temperature T_{co} of the superconducting grain or island, the resistance drops, reflecting the loss of the resistance of grains or islands. On cooling further, the resistance drops continuously as the Josephson coupling energy in the weak links begins to overcome the thermal fluctuations and introduce correlations between the phases of the superconducting wave functions on the various islands. Finally, at the lower temperature, called T_c , the phases lock together to give long range phase coherence and zero resistance. On physical grounds, one anticipates that $kT_c \approx E_J(T_c) = \hbar I_c(T_c)/2e$, when E_J is the Josephson coupling energy between adjacent grains, and I_c is the associated intergranular current. In fact in the mean field approximation $kT_c = (z/2) E_J(T_c)$ where z is the number of nearest neighbor grains.

1.9 EFFECTIVE MEDIUM PARAMETERS OF A GRANULAR SUPERCONDUCTOR

1.9.1 Model of a Granular Superconductor

To facilitate a semiquantitative discussion of the effects of granularity on the properties of high temperature superconductors, Tinkham and Lobb [1] adopt a highly simplified model of grains of ideal crystalline superconductor connected in three-dimensional cubic array by weak links, each having the critical current I_c , lattice spacing of the array and the volume of the grain being, a and V_g respectively are taken.

Two limiting regions occur in the granular superconductors, depending on how tightly coupled the grains are. A useful measure of

this coupling strength is the ratio of the macroscopic critical current density set by the Josephson effect coupling, namely $J_{CJ} = I_c^2/a^2$, to that set by the critical current density J_{CG} inside the grains (which was assumed to be larger than $\xi_g \approx 10 \text{ \AA}$ in high T_c systems and fill the majority of the sample volume) since J_c value greater than 10^6 A/cm^2 has been observed experimentally in the crystalline sample. Granular material with typical measured value of $J_c \approx 10^3 \text{ A/cm}^2$ will correspond to the loosely coupled limit, in which the measured J_c is limited by J_{CJ} .

In analyzing the response of the granular composite medium, it is important to separate two regions depending on the length scale a of the granular structure relative to the length scale $(\Phi_0/H)^{1/2}$ set by the size of an area containing one flux quantum. For fields low enough that $a < (\Phi_0/H)^{1/2}$ the electromagnetic response of the material can be treated as that of a homogeneous effective medium with suitably chosen parameters. For higher fields, the inhomogeneous structure plays an explicit role, with intrinsic parameters of the grains themselves determining the critical behavior. The following analysis is taken here to find the suitable parameters of a homogeneous effective medium i.e. in the limit $a < (\Phi_0/H)^{1/2}$.

1.9.2 Critical Current

Zero field macroscopic critical current of a granular super conductor will be set by the intergranular I_c

$$J_{CJ} = I_c^2/a^2 \quad (1.19)$$

where a is taken as the grain size.

1.9.3 Penetration Depth

In response to a magnetic field, a three dimensional array of junctions set up the screening currents, analogous to those in bulk samples, which prevents the field from penetrating deeply into the sample. The effective penetration depth λ_J is given by

$$\lambda_J = \left(\frac{c \phi_0}{8\pi^2 a J_{CJ}} \right)^{1/2} \quad (1.20)$$

Comparing this with the usual formula for the London penetration depth

$$\lambda_L = \left(\frac{mc^2}{4\pi n_s e^2} \right)^{1/2} \quad (1.21)$$

we see that we can define an effective density of superconducting electrons n_s [or $|\psi|^2$ in Ginzburg-Landau theory] that is proportional to $(a J_{CJ})$.

The equation (1.20) get reduced to the usual expression for the Josephson penetration depth in a classic tunnel junction if a is replaced by $(t+2\lambda)$, the thickness of the region penetrated by flux if the barrier thickness is t and λ is the London penetration depth in the grain. Taking the representative values $J_{CJ} = 10^3 A/cm^2$ and $a = 10^{-4}$ cm find $\lambda_J = 5 \times 10^{-4}$. The physical significance λ_J is that a sufficiently weak magnetic field will be screened exponentially over this length.

1.9.4 Coherence Length

In a conventional superconductor the GL coherence length $\xi(T)$ reduces to ξ_0 for $T \ll T_c$, if the metal is "clean" and to

$(\xi_0 l)^{1/2}$ if it is "dirty" i.e. if mean free path $l < \xi_0$; in both cases it diverges as $\left(1 - \frac{T}{T_c}\right)^{-1/2}$ near T_c .

The conventional interpretation of ξ as the distance scale over which $|\psi|$ varies is not applicable here, because in this loosely coupled grain regime the value of $|\psi|^2$ is determined by equation (1.20) and (1.21) and is not dependent on the applied fields or macroscopic boundary conditions. An alternative manifestation of ξ in the standard GL theory is that the maximum phase gradient $\nabla\gamma$ (i.e. that at J_c) is $\frac{1}{\sqrt{3}} \xi$. For the granular superconductor, the corresponding maximum phase gradient at J_{cJ} is $\nabla\gamma = \pi/2a$. From these two expressions we get

$$\xi_J = \frac{2a}{\sqrt{3\pi}} \approx 0.4a \quad (1.22)$$

for T well below T_c but nominally independent of T .

1.9.5 Thermodynamic Critical Field

The thermodynamic critical field H_c is defined by equating $H_c^2/8\pi$ with the condensation energy per unit volume. In the weak-field loosely coupled granular case, the most parallel energy is that resulting from the phase-locking of the Josephson coupling between grains. In cubic array model, each grain has 6 neighbors. Summing over these 6 links, dividing by 2 to cancel double counting and normalizing to a unit cell volume of a^3 we have,

$$H_{cJ}^2/8\pi = 3E_J/a^3$$

$$H_{cJ} = \left[\frac{12\phi_0 J_{cJ}}{ca} \right]^{1/2} \quad (1.23)$$

Inserting the representative value of J_{CJ} and a we get value of $H_{cJ} \simeq 1.6G.$

1.9.6 Ginzburg-Landau Parameter κ_J

$$\kappa_J = \frac{\lambda_J}{\xi_J} = \left(\frac{3\Phi_0 c}{32 J_{CJ} a^3} \right)^{1/2} \quad (1.24)$$

Representative value of κ_J for $YBa_2Cu_3O_7 \simeq 10.$

1.9.7 Lower Critical Field H_{c1J}

In case of a Type-II superconductor with high value, H_{c1} is given by

$$H_{c1} = \left(\frac{\Phi_0}{4\pi\lambda^2} \right) \ln \kappa \quad (1.25)$$

Similarly

$$H_{c1J} = \left(\frac{\Phi_0}{4\pi\lambda_J^2} \right) \ln \kappa_J$$

or
$$H_{c1J} = \left(\frac{2\pi a J_{CJ}}{c} \right) \ln(\lambda_J / \xi_J) \quad (1.26)$$

Representative value of $H_{c1J} \simeq 0.5 G.$ The physical significance of H_{c1J} is that it sets the limit for the strength of external fields that are screened exponentially in distance λ_J by reversible surface screening currents. Above H_{c1J} the flux penetrates into the junctions. In this way, a sort of "Bean model" penetration occur for $H > H_{c1J}$, in which the flux penetrates between the grains with field gradient $4\pi J_{CJ}/c$.

1.9.8 The Upper Critical Field H_{c2J}

In conventional Type-II superconductors, $H_{c2} = \frac{\phi_0}{2\pi\xi^2}$ of the

field at which the material makes a second order phase transition into the normal state. Applying the same formula to the granular system, using ξ_J

$$H_{c2J} = \frac{3\pi \phi_0}{8a^2} \quad (1.27)$$

which is dependent only on the grain size and has a value ≈ 24 G for $a = 1 \mu\text{m}$. Since the superconductivity of the grains is essentially unaffected by such small fields, this field does not have the conventional significance of marking the extinction of all the superconductivity. Rather, it marks the point at which the flux enclosed in each unit cell is sufficient to change by 2π the sum of four gauge-invariant phase differences γ_i around the perimeter of square plaquet. Since fluxoid quantization requires that the sum

$$\sum \gamma_i = 2\pi \phi/\phi_0 \pmod{2\pi} \quad (1.28)$$

where ϕ is the magnetic flux enclosed, a flux change by ϕ_0 is sufficient to complete a cycle.

1.10 SUPERCONDUCTING GLASS AND RELATED MODELS

1.10.1 What is a glass?

It is helpful to think of a glass in terms of a configurational space free energy diagram. This diagram represents the topology of the free energy surface as a function of the various configurations the system can take. A glassy state is typically prepared by cooling from a liquid-like state, where the system can

easily test all its available configuration space in a short time scale and find its lowest energy state. In the liquid-like state, the system is ergodic [18]. That is, the typical observation time (τ_{exp}) is much greater than the largest relaxation time (τ_{max}), and the system explores all the regions of phase space with the equilibrium probability. In the ergodic regime, the time average performed by the experiment will be equivalent to an average from equilibrium mechanics (Gibbs average). At these temperatures, the energy diagram is relatively smooth on the scale of thermal energy.

The configurational energy diagram of a glass is often a function of temperature such that as the temperature is lowered, the energy surface becomes more rough. There will be a temperature where the roughness becomes so high that the thermal energy is not sufficient to let the system test all of the configuration space in a short time. The phase space has become split up, with large energy barriers (hills) between the low energy states (valleys) as in Fig.1.5. One, then finds that τ_{max} has become very large. Therefore at low temperatures, the glass system is non-ergodic over experimental time scales. Naturally, the irreversible behavior is found in the non-ergodic regime. The crossover from ergodic to non-ergodic is what defines the glass transition. The temperature at which this crossover occurs is called the glass temperature, T_g .

If the system is cooled slowly, it will always have enough time to weight the lowest energy state with the highest probability, that is, if it is cooled slowly enough to have $\tau_{\text{exp}} \gg \tau_{\text{max}}$ at all temperatures passing through. Since τ_{max} quickly becomes enormous as the temperature becomes less than T_g , this indicates that one will have to have an infinite amount of patience to keep the sample in equilibrium while cooling it. This is a difficult thing to do experimentally. However, one might say that a relatively slowly cooled system (cooled at a reasonably slow rate), keeping all

independent variables constant, is in a quasi-equilibrium state (i.e., close enough to equilibrium for most purposes). The situation, however, is drastically different when the system is cooled to a temperature below the glass transition and then an independent variable, which alters the shape of the energy surface (like a conjugate field), is suddenly changed. Now the system can be trapped in a high energy state, and the thermal energy available is not sufficient to quickly relax the system to the lowest energy state. Progress towards the lowest energy state will occur, however, but because of the large energy barriers that must be overcome, it will occur very slowly. If this progression can be observed in an experiment, it will be seen as a nonexponential relaxation. The exact form for the relaxation depends on the microscopic details of the system under study. The idea of hierarchical relaxation [19] is useful in many instances.

A central issue is how the energy surface becomes rough. Or, in other words, why are some systems glasses and others not? The answer again depends on the microscopic details of the system. A common feature of glasses is some sort of frozen-in disorder. Many physical systems that exhibit glassy behavior require both frustration and disorder. A system is said to be frustrated when it has a Hamiltonian that is composed of many terms which cannot be simultaneously minimized. As a consequence, there are many alternate configurations that the system can take which have approximately the same energy. However, below the glass transition, to pass from one configuration to another usually requires the system to pass through intermediate configurations of much higher energy. A widely studied example of a glass is the spin glass. It is worth discussing a few main points of the spin glass as an introduction to the superconducting phase glass.

1.10.2 The Spin Glass

Spin glass systems are usually described by a Hamiltonian of the following form,

$$\mathcal{H} = - \sum_{\langle i,j \rangle} J_{ij} S_i \cdot S_j \quad (1.29)$$

where S_i and S_j are the spins of the i th and j th sites. The coupling energy, J_{ij} , varies in magnitude and sign due to random placement of the spins in the system. Such is the case in the example of Mn atoms at low dilution in bulk Cu. The Mn spins interact with each other through the conduction electrons of the Cu via the RKKY interaction [20-22]. The RKKY interaction is a function which oscillates with distance between spins as

$$J(R) = J_0 \frac{\cos(2k_F R + \phi_0)}{(k_F R)^3} \quad (1.30)$$

Therefore, depending on the distance between two spins, J_{ij} can either be positive (tending to align spins) or negative (tending to anti-align spins). For a system of randomly placed atoms, \mathcal{H} will generally have some frustration. There will be a temperature below which the thermal energy will become small in comparison to the coupling energy. The system will then become frozen into a particular configuration and will not be able to easily access the other configurations of the nearly equal energy. Because of the disorder and frustration there is no long range spin order, i.e., $\langle S_i \rangle = 0$, but there does exist a nonvanishing spin glass order parameter defined as $q = [\langle S_i^2 \rangle]_{av} \neq 0$ [23]. Here $\langle \rangle$ denotes a statistical mechanical average and $[\]_{av}$ is a configurational average.

In this system the canonical variables in the Hamiltonian are the spins, S_i . The field which is conjugate to the spins is the

magnetic field,

$$\mathcal{E} = - \sum_{\langle i,j \rangle} J_{ij} S_i \cdot S_j - \sum_i S_i \cdot H \quad (1.31)$$

Obviously, the application of a field can change the energy surface. It has the tendency to align the spins. If the field is applied above T_g and the sample is subsequently cooled in this field below T_g (that is, field cooled, FC), the spins will have a tendency to get aligned to some degree in the frozen-in state (i.e., $\langle S_i \rangle \neq 0$). When the field is turned off, the system will be trapped into a configuration where there is still some alignment of spins. However with the field off, the lowest energy state is one in which $\langle S_i \rangle = 0$. The system cannot be immediately relaxed to this state because of the presence of large energy barriers. At $T = 0$, it will remain at the spin aligned state since there is no thermal activation for the configuration to change. At finite temperatures, a slow relaxation to a $\langle S_i \rangle = 0$ state will be observed. Therefore, the aligned state is metastable. One can observe this relaxation by measuring the magnetic moment of the sample as a function of time. With the field on, the sample has a net moment. When the field is turned off it still has a remanent moment that decays with time as $\langle S_i \rangle \neq 0$ goes to $\langle S_i \rangle = 0$. This decreasing magnetization is termed the thermo-remanent magnetization. Alternatively, the system can be cooled through T_g in zero magnetic field so that $\langle S_i \rangle = 0$ at some low temperatures (zero field cooled, ZFC). By subsequently switching on the field, one sees a slow response of the system to a state of alignment and an increasing magnetization is be observed. The resulting magnetization in the FC and ZFC cases are generally different (Fig. 1.6), demonstrating the frozen-in nature of the non-ergodic regime. Below T_g , the configuration of the system is very dependent on thermomagnetic history. So we see that one can

experimentally probe the glassy nature of this system through the measurement of the moment versus time. As already mentioned, to predict the exact form of the relaxation function is essentially intractable for even simple glassy systems. Nonetheless, much work has been devoted to modeling the relaxation process in complex systems such as the spin glass [18].

1.10.3 The Superconducting Phase Glass - Granular Systems and Arrays

One can imagine a system similar to the case of a XY spin glass in which the spin is replaced by superconducting phase as the canonical variable. Consider a granular superconductor that is composed of randomly positioned superconducting grains embedded in a nonsuperconducting host matrix (either insulating or normal metal) as in Fig. 1.7.

The grains are coupled to each other by Josephson tunneling (insulating host) or by the proximity effect (normal metal host). If the grain size is less than the GL coherence length and the penetration depth of the grain material, a distinct order parameter can be written for each grain as $\psi_i = \psi_i e^{i\phi_i}$, and a Hamiltonian can be written for the energy coupling the grains,

$$\mathcal{H} = - \sum_{\langle i,j \rangle} J_{ij} \cos(\phi_i - \phi_j) \quad (1.32)$$

The coupling energy is $J_{ij} = (\hbar/2e)I_{ij}$ where I_{ij} is the critical current between grains i and j. (The requirement on the grain size is imposed so that amplitude fluctuations in the condensed wave function and magnetic field within a single grain can be ignored.) If the grains are coupled by Josephson tunneling, the critical current is given by the Ambegaokar-Baratoff [24] relation

$$I_{ij} = \frac{\pi \Delta(T)}{2e R_{ij}} \tanh \left[\frac{\Delta(T)}{2k_B T} \right], \quad (1.33)$$

where $\Delta(T)$ is the BCS gap parameter and R_{ij} is the normal state resistance of the junction. If the grains are proximity-coupled the critical current is given by

$$I_{ij} = C(1 - T/T_{cg})^2 \exp \left[-r_{ij}/\xi_n(T) \right] \quad (1.34)$$

where C is a constant, T_{cg} is the transition temperature of the grains, r_{ij} is the separation between grain centers, and $\xi_n(T)$ is the coherence length of the normal metal. In the presence of an applied magnetic field, the Hamiltonian becomes

$$\mathcal{H} = \sum_{\langle i,j \rangle} J_{ij} \cos(\varphi_i - \varphi_j - A_{ij}) \quad (1.35)$$

with $A_{ij} = \frac{2\pi}{\phi_0} \int_i^j \mathbf{A} \cdot d\mathbf{l}$

This Hamiltonian has some similarity to the XY spin glass Hamiltonian. However, here the source of the randomness is contained in A_{ij} due to the random positions of the grains. It should be noted that randomness in J_{ij} (which is always positive) does not produce frustration. Frustration effects can come only from the random A_{ij} . Therefore, J_{ij} can be treated as constant, since it doesn't contribute to the essential physics. Numerical work by Ebner and Stroud [25] shows that such a system does indeed have a frustrated Hamiltonian. For finite fields, a closed loop cluster cannot find a state which simultaneously minimizes all the bond energies. The granular superconductor system contains many frustrated loops. At high temperatures, the entire system can choose between many nearly degenerate "ground states". Of course there is only one true ground

state in a finite system, but others are excited by just a small energy above it. At lower temperatures, the system can get trapped in one of these ground states and is separated from the others by large energy barriers. So as before, the configurational free energy surface is very rough. As in the case of the spin glass, varying the magnetic field can change the energy surface, so that at low temperatures the system has a difficult time reaching the new ground state once the field is changed.

The canonical variables in the phase glass Hamiltonian are the phases on the grains. However, the magnetic field is not a conjugate field to the phase variables like it is to the spin variables in the spin system. Thus, the phase glass cannot be probed as directly as the spin glass can. The phases are related to the magnetic field response in a more indirect way. The magnetic moment of a cluster in this system is given by

$$\mu = \frac{1}{2c} \sum_{\langle i,j \rangle} \left\langle \mathbf{x}_{ij} \times \mathbf{I}_{ij} \sin(\varphi_i - \varphi_j - A_{ij}) \mathbf{x}_{ij} \right\rangle \quad (1.36)$$

where the sum is over all neighboring grains in a cluster, $\mathbf{x}_{ij} = (\mathbf{x}_i + \mathbf{x}_{ij})/2$ is the vector joining the origin to the position of the midpoint between the i^{th} and j^{th} grains, and $\mathbf{x}_{ij} = \mathbf{x}_j - \mathbf{x}_i$ is the vector distance between those grains. There is another immediate difference between the phase glass model and spin glass systems. In spin glasses the field tends to increase order in the system by aligning the spins, with higher fields tending to produce more order. For the phase glass, the field is the source of the frustration in the A_{ij} term. Higher fields do not increase the amount of order in the system. The formal thermodynamic treatment of the phase glass Hamiltonian involves treating the phases as classical variables within a canonical ensemble. The Helmholtz free energy is given as

$$F = -k_B T \ln Z, \quad (1.37)$$

$$Z = \int \left[\prod_i d\varphi_i \right] \exp \left(\frac{-E}{k_B T} \right). \quad (1.38)$$

The magnetic moment of the system is then

$$\mu = - \left[\frac{\partial F}{\partial H} \right]_T. \quad (1.39)$$

As is the case with the spin glass, ergodicity is broken at low temperatures. Thus, the formal thermodynamic treatment with its equilibrium probabilities is only useful in the ergodic region and has a little meaning in the non-ergodic regime. The phase glass system is expected to have many features in common with the spin glass. (1) One finds the moment of the sample to be dependent on the thermomagnetic history. For example, by slowly cooling the system in a field it will be in a quasi-equilibrium configuration; its magnetic moment being independent of time. On the other hand, if the sample is cooled through T_g in zero field, and then the field is turned on at low temperatures, one will find a different value for the moment (larger in magnitude). This moment will slowly relax towards the value of the moment on the quasi-equilibrium line. (2) The system can exhibit non-exponential relaxation in response to a change in magnetic field. (3) There does exist a glass transition temperature, T_g , where the thermal energy becomes large enough for the system to be treated as ergodic over experimental times. Many of these features have been observed in computer simulations of the phase glass model [25-27]. A mean field treatment of a granular superconductor also indicates the existence of a glass phase for this model [28].

1.11 ELECTRON PARAMAGNETIC RESONANCE

1.11.1 The Resonance Condition

A dc magnetic field applied to the paramagnetic species having magnetic moment causes splitting in the degenerate ground state level. The splitting depends on the strength of the magnetic field. Resonance occurs with absorption of energy from oscillating magnetic field perpendicular to the static magnetic field when the energy difference between two splitted energy levels matches with the quantum energy of the oscillating magnetic field i.e.

$$\hbar\nu_0 = E_2 - E_1 = g \beta H_0 \quad (1.40)$$

ν_0 is the resonance frequency, g is a dimensionless proportionality constant known as the Lande factor and its accurate value for free electron is 2.0023. β is Bhor-magneton and given as

$$\beta = \frac{e\hbar}{4\pi mc} \quad (1.41)$$

e and m are charge and mass of electron respectively, \hbar Plank's constant and c velocity of light. With these numerical values, the resonance conditions becomes

$$H_0 = \frac{0.71449}{g} \nu_0 \text{ (GHz)} \quad (1.42)$$

1.11.2 Thermal Equilibrium and Saturation

Consider a two level magnetic system having energy E_1 and E_2 ($E_2 > E_1$) with their equilibrium population N_1 and N_2 ($N_1 > N_2$) and total population N ($N_1 + N_2$) the Boltzman relation would give

$$\frac{N_1}{N_2} = \exp \left(\frac{E_2 - E_1}{K_B T} \right) \quad (1.43)$$

where T is the temperature of the system and K_B is Boltzman constant on applying a resonance rf field to such a system (i.e. $E_2 - E_1 = h\nu_0$)

$$\frac{dE}{dt} = P(E_2 - E_1)(N_1 - N_2). \quad (1.44)$$

Here P is the Einstein stimulated absorption probability. Equation (1.44) shows that with time increasing, the population difference $N_1 - N_2$ will decrease and magnitude of net absorption of energy will tend to be zero, making the system incapable of absorbing any more power. This situation is termed as the saturation condition.

1.11.3 Spin Lattice Relaxation

In a two level magnetic system described in section 1.11.2 the spin system has its maximum achievable energy when $N_2 - N_1 = 0$ (a higher energy state is possible when more than two levels are present) after absorption of incident microwave characterized by the rate constant k_2 (which is proportional to its power) as shown in Fig. 1.8.

Further, if one defines the spin temperature T_S corresponding to the situation at which Boltzman distribution would yield the observed population difference; and lattice temperature T_L as that of the environment around the spin system and let initially $T_S > T_L$. It can easily be shown that the rate $\frac{dE}{dt}$ of energy transfer from spin system to the lattice is

$$\frac{dE}{dt} = k_1 K_B (T_S - T_L) \quad (1.45)$$

where k_1 is the first order rate constant as shown in Fig. 1.8 and K_B is the Boltzman constant. Hence it is easy to see that under the influence of resonant microwave field as long as $k_1 > k_2$ the spin systems can efficiently release the extra energy to the lattice.

When $T_S \approx T_L$ a very little change in $N_2 - N_1$ from the unperturbed value will occur when $k_2 > k_1$ and the spin system can no longer release the extra energy to the lattice quickly enough. Thus $T_S - T_L$ and $N_2 - N_1$ will decrease. This leads to the saturation phenomenon.

Thus in case of strong spin-lattice coupling, the thermal equilibrium values of N_1 and N_2 are maintained and the energy is continuously absorbed under resonance conditions. A weak coupling leads to saturation even under low incident power levels, resulting in weak signals and distortion of the line shapes.

1.11.4 Crystal Field

In general discussion of EPR it is necessary to consider the influence on the paramagnet of its immediate environment. This environment is characterized by the existence of the elements of symmetry and the effect on the paramagnet is determined by the existence of such elements. Three theories have been developed to account for these facts : the crystal field, the ligand field and the molecular orbital theories. Indeed, these theories are closely related in that the symmetry properties and requirements remain exactly the same in all the three cases. The difference among them arise from assigning to chemical bonding and purely electrostatic effects, different relative importance.

In the crystal field theory, the paramagnetic ion is considered as subjected to purely electrostatic forces, so that its unpaired electrons may be simply described by atomic orbitals strictly localized in the paramagnetic ion. The influence of environment is then reduced to evaluating the form of electrostatic potential produced by the immediate neighbor atoms treated as point charges.

In the ligand field theory, the electrostatic approach is complemented with the assumption that some chemical bonding does infact exist between central atom and each of the nearest neighbor molecules, called the ligand molecules. In this approach, the unpaired electron can not be described in terms of pure atomic orbital. Since the electrons are no longer localized in the central ion. In fact if the covalence of metal ligand bond is small, this approach lead (for all practical purposes), to the crystal field results.

In the case of highly covalent bonding, it is necessary to treat the problem by using the molecular orbital theory and eventually describes the electrons by means of hybrid orbitals given by the linear combination of atomic orbitals (LCAO), resulting, in turn, from considerations based on the molecular symmetry.

Strong Field

Consider an example, when a transition ion V^{3+} with an unfilled d-shell, with two d-electrons is brought in such a field. If the electrostatic interaction is very strong, it will in general break down the coupling between the two orbital angular momenta ℓ_1 and ℓ_2 . As a consequence, the total angular moment L will lose its meaning and each electron will eventually orient in a magnetic field as if the other electron did not exist. This situation is known as strong field case.

Intermediate Field Case

If the electrostatic interaction is not strong enough to break ℓ_1 and ℓ_2 coupling but is still enough to break the L-S coupling, the angular momentum L orients itself in the magnetic field and so does S. Such a situation is called the intermediate field

case. Strong field and intermediate field cases are common in the first transition series (iron groups).

The Weak Field Case

The weak field case takes place when the interaction with ligand field consists only a higher order splitting of the levels corresponding to different value of $J = L+S$. The weak field case is encountered in the Lanthanide ions where the unfilled 4f-shell is well shielded against the ligand field 5p and 6s external electron shell.

1.11.5 Fine Structure

Many of the ions of the transition elements have more than one unpaired electrons and in their ground state have a total spin $S > 1/2$. It is useful to consider two theorems which have great significance in transition metals chemistry in general and EPR in particular.

- (i) Jahn-Teller theorem states that any non-linear molecule with an orbitally degenerate ground state is unstable and tends to distort in order to the degeneracy.
- (ii) Kramer's theorem deals with restrictions to the amount of degeneracy which can be removed by purely electrostatic field. If the system contains an odd number of electrons, such a field can not reduce the degeneracy of any level below two. Each pair forms what is known as a Kramer's doublet which can be separated only by a magnetic field.

In cases where $S > 1/2$ application of magnetic field will split the energy level into $2S+1$ magnetic levels. Transition between adjacent level according to selection rules $\Delta M_s = \pm 1$ are induced by

an oscillation field perpendicular to the static field. In the hypothetical simple system illustrated in Fig. 1.9(a) all these transitions will occur at the same frequency and a single line will be observed.

In general, however, paramagnetic ions are examined in crystals in which the powerful electrostatic fields are present. These crystalline fields may be sufficient to remove the degeneracy of the spin levels even in the absence of an external magnetic field, giving rise to a zero field splitting (ZFS). Such a situation is illustrated Fig. 1.9(b) for ion with total spin $S = 3/2$ where three different lines with unequal spacing and intensity are expected. It is apparent that transitions for which $\Delta M_s = \pm 1$ will occur at different fields if observed at constant frequency or vice versa. Such multiple transitions with unequal spacings and intensities in general are called the fine structure following conventional spectroscopic terminology. Their relative position will depend on the orientation of the crystal in the magnetic field, since in general, the crystalline fields are anisotropic.

REFERENCE

1. M. Tinkham and C.J. Lobb, from Solid State Physics, Vol.42, Eds. H. Ehrenreich and D. Turnbull, Academic Press, 1989.
2. B.Rosenblum and M.Cardona, Phys. Rev. Lett. **12**, 657 (1964).
3. Y.B. Kim and M.J. Stephen, Superconductivity, Vol.1, Ed. R.D. Parks, Marcel Dekker, New York, 1969.
4. K.A. Muller, M. Pomeranz, C.M. Knoedler and D. Abraham, Phys. Rev. Lett., **45**, 832 (1980).
5. A.V. Narlikar, C.V. Narasimha Rao and S.K. Agarwal, Studies of High Temperature Superconductor, Vol. 1, Ed. A. Narlikar, P. 341 (NOVA Science Publisher 1989).
6. J.M. Tarascon, L.H. Green, P. Barboux, W.R. McKinnon, G.W. Hull, T.P. Orlando, S. Foner and E.J. McNiff Jr., Phys. Rev. B **36**, 8393 (1987).
7. V.L. Ginzburg and L.D. Landau, Zh. Eksperim i Teor. Fiz. **20**, 1064 (1950).
8. A.A. Abrikosov, Zh. Eksperim. i Teor. Fiz. **32**, 1422 (1957) [Sov. Phys. JETP **5**, 1174 (1957)].
9. J. Bardeen and M.J. Stephen, Phys. Rev. **140**, A 1197 (1965).
10. M. Timkham, Introduction to Superconductivity, P. 67 (Robert E. Krieger Publishing, 1975).
11. C.P. Bean, Phys. Rev. Lett. **8**, 250 (1962).
12. G. Ravi Kumar and P. Chaddah, Phys. Rev. B **39**, 4704 (1989).
13. Y.Yeshurun and A.P.Malozemoff, Phys. Rev. Lett. **60**, 2202 (1988).
14. P.W. Anderson, Phys. Rev. Lett. **9**, 309 (1962).
15. Y.B. Kim, C.F. Hempstead and A.R. Strand, Phys. Rev. Lett. **9**, 306 (1962).

16. Y.B. Kim, C.F. Hempstead and A.R. Strand, Phys. Rev. 129, 528 (1963).
17. S. Nagata, P.H. Kessom and H.R. Harrison, Phys. Rev. B 19, 1633 (1979).
18. K. Binder and A.P. Young, Rev. Mod. Phys. 58, 801 (1986).
19. R.G. Palmer, from Heidelberg Colloquium on Glassy Dynamics, Lecture Notes in Physics, Vol.275, Eds. Van Hemmen and I. Morgenstern, Springer-Verlag, 1986.
20. M.A. Ruderman and C. Kittel, Phys. Rev. B 96, 99 (1954).
21. T. Kasuya, Prog. Theor. Phys. 16, 45 (1956).
22. K. Yosida, Phys. Rev. 106, 893 (1957).
23. S.F. Edwards and P.W. Anderson, J. Phys. F 5, 965 (1975).
24. V. Ambegaokar and A. Baratoff, Phys. Rev. Lett. 10, 486 (1963) erratum 11, 104 (1963).
25. C. Ebner and D. Stroud, Phys. Rev. B 31, 165 (1985).
26. J. Choi and J.V. Jose, Phys. Rev. Lett. 62, 320 (1989).
27. I. Morgenstern, K.A. Muller, J.G. Bednorz, Z. Phys. B 69, 33 (1987).
28. S. John and T.C. Lubensky, Phys. Rev. B 34, 4815 (1986).

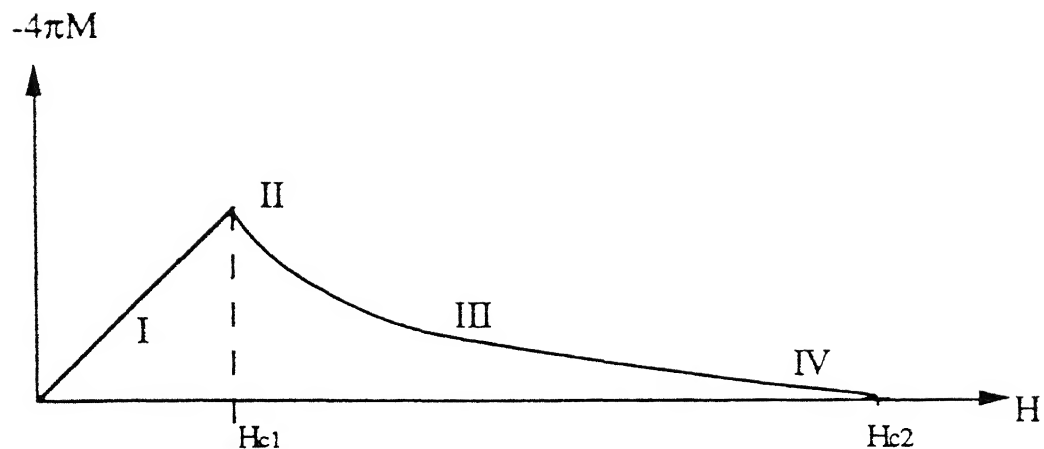


Fig. 1.1 The magnetization curve for an ideal Type-II superconductors. Region I is the Meissner region where flux is completely excluded. Regions II, III, and IV are part of mixed state where flux vortices resides in the sample. Flux first enters at H_{c1} and superconductivity is destroyed at H_{c2} .

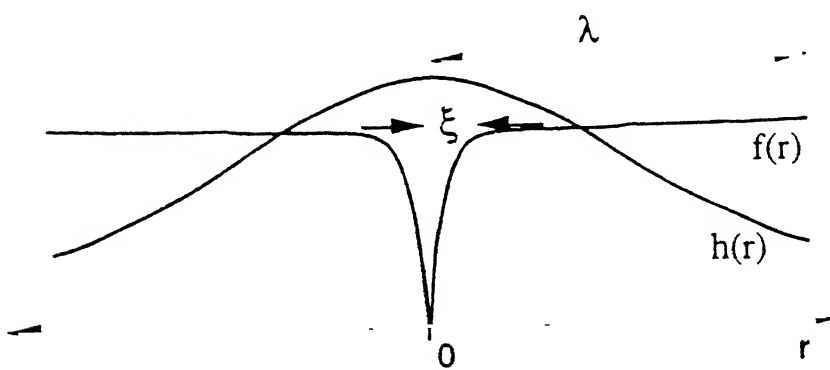


Fig. 1.2 The structure of an isolated vortex in a Type-II superconductor in the Abrikosov picture. Given here schematically are the local field, $h(r)$ and the amplitude of normalized order parameter, $f(r) = \varphi(r)/\varphi_0$

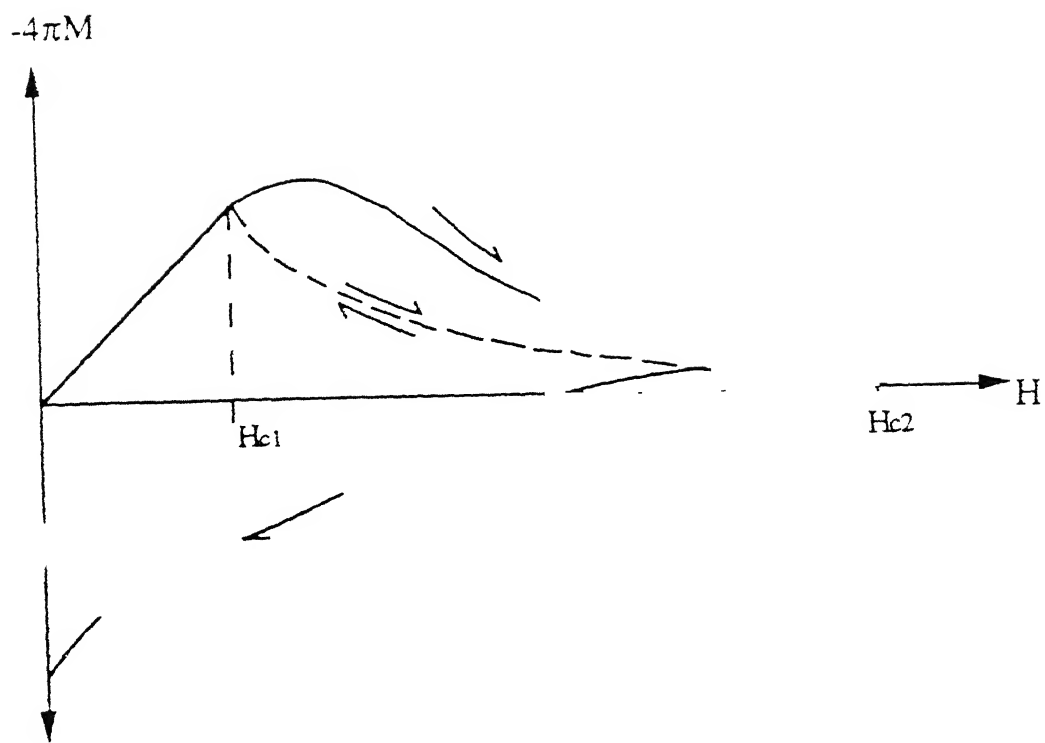


Fig. 1.3 A schematic representation of the magnetization of a Type-II superconductor with pinning (shown as the solid line) and without pinning (shown as the dashed line).

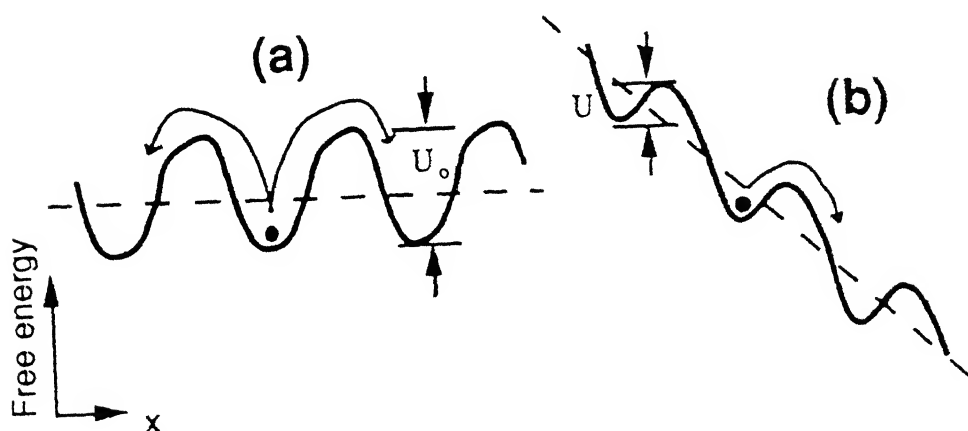


Fig. 1.4 A schematic representation of flux bundles hopping over barriers between pinning sites. (a) The case where there is no driving force, i.e. no force present to reduce the effective well depth. (b) The case where a flux density gradient or an applied current reduces the effective well depth. Down-hill jumps are favored in this case.

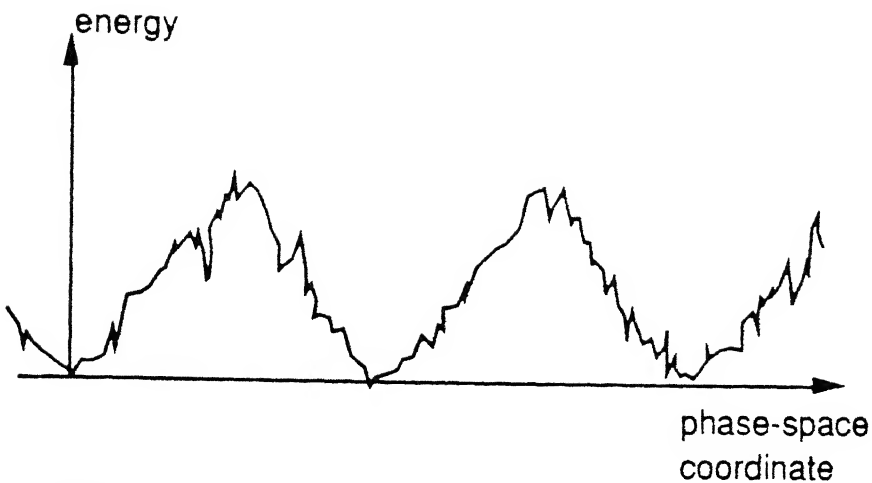


Fig. 1.5 A schematic plot of the configurational space of a glass. It is plotted here as the coarse-grained free energy versus some phase coordinate which represents alternate configurations.

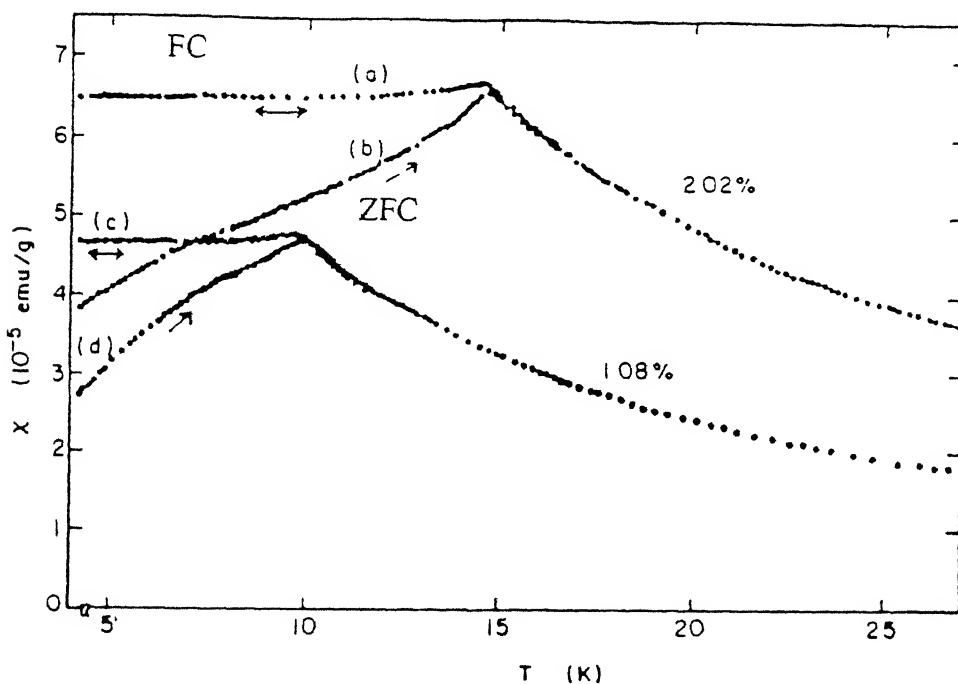


Fig. 1.6 Static susceptibilities of CuMn spin glass versus temperature in a 5.9G field. Shown here is data for two samples with different atomic percentage of Mn. Below T_g susceptibility is larger for the field cooled (FC) than it is for zero field cooling (ZFC) [Ref. 17].

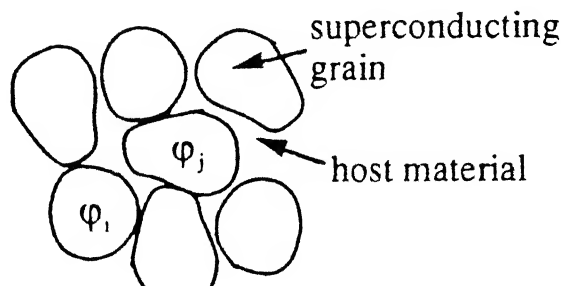


Fig. 1.7 The physical picture of superconducting phase glass. The host material can be either an insulator or normal metal.

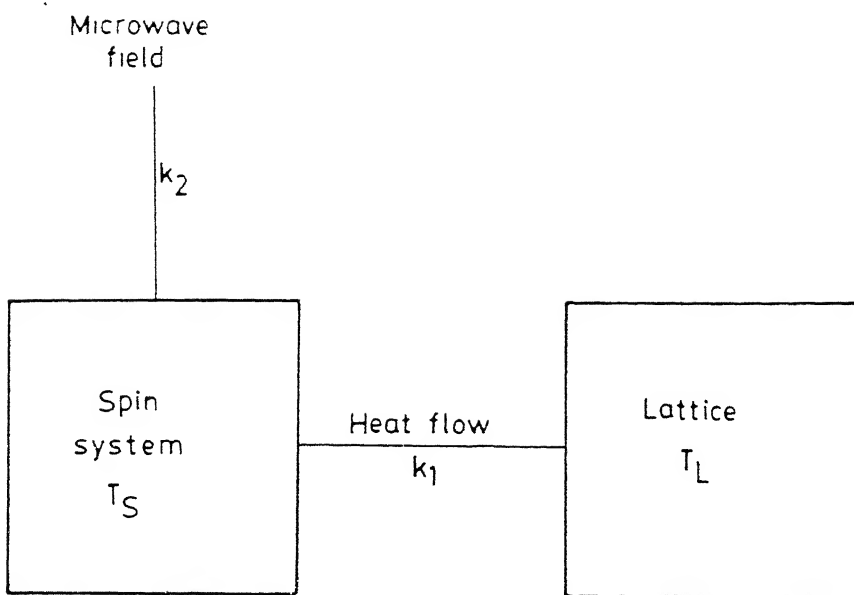


Fig. 1.8 Schematic diagram for microwave field and spin-lattice interaction. T_S and T_L represents the spin and lattice temperature respectively. K_1 and K_2 are rate constant for the flow of energy.

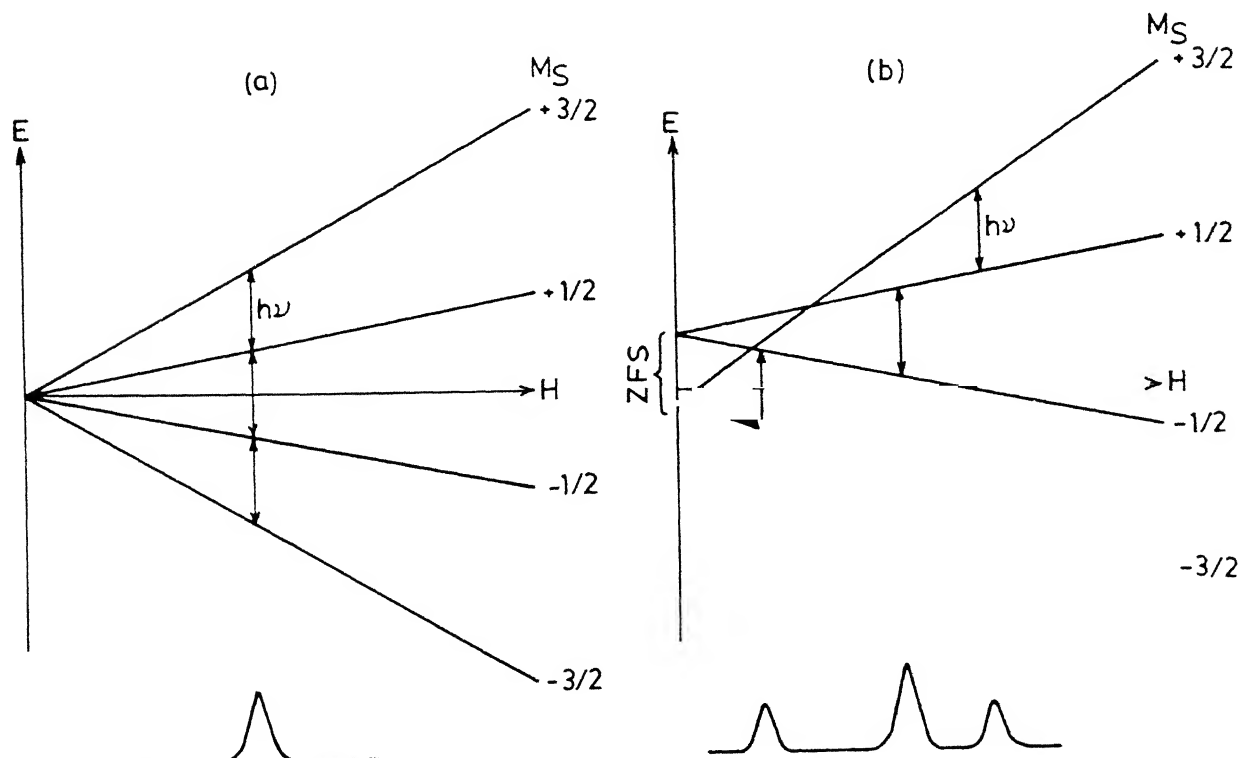


Fig. 1.9 Schematic energy levels for $S = 3/2$. The variation of energy levels with magnetic field is depicted in (a) no zero field splitting and (b) finite zero field splitting ($\Delta h\nu$).

CHAPTER-II

EXPERIMENTAL

Abstract

Brief description of EPR spectrometer, Helmholtz coils, current source and design of low temperature cell is given. Preparation of $\text{YBa}_2\text{Cu}_3\text{O}_{7-\delta}$ is given. Also the method of estimation of the oxygen content in $\text{YBa}_2\text{Cu}_3\text{O}_{7-\delta}$ is discussed.

2.1 EXPERIMENTAL APPARATUS

2.1.1 EPR Spectrometer

EPR and low field non-resonant microwave absorption in High T_c superconductors were carried out on Varian E-109-EPR Spectrometer operating at X-band (≈ 9.4 GHz) microwave frequency. A block diagram of EPR Spectrometer are shown in Fig.2.1. The EPR Spectrometer consists of:

- (1) Electromagnet: It provides the homogeneous magnetic field at the sample cavity which can be varied from near zero to 20 K Gauss.
- (2) Magnetic Power Supply : It provides stable controlled current to the coils of electromagnet.
- (3) The scanning unit supplies a control voltage to the input of current regulated magnet power supply. This control voltage can be varied linearly with respect to time, thus resulting in a linear sweep of the magnetic field. In Varian E-109 spectrometer the scan of the magnetic field is accomplished by field control module having a field set and scan range function. Field set gives the magnetic field at the center of recorder chart and scan range controls the width of the scan. The scan is symmetrical about the center value indicated by field set.
- (4) The static magnetic field at the sample location within the resonant cavity is modulated by 100 KHz sweep generator. The sweep generator also supplies a phase reference voltage to the signal phase detector. The auto sweep generator supplies an additional magnetic field modulation to the cavity as well as sweeps for the oscilloscope X-axis.
- (5) Klystron Oscillator : It produces r.f. energy which is used to irradiate the sample. A variable attenuator is placed between the Klystron and hybrid tee to control the amount of r.f. power

- applied at the sample.
- (6) The hybrid tee is a device which does not allow microwave power to pass in a straight line, i.e. from one arm to the opposite arm. The power emitted from arm 1 is equally divided among arms 2 and 3. This is similar to a balance bridge. Any change in terminating impedance of the arms 2 or 3 will unbalance it and crystal detector in arm 4 will receive the energy.
 - (7) The resonant rectangular sample cavity of reflection kind operating in TE_{102} mode was used which has a very high Q ($Q = \omega \times (\text{energy stored}/\text{power lost})$). At resonance the impedance of the cavity is changed and signal is reflected to the crystal detectors in the hybrid tee.
 - (8) The crystal detector demodulates the microwave energy. The frequency of the signal voltage containing the EPR information corresponds to the frequency of the sweep voltage used to modulate the static magnetic field and to provide a phase reference for the signal phase detector.
 - (9) The ac amplifier following the crystal detector simply amplifies the signal information. The control of the modulation field and ac amplifier is performed by High Frequency Module in Varian E-109.
 - (10) The oscilloscope module is a means for rapid visual display of EPR signals.
 - (11) The signal phase detector combined with an integrator and X-Y recorder provides a mean of displaying first harmonic presentation of EPR signal.

AUTOMATIC FREQUENCY CONTROL (AFC) The AFC electrically tunes the output frequency of the Klystron to lock to the resonant frequency of the sample cavity. The block diagram of AFC is shown in Fig. 2.2. A

control frequency of 10KHz is provided by an oscillator to both the AFC phase detector and the power supply for the Klystron reflector. In the AFC phase detector 10KHz voltage is used as phase reference while in the Klystron power supply it is used to vary the reflector voltage, thus resulting in a 10KHz modulation of the Klystron output frequency. This frequency modulation causes the Klystron frequency to vary with respect to the resonant frequency of the sample cavity. When the Klystron center frequency (f_o) corresponds to the resonant frequency of the sample cavity (f_r), a voltage, the fundamental frequency of which is second harmonic of 10KHz (20KHz) is reflected from the cavity and appears at the crystal detector (as shown in figure 2.3). If the center frequency of the Klystron is shifted from that of the resonant cavity, the frequency of the voltage appearing at the detector is 10KHz. Its phase is dependent on whether the klystron frequency is higher or lower than the resonant cavity frequency. The amplitude of this reflected 10 KHz signal depends on the relative difference between f_o and f_r . This error voltage is amplified by an ac amplifier, then phase detected and filtered. The result is dc output voltage which is used to control the klystron reflector voltage so that center frequency of the klystron corresponds to the frequency of the resonant cavity.

2.1.2. Helmholtz Coils

Low field nonresonant microwave absorption can not be studied by Varian electromagnet as it has remenent field of an order of 20G. So we require an arrangement which can sweep the magnetic field from zero to 100 Gauss and having uniformity in the large area compared to the sample area. There are two ways to produce a uniform magnetic field (i) long solenoid (ii) Helmholtz coils (a pair of two circular coils). Long solenoid is not suitable from the

consideration of the geometry of the resonant cavity. Helmholtz coils is suitable for producing uniform magnetic field at the location of the sample in the resonant cavity. It consists of co-axial circular wire, r distance apart (where r is the radius of each circular wire). The field distribution is shown in Fig. 2.4. The field due to circular wire at the axis at a distance x is given by

$$H(x) = \frac{2 \pi n r^2 I}{(r^2 + x^2)^{3/2}} \quad (\text{where } I \text{ is in emu.}) \quad (2.1)$$

n = number of turns in the coil

I = current through the coil

The field at the center of the Helmholtz coils i.e. at a distance $r/2$ (which is the superposition of the field due to both coils) [1a] is

$$H(r/2) = \frac{32 \pi n I}{5 \sqrt{5} r} \quad (2.2)$$

In designing Helmholtz coils, the following things should be considered :

- (i) The space available around the cavity and dimension of the cavity.
- (ii) The maximum current which will flow through the coil to choose the gauge of the wire.
- (iii) Deciding the number of turns in the coil is done according to the strength of the field required. To make Helmholtz coils, wires were wound on aluminium case so that the case works like heat sink for the heat generated in the wire.

2.1.3. Current Source

It supplies stable and controlled current to the Helmholtz coils. The maximum current supplied by it is one ampere. The circuit diagram is shown in Fig. 3.5. The current passing through the

Helmholtz coils is given by

$$I_H = \frac{V_{ref}}{R} \quad (2.3)$$

Thus, we can vary the current I_H by varying the resistance R or the reference voltage V_{ref} . The stability of the current depends on the stability of the V_{ref} and the stability of the resistance R. Scanning of magnetic field can be performed by scanning V_{ref} . The scanning of the magnetic field should be coupled with the recorder of the spectrometer. This is performed by taking the output from the In/Out Jack (J007) at the rear of the Field Control module (E-203B) of Varian E-109 which gives -10V to +10V, as the recorder moves from extreme left to the extreme right. This output is fed to the pin no. 3 (non-inverting input of 741). The I_H is zero for negative reference voltage. Scan range is selected by changing the resistance R. And for fixed R, the scan range is changed by feeding the scan voltage to the potentiometer and the output of the potentiometer is fed to the V_{ref} in the circuit diagram. A dual regulated power supply of +15V and -15V with 500mA current rating is required for activating the ICC741 and an unregulated power supply of one ampere rating is required for drawing current for Helmholtz coils. The circuit diagram is shown in Fig. 2.6. The magnetic field of the Helmholtz coils was calibrated by monitoring the shift in the DPPH signal. The following facilities are available in the current source :

- (i) It works in both scan and constant field modes. There is a switch which selects the required mode.
- (ii) The magnetic field can be reversed by selecting the switch (forward/backward)..
- (iii) Scan range can be varied in steps.
- (iv) The stability of the field is up to ± 0.2 Guass.

2.1.4. Low Temperature Cell

The low temperature cell for studying the EPR at liquid nitrogen temperature is shown in Fig.2.7. It is an evacuated double walled dewar of quartz having a long neck. To study at the liquid nitrogen temperature the sample is taken in the quartz capillary tube and dipped directly in the liquid nitrogen. After slight modifications, the same dewar is used for studying the EPR as a function of temperature from 85°K to room temperature. The modifications are shown in Fig. 2.7. A stopper has been used to keep nitrogen out of the dewar neck as shown in Fig. 2.7. A copper capillary tube of diameter 5 mm having one end closed with a copper rod of 2 cm length and 3 mm diameter having paddle shaped tip, passes through the stopper into liquid nitrogen bath. The thin copper blade may be inserted into the cavity oriented in the plane of rf electric field with no serious consequence. Non-magnetic heater wire was wounded on the rod near the sample. Heater wire and thermocouple were taken out through the capillary tube. The current to the heater was supplied by the constant current source. The temperature was controlled manually by adjusting the heater current. The stability of the temperature was within $\pm 0.1^{\circ}\text{K}$. The low temperature cell for studying the temperature variation below liquid nitrogen is shown in the Fig.2.8. This is based on cold finger method. The liquid nitrogen is pumped out rapidly which causes it to freeze. From this cell we can study up to the freezing temperature of liquid nitrogen.

2.2. Synthesis of $\text{YBa}_2\text{Cu}_3\text{O}_{7-\delta}$

Preparation of multiphase $\text{YBa}_2\text{Cu}_3\text{O}_{7-\delta}$ compound having resistive transition temperature at 91 K is relatively easy [1]. However, to understand the high T_c superconductivity, logic demands that measurement of physical properties should be done on high

quality samples. But this field has seen many bad samples studied with very precise experiment [2]. Preparation of well-defined single phase materials with uniform oxygen stoichiometry is considerably difficult and time consuming. The synthetic routes employed so far are mainly those employed for ceramic processing. The method can be divided in the flowing sequence of steps.

- (i) Drying the starting materials, Y_2O_3 , $\text{BaCO}_3/\text{Ba}(\text{NO}_3)_2$, CuO of high purity, in the oven for 24 hours.
- (ii) Preparation of a homogeneous mixture of the three metals (Y:Ba:Cu) in the appropriate stoichiometric ratio. To avoid the other phase at the grain boundary the deviation in the stoichiometric ratio should be less than 1%. For achieving the single phase, the starting materials should be at least 99.9% pure. The importance of homogeneous starting material with extremely small particle size for the preparation of well defined single phase has been highlighted by C.N.R.Rao and Gopalkrishnan [3].
- (iii) Formation of single phase oxygen deficient $\text{YBa}_2\text{Cu}_3\text{O}_{7-\delta}$.
- (iv) Annealing in oxygen to obtain high T_c phase ($0 < \delta < .2$)

According to the preparation of homogeneous mixture there are following method of preparation.

2.2.1 Solid State Reaction Method

Since the discovery of high T_c materials several reports on its preparation by Solid state reaction method starting from the constituent oxide/carbonate/nitrate are available [1-14]. In this method a series of grinding and heating with varying temperature and time span is required. If the heating temperature is lower than 800°C , it leads to the formation of impurity phases [6] such as

BaCuO_2 and Y_2BaCuO_5 . the 1-2-3 phase decomposes into mixture of Y_2BaCuO_5 when it is heated above 970°C [1,6]. Also, 1-2-3 reacts with the crucible material during extended heating period [1,5]. It reacts with silica, platinum and alumina. The only material which is found to be inert to 1-2-3 is silver and to some extent gold. Oxygen uptake in $\text{Y}_2\text{BaCu}_3\text{O}_{7-\delta}$ occurs above 400°C when it is heated in oxygen environment. The time and temperature of treatment vary with the size and density of the sintered compacts. In addition, the cooling rate in oxygen atmosphere is also crucial. In our lab we have prepared the single phase 1-2-3 sample as follows. Stoichiometric ratio of five gram and Y_2O_3 (99.9%), BaCO_3 (99%) and CuO (99%) was taken in the beaker and mixed in methanol by magnetic stirrer for 6 to 12 hours. After evaporation of methanol, the powder was again grinded in the mortar and pestle for one or two hours. The well stoichiometric homogeneous mixture is necessary to avoid any other phases. After making pellet of the well mixed powder the first heat treatment was done in air at 930°C for 24 hours in alumina boat. The sample was taken out of the furnace and regrinded, pelletised and put back in the furnace for sintering in air at 930°C . Again sample was regrinded, pelletised (approx. 2 mm thick) and put back in the furnace at 930°C . It was sintered at 930°C for 4 days. In the process of sintering, thermal cycling from 930°C to 890°C was done at every four or six hours in order to develop microcracks, which promotes grain growth and constant homogenization [2]. The sample was taken out, regrinded, and taken in alumina boat and put into the quartz tube placed in the tubular furnace. Oxygen flowed through the quartz tube and heated to 930°C in 4-6 hours, sintered for 12 to 24 hours, furnace cooled to 430°C and heated to 930°C , sintered for 2-12 hours. It was then cool to 430°C in 12-36 hours and left to oxygenate at 430°C for 2 days and the furnace was switched off.

2.2.2 Co-precipitation Methods

Co-precipitation method is generally used on laboratory scale for preparation of substances such as ferroelectrics, Yttrium Iron Garnet used in microwave devices and for catalysis. High T_c superconductors are commonly prepared by hydroxy carbonate and oxalate precipitation method [15-18]. In this method, aqueous solution containing a stoichiometric cation ratio is precipitated by anions to yield a precursor, which is then heat-treated to form the desired phase. The pre-requisites for the formation of homogeneous precipitates are (i) control of pH, (ii) absence of concentration gradient during the precipitation, and (iii) use of non-interfering counter ions.

Hydroxycarbonate Precipitation Method In this method stoichiometric solution of Y-, Ba-, Cu-nitrates (0.30M) is neutralized to pH 8 and precipitated using excess K_2CO_3 or Na_2CO_3 , then the precipitate is filtered, washed and dried at $100^{\circ}C$ and then calcined at $900^{\circ}C$ and sintered at $930^{\circ}C$.

Oxalate Precipitation method In this method, nitrate solution containing Y, Ba, Cu cations with excess Ba ions are precipitated using oxalic acid. Sodium hydroxide is used to control the pH in the range 4 to 6 in order to minimize the cation losses. This process yields submicronic, homogeneous precursor. However, the solubility of $BaCO_3$ and $SrCO_3$ makes attainment of stoichiometry difficult even with careful pH control and with addition of excess reagents.

2.2.3 Chemical Precursor Method

In conventional solid-state reaction method the main

problem is the formation of intermediate phases, such as BaCuO_2 and Y_2BaCuO_5 . These compounds undergo eutectic reaction in oxygen atmosphere below 930°C . These eutectic reactions lead to the formation of grain boundary phase [19] which lowers the critical current values. To minimize eutectic formation and enhance desirable microstructural and electronic properties, in convention solid state reaction method it has been necessary to perform multiple intermediate grindings of the mixed oxide followed by sintering at progressively higher temperatures. This has made the synthesis of superconductors more time consuming and non-reproducible due to temperature variations, atmospheric reactions and container interactions. In order to simplify the Y-1-2-3 superconductor synthesis and to obtain more control and reproducibility in processing, an alternative route called chemical precursor has been suggested [19]. The basic synthesis approach involves a solid state reaction of the $\text{Y}_2\text{Cu}_2\text{O}_5$ with BaCuO_2 compounds to form the Y-1-2-3 compound. The precursors $\text{Y}_2\text{Cu}_2\text{O}_5$ and BaCuO_2 is synthesized individually mixed and further reacted to form the Y-123 superconductors. For details see the reference [19].

2.2.4 Sol-Gel

In the ceramic field the term sol-gel is an abbreviation of solution-gellation term and refers to the process in which organometallics such as alkoxides are partly hydrolysed and then polymerised into a gel. For the high T_c superconductors a number of different sol-gel methods have been suggested for processing of bulk powders, for fibre spinning and for thick film formation. These methods include, fluoroacetate [20], water soluble organometallics [21], citric acid [22-28], alkoxide polymerisation [29-30], colloidal mixture of hydroxide and acetates [31] and homogeneous solution made

of acetates [32]. Experimental procedures are varied and require precise conditions for the formation of homogeneous and amorphous gels. For the preparation of high T_c superconductors, most commonly used processes are citric acid, alkoxide and acetate polymerization. We prepared the YBaCuO by citrate combustion method exactly in the same way as in ref. 22 as follows: Y_2O_3 (99.9%), CuO (99%) and $Ba(NO_3)_2$ (99.5%) were taken separately in stoichiometric ratio, Y_2O_3 and CuO were dissolved in 65% nitric acid and $Ba(NO_3)_2$ was dissolved in distilled water by heating. The three solutions were mixed together followed by the addition of 0.7 mol of citric acid. The last step was performed to form a solid residue. The solid residue is redissolved on neutralization with dropwise addition of 25% NH_4OH (liquor ammonia) which is added to precisely adjust the pH of the solution to 6.8 using pH meter. This results in a deep-blue solution. 100 ml of this solution was taken in 2 liter pyrex beaker and was gradually heated on hot plates. On heating, the homogeneous mixture swelled into a foam of fine flakes which nearly filled the entire vessel (2 liter beaker) when the fire was triggered by self-ignition of ammonium nitrate. In this way we got a fine brownish powder. The heat treatment of the powder was done exactly in the same way as in the case of solid state reaction method described earlier. In our lab we have prepared the sample by solid state reaction method and citrate combustion method.

2.3 RESISTANCE MEASUREMENT

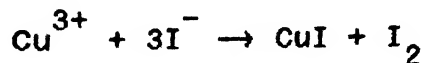
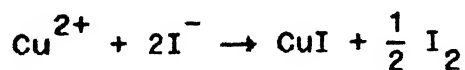
Resistance measurement was done by standard four probe technique. The block diagram of the apparatus is shown in Fig.2.9. The temperature of the sample was varied by slowly pushing the sample inside the liquid nitrogen container as shown in Fig.2.10 (There is a temperature gradient inside the container from room temperature to

liquid nitrogen). To maintain slow variation of temperature, a bigger container having very small amount of liquid nitrogen at the bottom was taken. The temperature of the sample was measured by copper-constantan thermocouple placed near the sample. The stability of temperature was $\pm 1^{\circ}\text{K}$. Home-made constant current source was used which has a stability of $10 \mu\text{A}$. Kiehelay nano-voltmeter was used to measure the voltage developed. Resistance measurements for some samples were done in APD Cryogenics model Displex DA-202. In this close He-cryostat, temperature was stable within 0.1°K .

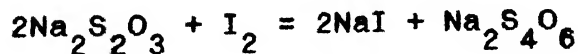
2.4 ESTIMATION OF OXYGEN IN $\text{YBa}_2\text{Cu}_3\text{O}_{7-\delta}$

There are two methods for estimating the oxygen content in $\text{YBa}_2\text{Cu}_3\text{O}_{7-\delta}$
(i) Thermogravimetric Method, and (ii) Chemical analysis method (usually iodometric titration) [32-34],

Iodometric Method In conventional iodometric method Cu^{2+} and Cu^{3+} materials are dissolved in acidic iodide solution, resulting in reduction of all Cu species to solid Cu^+ iodide and liberation of neutral iodine



The total amount of iodine liberated is then titrated with standardized sodium thiosulfate solution according to the reaction,



in presence of starch solution. The amount of oxygen is estimated using the analysed mean value of copper ions with charge neutrality

condition assuming Y^{3+} , Ba^{2+} and O^{2-} as fixed valence. The above method has following disadvantages:

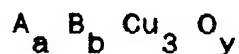
(i) It gives average oxidation state and does not tell the ratio of Cu^{2+} and Cu^{3+} . (ii) In a medium of sufficient acidity to dissolve highly refractory materials such as $\text{YBa}_2\text{Cu}_3\text{O}_{7-\delta}$ at reasonable rate serious error can result from Cu-catalyzed oxidation of I^- by atmospheric oxygen.

The above problem can be circumvented in the following way [35]. The first of these two problems can be overcome by carrying out the titration in presence of citrate which complexes Cu^{2+} and prevents its further reduction. The second problem can be minimized by dissolving the material in 4.4M HBr and converting the Br_2 formed by reduction of Cu^{3+} to I_2 by subsequent reaction with I^- at much lower acidity.

Procedure 44 mg weighed sample was dissolved in 2 ml ice cold $\approx 4.4\text{M}$ HBr, made by 1:1 dilution of commercial 48% HBr, in ≈ 5 ml capped vial with teflon coated magnetic bar stirrer. The capped mixture was warmed to room temperature and stirred for 10 minutes. It was then transferred quantitatively to 50 ml conical flask containing 20 ml of ice cold 0.2M KI and enough concentrated NH_3 to neutralize all but about 1 m mol of the added acid so that medium remained acidic. The solution in flask was stirred gently during the addition. The ≈ 5 ml vial and transfer pipet were washed twice with 2 ml portion of 2M KBr. 5 ml of 1M sodium citrate was then added to the flask and the solution was brought to room temperature and stirred until the dissolution of CuI precipitate was complete. The amount of Iodine present was titrated with standardized 0.1M sodium thiosulfate with microburette. When solution began to change color, 2 drops of 1%

aqueous starch was added and titration was continued until the dark blue color changed to pale blue.

Since HBr solution usually contains some bromine, a blank correction is required. This is accomplished by carrying out the above procedure in the absence of oxide sample. In our case the blank correction was negligible. The oxygen content in the sample can be estimated as follows. Let an oxide has the formula



$$y = (\alpha E + \beta) / (2 - 16E)$$

where $E = \text{mol of } S_2 O_3^{2-} \text{ used/gram of sample}$

$= \text{mol of } Cu^{3+} \text{ /gram of sample}$

$$\alpha = a M_A + b M_B + c 63.5$$

M_A and M_B molar masses of metal A and B respectively,

$$\beta = 3a + 2b + 2c.$$

REFERENCE

- 1(a) Leigh Page and Norman Isley Adams, Principles of Electricity, pp.223 (de-Van Nostrand Company Inc., Princeton New-Jersey).
- 1(b) U.V. Varadaraju and G.V. Subba Rao, Studies of High Temperature Superconductors, Ed. A.V.Narlikar, NOVA Publisher, pp.229(1989).
- 2 J.L. Smith, W.L. Hults, A.P.Clarke and K.A. Johnson, Proceedings of Workshop on High T_c Superconductivity, Huntsville, Alabama 23-25 May 1989 (Preprint).
- 3 C.N.R. Rao and J. Gopalkrishnan, Acc. Chem. Res. (ACS), 20 228 (1983).
- 4 S.K. Agarwal, B. Jayrama, A. Gupta and A.V. Narlikar, Phase Transitions 10, 17 (1987); B.Jayrama, S.K.Agarwal, A. Gupta and A.V. Narlikar, Solid State Commn. 63, 713 (1987).
- 5 D.W. Murphy, D.W. Johnson (Jr.), S. Jin and R.E. Howard, Science, 241, 922 (1988).
- 6 Z. Gabelica, G. Demortier, G. Deconninck, F. Bodart, A.A. Lucas, M. Renier, Ph. Lambin, J.P. Vigneron and E.G. Derouane, Solid Stat. Commn., 64, 1137 (1987).
- 7 J.M. Tarascon, P.B. Baroux, B.G. Bagley, L.H. Greene and G.W. Hull, Mater. Science and Engineering B 1 , 29 (1988).
- 8 Y. Le Page, W.R. McKinnon; J.M. Tarascon, L.H. Greene, G.W. Hull and D.M. Hwang, Phys. Rev. B 55, 7245 (1987).
- 9 R.M. Hazen, L.W. Finger, R.J. Angel, C.T. Prewitt, N.L. Ross, M.K. Mao, C.G. Hadidiacos, P.H. Hor, R.L. Meng and C.W. Chu, Phys. Rev. B 35, 7238 (1987).
- 10 J.E. Greidan, A.H. O'Reilly, and C.V. Stager, Phys. Rev. B 35, 8770 (1987).
- 11 P.K. Gallagher, H.B. O'Bryan, S.A. Sunshine, and D.W. Murphy, Mat. Res. Bull. 22, 995 (1987).

- 12 L.F. Schneemeyer, J.V. Waszczak, T. Siegrist, R.B. Van Dover, L.W. Rupp, B. Batlog, R.J. Cava and D.W. Murphy, *Nature*, **328**, 601 (1987).
- 13 G.F. Holland and A.M. Stacy, *Acc. Chem. Res.* (ACS) **21**, 8 (1988).
- 14 J.M. Williams, B.K. Flandermeyer and R.B. Popel, *Inorg. Chem.* **26**, 1474 (1987).
- 15 J.W. Severin, G. DeWith and H.A.M. Van Hal, *Physica C*, **152**, 159 (1988).
- 16 K. Kaneko, H. Ihora, M. Hirabayashi, N. Terada and K. Senzaki, *Jpn. J. Appl. Phys.* **26**, L734 (1987).
- 17 A.M. Kini, U. Gieser, H.C.I. Kao, K.D. Caruso, H.H. Wang, M.R. Monghan and J.M. Williams, *Inorg. Chem.* **26**, 1837 (1987).
- 18 Yu Zhang, Z. Fang, Muhammad M., K.V. Kao, V. Skumryev, H. Medelius and J.L. Costa, *Physica C*, **108** (1989).
- 19 D.E. Petersen, K.A. Kubat-Martin, T.G. George, T.G. Zocco and J.D. Thompson, *J. Materials Research* (preprint).
- 20 A. Gupta, R. Jagannathan, E.I. Cooper, E.A. Gies, I.J. Landamm and B.W. Hussey, *Appl. Phys. Lett.* **52**, 2077 (1988).
- 21 M.E. Gross, M. Hong, S.H. Liou, P.K. Gallagher and J. Kwo, *Appl. Phys. Lett.* **52**, 160 (1988).
- 22 R. Pankajavalli, J. Janaki, O.M. Sreedharan, J.B. Gnanamoorthy, G.V.N. Rao, V. Sankara Sastry, M.P. Janawadkar, Y. Hariharan and T.S. Radha Krishnan, *Physica C*, **156**, 737 (1988).
- 23 Y.M. Chiang, S.L. Furcone, J.A.S. Ideda and D.A. Rudman, *Mater. Res. Soc. Symp. Proc.*, **99**, 307 (1988).
- 24 C. Marcilly, P. Courty and B. Delmon, *J. Am. Ceram. Soc.* **53**, 56 (1970).
- 25 D.J. Anderson and F.R. Sale, *Powder Metall.*, **22**, 14 (1979).
- 26 M.S.G. Baythoun and F.R. Sale, *J. Mater. Sc.* **17**, 2157 (1982).
- 27 H. Zhang, Y. Teraoka and N. Yamazoe, *Chem. Lett.*, **4**, 665 (1987).

- 28 C. Chu, and B. Dunn, J. Am. Ceram. Soc., 70, 375 (1987).
- 29 G. Kordas, K. Wu, U.S. Brahme, T.A. Friedmann and D.M. Einstberg, Mater. Lett. 5, 417 (1987).
- 30 S. Shibata, T. Kitagawa, H. Okazaki, T. Kimura and T. Mirakami, Jap. J. Appl. Phys. 27, L53 (1988).
- 31 P. Barboux, J.M. Tarascon, L.H. Greene, G.W. Hull and B.G. Bagley, J. Appl. Phys. 63, 2725 (1988).
- 32 D.C. Harris and T.A. Hewston, J. Sol. State. Chem. 69, 182 (1987).
- 33 Koji Kishio, Jun-ichi Shimoyama, Tetsuya Hasegawa, Koichi Kitazawa and Kazuo Fueki, Jpn. J. Appl. Phys. 26, 1228 (1987).
- 34 A. Manthiram, J.S. Swinnea, Z.T. Sui, H. Steinfink and J.B. Goodenough, J. Am. Chem. Soc., 109, 6667 (1987).
- 35 Evanstt. Appleman, Lester R. Morss, Aravinda M. Kini, Urs Geiser, A. Umezawa, G.W. Crabtree and K. Douglas Carlson, Inorganic Chemistry, 26, 3237 (1987).

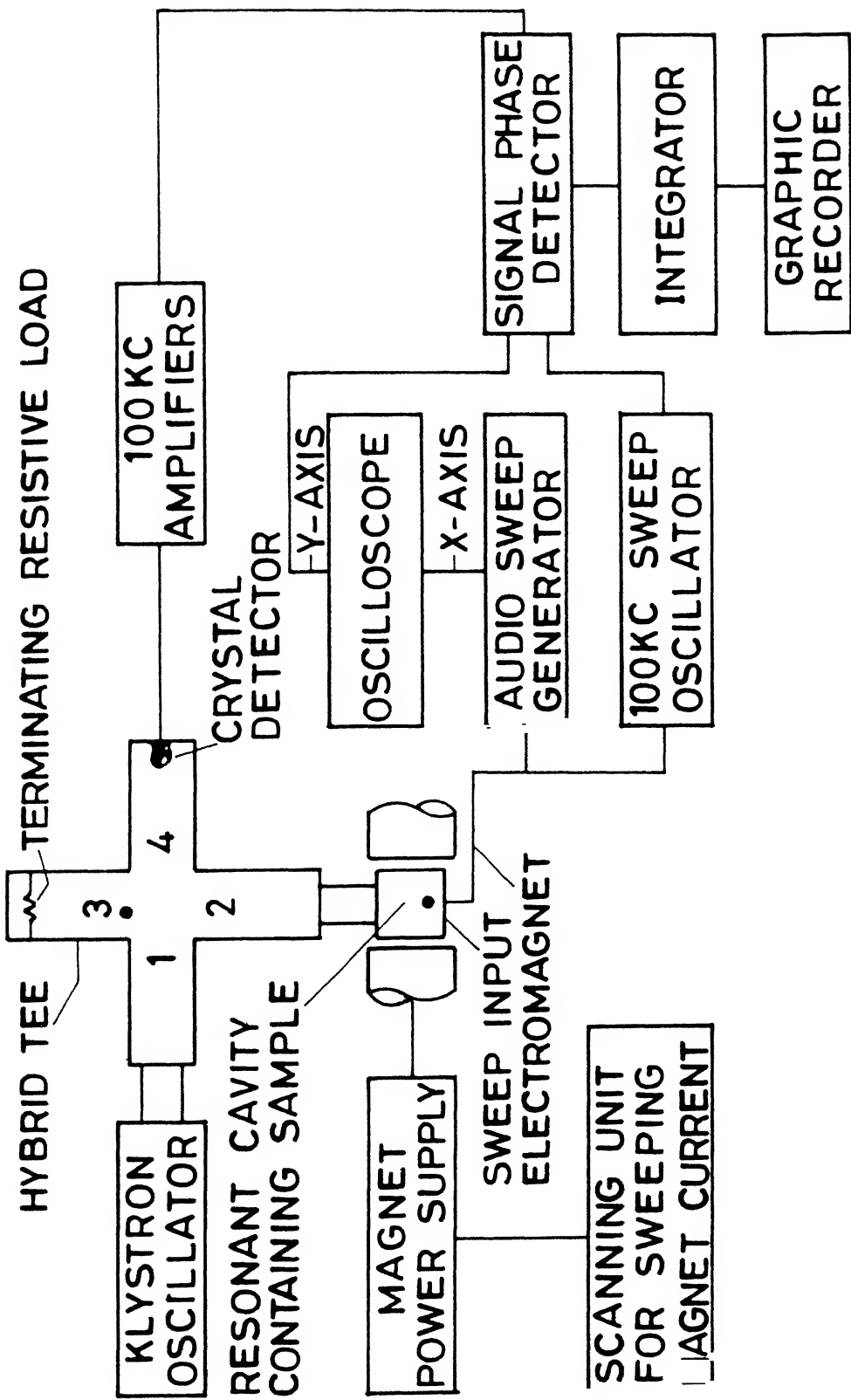


FIG. 2.1 BLOCK DIAGRAM OF AN EPR SPECTROMETER.

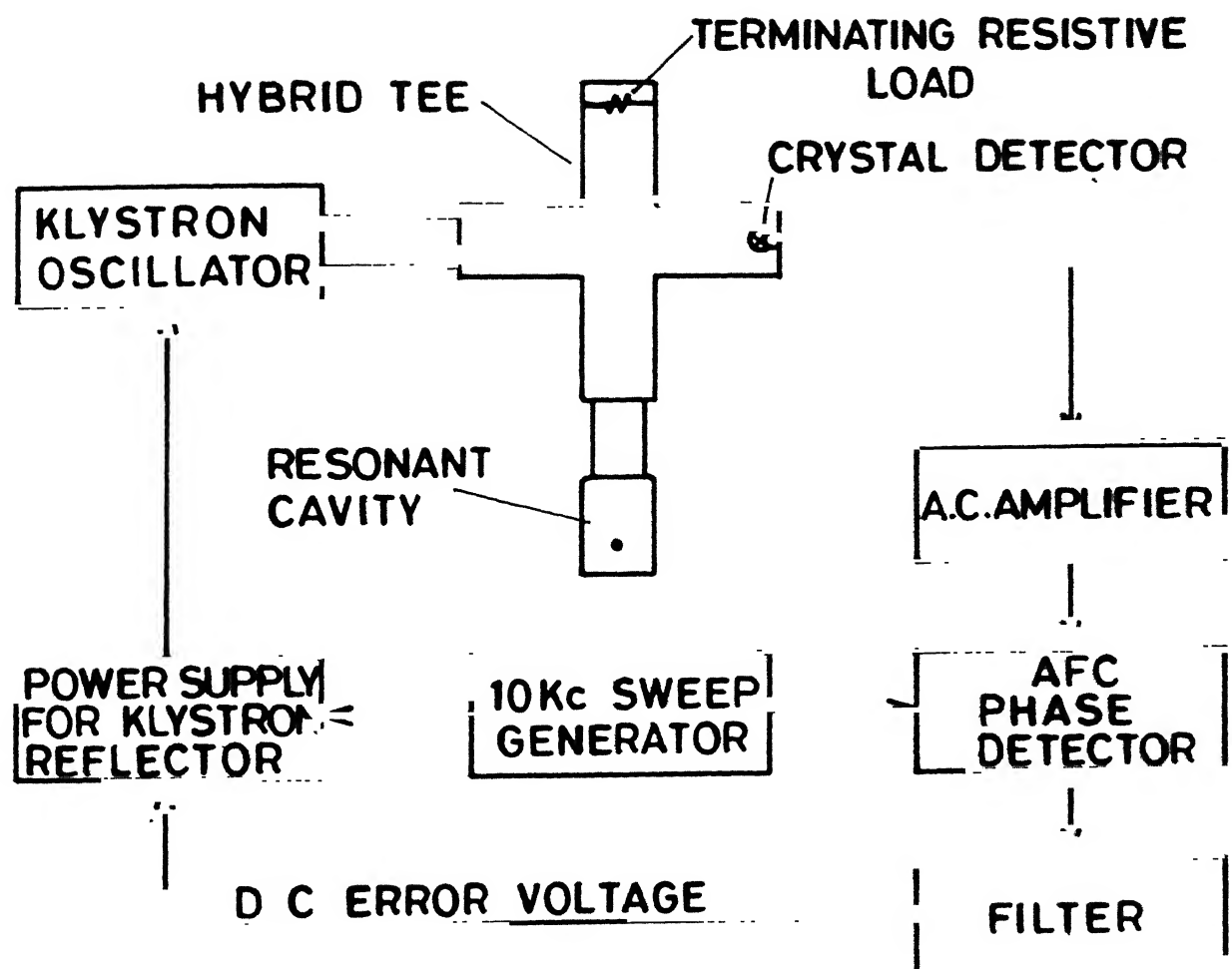


FIG. 2.2 BLOCK DIAGRAM OF AN AFC SYSTEM.

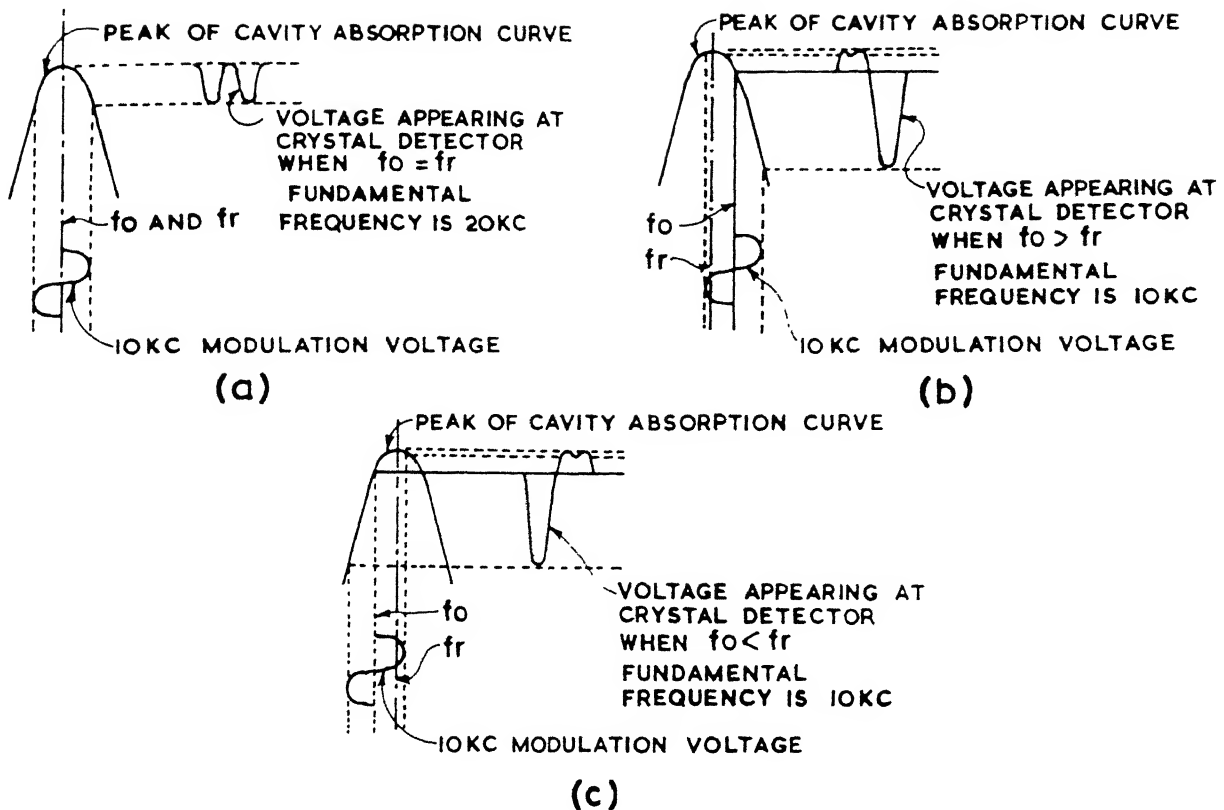


FIG. 2.3 OUTPUT VOLTAGES FROM CAVITY AS RESULT OF AFC MODULATION.

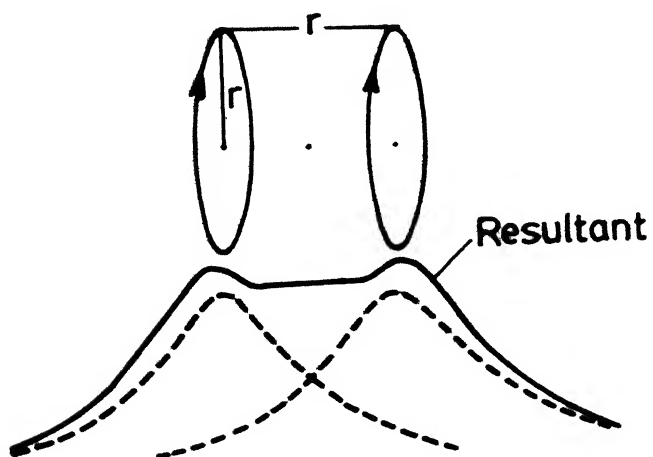


Fig. 2.4 The field distribution of Helmholtz coil along axis

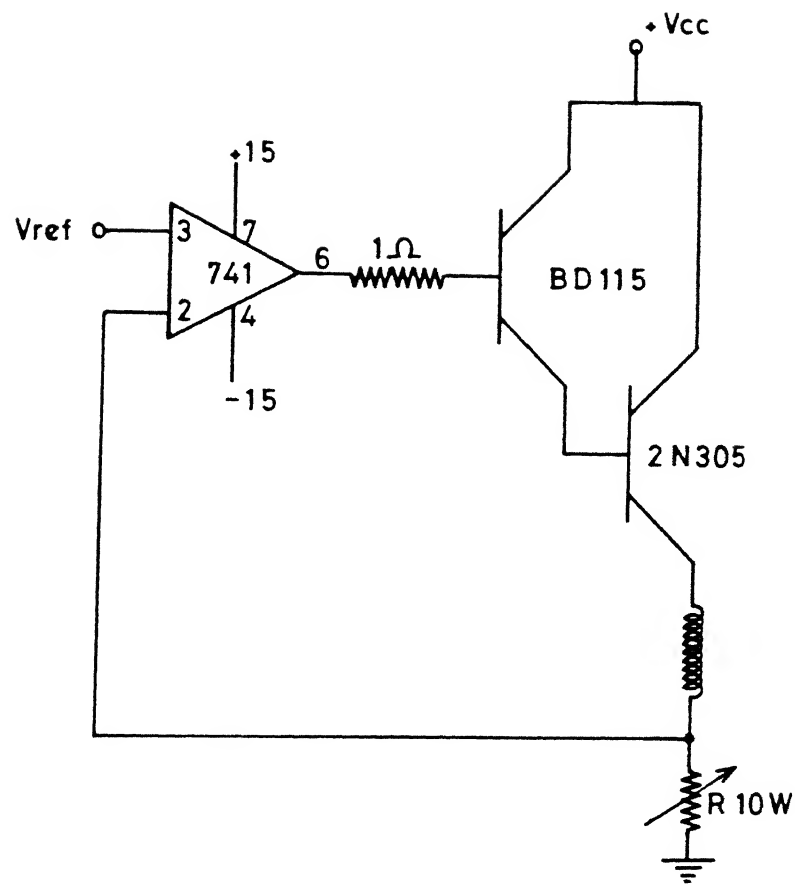


Fig.2.5 Circuit diagram for current source.

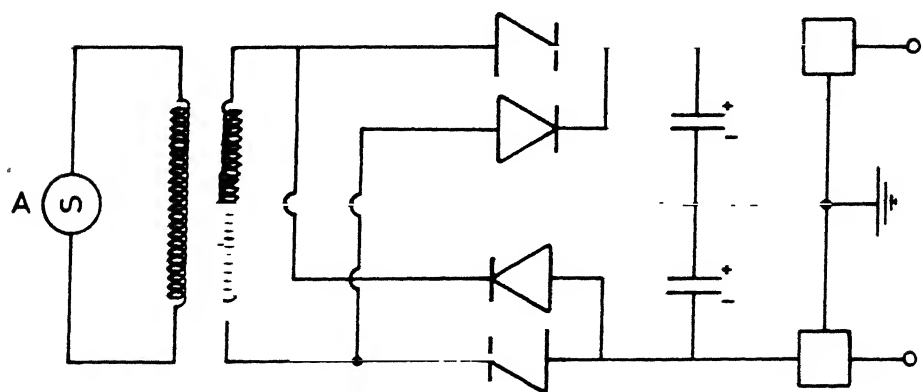


Fig.2.6 Circuit diagram for dual power supply.

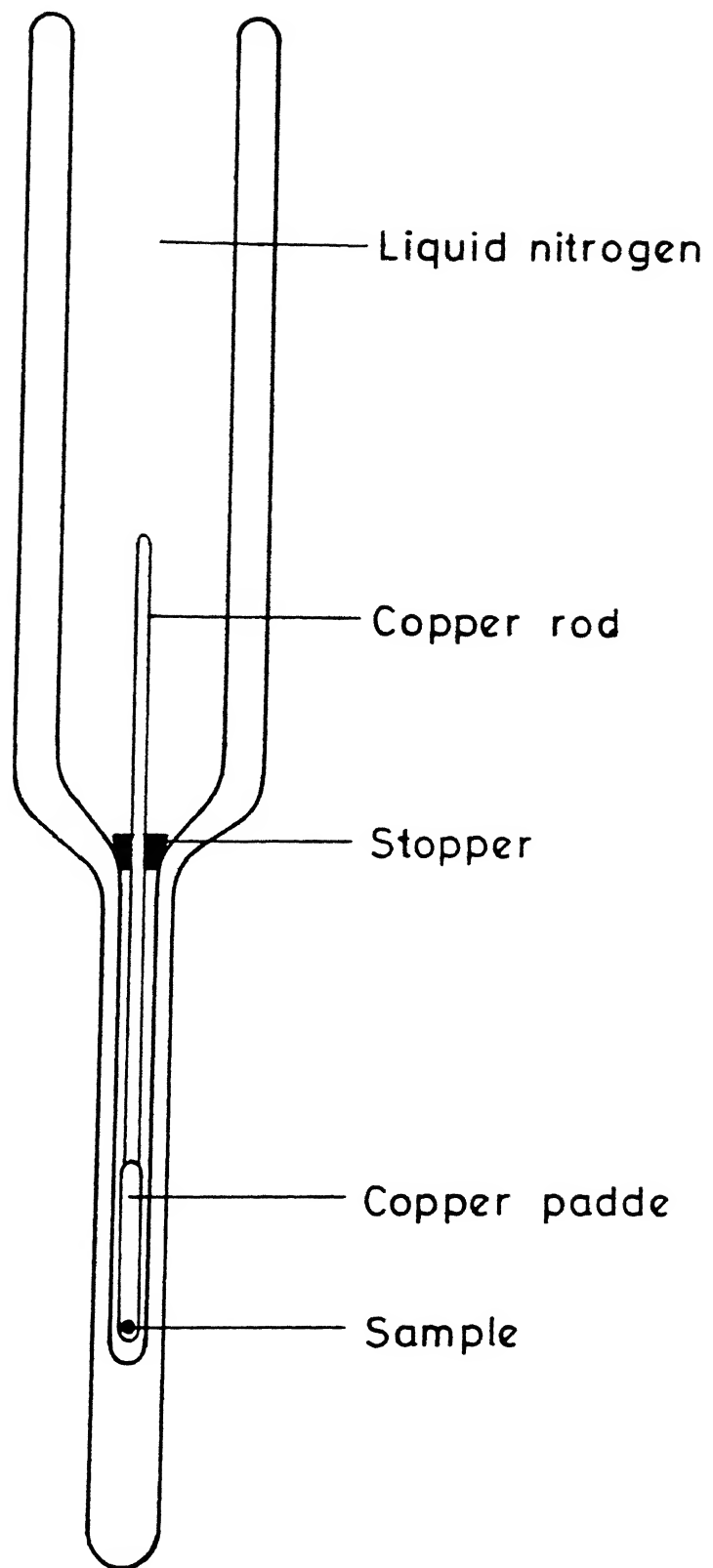


Fig. 2.7 Low temperature cell for EPR study.

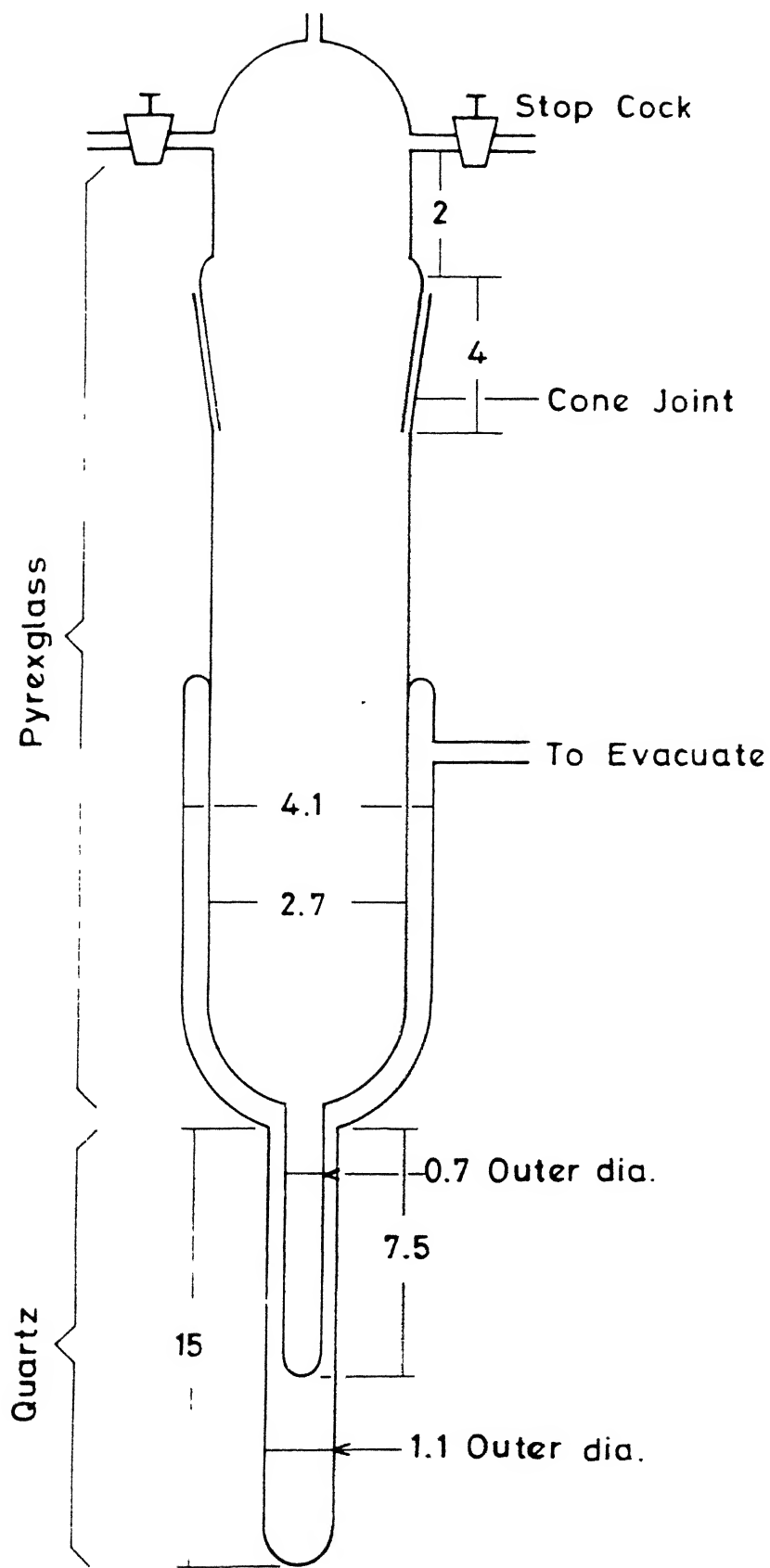


Fig. 2.8 LOW TEMPERATURE CELL

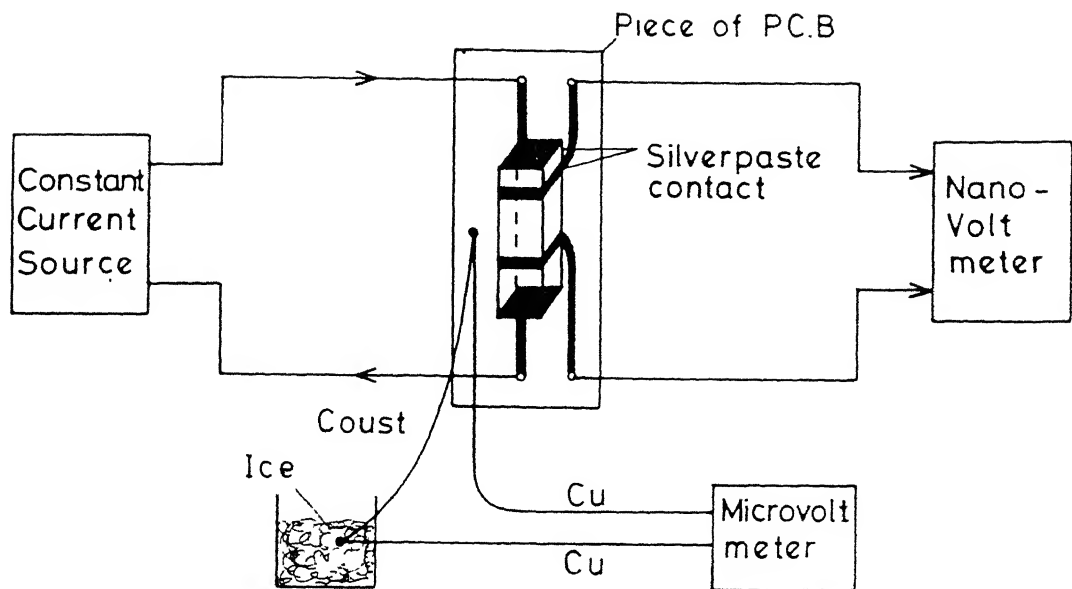


Fig.2.9 Schematic diagram for resistance measurement by four probe technique

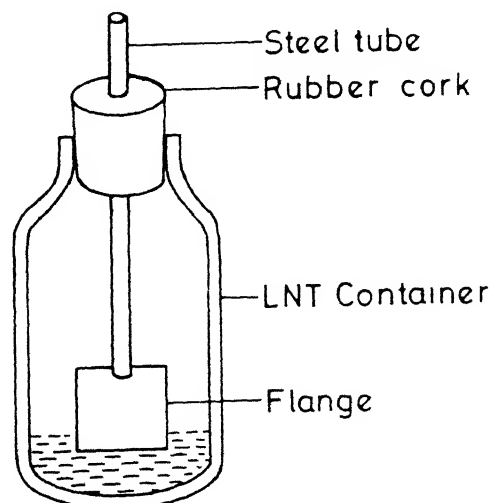


Fig.2.10 A set up for varying the sample temperature from room temperature to liquid nitrogen for resistance measurement.

CHAPTER III

ELECTRON PARAMAGNETIC RESONANCE (EPR) IN HIGH T_c SUPERCONDUCTORS

Abstract

Characterization of $\text{YBa}_2\text{Cu}_3\text{O}_{7-\delta}$, Hf-doped $\text{YBa}_2\text{Cu}_3\text{O}_{7-\delta}$ and $\text{Tl}_2\text{Ba}_2\text{CaCu}_2\text{O}_{8+\delta}$ by X-ray, resistance measurement and SEM are given. EPR of these characterized samples are studied. It is found that all high T_c superconductors is EPR silent, and the observation of the weak signal of Cu^{2+} in these samples is attributed to the impurity phases which are formed during the synthesis of the samples. Various possible explanations for EPR silence of superconductors are discussed.

Publication based on this chapter :

H.D. Bist, P.K. Khulbe, Md. Shahabuddin, Prem Chand, A.V.Narlikar, B. Jayarama and S.K. Agarwal, Solid Stat. Commun. 65, 899 (1988).

3.1 INTRODUCTION

Since the discovery of high temperature cuprate superconductors by Bednorz and Müller [1] a great deal of experimental work using different techniques have been done in La-Sr-Cu-O, Y-Ba-Cu-O, Bi-Sr-Ca-Cu-O and Tl-Ba-Ca-Cu-O. In particular, many studies on EPR signal of Cu²⁺ have been reported [12-22]. Most of these studies have shown the same features of EPR signal of high T_c superconductors, but they differ in interpretation. Some attributed this signal to that of the superconductors while other attributed it to the impurity phases which are formed in very small amount during the synthesis of the superconductor samples. EPR studies in different oxygen content YBa₂Cu₃O_{7-δ} [16,17] and in non-superconducting materials [15,16,18] related to the YBa₂Cu₃O_{7-δ} have also been reported to verify whether the EPR signal observed is from the superconducting materials or from other impurity phases [15, 16, 18].

We have studied the EPR signal of pure YBa₂Cu₃O_{7-δ} having different oxygen content, Hf-doped YBa₂Cu₃O_{7-δ} and came to the conclusion that YBa₂Cu₃O_{7-δ} is EPR silent and the signal which we get is due to other impurity phase. This shows that EPR studies can be utilized in characterization of samples of high T_c superconductors. Various possible explanation for the absence of EPR signal of Cu²⁺ in high T_c superconductors have been reported [15,17,25-28]. Yet there is no satisfactory explanation for the absence of EPR signal of Cu²⁺ in high T_c superconductors.

3.2 SAMPLE PREPARATION

Preparation of pure YBa₂Cu₃O_{7-δ} samples by different routes has been described in detail in Chapter 2. Initially, polycrystalline pure YBa₂Cu₃O_{7-δ} and hafnium doped YBa₂Cu₃O_{7-δ} used

in the present studies were received from the group of Dr. A.V. Narlikar in National Physical Laboratory, New Delhi (NPL). Those samples were characterised by resistance measurement and powder X-ray diffraction at NPL itself. Hereafter, pure $\text{YBa}_2\text{Cu}_3\text{O}_{7-\delta}$ sample from NPL will be referred as sample NPL. Later on, we prepared pure $\text{YBa}_2\text{Cu}_3\text{O}_{7-\delta}$ in our Laboratory by two different routes. The two methods differ upto the mixing of Y_2O_3 , CuO and BaCO_3 in stoichiometric ratio. The heat treatment and the environment in which heat treatment was given, were exactly the same. In fact, both samples were placed side by side for heat treatment. The methods used are (a) Solid state reaction method described in section 2.2.1 and (b) Sol-gel method or citrate combustion method described in section 2.2.4. In the preparation of these two samples the purity of Y_2O_3 , CuO and BaCO_3 was 99.9%, 99% and 99% respectively. Now onwards we shall call sample prepared by the methods (a) and (b) as Sample A and Sample B respectively. The third sample of pure $\text{YBa}_2\text{Cu}_3\text{O}_{7-\delta}$ in the present study was prepared by Solid State reaction method but the purity of the chemical used was very high, i.e., 99.999%. The third sample will be referred to as sample C. Characterisation of the Samples A, B and C by resistivity measurement, powder X-ray diffraction and Scanning electron microscope (SEM) are described in the sections that follow.

The Hafnium doped $\text{YBa}_2\text{Cu}_3\text{O}_{7-\delta}$ which we got from NPL was prepared by solid state oxide mixing technique in the same way as the Zr-substituted $\text{YBa}_2\text{Cu}_3\text{O}_{7-\delta}$ reported in reference [2]. The $\text{Tl}_2\text{Ba}_2\text{CaCu}_2\text{O}_{2.8+\delta}$ sample used in the present study also came from Dr. Narlikar's group in NPL.

3.3 RESISTANCE MEASUREMENT

Resistance of all samples was measured as a function of temperature to find the transition temperature (T_c) at which they become superconductors. Resistance measurement is the first and perhaps the easiest way to check the superconductivity and to find the T_c . Before performing other measurements on the samples we characterised all the samples by resistance measurement. Resistance measurement was done by standard four probe technique described in section 2.3. The resistance of different samples as a function of temperature are shown in Figs. 3.1, 3.2, and 3.3. Fig. 3.1 shows the resistance of sample NPL and $Tl_2Ba_2CaCu_2O_{8+\delta}$, Fig. 3.2 shows that of 0.5 % Hf-doped $YBa_2Cu_3O_{6.7-\delta}$, and Fig. 3.3 shows that of sample A and sample C. From these figures it is clear that all the samples show metallic behaviour from room temperature to transition temperature except for Sample A in which there is an increase in resistance with decreasing temperature around 130 K. This is due to the non-uniformity in oxygen uptake of $YBa_2Cu_3O_{6.7-\delta}$. Superconducting transition temperature and metallic behavior of $YBa_2Cu_3O_{6.7-\delta}$ are very much sensitive to the value of δ [3]. For $\delta = 0$ to 0.2, T_c is 90 K and drops to ~ 50 K for $\delta > 0.2$. As δ increases the metallic behaviour decreases for $\delta \geq 0.3$, and the sample behaves like a semiconductor from room temperature to transition temperature [3]. Semiconductor type behaviour around 130 K in Sample A is because of lower oxygen content portion of Sample A.

The zero resistance transition temperature for Sample NPL, Sample A, Sample C, 0.5% Hf-doped $YBa_2Cu_3O_{6.7-\delta}$ and $Tl_2Ba_2CaCu_2O_{8+\delta}$ are 89 K, 89 K, 90 K, 90 K and 104 K respectively. The inset of Fig. 3.2 shows the Hf-concentration dependence of various parameters such as onset temperature T_o , zero resistance

temperature T_c and mid point temperature T_m for different doping. All the parameters are seen to decrease marginally indicating that Hf-substitution does not affect these parameters drastically. Because of the compatible ionic radii of Hf, it may be substituted at Y, Ba, and Cu sites [4]. Since the variation in transition temperature is same in all the cases irrespective of different sites for cation substitution, it indicates that Hf is possibly substituting for Y which has been a relatively insensitive site for T_c in $\text{YBa}_2\text{Cu}_3\text{O}_{7-\delta}$ [5].

3.4 POWDER X-RAY DIFFRACTION

Powder X-ray diffraction (PXD) spectra of samples were taken on an automated SEIFERT ISO-DEBUYFLEX 2002 using Ni-filtered $\text{CuK}\alpha$ radiation. Samples in the form of fine powder were spread uniformly over glass slide and few drops of methanol was poured on it so that the powder sticks to the glass slide. The glass slide was then mounted in the sample compartment. Diffraction profiles were scanned in 2θ mode from 6° to 90° . The recorded spectra of Samples A, B, and C are shown in Figs. 3.4(a), 3.4(b) and 3.4(c) respectively. From Figs. 3.4(a) and 3.4(b) it is clear that all samples are in single orthorhombic phase. The PXD profile region of 2θ between 44° and 51° is sensitive to biphasics behaviour [6]. Comparing the PXD profiles of our samples with the PXD profiles of reference [6,7] we observed that our samples contain only orthorhombic phase. If impurity phases are less than 3% it can not be detected by X-ray powder diffraction.

3.5 SCANNING ELECTRON MICROPHOTOGRAPH STUDIES

Scanning electron microphotograph (SEM) of Hf-doped $\text{YBa}_2\text{Cu}_3\text{O}_{7-\delta}$ samples were taken on JEOL JSM35CF Scanning microscope

at NPL, New Delhi. SEM for all other samples were taken on JEOL JSM84A at I.I.T. Kanpur. The SEM of 0.5% and 2% Hf-doped samples are shown in the Figs. 3.5(a) and 3.5(b). From figure it is clear that the particle size decreases with increasing Hf-doping [5]. In 0.5 and 2% Hf-doped YBaCuO average particle sizes are 10 μm and 6 μm respectively. In Fig. 3.5(c), a typical twin boundary is shown, taking the photograph at a higher magnification.

SEM of pure $\text{YBa}_2\text{Cu}_3\text{O}_7$, i.e., the Sample A and Sample B which were prepared by two different routes but given same heat treatment as described in section 3.2, are shown in Fig. 3.6. From Figs. 3.6(a) and 3.6(b) it is clear that the particle size of Sample A, which was prepared by solid state reaction method, is larger than that of Sample B prepared by citrate combustion technique. SEM of Sample C, which was prepared by Solid State reaction method using ultra pure chemical and that of $\text{Tl}_2\text{Ba}_2\text{CaCu}_2\text{O}_8$ sample are shown in Figs. 3.6(c) and 3.7(a) respectively.

In case of Sample A and Sample B, sintering was done for 5 days at 930°C in air and oxygenation was done for 48 hours at 500°C , but in case of Sample C the sintering at 930°C was done for 3 days and oxygenation was done for 30 hours. From SEM of Sample A and Sample B as shown in Fig. 3.6 the grain boundary and grains are very clear. But in case of Sample C the grain boundary and growth of grain is not very much clear. Therefore, it is clear that sintering condition changes the microstructure of the samples. The sample deteriorates with time because it reacts with the humidity and CO_2 of the atmosphere and also it loses the oxygen content. Several studies have reported the environmental effects on $\text{YBa}_2\text{Cu}_3\text{O}_{7-\delta}$ [8-11]. Mainly the surface of the sample degrades too much on exposure to air and humidity [8]. The SEM of the Sample B after three months is shown in Fig. 3.7(b). It clearly shows a

drastic change in the microstructure. When T_c of that sample was measured it was found that it was not a superconductor, even at the liquid nitrogen temperature. When this deteriorated Sample B was resintered after crushing and reannealed in oxygen, it recovered its T_c and also its grain size had increased, which is shown in the Fig. 3.7(c).

3.6 ELECTRON PARAMAGNETIC RESONANCE (EPR)

EPR spectra of samples were recorded on an X-band EPR spectrometer (Varian E-109). The magnetic field was calibrated with digital NMR gaussmeter (Varian E-500) and was modulated with 100 KHz for EPR detection. The frequency of the resonant cavity was measured by using a standard g-marker (DPPH g = 2.0036 + 0.0002). The sample was kept in a sealed quartz tube and a thermocouple sensor was attached to it to monitor its temperature.

Pure $\text{YBa}_2\text{Cu}_3\text{O}_{7-\delta}$

We have taken the EPR spectra of pure $\text{YBa}_2\text{Cu}_3\text{O}_{7-\delta}$ samples prepared in different batch and by different routes. Initially the pure $\text{YBa}_2\text{Cu}_3\text{O}_{7-\delta}$ (Sample NPL described in section 3.2 for EPR studies came from NPL. The room temperature (RT) EPR spectra of the Sample NPL are shown in the Fig. 3.8[12]. The spectrum is powder like and consists of multiple peaks typical of $S = 1/2$ species showing g-value anisotropy. Since the expected paramagnetic species should arise from the valence states of Cu^{2+} and/or Cu^{3+} , it becomes clear from the EPR spectrum that the dominant valence is Cu^{2+} . For an orthorhombic symmetry Cu^{2+} will show g-value anisotropy and in powder spectrum X, Y, and Z components are expected to be resolved. The two principal g-factor are clearly resolved and third one is very weak. The g-factors are $g_1 = 2.20 \pm 0.02$,

$g_2 = 2.13 \pm 0.02$ and $g_3 = 2.06 \pm 0.02$. The hyperfine structure is not resolved at all, which implies that the hyperfine interaction parameter A is undetectably small. The temperature dependence of EPR spectra of Sample NPL are shown in the Fig. 3.9. The intensity of EPR spectrum near $g \approx 2$ increases slowly as we go to lower temperatures and below 90K. It becomes very difficult to record the spectrum around $g \approx 2$ with the spectrometer parameters kept similar to those for recording the spectra at room temperature.

The room temperature EPR spectra for the pure $\text{YBa}_2\text{Cu}_3\text{O}_{7-\delta}$ Sample C, prepared by solid state decomposition method using ultra pure chemical described earlier in section 3.2, are shown in Fig. 3.10. For EPR spectra recording, the weighed sample was taken in powder form in the sealed quartz tube. In Fig. 3.10 the EPR spectra of the same sample having different oxygen content are shown. The oxygen content are written on each spectra. The samples with different oxygen contents were obtained from the master sample having oxygen content 6.85. The oxygen content 6.8 was obtained by sintering the master sample at 930°C and then furnace cooling in the air environment. The sample having oxygen content 6.3 was obtained by sintering the master sample in the argon environment at 500°C and then furnace cooling in the same environment. The sample having oxygen content 6.0 was obtained from master sample by sintering the sample at 900°C in the argon environment for 12 hours and then furnace cooling. The oxygen contents of the samples were estimated by iodometric titration discussed in section 3.4. All spectra are found to be powder-like and consist of multiple peaks typical of $S = 1/2$ showing g anisotropy and it appears that it is due to copper complex. The presence of two resolved components in all cases with $g_1 = 2.21 \pm 0.02$ and $g_2 = 2.05 \pm 0.02$ indicate the axial symmetry of the Cu^{2+}

environment. The hyperfine structure is not resolved, perhaps due to higher concentration of paramagnetic ions. The g-value and line shape are insensitive to the oxygen content of the sample. Although there is a little change in the intensity but it is not systematic.

The EPR spectra of another batch of sample $\text{YBa}_2\text{Cu}_3\text{O}_{6.95-\delta}$ having different oxygen content are shown in Fig. 3.11. This sample was also prepared by oxide decomposition. Samples with different oxygen contents were obtained from the sample with oxygen content 6.95 by sintering it at different temperatures in a Helium environment. During the process of sintering of this sample at 950°C in Helium environment, the temperature had risen to 1000°C for some time. This has caused the formation of a small portion of other phases which is reflected in the EPR signal of $\text{YBa}_2\text{Cu}_3\text{O}_6$. In case of $\text{YBa}_2\text{Cu}_3\text{O}_{6.95}$ the signal is negligible. If we take the same sample in the form of pellet, it does not show any signal, although it shows very small humps in powder form as shown in Fig. 3.11(a). Also in case of $\text{YBa}_2\text{Cu}_3\text{O}_{6.95}$ there is high microwave loss which causes much problem in balancing the bridge. The dielectric loss is due to the increase in the metallic behaviour of the sample with increasing oxygen content. When the EPR spectra of $\text{YBa}_2\text{Cu}_3\text{O}_{6.9}$ were taken after six months, there was an increase in the intensity of EPR signal. Now the problem of balancing the bridge is over, which shows that the dielectric loss is less.

Hf-doped $\text{YBa}_2\text{Cu}_3\text{O}_{6.95-\delta}$

The EPR spectra recorded at room temperature and liquid nitrogen temperature for the three samples having 0.5%, 1% and 2% Hafnium are shown in Fig. 3.12 [13]. All the spectra were recorded in similar conditions and with the same amount of the samples, for

comparison. The EPR signal intensity increases with increasing Hf-concentration. Also, the signal demonstrates the axial symmetry of the g-tensor ($g_{\parallel} = 2.4 \pm 0.02$, $g_{\perp} = 2.08 \pm 0.02$). The Hf-doping of $\text{YBa}_2\text{Cu}_3\text{O}_{7-\delta}$ increases the stability of the sample against ageing. It has been confirmed by recording the EPR spectra after one month duration. The change in the signal strengths recorded at similar experimental conditions was negligible.

The EPR spectra of Thallium and Bismuth samples were recorded at room temperature but they do not show the EPR signal near $g \approx 2$.

3.7 DISCUSSION

The basic question is whether the high T_c superconductor $\text{YBa}_2\text{Cu}_3\text{O}_{7-\delta}$ is EPR silent. If high T_c superconductors are EPR silent, then what is the origin of the EPR signals from the samples studied. The second question is what is the probable cause for the absence of EPR signal in high T_c superconductors.

The pure $\text{YBa}_2\text{Cu}_3\text{O}_{7-\delta}$ is EPR silent and several groups of workers have supported this view [14-19]. We will discuss later on how our experimental observations support the idea that $\text{YBa}_2\text{Cu}_3\text{O}_{7-\delta}$ is EPR silent.

Several groups of workers have studied the EPR of the other phases which generally are formed during the preparation of $\text{YBa}_2\text{Cu}_3\text{O}_{7-\delta}$. The main phases are Y_2BaCuO_5 and BaCuO_2 . R.N.de-Mesquita et al [16], W.R. McKinnon et al [15] and Jiang-Tsu Yu et al [17] have studied the EPR of Y_2BaCuO_5 [21,22] and BaCuO_2 . The X-band and Q-band EPR spectra of Y_2BaCuO_5 at $T = 297\text{K}$ are shown in Figs. 3.13(a) and 3.13(b) respectively [16]. The theoretical fit gives $g_x = 2.08 \pm 0.01$, $g_y = 2.12 \pm 0.02$ and $g_z = 2.25 \pm 0.01$. In X-band the three g values are not resolved but in Q-band they are clearly resolved. The three components clearly

indicate that Cu^{2+} ions are located at a site having orthorhombic symmetry [16]. BaCuO_2 also gives EPR signal at RT and the theoretical fit gives $g_x = g_y = 2.055 \pm 0.005$, and $g_z = 2.24 \pm 0.01$. In $\text{BaCuO}_{2.02}$ Cu^{2+} ions are located at the site having tetragonal symmetry.

A comparison of the EPR spectra of the Sample NPL shown in Fig. 3.8 with the EPR spectra of Y_2BaCuO_5 shown in Fig. 3.13 clearly reveals that the signal is not due to high T_c phase of $\text{YBa}_2\text{Cu}_3\text{O}_{7-\delta}$ but due to Y_2BaCuO_5 , which is formed during the synthesis of $\text{YBa}_2\text{Cu}_3\text{O}_{7-\delta}$. The room temperature EPR spectra of pure $\text{YBa}_2\text{Cu}_3\text{O}_{7-\delta}$ having different oxygen contents are shown in Fig. 3.10. It is clear from the figure that there is no change in the g-value and the shape of the EPR signal, with the variation of oxygen content. Though a marginal change in the intensity is observed. The intensity of the EPR signal in Sample C is very weak in comparison to that in Sample NPL. Sample C was sintered for longer time than Sample NPL and regrinding in the later sample was done many more times in comparison to Sample NPL. Therefore, it is clear from above observations that, by increasing the regrinding and sintering time, one can decrease the possibility of formation of other phases in the sample. Comparing the EPR signal of Sample C with that of Y_2BaCuO_5 and BaCuO_2 , it is clear that the EPR signal in Sample C is either due to Y_2BaCuO_5 or BaCuO_2 . Another batch of sample $\text{YBa}_2\text{Cu}_3\text{O}_{7-\delta}$ which was regrinded several times and sintered for longer time than Sample C and having oxygen content 6.95 shows a negligible EPR signal as shown in Fig. 3.11. The EPR signal in the same sample, but having oxygen content 6.3, shows increase in the signal intensity. As the oxygen content increases the metallic behaviour increases. This is evident in case of $\text{YBa}_2\text{Cu}_3\text{O}_{6.95}$ because in this case the bridge does not balance

easily. Due to metallic behaviour there is skin depth problem and the microwave is not exposed to the whole material which contains a very low percentage of impurity phase Y_2BaCuO_5 and BaCuO_2 . As the oxygen content in $\text{YBa}_2\text{Cu}_3\text{O}_{7-\delta}$ decreases metallic behaviour decreases, i.e. resistivity increases and the skin depth increases, and therefore, microwave is exposed to the whole impurity phase. Consequently, the intensity of the EPR signal increases. The sudden change in the EPR signal of $\text{YBa}_2\text{Cu}_3\text{O}_{6.13}$ sample of this batch as shown in Fig. 3.11 is due to the formation of Y_2BaCuO_5 phase during annealing $\text{YBa}_2\text{Cu}_3\text{O}_7$ sample at 970°C in Helium environment because the temperature had risen to 1000°C for some time during sintering. We can thus conclude that $\text{YBa}_2\text{Cu}_3\text{O}_{7-\delta}$ ($\delta + 1$ to 0) is EPR silent irrespective of the value of δ , while according to Owens et al [17] $\text{YBa}_2\text{Cu}_3\text{O}_7$ and $\text{YBa}_2\text{Cu}_3\text{O}_6$ are EPR silent but $\text{YBa}_2\text{Cu}_3\text{O}_{6.13}$ is not. The observed EPR signal in $\text{YBa}_2\text{Cu}_3\text{O}_{7-\delta}$ is due to impurity phases, mainly Y_2BaCuO_5 and BaCuO_2 . These impurity phases are very less in amount and could not be detected by X-ray. The percentage of this impurity phase can be estimated by comparing the integrated intensity of the EPR signal of the weighed $\text{YBa}_2\text{Cu}_3\text{O}_{7-\delta}$ with the integrated intensity of weighed standard sample having similar line shape under similar recording conditions. We have estimated the percentage of impurity in Sample C using $\text{CuCl}_2 \cdot 2\text{H}_2\text{O}$ as standard and found that the percentage of impurity is around 1%. From these observations, it is obvious that the EPR is a very sensitive tool for characterizing the high T_c superconductors.

In metallic systems, generally the spin lattice ($\frac{1}{T_1}$) and spin-spin ($\frac{1}{T_2}$) relaxation rates are equal. Spin relaxation rates in metals were analysed in detail by Elliot [23], who considered the combined effects of resistivity scattering and spin orbit

interaction. The electron spin relaxation rate is given by [24]

$$T_1^{-1} = T_2^{-1} \approx \alpha (\Delta g)^2 \tau_R^{-1} \quad (3.1)$$

where τ_R^{-1} is the resistivity relaxation rate (the average time between resistive scattering events), α is a numerical factor and Δg is deviation from the free spin of the electronic g-value. The value of τ_R^{-1} for $\text{YBa}_2\text{Cu}_3\text{O}_{7-\delta}$ is estimated to be of the order of 10^{15} s^{-1} by Janes et al., [25] using the formula

$$\tau_R^{-1} = \frac{n e^2 \rho}{m^*} \quad (3.2)$$

where n is the electron density, e is the electronic charge, m^* is the electronic effective mass and ρ is the electrical resistivity. Substituting the value of τ_R^{-1} in equation (3.1), the value of T_1^{-1} comes out to be around $2 \times 10^{13} \text{ s}^{-1}$ at room temperature, if we take $\Delta g = 0.15$ which is the typical value for Cu^{2+} . Using the value of T_1^{-1} , the line width of Cu^{2+} signal is calculated assuming a Lorentzian line shape, by the formula

$$T_1^{-1} = \frac{3 \pi g \beta \Delta H_{pp}}{h} \quad (3.3)$$

where h is the Planck's constant, β is the Bohr magneton and ΔH_{pp} is the signal line width (peak to peak). Estimated value of ΔH_{pp} is around 1150 KG, which is too broad to be detected.

It is observed that insulating and semiconducting materials of the same family, i.e., $\text{YBa}_2\text{Cu}_3\text{O}_6$ and La_2CuO_4 are also EPR silent even above the long-range antiferromagnetic ordering temperature, which shows that the broadening of the line-shape in the metallic $\text{YBa}_2\text{Cu}_3\text{O}_7$ is not the cause for its EPR silence. Mehran and Anderson [26] have contend that EPR silence is not

simply a manifestation of dipolar or exchange broadening, but Heisenberg exchange narrowing of the lines also is a dominant process. Sreedhar and Ganguly [27] reported that, these systems possess long range 180° Cu-O-Cu interaction and no EPR singal. It is well established that for 2D antiferromagnetic system, EPR is usually observed only at temperatures much higher than T_N (Neel temperature) [28]. But the absence of EPR signal even upto 600° K in La_2CuO_4 [29] rule out the possibility of 2D antiferromagnetic ordering being the cause of the absence of EPR signals.

McKinnon et al. [14] suggested a possible cause for the absence of EPR signal in high T_c superconductors on the basis of resonating valence bond theory. According to this theory, a linear Cu-O-Cu can result in "resonating" valence bonds as well as the formation of canonical structures consisting of arrays of $(\text{Cu}-\text{O}-\text{Cu})^{++}$ "molecules" having ${}^1\Sigma$ ground state and very remote triplet states. The mechanism of bond formation is that of the superexchange between d-electrons on two adjacent copper ions and the p-electrons on the intervening oxygen. Thus $\text{YBa}_2\text{Cu}_3\text{O}_{7-\delta}$ is EPR silent due to the presence of virtually inaccessible triplet state. But still the cause for the absence of EPR signal in the whole family of high T_c superconductors is not resolved yet.

REFERENCE

- 1 J.G. Bednorz and K.A. Müller, Z. Phys. B 69, 189 (1986).
- 2 B. Jayram, S.K. Agarwal, K.C. Nagpal, A. Gupta and A.V. Narlikar, Mat. Res. Bull. 23, 701 (1988).
- 3 C.N.R. Rao, Chemistry of Oxide Superconductors, edited by C.N.R. Rao, Blackwell Scientific Publications, 5 (1988).
- 4 A.V. Narlikar, C.V. Narshima Rao and S.K. Agarwal, Studies in High Temperature Superconductors vol.1, edited by A.V. Narlikar (NOVA Science Publishing, New York, 1989).
- 5 A.G. Vedeshwar, Md. Shahabuddin, Prem Chand, H.D. Bist, S.K. Agarwal, V.N. Moorthy, C.V.N. Rao and A.V. Narlikar, Physica C, 158, 385 (1989).
- 6 A.J. Jacobson, J.M. Newsam, D.C. Johnston, J.P. Stokes, S. Bhattacharya, J.T. Lewandowski, D.P. Goshorn, M.J. Higgins and M.S. Alvarez, Chemistry of Oxide Superconductors, edited by C.N.R.Rao, 43 (Blackwell Scientific Publication (1988)).
- 7 R.J. Cava, B. Batlogg, R.B. van Dover, D.W. Murphy, S. Sunshine, T. Siegrist, J.P. Remeika, E.A. Rietman, S. Zahurak and G.P.Espinosa, Phys. Rev. Letts. 58, 1676(1987).
- 8 S.L. Qui, M.W. Ruckman, N.B. Brookes, P.D. Johnson, J. Chem. C.L.Lin, B.Sinkovic, and M. Strongin, Phys. Rev. B 37, 3747 (1988).
- 9 J.G. Thompson, B.G. Hyde, R.L. Withers, J.S. Anderson, J.G. Fitz Gerald, J. Bitmead, M.S. Paterson, and A.M. Steward, Mater. Res. Bull. 22, 1715 (1987).
- 10 L.B. Harris and F.K. Nyang, Solid State Commun. 67, 359 (1988).
- 11 Temel H. Büyüklimanlı and Joseph H. Simmons, Phys. Rev. B 44, 727 (1991).
- 12 H.D. Bist, P.K. Khulbe, Md. Shahabuddin, Prem Chand, A.V. Narlikar, B.Jayrama and S.K. Agarwal, Solid Stat. Commun. 65, 899 (1988).
- 13 A.G. Vedeshwar, Md. Shahabuddin, Prem Chand, H.D. Bist, S.K. Agarwal, V.N. Moorthy, C.V.N. Rao and A.V. Narlikar, Physica C 158, 385 (1989).

- 14 G.J. Bowden, P.R. Ellison, K.T. Wan, S.X. Dov, K.E. Easterling, A. Boodilon, C.C. Sorrel, B.A. Cornell and S. Separovic, *J. Phys. C* **20**, L545 (1987).
- 15 W.R. McKinnon, J.R. Morton, K.F. Preston and L.S. Selwyn, *Solid Stat. Commun.* **65**, 855 (1988).
- 16 R.N. de Mesquita, J.H. Castilho, G.E. Berberis, C. Rettori, I. Torriami, O.F. de Lima, S. Gama, R.F. Jardim, M.C. Terrile, H. Basso and O.R. Nascimentno, *Phys. Rev. B* **39**, 6694 (1989).
- 17 F.J. Owen's, B.L. Ramakrishna and Z. Iqbal, *Physica C*, **156**, 221 (1988).
- 18 Jiang-Tsu Yu and K.H. Lii, *Solid Stat. Commun.* **65**, 1379 (1988).
- 19 D.C. Vier, S.B. Oseroff, C.T. Salling, J.F. Smyth, S. Schultz, Y. Dalichaouch, B.W. Lee, M.B. Maple, Z. Fisk and J.D. Thompson, *Phys. Rev. B* **36**, 8888 (1987).
- 20 K. Kojima, K. Ohbayashi, M. Udagawa and T. Hihara, *Jpn. J. Appl. Physics*, **26**, L545 (1987).
- 21 T. Kobayashi, H. Katsuda, K. Hayashi, M. Tokumoto and H. Ihara, *Jpn. J. Appl. Physics* **27**, L670 (1988).
- 22 K. Kojima, K. Ohbayashi, M. Udagawa and T. Hihara, *Jpn. J. Appl. Phys.* **26**, L766 (1987).
- 23 R. J. Elliott, *Phys. Rev.* **96**, 266 (1954).
- 24 R.N. Edmonds and P.P. Edwards, *Proc. Roy. Soc. London, Ser. A* **395**, 341 (1984).
- 25 R. James, K.K. Singh, S.D. Burnside and P.P. Edwards, *Solid State Commun.* **79**, 241 (1991).
- 26 F. Mehran and P.W. Anderson, *Solid State Commun.* **71**, 29 (1989).
- 27 K. Sreedhar and P. Ganguly, *Inorg. Chem.* **27**, 2261 (1988).
- 28 S.B. Oseroff, D. Rao, F. Wright, D.C. Vier, S. Schultz, S.T. Thomson, Z. Fisk, S.W. Cheong, M.F. Hundley, M. Tover, *Phys. Rev. B* **40**, 1934 (1990).
- 29 P.W. Anderson, *Mat. Res. Bull.* **8**, 153 (1973).

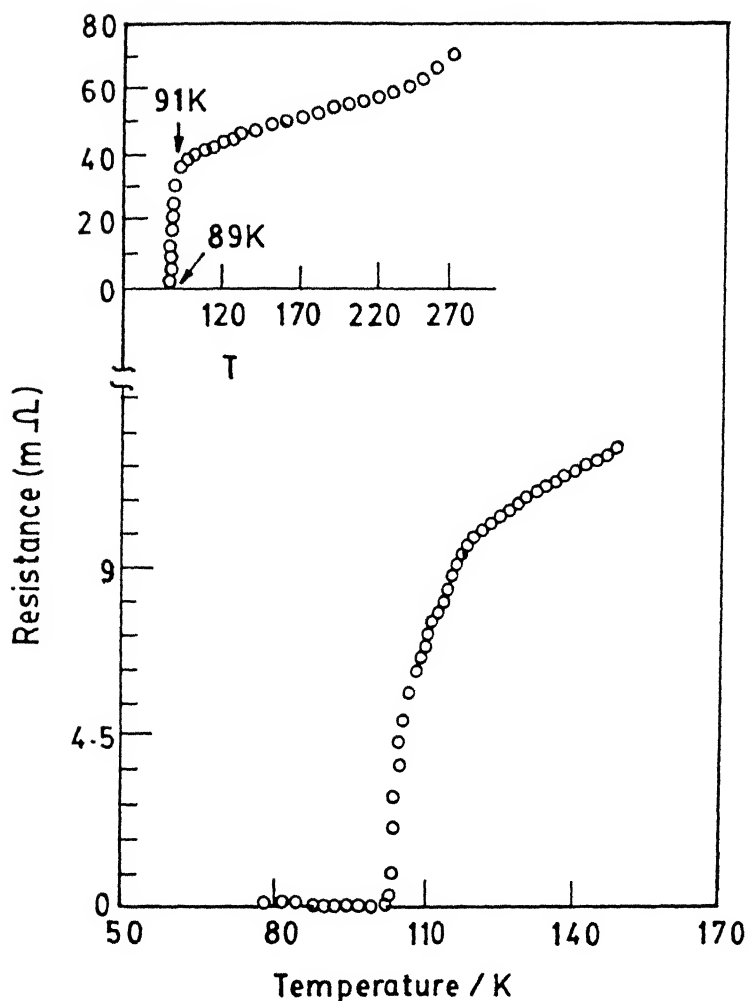


Fig. 3.1 The resistance of $Tl_2Ba_2CaCu_2O_{8+\delta}$ as a function of temperature. Inset shows that of $YBa_2Cu_3O_{7-\delta}$ (Sample NPL)

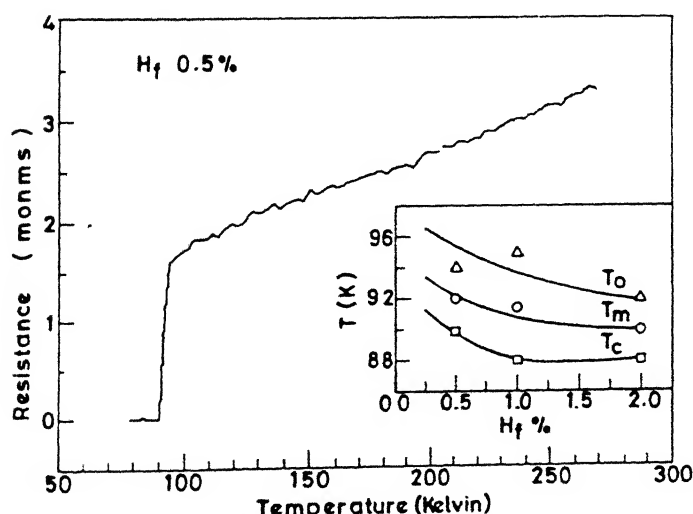


Fig. 3.2 Variation of resistance with temperature for 0.5% Hf-doped $YBa_2Cu_3O_{7-\delta}$. Inset shows the variation of T_o , T_m and T_c

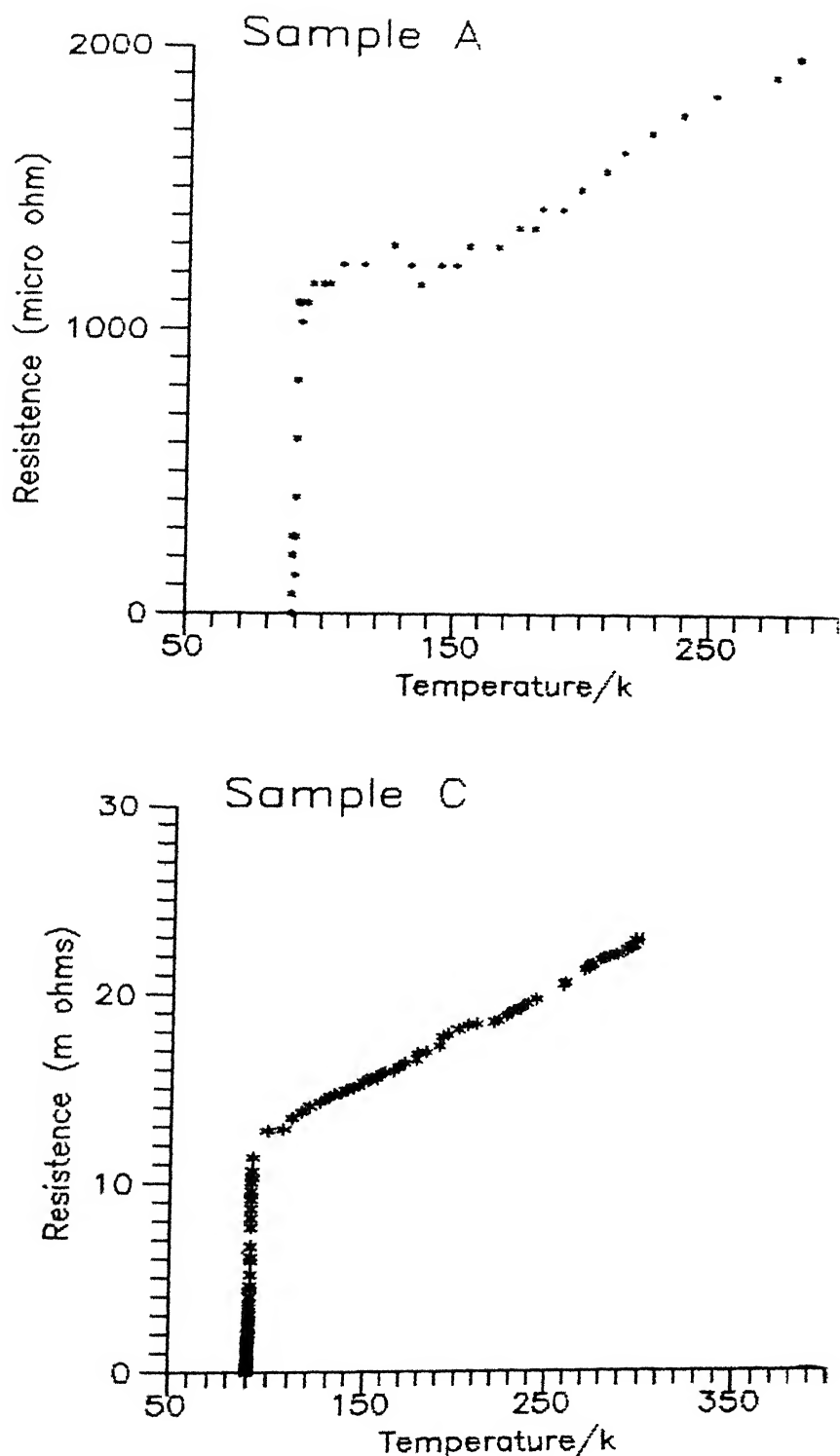


Fig. 3.3 Resistance of $\text{YBa}_2\text{Cu}_3\text{O}_{7-\delta}$ as a function of temperature

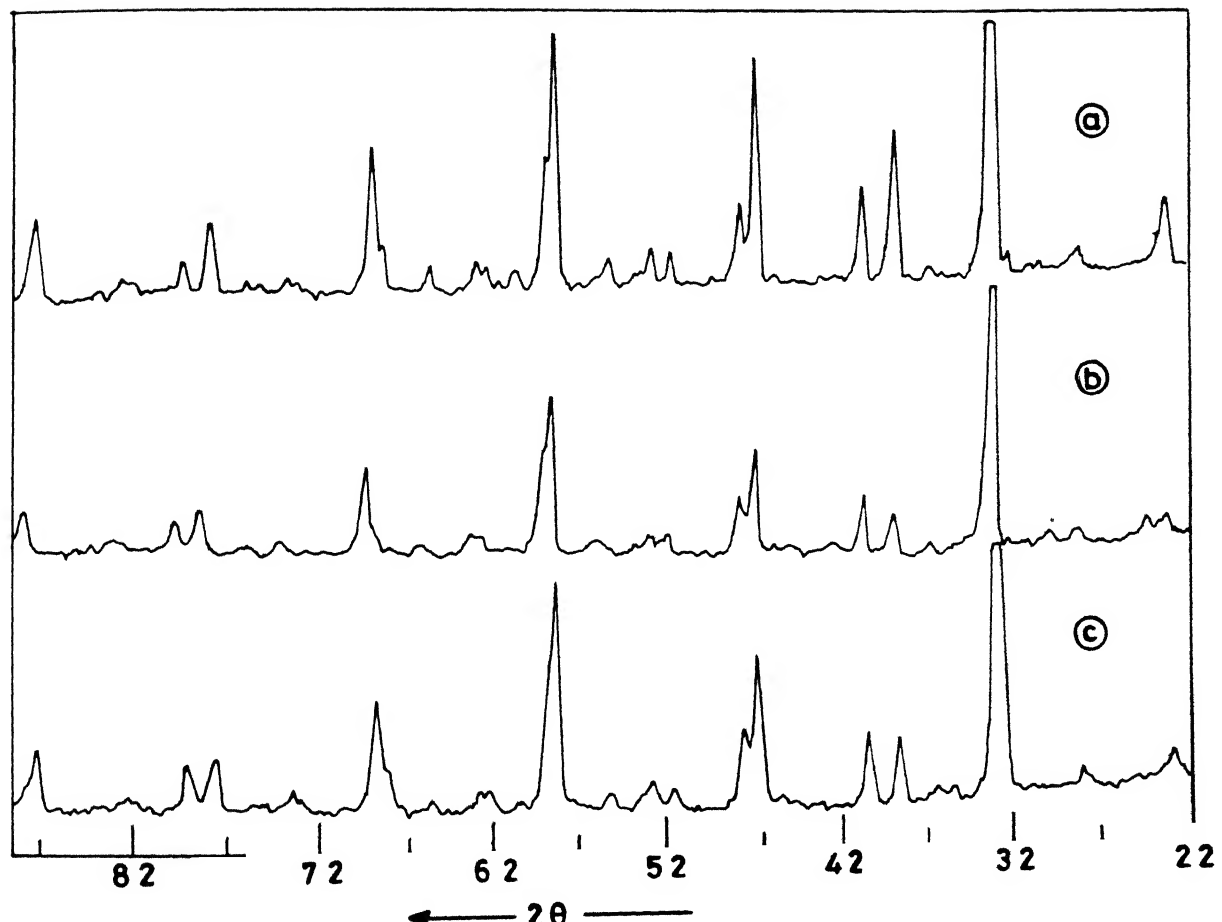


Fig. 3.4 Powder X-ray diffraction of $\text{YBa}_2\text{Cu}_3\text{O}_{7-\delta}$ (a) Sample A (b) Sample B
(c) Sample C

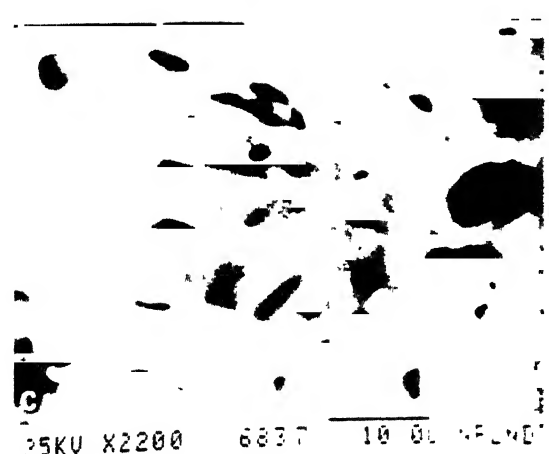
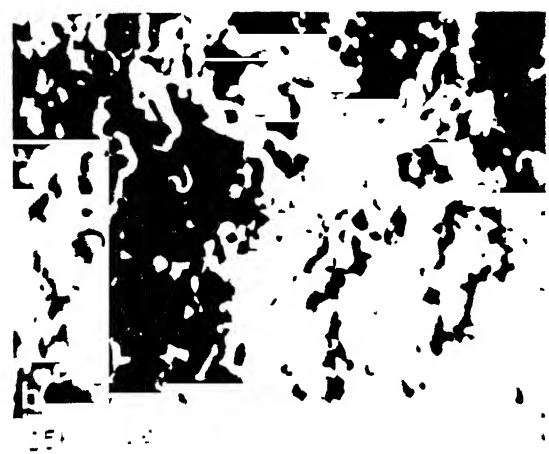


Fig.3.5 SEM micrograph of sample doped with (a) 0.5% Hf (b) 2% Hf (c) twin boundary structure in 2% Hf-doped sample.

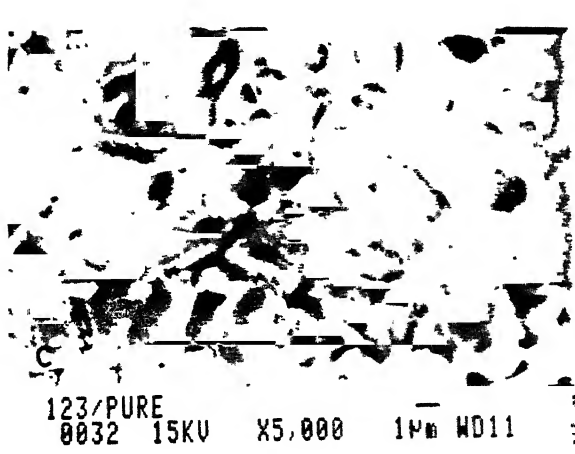
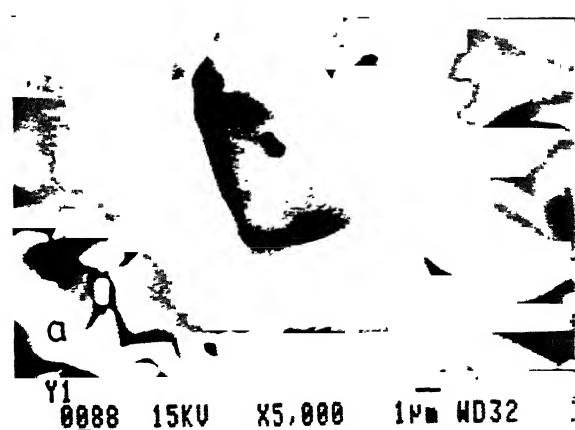


Fig.3.6 SEM micrograph of $\text{YBa}_2\text{Cu}_3\text{O}_{7-\delta}$
(a) Sample A (b) Sample B (c) Sample C

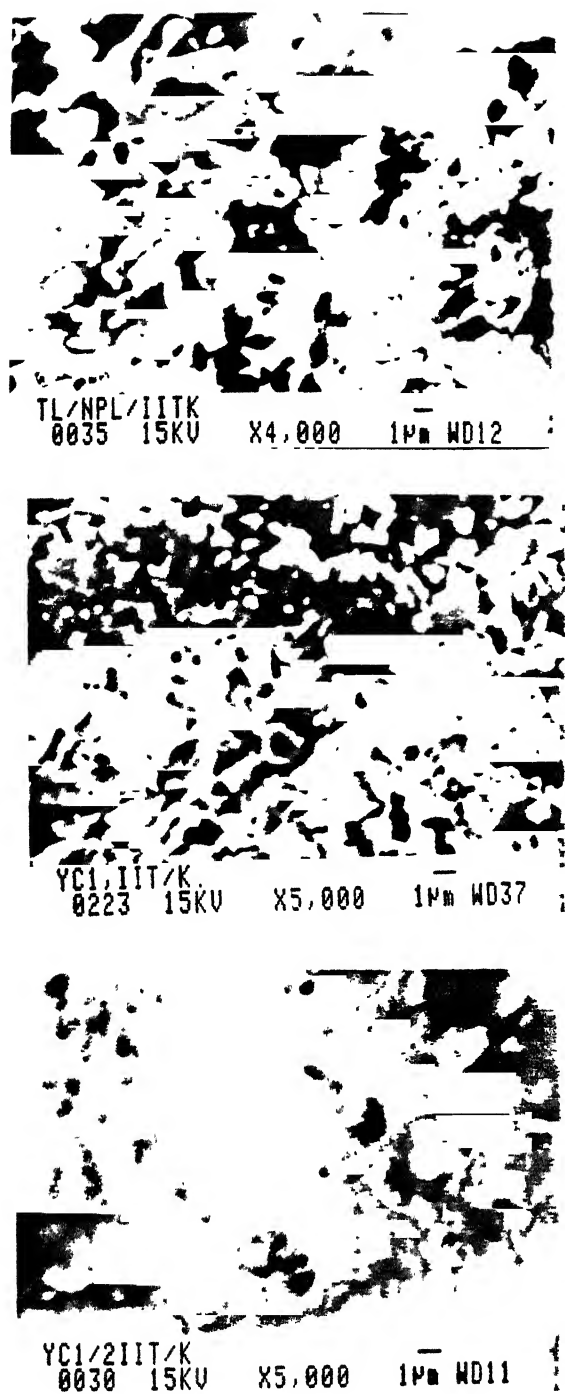


Fig. 3.7 SEM micrograph of (a) $Tl_2Ba_2CaCu_2O_{8+\delta}$
 b) Sample B (after three months of preparation)
 c) Sample D (see text)

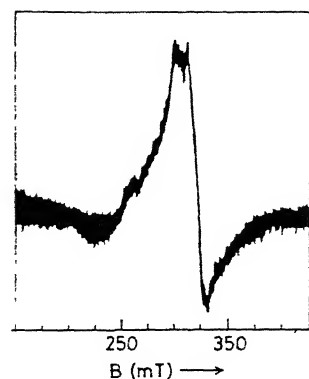


Fig. 3.8 X-band EPR spectrum of $YBa_2Cu_3O_{7-\delta}$
 (Sample NPL) at room temperature

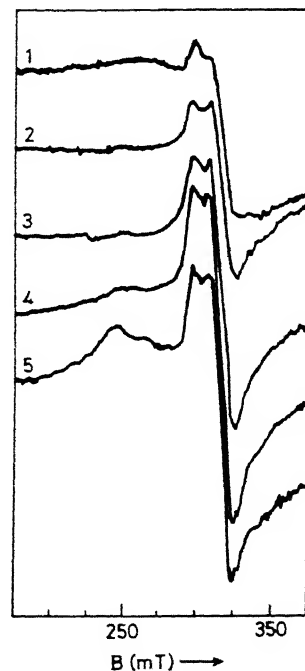


Fig. 3.9 Temperature dependence of the
 X-band EPR signal in $YBa_2Cu_3O_{7-\delta}$ (Sample NPL)
 The curves 1, 2, 3, 4 and 5 are at temperatures
 298, 142, 122, 109 and 89 K respectively

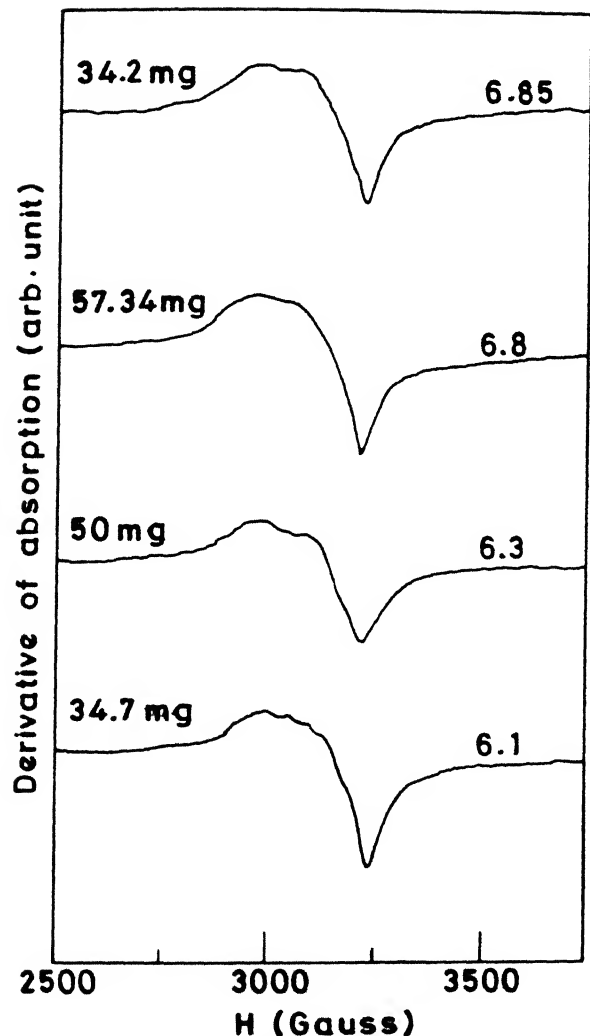


Fig. 3.10 Room temperature X-band EPR spectra of pure $\text{YBa}_2\text{Cu}_3\text{O}_{7-\delta}$ (Sample C) with different oxygen content. Oxygen content and weight of the sample are shown in each spectrum (Recording conditions are same for all spectra)

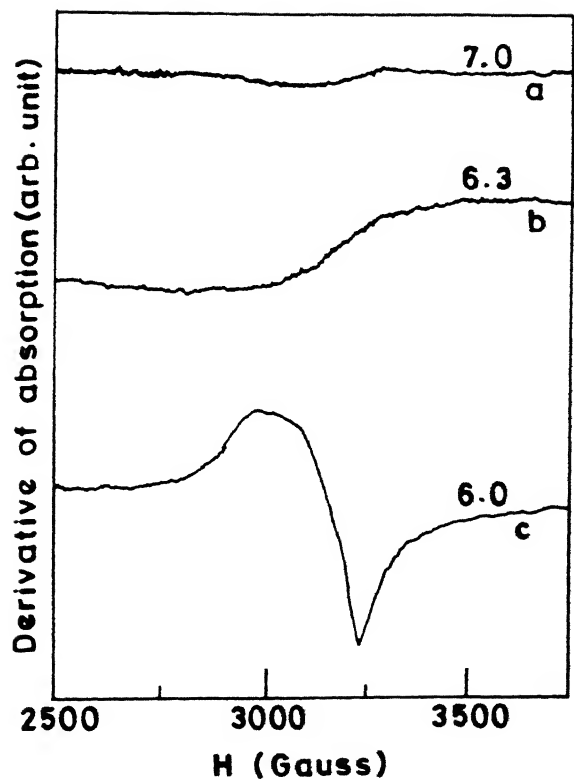


Fig. 3.11 Room temperature EPR spectra of pure $\text{YBa}_2\text{Cu}_3\text{O}_{7-\delta}$ (another batch) with different oxygen content. Oxygen contents are written on each spectrum (Recording conditions are same for all spectra)

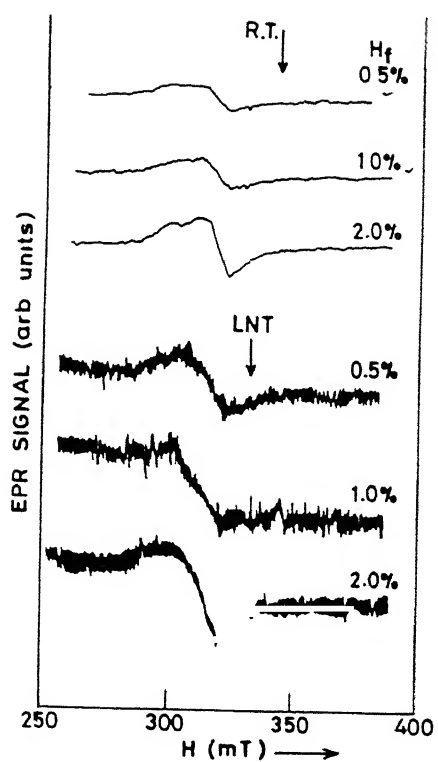


Fig. 3.12 X-band EPR signal at RT (300K) and LNT (77K) for the Hf-doped $\text{YBa}_2\text{Cu}_3\text{O}_{7-\delta}$ (Recording conditions: Power 20mW, Gain 10^4 and Modulation amplitude 4G)

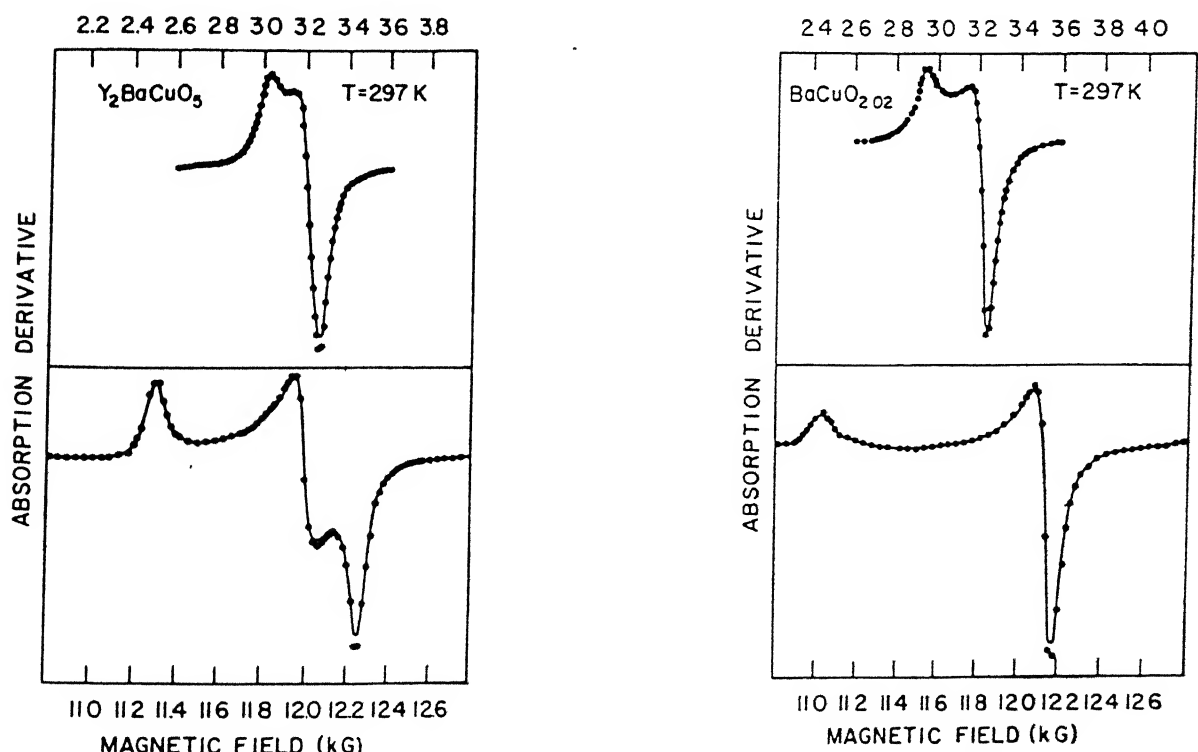


Fig. 3.13(a) EPR powder spectra of Y_2BaCuO_5 at T=297 K (1) X-band (9.5GHz)
(2) Q-band (35 GHz) (Ref.16)

Fig. 3.13(b) EPR powder spectra of $\text{BaCuO}_{2.02}$ at T=297 K (1) X-band (9.5GHz)
(2) Q-band (35 GHz) (Ref.16)

CHAPTER IV

DERIVATIVE OF LOW FIELD DEPENDENT MICROWAVE ABSORPTION IN $\text{YBa}_2\text{Cu}_3\text{O}_{6.85}$, HF-DOPED $\text{YBa}_2\text{Cu}_3\text{O}_{7-\delta}$ AND $\text{Tl}_2\text{Ba}_2\text{CaCu}_2\text{O}_{8+\delta}$ SUPERCONDUCTORS AND ITS TEMPERATURE DEPENDENCE

Abstract

Derivative of low field dependent microwave absorption (DLFDMA) of pure $\text{YBa}_2\text{Cu}_3\text{O}_{7-\delta}$ (prepared by different methods and having different particle sizes), Hf-doped $\text{YBa}_2\text{Cu}_3\text{O}_{7-\delta}$ and $\text{Tl}_2\text{Ba}_2\text{CaCu}_2\text{O}_{8+\delta}$ are studied. The peak position (H_m) of DLFDMA shifts towards lower field as the particle size of the samples is increased. The parameter H_m is related to H_{c1J} of the intergranular junctions. The peak height h_p grows very fast as we go few degrees below the transition temperature T_c . The peak position does not show any shift near T_c while the hysteresis area decreases with increasing temperature and vanishes at T_c . The peak height and hysteresis area vary as $(T_c - T)^\alpha$ where α varies from sample to sample and its range is from 0.5 to 3.5. The results are explained in terms of the model proposed by Dulcic et al. This model assumes that there exists a large number of random intergranular Josephson junctions which can be represented by a single representative junction.

Publications based on this chapter:

- (i) A.G.Vedeshwar, Md. Shahabuddin, Prem Chand, H.D.Bist, S.K.Agarwal, V.N.Moorthy, C.V.N.Rao and A.V.Narlikar, Physica C, 158, 385 (1989)
- (ii) A.G.Vedeshwar, H.D.Bist, Md. Shahabuddin, S.K.Agarwal, V.N.Moorthy, C.V.N. Rao and A.V.Narlikar, Phys. Lett. A, 139, 415 (1989).

4.1 INTRODUCTION

The recently discovered high T_c superconducting materials provide puzzles, both on microscopic and macroscopic levels. At the microscopic level it is the mechanism for pairing that is being debated. At the more phenomenological level it is the apparent glass-like properties of these materials [1-5] or the giant flux-creeps [6] that is drawing experimental and theoretical attention. Microwave absorption studies in normal metals and conventional superconductors have been used since long [1-3] to get information about the superconducting state below T_c ($\rho = 0$). For phonon superconductors, the microwave surface resistance provides a well established method for studying the flux-flow surface losses in bulk samples. The high T_c superconductors are granular in nature and contain many Josephson junctions or weak links. While measuring the microwave response of ceramic high T_c superconductors, the properties originating from junctions and weak links, may dominate. A high T_c superconductor exhibits large amount of field dependent microwave absorption at very low field below T_c [4-8,12-21]. This absorption has been attributed to the losses in the intergranular Josephson junctions [8,13]. The field dependent microwave absorption was measured with [12-21] and without modulation field [4-7]. Magnetic field modulation and lock-in detection system usually give derivative of the absorption with respect to the field. The derivative signal of the microwave absorption in high T_c superconductors shows peak at low fields (1 to 10G). The dependence of the peak position on temperature is not much clear. Some workers report that there is no temperature dependence [13] while others report that the temperature dependence is much pronounced [14-18]. The modulated microwave absorption has also been observed in the conventional superconductors Pb and Nb having

oxidised surface [8].

The origin of the field dependent microwave absorption in high T_c superconductors has been the subject of continued debate. Kachaturyan et al. [13] attributed the microwave absorption to the flux penetration in a system of Josephson coupled superconducting grains but no model for loss mechanism was elaborated. Some workers [25,38] considered damped motion of fluxons as the loss mechanism and derived expressions for complex surface impedance. This mechanism is known to work in classical Type-II superconductors above the lower critical field H_{c1} [26,27]. To account for the change of signal sign on the reversal of sweep direction, the model of damped fluxon dynamics was combined with the critical state model, and it was suggested that partial pinning and depinning of fluxons is the cause of nonlinear effect [28,29].

We studied the derivative of the low field dependent microwave absorption of pure $\text{YBa}_2\text{Cu}_3\text{O}_{7-\delta}$, Hf-doped $\text{YBa}_2\text{Cu}_3\text{O}_{7-\delta}$ and $\text{Tl}_2\text{Ba}_2\text{CaCu}_{8+\delta}$ as a function of grain size and temperature, and explain our results in the light of the model proposed by Dulcic et al. [32,33].

4.2 EXPERIMENT

The derivative of low field dependent microwave absorption (DLFDMA) of high T_c superconductors were recorded on a conventional X-band Varian E109 EPR spectrometer. The following modifications were done to ensure that the scan of the magnetic field is from zero, because the electromagnet has remanent magnetic field of the order of 20 gauss. For this the cavity was taken out of the large electromagnet. A pair of Helmholtz coils was placed on the cavity and the current was fed to the Helmholtz coils by the home made current source and it was coupled to the scan of the EPR

spectrometer. The magnetic field of the Helmholtz coils was calibrated using digital Gaussmeter (RFL912) within an accuracy of 0.5G. The sample was centered in an X-band TE₁₀₂ cavity (9.3GHz). The direction of the external magnetic field H_o was taken as z-axis. This field was modulated at 100 KHz with peak to peak amplitude varying from 1.0 mG to 10G. The microwave magnetic field H₁ was parallel to the x-axis and had its maxima at the sample position. Its amplitude could vary from less than 1 mG to 1 G. The microwave electric field E₁ was parallel to H_o but it was arranged such that it had a node at the sample position. The cavity was matched to the exciting wave guide for zero reflected power, and automatic frequency control circuitry adjusts the klystron frequency so that changes in the reflected power are due to energy absorbed within the cavity. The detector senses the component of the reflected power modulated at ω_m i.e. detected modulation are in phase with H_o modulation.

To study the effect of temperature variation on DLFDMA, a home made low temperature cell with a temperature control of $\pm 0.1^{\circ}\text{K}$ near T_C was used. Sample in the cylindrical shape was placed at the one end of the copper rod whose other end was always dipped in liquid nitrogen. The orientation of the sample in the magnetic field was such that the direction of the magnetic field was along the length of the sample. This orientation was done to minimize the demagnetization ratio. The temperature of the sample was made to change by heating near the sample. To monitor the temperature of the sample, a copper constantan thermocouple was attached to the sample. The samples were prepared according to the procedure described in section 3.2.1. All samples were characterized by resistance measurement, X-ray, SEM and EPR, which are already described in sections 3.3, 3.4, 3.5 and 3.6 respectively.

4.3 LOW FIELD DEPENDENT MICROWAVE ABSORPTION

4.3.1 Conventional Superconductors Pb and Nb

The field dependent microwave absorption of Pb and Nb are shown in Fig. 5.1. Surface of Pb was oxidised by exposing it to air while the surface of Nb was oxidised electrolytically. The DLFDMA in superconductors increases with increasing field-strength, and reaches a maximum, and then decreases with a long tail extending upto very large field. This signal is not always reversible and shows open hysteresis loop. The signal changes sign upon reversal of field-scan at any field within the cycle. The change in the sign of the signal upon reversal of the field-scan occurs generally at lower modulation field. The effect of modulation field on the derivative of field dependent microwave absorption will be discussed in next chapter. The essential feature of Pb spectrum is that despite Pb being a Type-I superconductor there is substantial hysteretic microwave absorption at all fields. The absorption occurs not only upto H_c ($\approx 520G$) at 4.3K but even beyond the critical field for surface superconductivity H_{c_3} ($\approx 880G$) [8]. Nb spectrum also shows hysteretic absorption in a 10 kG field, which is determined principally by a surface superconducting layer in such an oxidised sample [9]. The maximum in the forward scan and minimum in the backward scan correspond to H_{c_2} of the surface layer [9]. The small minimum at 3.3 KG is due to defect spin resonance [8].

Viscous flux motion is usually the reason behind dissipation in bulk superconductors even at microwave frequencies [10]. The oxidised surface of the conventional superconductors is granular in nature and consists of many islands connected by weak

links where magnetic flux penetrate at lower field and causes the microwave absorption [11].

4.3.2 High T_c Superconductors

Below the transition temperature, all high T_c superconductors exhibit a large microwave absorption at very low magnetic fields [4-8,12-21]. A typical DLFDMA of zero field cooled (ZFC) pure $\text{YBa}_2\text{Cu}_3\text{O}_{7-\delta}$ is shown in Fig. 4.2. The principal feature of the spectrum is that the signal is minimum at zero field and attains its maximum at very low field (1 to 20G) followed by a long tail. With small modulation field the signal changes sign on reversing the field sweep. The signal shows memory effect because it depends on the range of the field scan. We will discuss the modulation field effect in Chapter 5, and field trapping and memory effect in Chapter 6.

Pure $\text{YBa}_2\text{Cu}_3\text{O}_{7-\delta}$

Low field dependent microwave absorption in high T_c superconductors at very low field is due to the granular nature of the material. Thus, any change in the microstructure of the sample should be reflected in the DLFDMA. Since the microstructure of the sample, i.e. grain size and grain boundary, depend on the heat treatment of the sample and the route by which the sample has been prepared; we have studied the DLFDMA of pure $\text{YBa}_2\text{Cu}_3\text{O}_{7-\delta}$ having different average grain size. We studied four samples of pure $\text{YBa}_2\text{Cu}_3\text{O}_{7-\delta}$. Sample A and Sample B were prepared by solid state decomposition method and citrate method respectively. Sample C was prepared in another batch by solid state decomposition using ultra pure chemicals. Sample D was prepared by regrinding and reheating

sample B. The details of the sample preparation are described in section 3.2. All the samples were characterized by resistivity measurement, X-ray and SEM, as described in sections 3.3, 3.4 and 3.5 respectively. SEM measurements show that the average grain size of sample A, sample B, sample C and sample D are 8 μm , 2.5 μm , 3.5 μm and 5 μm respectively.

The DLFDMA of the zero field cooled Samples A, B, C and D of pure $\text{YBa}_2\text{Cu}_3\text{O}_{7-\delta}$ and $\text{Tl}_2\text{Ba}_2\text{CaCu}_2\text{O}_{8+\delta}$ at LNT are shown in Figs. 4.3(a), (b), (c), (d) and (e) respectively. The particle size and the peak position of DLFDMA of these samples are shown in Table 4.1. The peak position (H_m) shifts towards lower field as the particle size (d) increases. The plot of peak position versus particle size is shown in Fig. 4.4.

TABLE 4.1

Sample	Sample A	Sample B	Sample C	Sample D	Tl-Ba-Ca-Cu-O
Particle size in μm	8	2.5	3.5	5.00	3.9
Peak position (exp.) in G	2	13	5.4	5.00	6.9
Peak position (calculated) in G	3	12	5.3	4.8	6.1

Hf-Doped $\text{YBa}_2\text{Cu}_3\text{O}_{7-\delta}$

For low field dependent microwave absorption, equal amount of samples having different Hf-percentage were taken in spherical shape (1.5 mm diameter). The samples were protected from

humidity by sealing them in quartz tube. All the samples were characterized by resistance measurement, X-ray and SEM, as described in Chapter 3.

The derivative of low field dependent microwave absorption (DLFDMA) of various Hf-doped samples are shown in Fig. 4.5 [12]. The spectra were recorded in 100 KHz field modulation with an amplitude of 1 Gauss, microwave power of 0.2 mW and gain of 10^2 . The above parameters were kept constant throughout the recording of the spectra of all the samples. The samples did not show any hysteresis for fields scanned up to 10 Gauss with 1G modulation field amplitude. However, for larger fields, the hysteresis is appreciable.

The DLFDMA for each of the samples has been recorded in the following way. (i) First, the sample was zero field cooled to LNT and the signal in the forward direction was recorded followed by reverse sweep recording back to the zero field. (ii) Then the sample was heated to RT and subsequently cooled to LNT in zero magnetic field. Now, the signal in the negative direction was recorded, exactly the same way as in step (i). The starting point in either direction is indicated by small horizontal bar in Fig. 4.5. For magnetic sweeps from 0 to -40G and 0 to +40G, the derivative signals are almost symmetrical about the zero of the magnetic field with asymptotic tails extending on either side. However, in Fig. 4.5 the signals are shown only up to 25G for clarity. This indicates that the absorption extremum is centered around zero of magnetic field. To settle this issue whether this absorption extremum is associated with the absorption maximum or minimum at zero field, the shape of the DLFDMA and EPR signal at LNT as shown in Fig. 3.15 are compared. Since the EPR signals refer to the absorption peaks at resonance, the phase reversal of

DLFDMA as compared to EPR signals suggest that there exists absorption minimum at the zero of the magnetic field for the low field dependent microwave absorption. By integrating the derivative signal of the Fig. 4.5, we obtain the absorption signal, which is shown in the inset. It is clear that the sharpness of the absorption minima decreases with increasing concentration of Hf.

One more interesting feature of the DLFDMA is that there is considerable hysteresis and the curves shown in Fig. 4.5 are the representative hysteresis loop for the Hf- substituted sample for the field scan of $\pm 40\text{G}$. The hysteresis effect and flux trapping will be discussed in Chapter 6.

The decrease in the intensity of DLFDMA with increasing Hf-substitution is mainly due to decrease in the porosity and particle size. This decrease in intensity clearly indicates that the particle size in the Hf-substituted samples are smaller than that in the parental compound.

4.4 TEMPERATURE DEPENDENCE OF THE DERIVATIVE OF THE LOW FIELD DEPENDENT MICROWAVE ABSORPTION (DLFDMA)

The temperature dependence of the DLFDMA in $\text{YBa}_2\text{Cu}_3\text{O}_{7-\delta}$ reported in the literature by different groups is contradictory. Some groups reported that the peak position of the DLFDMA is independent of the temperature [6] while others reported that the peak position of the DLFDMA shifts towards lower field as the temperature of the sample increases towards T_c [14-18a]. We have studied the temperature dependence of the DLFDMA in Hf-doped $\text{YBa}_2\text{Cu}_3\text{O}_{7-\delta}$ and observed a shift in the peak position with temperature. Also, we have studied the temperature dependence of the DLFDMA in various samples of YBaCuO prepared by different routes and different heat treatment, and under different recording

conditions, to see whether temperature dependence of DLFDMA is sample-dependent or depends on the recording condition.

4.4.1 $\text{YBa}_2\text{Cu}_3\text{O}_{7-\delta}$

Temperature dependence of DLFDMA of pure $\text{YBa}_2\text{Cu}_3\text{O}_{7-\delta}$ prepared by different methods i.e., sample A and Sample B (described earlier) was studied. The actual recorded spectra of DLFDMA at different temperatures for sample A and sample B are shown in Fig. 4.6 and Fig. 4.7 respectively. The spectra were recorded as follows : (i) Samples were cooled in zero field to the desired temperature below the transition temperature, and (ii) magnetic field was scanned in the forward direction upto 40G in sample A and 126G in sample B and then scanned backward to zero, keeping the temperature constant. (iii) Temperature of the sample was increased to a desired temperature without destroying the memory effect and then step (ii) was repeated. While heating the sample, the temperature was always kept below T_c . From Fig. 4.6 and 4.7 it is clear that the peak position (H_m) of the DLFDMA is independent of temperature in both the samples. The shift in the peak position occurs towards higher field in the field-exposed sample with respect to zero field cooled sample as is clear from Fig. 4.7. The peak height of DLFDMA decreases with increasing temperature and vanishes at T_c . It is clear from Fig. 4.6 that the peak in the derivative signal disappears above 88K while the oscillation persists. The hysteresis effect also becomes pronounced. Finally at T_c both the oscillation and hysteresis vanish.

The plot of log of peak height of DLFDMA of sample A and sample B as a function of temperature are shown in Figs. 4.8 (a) and (b). The peak heights of forward and backward scan show

exactly the same variation as a function of temperature. In case of sample B the data have been multiplied by a constant so that backward and forward scans do not overlap. Experimental data of the peak height (h_p) of DLFDMA as function of $(T_c - T)$ has been fitted to a mathematical expression. In all the samples the power law fits well which has been shown by the smooth curve in Figs. 4.8(c) and (d) while the discrete points show the experimental points. In case of sample A, the best fit for forward scan gives $h_p = 0.54(T_c - T)^{2.34}$ while for backward scan it gives $h_p = 0.15(T_c - T)^{3.4}$. For sample B, the best fit for forward and backward scans give $h_p = 2.329(T_c - T)^{1.1}$ and $3.41(T_c - T)^{1.2}$ respectively. Kachaturyan et al [13] showed that the peak height varies exponentially as a function of temperature near T_c but we did not observe the exponential behavior. In all the samples we see that the peak height varies as power of $(T_c - T)$.

The temperature dependence of DLFDMA of pure $\text{YBa}_2\text{Cu}_3\text{O}_{7-\delta}$ prepared by solid state decomposition using ultra pure oxide and carbonates, called sample C, characterized by XRD, SEM and EPR discussed in Chapter 3 was also studied. The temperature dependence of DLFDMA was recorded in two conditions. In the first condition, the sample was always cooled in zero field to the desired temperature below transition temperature and spectra were recorded. In this case, every time the sample was cooled in zero field and after recording the spectra of DLFDMA the sample was heated above T_c to destroy the magnetic memory effect. In the second condition the DLFDMA were recorded exactly in the same way as in the case of the Sample A and B discussed in the earlier paragraph.

The actual recorded spectra of DLFDMA of sample C as a function of field at different temperatures under the first condition (i.e. zero field cooled at each temperature) and second

condition (i.e. sample is exposed to the magnetic field) are shown in Figs. 4.9 and 4.10 respectively. We see that the peak position in either recording condition does not depend upon the temperature near T_c . But peak height (h_p) decreases with increasing temperature and vanishes at T_c .

Sample B was regrinded and heat treated and finally annealed in oxygen. This sample is called sample D. The actual recorded spectra of DLFDMA of sample D as a function of field at different temperatures are shown in Fig. 4.11. For each recording, the sample was cooled in zero field. In this sample also we did not see any shift in the peak position as function of temperature, while the peak height decreases with increasing temperature and vanishes at T_c . In sample B, C and D the oscillation superimposing on the absorption signal is not so much pronounced as in case of sample A.

4.4.2 $Tl_2Ba_2CaCu_2O_{8+\delta}$

The temperature dependence of DLFDMA of sample $Tl_2Ba_2CaCu_2O_{8+\delta}$ as a function of field was studied. The recorded spectra of DLFDMA of $Tl_2Ba_2CaCu_2O_{8+\delta}$ at different temperatures are shown in Fig. 4.12. Spectra were recorded in the second condition (i.e., in fixed field exposed condition). From the figure it is clear that the peak position is independent of temperature, while peak height decreases with increasing temperature and vanishes at T_c . The resistance measurement shows that the zero resistance temperature is 104K but the fall in the resistance starts at $118^{\circ}K$. The presence of DLFDMA till $118^{\circ}K$ indicates the presence of a higher T_c phase. Thus DLFDMA is a sensitive tool to find out the presence of very small percentage of higher T_c phase in the bulk sample of relatively lower T_c phase.

From above measurements we see that in all the samples the peak position is independent of the temperature near T_c and remains the same in both the recording conditions i.e., in zero field cooled and fixed field exposed at different temperatures. Those groups who have observed a change in the peak position might have not taken care of the field exposed or it might be due to hysteresis of the large electromagnet. This is because, large electromagnet has a remanent magnetic field and its magnitude depends upon the magnetic field value from which it has been switched off. The magnitude of remanent field depends upon the time between two consecutive scan. If this time is large, the variation in remanent magnetic field is small. Usually, the variation in the remanent magnetic field is of the order of 2 to 5G. To circumvent these difficulties, in our experimental set up, the magnetic field scan was done using the Helmholtz coils outside the large electromagnet.

The peak height (h_p) of DLFDMA for all the samples was plotted as a function of temperature. The plot of $\log(h_p)$ of backward and forward scan of DLFDMA of zero field cooled (ZFC) sample C, fixed field exposed sample C, ZFC sample D and fixed field exposed sample, $Tl_2Ba_2CaCu_2O_{28+\delta}$ are shown in Figs. 4.13(a), (b), (c) and (d) respectively. From these figures, it is clear that in all the samples the peak height falls very fast near T_c . Also, we have plotted the peak height as a function of $T_c - T$. In all the samples the peak height h_p varies as a power of $(T_c - T)$. The plot of peak height (h_p) as a function of $(T_c - T)$ for ZFC sample C and 60G field exposed sample C, ZFC sample D and 60G field exposed sample $Tl_2Ba_2CaCu_2O_{28+\delta}$ are shown in Figs. 4.14(a), (b), (c) and (d) respectively. The discrete points show the experimental data and smooth curve shows the best fit. In all these cases the

best mathematical expression for the experimental data is $h_p = A(T_c - T)^\alpha$. The value of A and α for different samples are given in Table 4.2.

4.4.3 Hysteresis Area

A considerable amount of hysteresis is found in all the samples of high T_c superconductors. From Figs. 4.6, 4.7, 4.9, 4.10, 4.11 and 4.12 it is clear that the hysteresis area varies systematically with temperature except in sample A in which there is large oscillation. The hysteresis area decreases with increasing temperature and vanishes at T_c in all the samples except for sample A. The variation in the area is slow at lower temperatures but become fast near T_c . The plot of log (hysteresis area) of sample C, sample A and B, and sample $Tl_2Ba_2CaCu_2O_{8+\delta}$ as a function of temperature are shown in Figs. 4.15 (a), (b) and (c) respectively. The plot of hysteresis area as a function of $(T_c - T)$ are shown in Fig. 4.16. The hysteresis area varies as $(T_c - T)^\beta$ near T_c . The smooth curve shows the best fit. The best fit mathematical expression for the experimental results is of the form of hysteresis area (ΔA) = $B(T_c - T)^\beta$. The values of β and B are given in Table 4.2.

4.5 DISCUSSION

The usefulness of the DLFDMA in characterizing granular superconductors has been highlighted in several studies [2-4,19-20]. Durny et.al. [19] have suggested that it is a better indicator of the bulk transition than either resistivity or susceptibility. In conventional resistivity measurement, contact is required and superconducting transition can be detected only when contacts to the sample are connected to the superconducting

TABLE 4.2

$$\text{Peak height } (h_p) = A(T_c - T)^\alpha ; \text{ Hyst. area } \Delta A = B(T_c - T)^\beta$$

The value of A, α , B and β for different samples.

Sample	A		α		B	β
	Forward scan	Backward scan	Forward scan	Backward scan		
YBaCuO Sample A	0.54	0.15	2.34	3.46	None	None
YBaCuO Sample B	2.33	4.41	1.14	1.21	3.82	0.65
FC YBaCuO Sample C	5.74	-	0.96	-	10.73	0.61
Field exposed YBaCuO Sample C	5.97	4.87	0.64	0.68	5.09	0.37
YBaCuO Sample D	3.058	-	0.83	-	-	-
Tl-Ba-Ca-Cu-O	0.97	1.42	2.18	1.67	0.1	2.38

material, while the microwave method does not require continuity. This method is extremely sensitive since the signal is four or five orders of magnitude greater than the sensitivity limit of the EPR spectrometer [13,21]. In order to fully utilize the DLFDMA a thorough understanding of the mechanism responsible for it is required.

Kachaturyan et al. [13] attribute this low field absorption to grain decoupling by a low magnetic field which increases the effective volume through which microwaves penetrate.

They relate both the low field microwave signal and a drastic reduction of the diamagnetism from 97% below 5G to 61% above 15G in $\text{YBa}_2\text{Cu}_3\text{O}_{7-\delta}$ [22] to the grain isolation which occurs when the Josephson junction can no longer sustain the screening current induced by the magnetic field. Stankowski et al. [23] related the power absorption to the voltage generated across each junction by the inverse ac Josephson effect.

Another approach to understand the DLFDMA of high T_c superconductors appears to be that of linking it to the high frequency ac susceptibility [19,20]. The diamagnetic response theory of weakly coupled superconducting cluster given by Ebner and Stroud [24] shows the frustration in the manner of spin glass. The frustration means that at finite fields, any cluster with closed loops can not find a state that simultaneously minimizes all the bond energies. A largely frustrated cluster with many closed loops can choose between numerous competing ground states with nearly equal energy. In a finite cluster, only one of these is the true ground state and others will lie only a small energy above it. The various levels will cross one another as the field is varied and the cluster must hop from one configuration to another in order to stay in the ground state. The projected area of the cluster perpendicular to the field can be calculated by $S = \phi_0 / 2H_{c1}^*$ where H_{c1}^* is the field at which ac and dc susceptibility starts to differ or the first flux slippage occurs and ϕ_0 = flux quanta. Blazey et al. [20] associated this field H_{c1}^* to the field (H_m) at which the peak occurs in DLFDMA of ZFC. However this procedure is open to criticism because the above formula applies only to single loop of many identical junctions [24]. In the random clusters, Ebner and Stroud found that the area S is roughly a^2 where a is the superconducting grain radius. The calculated value of S assigning

H_m^* to H_{c1}^* is very much smaller than the grain size. Stankowski et al. [23] associated H_m with the first minimum on the I_m versus field curve.

Portis et al. [25] considered damped motion of fluxons as the loss mechanism and derived expressions for the complex surface impedance. The same mechanism was also known in classical Type-II superconductors above the lower critical field H_{c1} [26,27]. Later, Portis et al. [28-29] combined the critical state model and partial pinning and depinning of fluxons with damped fluxon dynamics to give an explanation for the nonlinear effect observed in DLFDMA. M.D. Sastry et al. [30] proposed a model suggesting formation of antiferromagnetically coupled copper dimer, with its excited triplet state separated by about 300 cm^{-1} as in case of copper acetate. In such a case resonant absorption occurs around 0.3 cm^{-1} in the excited $M_s = 0$ and $M_s = \pm 1$ states at near zero fields. Lin et al. [31] have shown that the low field signals are non-resonant in nature. Sastry proposition is that non-resonant signal arises due to non-resonant reflection of the microwave below H_{c1} and resonant absorption does take place around 0.3 cm^{-1} close to T_c and gets buried in the predominant non-resonant reflection signal with lowering of temperature.

Dulcic et al. [32,33] has given a model which explains the most of our results of the DLFDMA. According to this model, the modulated signal consists of two components. One of them is independent of the direction of the field sweep and identified as the derivative of the unmodulated absorption curve. The other component had opposite sign in forward and reverse field sweeps.

MODEL

The microwave absorption in a granular superconductor can be treated by considering the microwave response of single representative junction [32,33]. If the sample is exposed to a dc field H and microwave field $H_1 \cos \omega t$, appropriate currents are induced on its surface. For a junction on the surface, driven by dc current I_0 and microwave current $I_1 \cos \omega t$, the response is determined by the equation

$$C \hbar \frac{d^2 \phi}{dt^2} + \frac{\hbar}{2eR_n} \frac{d\phi}{dt} + I_c \sin \phi = I_0 + I_1 \cos \omega t \quad (4.1)$$

where C is the capacitance, R_n the normal resistance and I_c the critical current of the junction [34]. In the absence of the microwave field, the phase would adjust to an equilibrium value ϕ_0 given by $I_c \sin \phi_0 = I_0$. In a complicated net work of interconnected junction the phases will tend to arrange so that the coupling energies are minimised. Thus each junction may have different I_0 . As the dc field is swept, there will be rearrangements of phases i.e. phase jumps at individual junction [24]. This process will give rise to an increased noise signal which is seen superimposed over the broad signal (Fig. 4.6). However, the broad feature of the signal can be explained if an averaged current $I_0 < I_c$ is assumed. The non-linear equation (4.1) can not be solved analytically. However, for small microwave currents only small oscillation will be induced, i.e.

$$\phi(t) = \phi_0 + \phi_1(t), \quad |\phi_1| \ll |\phi_0| \quad (4.2)$$

so that one can obtain linear equation in $\phi_1(t)$ whose solution is straight forward. The capacitive term is usually neglected in very

small junction and the absorbed power becomes

$$P = P_n \frac{1}{1+\eta} \quad (4.3)$$

where $P_n = \frac{1}{2} I_1^2 R_n$ is the absorption in the limit of high fields when the junction becomes normal and the parameter η is given by

$$\eta = \frac{\frac{I_c^2 \cos^2 \phi_0}{\left| \frac{\hbar \omega}{2eR_n} \right|^2}}{} \quad (4.4)$$

Since the standard EPR spectrometer operates with linear detector, the signal is proportional to the square root of the absorbed power, i.e.,

$$(S/S_n) = (P/P_n)^{1/2} \quad (4.5)$$

Magnetic field reduces the critical current of Josephson junction. For an idealized small junction (i.e. the junction length L is less than the Josephson penetration length $\lambda_J = \left[\phi_0 / 2\pi\mu d J_c(0) \right]^{1/2}$) the variation of the critical current is given by the well known diffraction formula

$$J_c(H) = J_c(0) \left| \frac{\sin \pi H/H_0}{\pi H/H_0} \right|, \quad (4.6)$$

where the characteristic field H_0 , the field at which junction contains one quantum of flux, is given by

$$H_0 = \frac{\phi_0}{\mu d L} \quad (4.7)$$

where μ is the permeability and $d = 2\lambda + t$ is the effective junction thickness, where λ is the London penetration depth and t is the

barrier thickness. But in reality the high T_c samples contain a large number of junctions with different lengths and orientations. Peterson et al. [35] have performed averaging of Fraunhofer diffraction pattern over junction length taking different statistical distribution with various mean values, widths and orientations and found that the Fraunhofer patterns smears out and fitted very well to the experimental data as shown in Fig. 4.17. The dominant junction variable governing this smearing is the junction area. Dulcic et al. have taken this smeared value of Josephson junction critical current $I_c = I_c(0)F(H)$ as shown in the Fig. 4.18(a). $I_c(0)$ should also be reduced by $F(H)$ so that ϕ_0 remains constant when field is swept in a given direction $\eta = \eta_0 F^2(H)$ where η_0 is the value of η at zero field. Besides the field dependence there is also dependence of I_c on temperature so that $\eta_0(T)$ is expected to increase as the temperature is lowered. The normalised microwave absorption (S/S_n) for different value of η_0 has been calculated from equation (4.3) by Dulcic et al. and are shown in Fig. 5.18(b) which looks exactly like the experimental curve of the microwave absorption without modulation field [36,37].

The technique of field modulation and lock-in detection does not yield a simple derivative of equation (4.3). If a small modulation field $A_m \cos \omega_m t$ is superimposed on H , one can replace I_0 in equation (4.1) by $I_0 + I_m \cos \omega_m t$. For small modulation amplitude A_m , we have

$$F(H+A_m \cos \omega_m t) = F(H) + F'(H)A_m \cos \omega_m t. \quad (4.8)$$

When these changes are introduced in equation (4.1), and the adiabatic approximation is used for the oscillation at the relatively low modulation frequency, one obtains the modulated signal [25],

$$S_m = \left[\frac{\frac{RI_1^2}{2}}{\left(\frac{\hbar\omega_m}{2eR} \right)^2} \right]^{1/2} \cdot \frac{I_c}{(1+\eta)^{3/2}} \left[-\frac{dI_c}{dH} A_m + I_m \sin \phi_o \right] \cos \omega_m t \quad (4.9)$$

The first term in equation (4.9) is reversible, i.e. independent of the direction of field sweep and second term changes sign when sweep direction is reversed (ϕ_o to $-\phi_o$), because the induced boundary current changes the sense of flow. This term gives hysteresis in the observed signal. The equation (4.9) is the final expression for the microwave absorption using technique of field modulation (i.e. using standard EPR spectrometer).

For larger value of A_m the dominating term is the first term in equation (4.9). The factor $I_c/(1+\eta)^{3/2}$ can be approximated to $1/I_c^2$. We see from Fig. 4.17 that $\frac{dI_c}{dH}$ is minimum at $H = 0$ and increases very fast with increasing field and again starts to decrease for further increasing field at slower rate. Equation (4.9) shows that with scanning the field S_m starts from zero and attains the maximum value at the field at which $\frac{|dI_c/dH|}{I_c^2}$ attains the maximum and starts to decrease on further increasing the field with long tail with reversing the field sweep the second term changes sign and shows the hysteresis in S_m . Thus this clearly explain the experimental observation of DLFDMA at LNT as shown in Fig. 4.2.

The peak position of S_m occurs at the field where $|\frac{dI_c}{dH}|/I_c^2$ is maximum. We see from Fig. 4.17 that $|\frac{dI_c}{dH}|$ is maximum approximately at $(H/H_o) = 1/2$. So we expect the maxima of the signal at the field at $H_o/2$ where H_o is given by equation (4.7). This H_o depends on the value of λ and L . At constant temperature λ is constant. So H_o will change with changing L . As L , the

junction length i.e. the average grain size, increases H_o will decrease. So the peak position of S_m will shift towards lower field. This has been clearly observed in Fig. 4.3 in which the peak position of DLFDMA shifts towards lower field with increasing grain size. The calculated value of peak position i.e. $H_o/2$ from equation (4.7), taking average grain size as junction length L, is given in Table 4.1, which approximately matches with the observed value of peak position.

The lowering of the temperature of the samples below T_c causes rapid increase in the critical current of Josephson junction and so the signal S_m given by equation (4.9) increases rapidly as we lower the temperature below T_c . From Figs. 4.6, 4.7, 4.9, 4.10, 4.11 and 4.12, it is observed that the peak height (h_p) of DLFDMA increases very rapidly as we lower the sample temperature from T_c . We have analysed the experimental data which show the power law dependence of h_p . From equation (4.9), it is clear that S_m should vary as $(T_c - T)^\alpha$ near T_c , because $I_c(0,T)$ vary as $(T_c - T)^\alpha$ near T_c . We get different exponent for different samples. This is probably due to different types of links between superconducting grains of different samples.

In all the samples and under different recording conditions, as described in section 4.4, we observed that the peak position H_m of the DLFDMA is independent of temperature near T_c . From equation 4.9 the peak occurs approximately at $H_o/2$ and H_o is given by equation 4.7 i.e. $H_o = \phi_o / \mu dL$ where $d = 2\lambda + t$. As the temperature decreases, λ decreases and so we should see the shift in the peak position H_m of DLFDMA as we lower the temperature near T_c . If $t \gg \lambda$, $d = t$ in that case H_o will remain constant and so H_m . If t and λ are comparable then one should see the shift in the peak position as a function of temperature. Thus shift in the peak

position is sample dependent. The variation of hysteresis area as a function of temperature are shown in Fig.4.14. The hysteresis area decreases with increasing temperature and vanishes at T_c . In equation (4.9) the second term gives rise to the hysteresis in the DLFDMA. As we lower temperature from T_c the value of I_m increases and so we see increase in hysteresis area with the lowering of temperature.

In conclusion, the model proposed by Dulcic et al. explains all our observations of the temperature dependence and grain size dependence of DLFDMA.

REFERENCES

1. B.Rosenblum and M.Cardona, Phys. Rev. Lett. **12**, 657 (1964).
2. Y.B. Kim and M.J. Stephen, Superconductivity, Vol.1, Ed. R.D. Parks, Marcel Dekker, New York, 1969.
3. K.A. Müller, M. Pomeranz, C.M. Knoedler and D. Abraham, Phys. Rev. Lett. **45**, 832 (1980).
4. A. Dulcic, B. Leontic, M. Peric and B. Rakvin, Europhys. Lett. **4**, 1403 (1987).
5. M. Peric, B. Rakvin, M. Prester, N. Brniecevic and A. Dulcic, Phys. Rev. B **37**, 522 (1988).
6. M. Giura, R. Marcon and R. Fastampa, Phys. Rev. B **40**, 4437 (1989).
7. E.J. Pakulis and T. Osada, Phys. Rev. B **37**, 5940 (1988).
8. K.W. Blazey, Earlier and Recent Aspects of Superconductivity, Editors - J.G. Bednorz, K.A.Müller, Springer Series in Solid State Sciences, Vol. 90; p. 263 (Springer-Verlag Berlin, Heidelberg 1990).
9. J. Halbritter, Appl. Phys. A **43**, 1 (1987)
10. A.R. Strnad, C.F. Hempstead and Y.B. Kim, Phys. Rev. Lett. **13**, 794 (1964).
11. M. Cardona, J. Gittleman and B. Rosenblum, Phys. Lett. **17**, 92 (1965).
12. A.G. Vedeshwar, Md. Shahabuddin, Prem Chand, H.D. Bist, S.K. Agarwal, V.N. Moorthy, C.V.N. Rao and A.V. Narlikar, Physica C, **158**, 385 (1989).
13. K.Kachaturyan, E.R. Weber, P. Tejedor, A.M. Stacy and A.M. Portis, Phys. Rev. B **36**, 8309 (1987).
14. S.V.Bhat, P.Ganguly and C.N.R.Rao, J. Phys. C **20**, L559(1987).

15. A.I. Isapin, S.V. Stepanov and L.A. Blumenfeld, Phys. Lett. A 132, 375 (1988).
16. A.G. Vedeshwar, H.D. Bist, Md. Shahabuddin, S.K. Agarwal, V.N. Moorthy, C.V.N. Rao and A.V. Narlikar, Phys. Lett. A 139, 415 (1989).
17. V. Foukis, O. Dobbert, K.P. Dinse, M. Lehnig, T. Wolf and W. Goldacker, Physica C, 156, 467 (1988).
18. A.R. Harutyunyan, L.S. Grigoryan, M. Baran, S. Piechota, Phys. Lett. A 133, 339 (1988).
- 18a. V. Katae, N. Kanauf, B. Büschner and D. Wohlleben, Physica C 184, 165 (1991).
19. R. Durny, J. Hantala, S. Ducharme, B. Lee, O.G. Symco, P.C. Taylor, D.J. Zhang and J.A. Xu, Phys. Rev. B 36, 2361 (1987).
20. K.W. Blazey, K.A. Müller, J.G. Bednorz, W. Berlinger, G. Amoretti, E. Buluggiu, A. Vera, and F.C. Matacatta, Phys. Rev. B 36, 7241 (1987).
21. H.D. Bist, P.K. Khulbe, Md. Shahabuddin, Prem Chand, A.V. Narlikar, B. Jayraman, and S.K. Agarwal, Solid State Commun. 65, 899 (1988).
22. J.F. Kwak, E.L. Venturiui, D.S. Ginley and W. Fu, in Proceedings of the International Workshop on Novel Mechanism of Superconductivity, Berkley, June 1987, ed. V.Z. Krezin and S.A. Wolf (Plenum, New York 1987).
23. J. Stankowski, P.K. Kahol, N.S. Dalal, and J.S. Moodera, Phys. Rev. B 36, 7126 (1987).
24. C. Ebner and D. Stroud, Phys. Rev. B 31, 165 (1985).
25. A.M. Portis, K.W. Blazey, K.A. Müller and J.G. Bednorz, Europhysics Lett. 5, 467 (1988).
26. J.I. Gittleman and B. Rosenblum, Phys. Rev. Lett. 16, 734 (1966).
27. J.I. Gittleman and B. Rosenblum, J. Appl. Phys., 39, 2617 (1968).

28. A.M. Portis, K.W. Blazey and F. Waldner, Physica C, 153-155, 308 (1988).
29. K.W. Blazey, A.M. Portis and J.G. Bednorz, Solid State Commun. 65, 1153 (1988).
30. M.D. Sastry, Studies of High Temperature Superconductors, Ed. Anant Narlikar, Vol. 2, p.265 (NOVA Science Publishers, 1989) and references therein.
31. T.S. Lin, W. Francisz and L.G. Sobotka, Nature 8th May 1988 Issue Correspondence section.
32. A. Dulcic, B. Rakvin and M. Pozek, Europhys. Lett. 10, 593 (1989).
33. A. Dulcic, R.H. Crepeau, J.H. Freed, L.F. Schneemeyer and J.V. Waszczak, Phys. Rev. B 42, 2155 (1990).
34. A. Barone and G. Paterno, Physics and Application of the Josephson Effect (Wiley, New York, 1982).
35. R.L. Peterson and J.W. Ekin, Phys. Rev. B 37, 9848 (1988).
36. M. Giura, R. Marcon and R. Fastampa, Phys. Rev. B 40, 4437 (1989).
37. E.J. Pakulis and T. Osada, Phys. Rev. B 37, 5940 (1988).
38. R. Marcon, R. Fastampa, M. Giura and E. Silva, Phys. Rev. B 43, 8012 (1991).

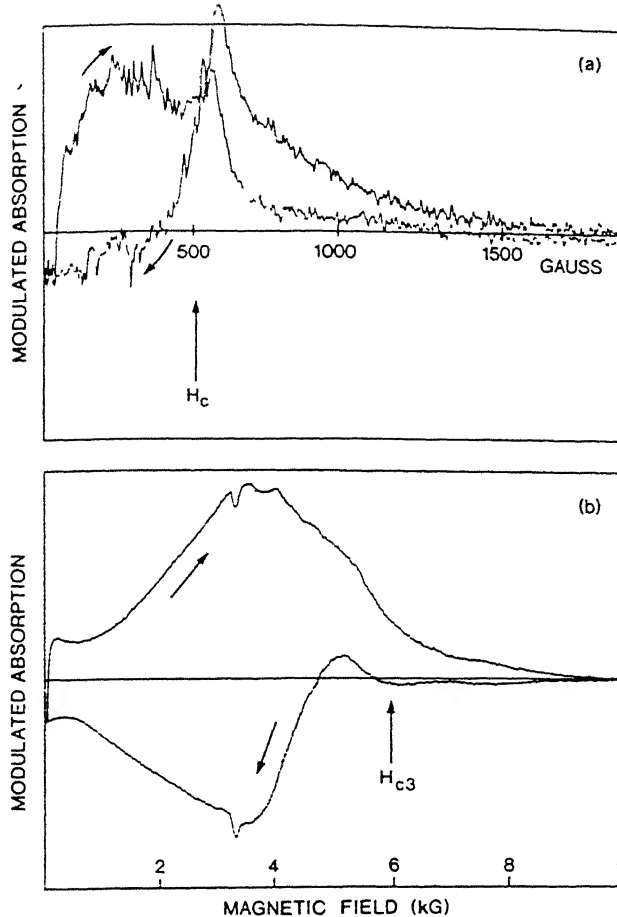


Fig. 4.1 Field dependence of the modulated microwave absorption of (a) small lead plate at 4.3K (microwave power 0.1mW, frequency 9.45GHz, field modulation 0.2G) and (b) a small anodically oxidised niobium plate at 4.4K (microwave power 0.5mW, frequency 9.44GHz, field modulation 1G)

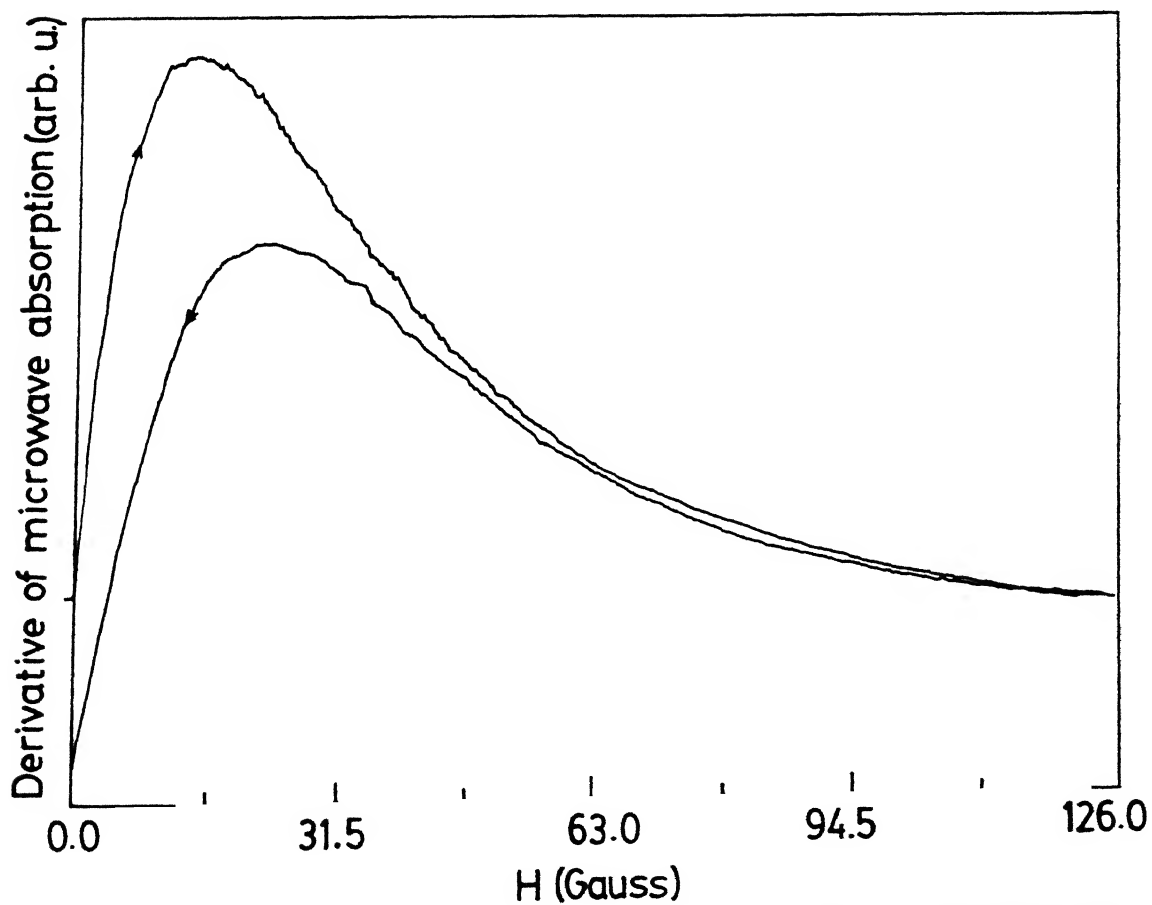


Fig. 4.2 A typical derivative of field dependent microwave absorption as a function of magnetic field of pure $\text{YBa}_2\text{Cu}_3\text{O}_{7-\delta}$ (Sample B) at 82.4K (microwave power 1 mW, modulation field 1G, frequency 9.33 GHz)

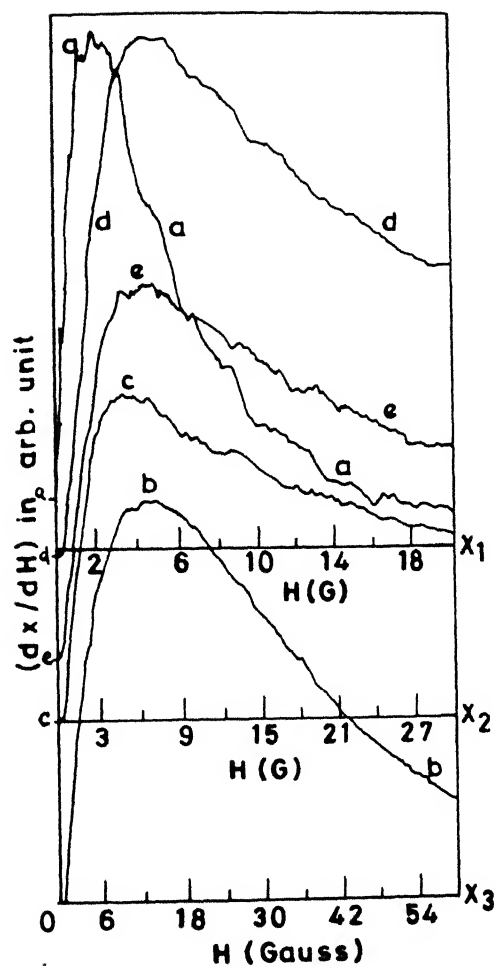


Fig. 4.3 DLFDMA as a function of magnetic field of ZFC samples with different grain size (a) Sample A (b) Sample B (c) Sample C (d) Sample D and (e) $Tl_2Ba_2CaCu_2O_{8+\delta}$ at LNT. (microwave power-1mW, modulation field 1G)

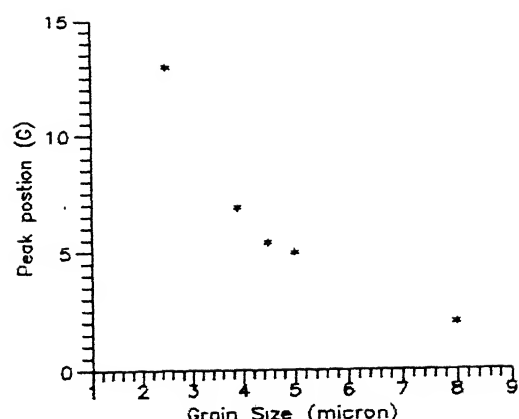


Fig. 4.4 Variation of peak positions of DLFDMA as a function of grain size of the samples

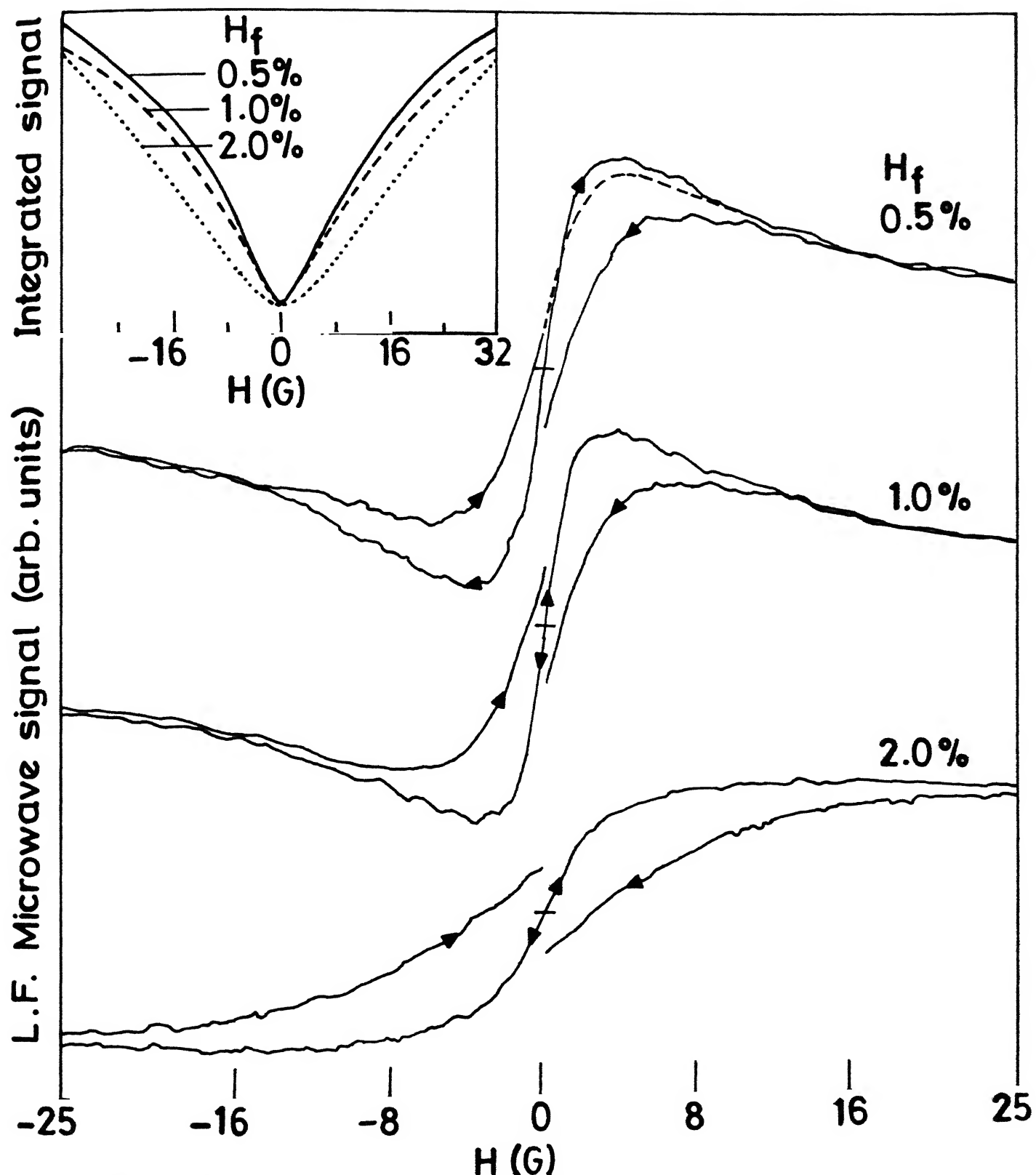


Fig.4.5 DLFDMA of Hf-doped samples at LNT. Samples were freshly cooled at zero field for recording in either direction of the fields. The starting point in either direction is indicated by horizontal bar. The inset shows the numerical integration of these curves (For all curves mod ampl.=1G, power =0.2mW)

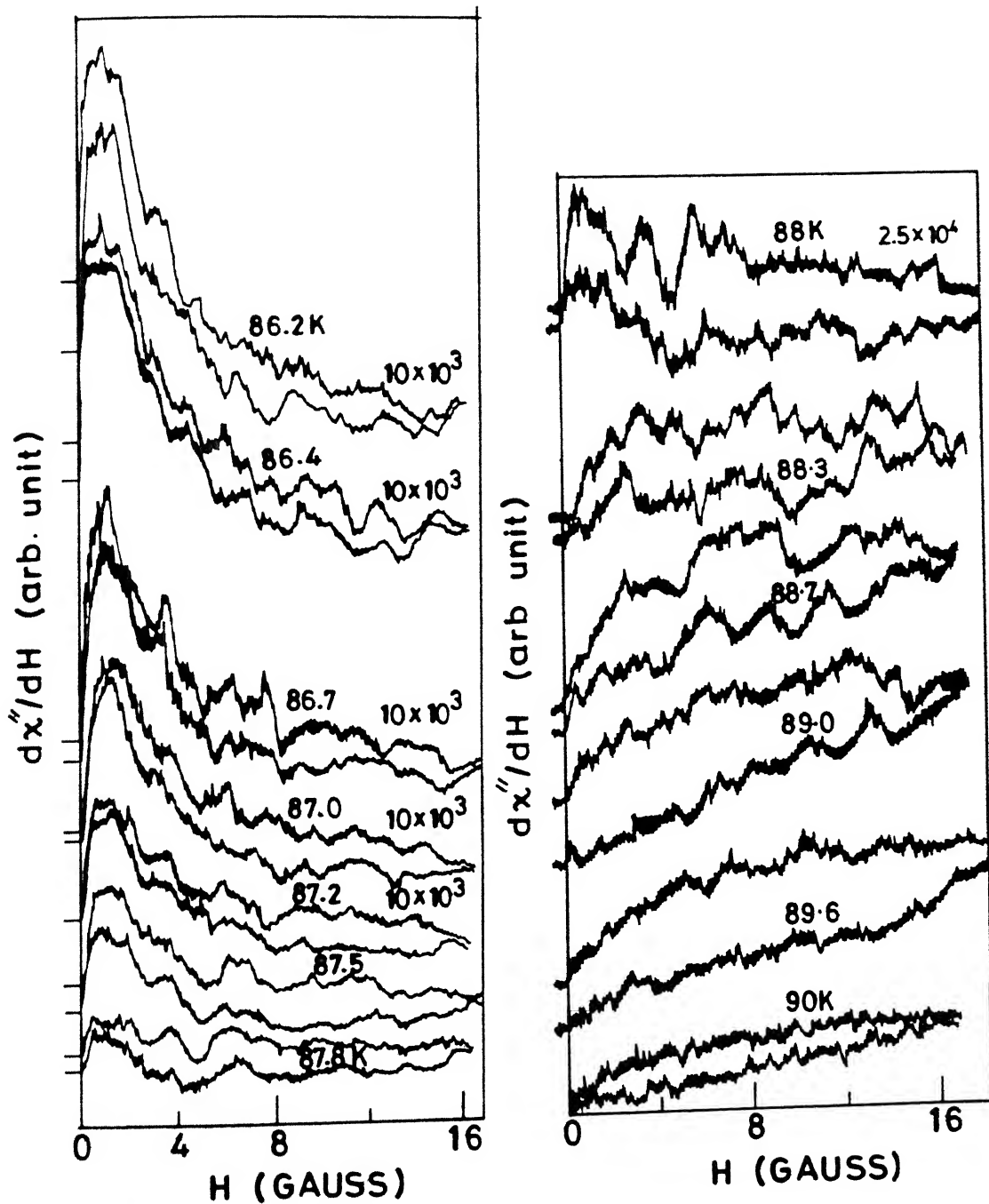


Fig.4.6 Actual recorded DLFDMA of Sample A as a function of field at different temperatures . The temperatures are specified at each spectrum and gain on the top (Power 1mW, Mod ampl. 1G)

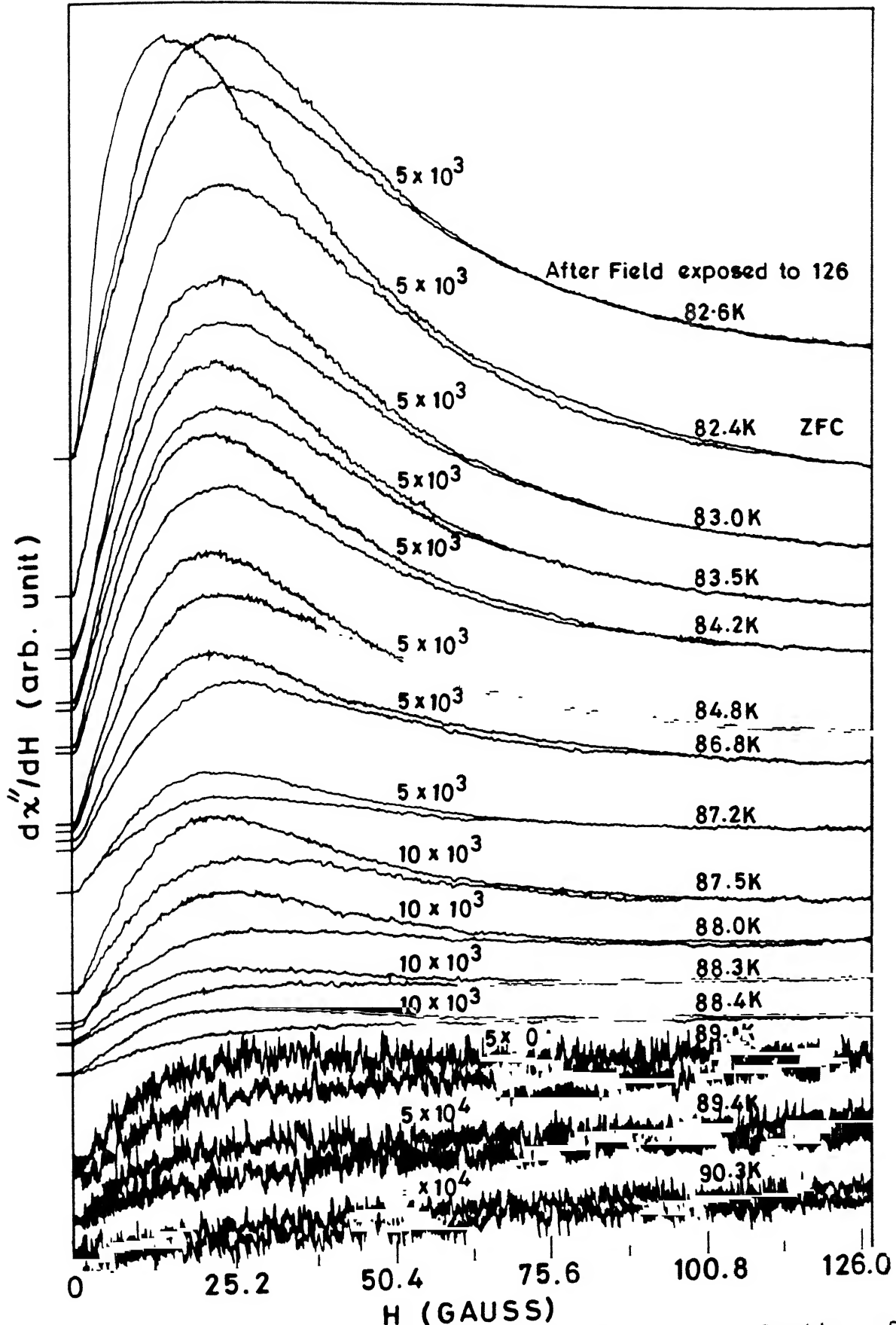


Fig. 4.7 Recorded spectra of DLFDMA of Sample B as a function of field at different temperatures. Forward and backward scans are shown by an arrow head. Temperatures and gains are specified at each spectra

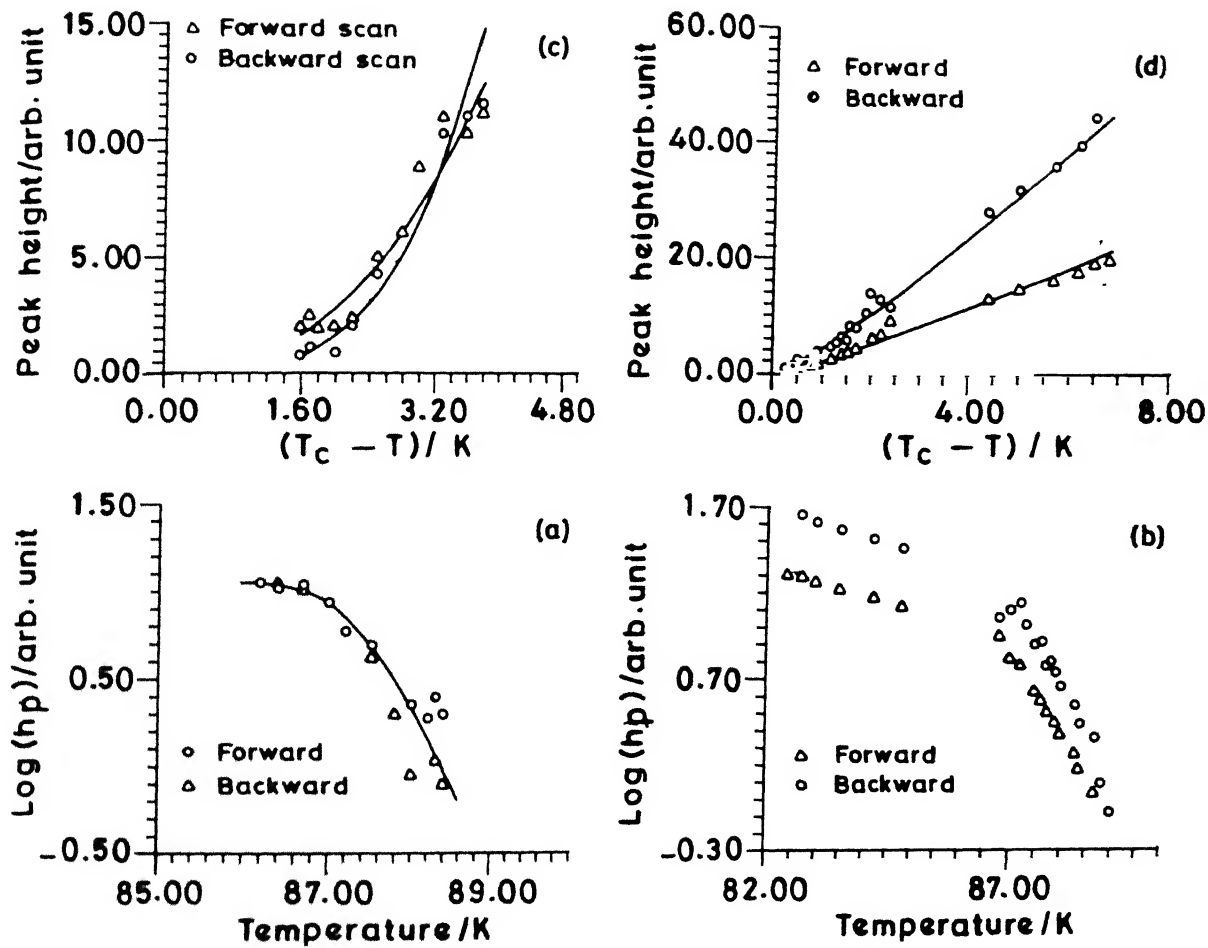


Fig. 4.8 Plot of \log of peak height (h_p) of DLFDMA Vs temperatures of $\text{YBa}_2\text{Cu}_3\text{O}_{7-\delta}$ (a) Sample A (b) Sample B. Plot of h_p of DLFDMA as a function of $(T_c - T)$ $\text{YBa}_2\text{Cu}_3\text{O}_{7-\delta}$ (c) Sample A (d) Sample B. The smooth curves show the best fit to the experimental data (see text for details)

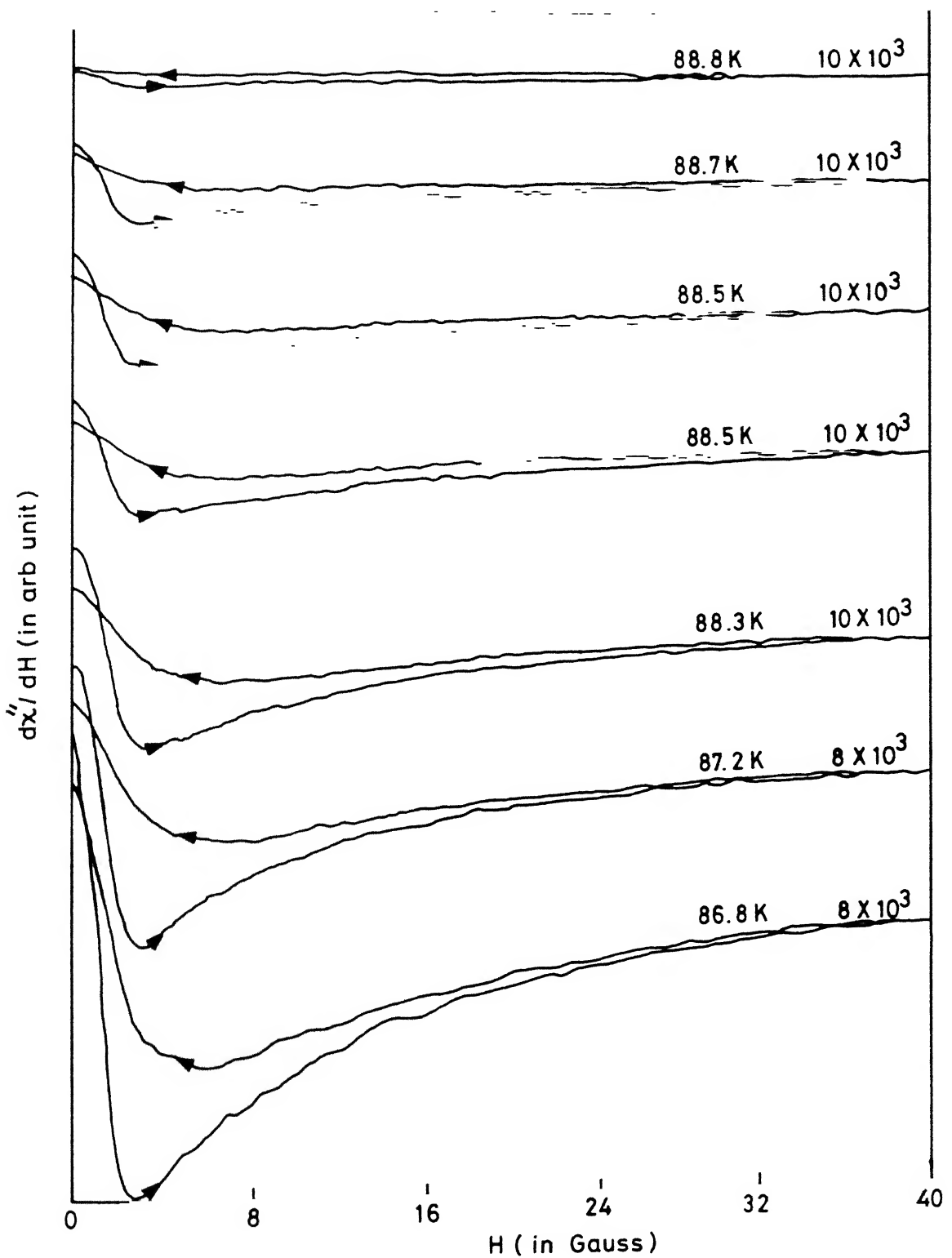


Fig.4.9 Actual recorded spectra of DLFDMA of $\text{YBa}_2\text{Cu}_3\text{O}_{6.85}$ (Sample C) as a function of field at different temperatures. For recording the spectra at each temperature, the sample was cooled in zero field. Gain and temperatures are specified at each spectrum (microwave power 1mW, Mod ampl. 1G)

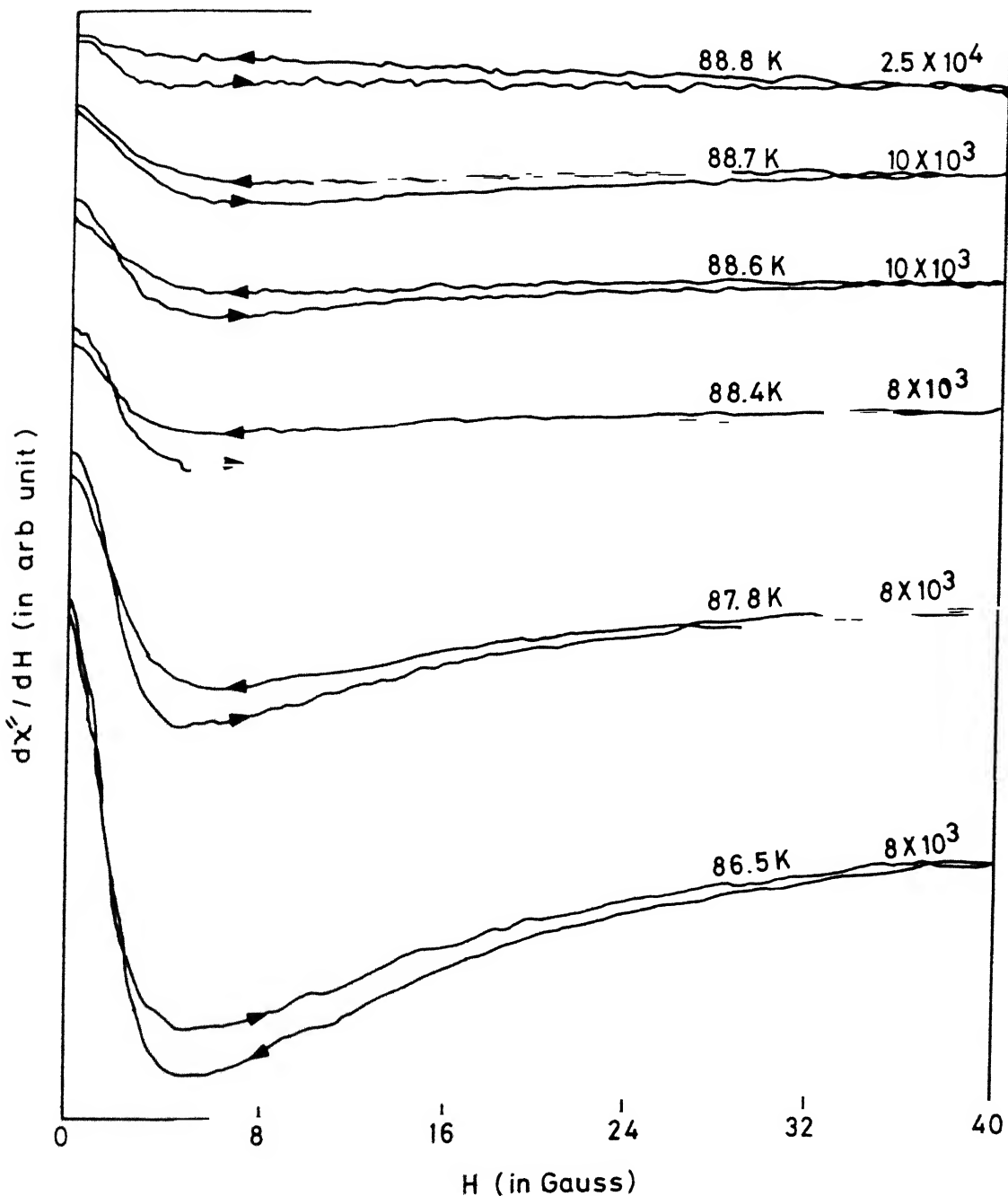


Fig. 4.10 Actual recorded spectra of DLFDMA of $\text{YBa}_2\text{Cu}_3\text{O}_{6.85}$ (Sample C) as a function of field at different temperatures. At all temperatures samples were already exposed to 40G magnetic field. Gain and temperatures are specified at each spectrum (microwave power 1mW, Mod. ampl. 1G)

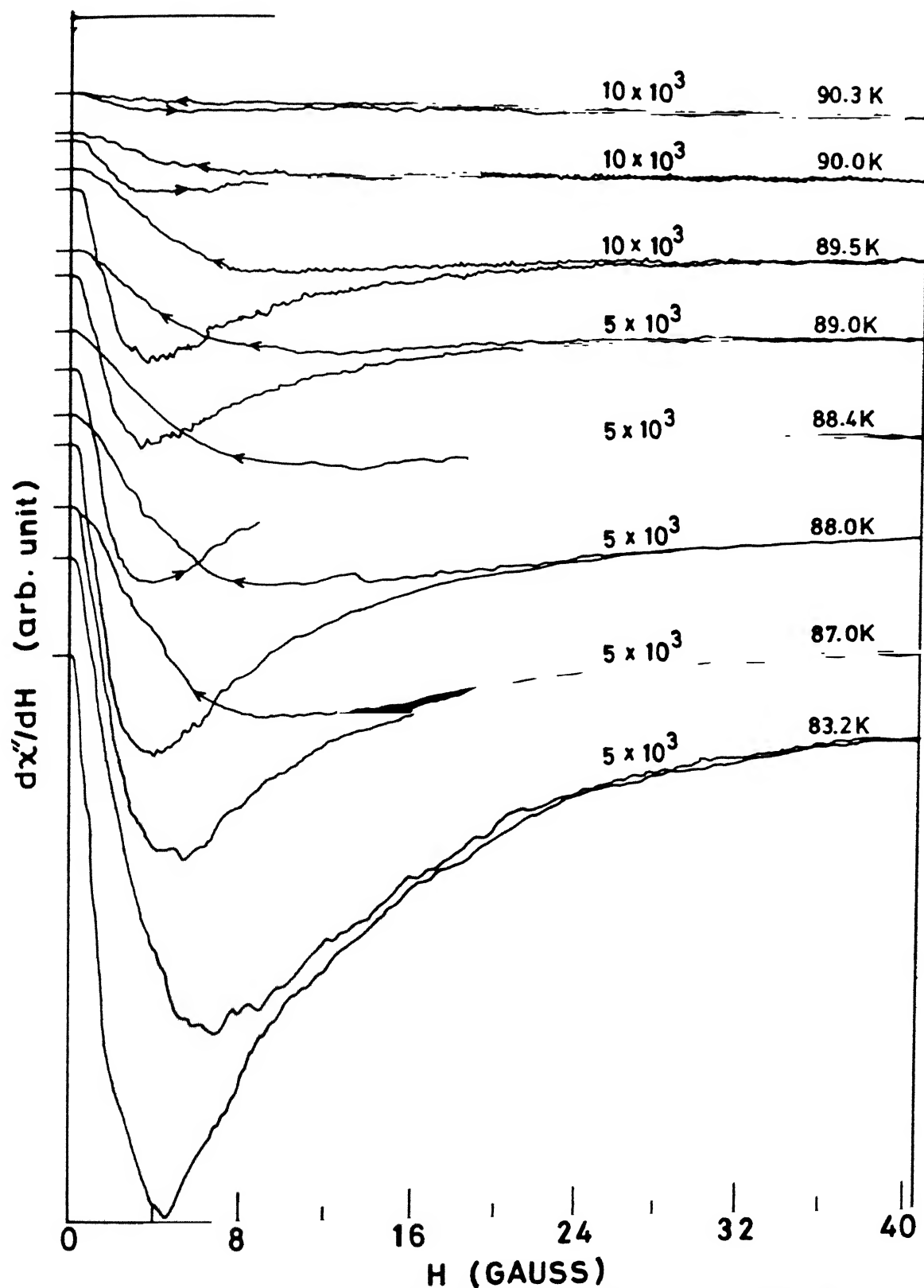


Fig.4.11 Actual recorded spectra of DLFDMA of $\text{YBa}_2\text{Cu}_3\text{O}_{7-\delta}$ (Sample D) as a function of field at different temperatures. For recording the spectra at each temperature, the sample was cooled in zero field. Gain and temperatures are specified at each spectrum (microwave power 1mW, Mod. ampl. 1G)

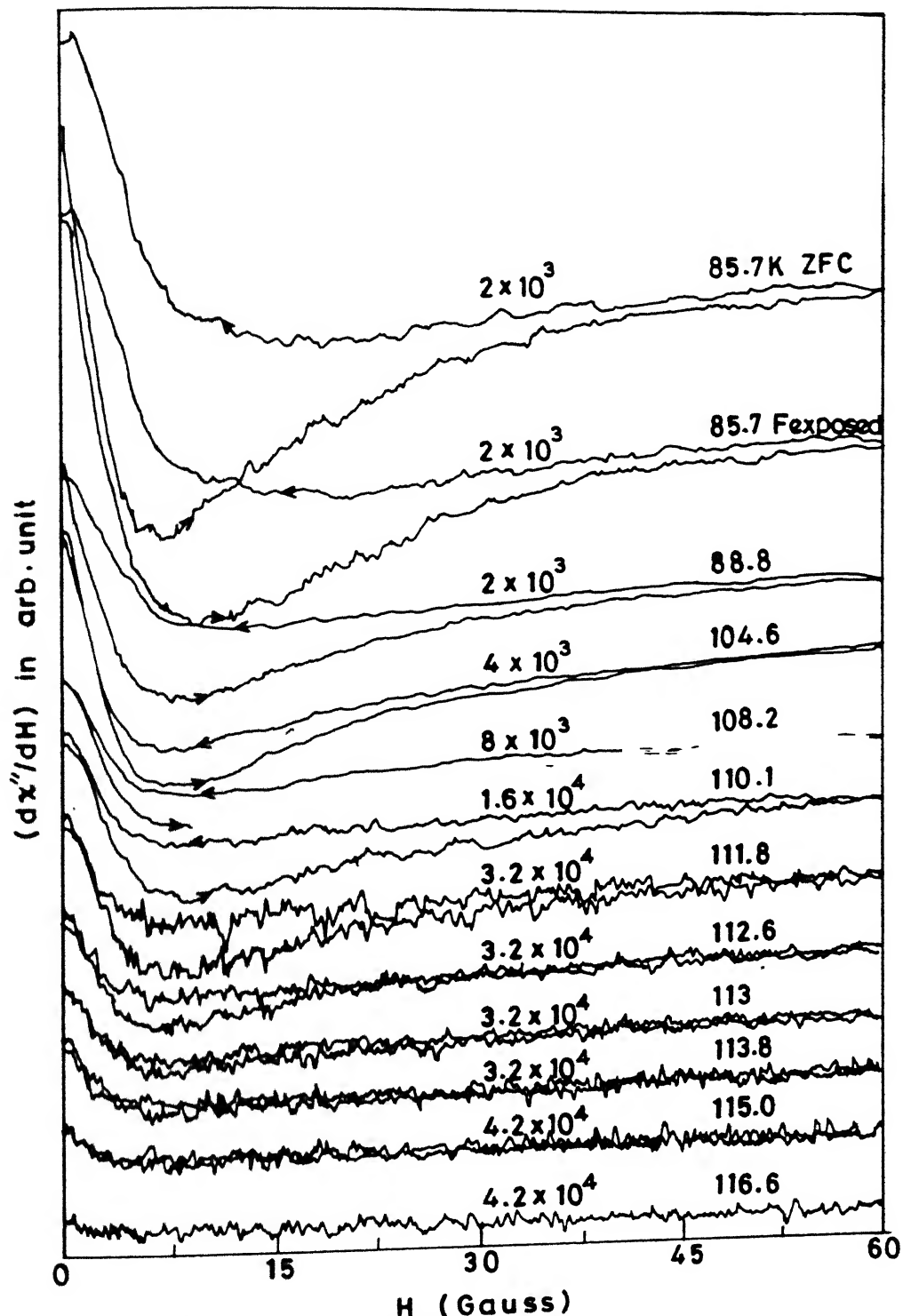


Fig. 4.12 Actual recorded spectra of DLFDMA of $Tl_2Ba_2CaCuO_{8+\delta}$ as a function of field at different temperatures. At all temperatures samples were already exposed to 60G magnetic field. Gain and temperatures are specified at each spectrum (microwave power .5mW, Mod. ampl. 1G)

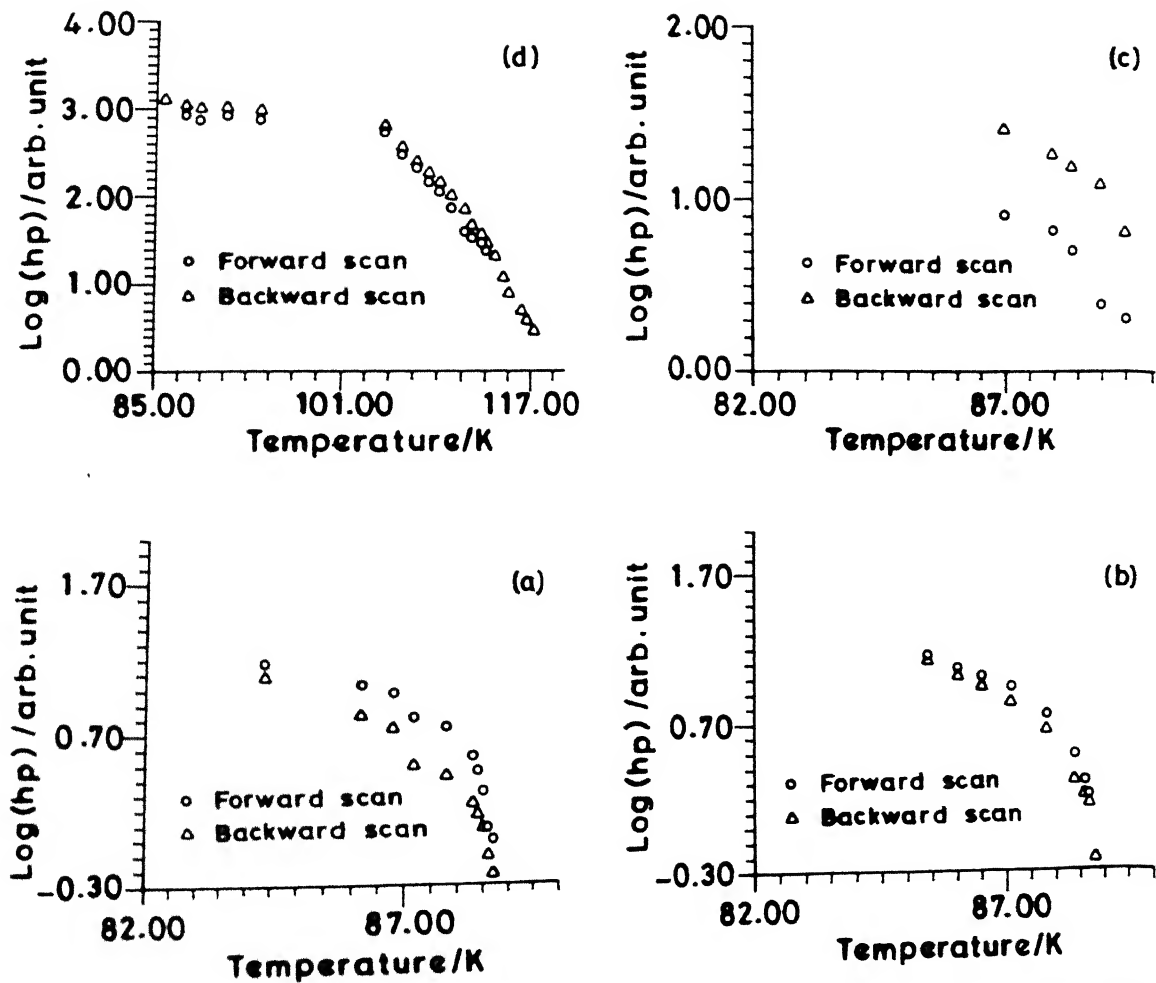


Fig.4.13 Plot of $\log(h_p)$ as a function of temperature (a) Sample C (ZFC at each temperature) (b) Sample C (60G filed exposed) (c) ZFC Sample D (d) $Tl_2Ba_2CaCuO_{8+\delta}$ (60G field exposed at each temperature)

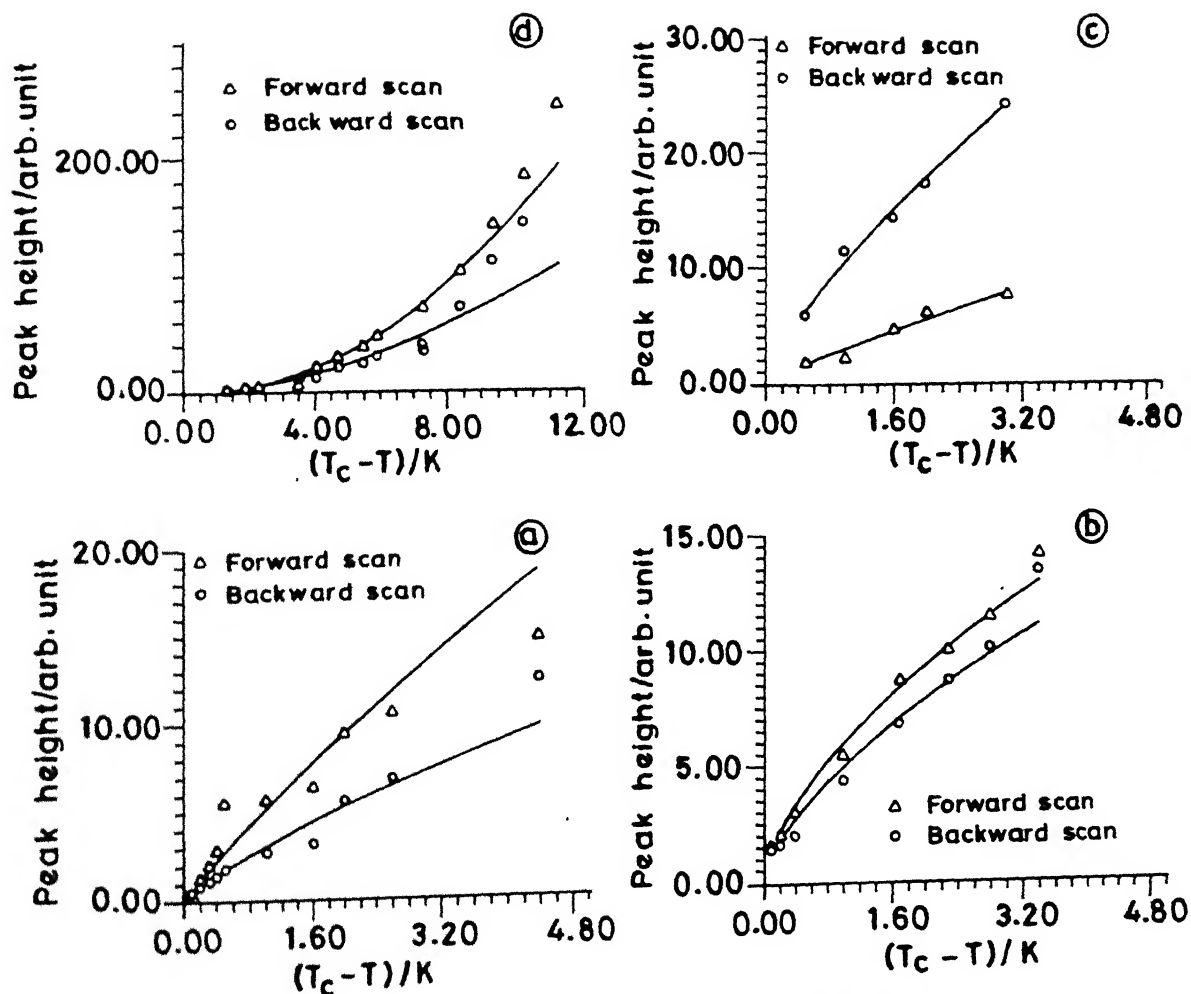


Fig. 4.14 The plot of peak height of DLFDMA as a function of $(T_c - T)/K$ (a) ZFC Sample C (b) 60G field exposed Sample C (c) Sample D and (d) $Tl_2Ba_2CaCuO_{8+\delta}$

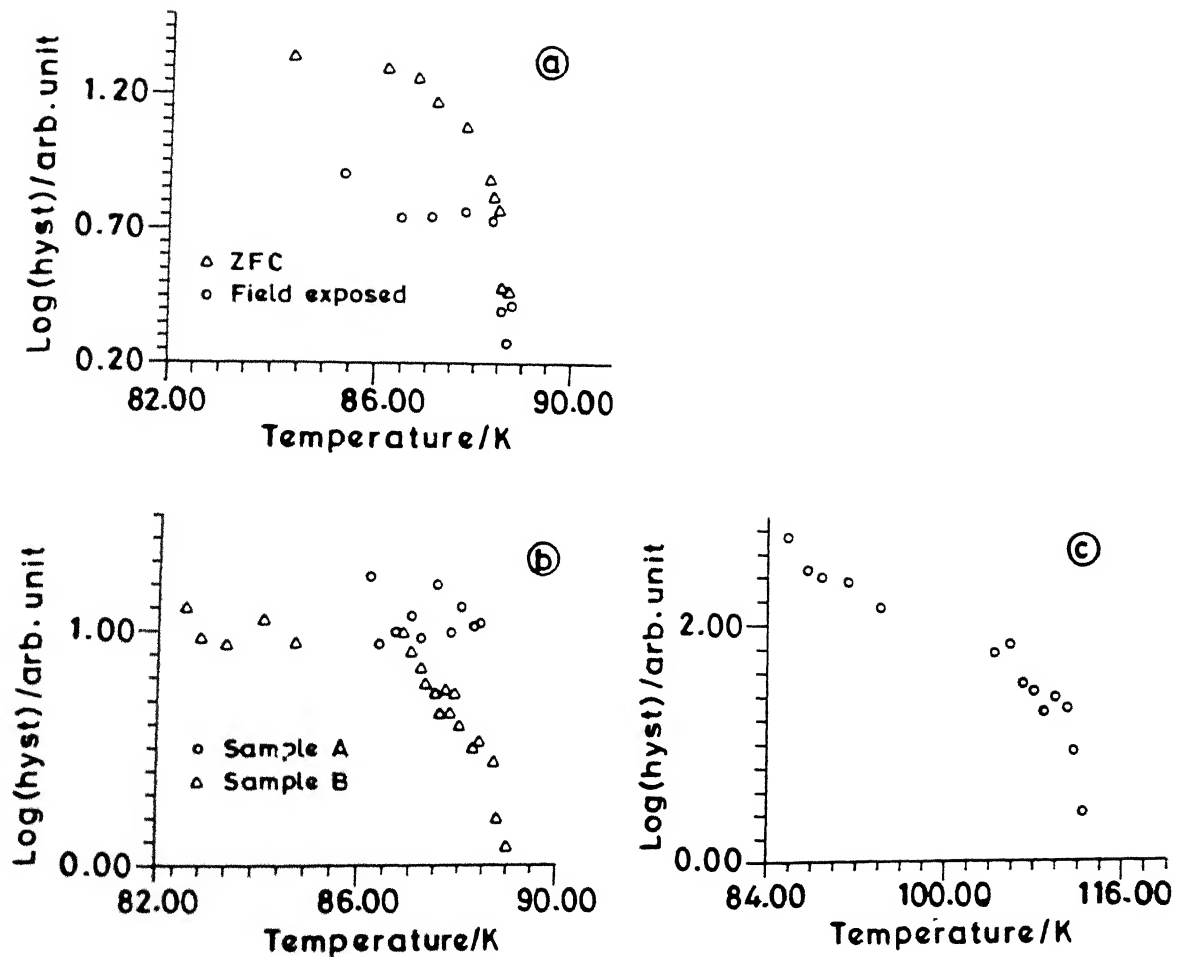


Fig. 4.15 The plot of log (hysteresis area) of DLFDMA as a function of temperature (a) Sample C (b) Sample A and Sample B and (c) $Tl_2Ba_2CaCuO_{8+\delta}$

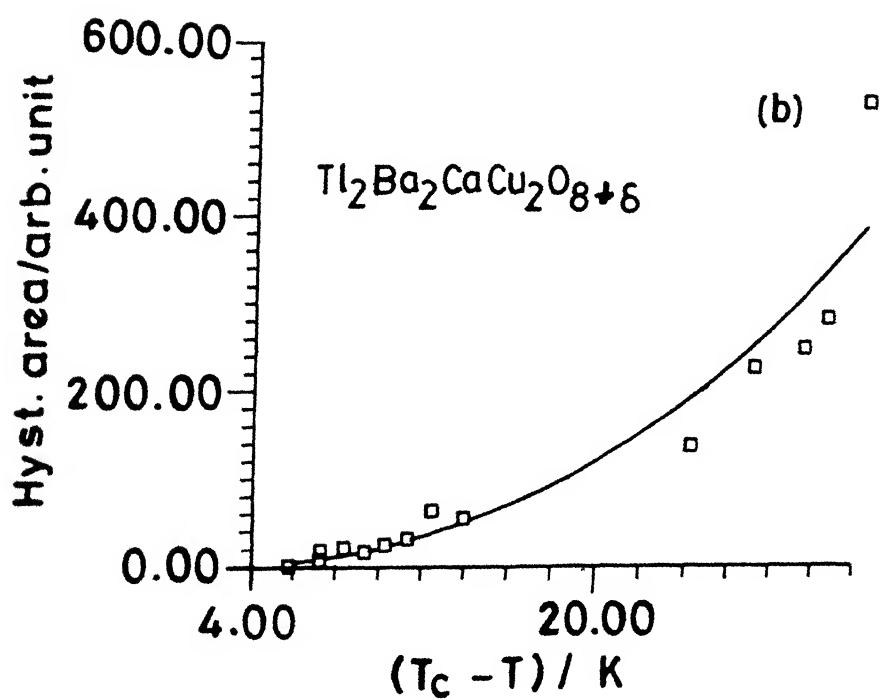
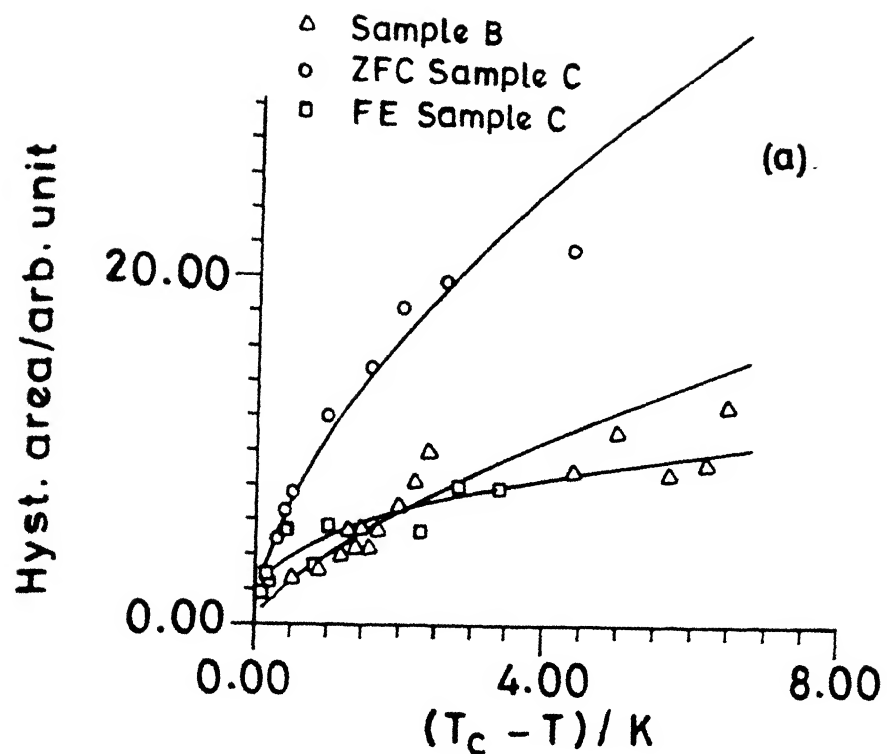


Fig. 4.16 Hysteresis area of DLFDMA as a function of $(T_c - T)$

(a) $YBa_2Cu_3O_{7-\delta}$ and (b) $Tl_2Ba_2CaCu_2O_{8+\delta}$

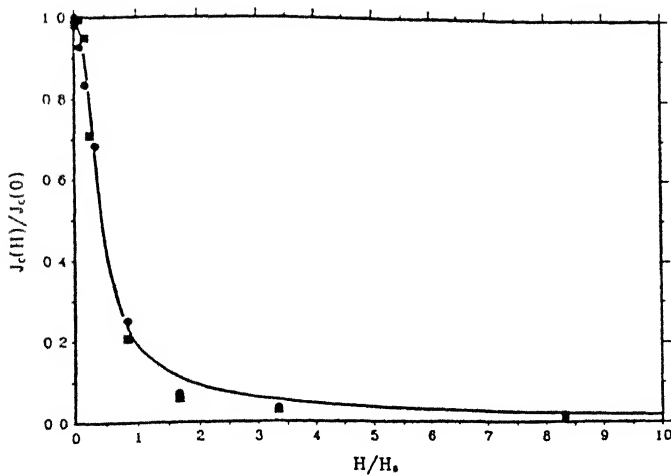


Fig. 4.17 Normalised transport critical density Vs applied field normalized to a characteristic field H_0 . The smooth curve is calculated for skewed triangular distribution of junctions length (Ref.[35])

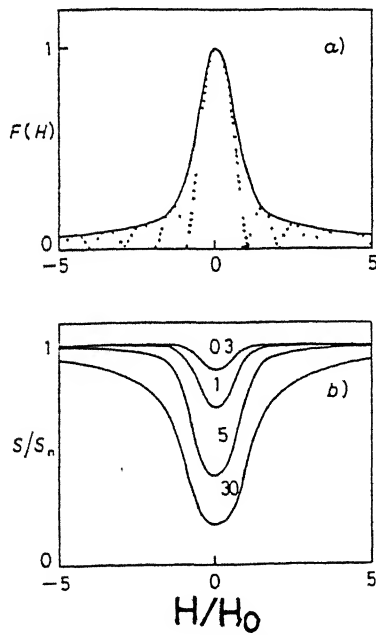


Fig. 4.18(a) The diffraction pattern and its envelope $F(H)$ as the reduction factor for the critical current in Josephson junctions. (b) Calculated microwave absorption signals for different values of η_0 indicated by the numbers (Ref.[32])

CHAPTER V

EFFECT OF MODULATION FIELD AMPLITUDE AND MICROWAVE POWER ON DERIVATIVE OF LOW FIELD DEPENDENT MICROWAVE ABSORPTION (DLFDMA) IN $\text{YBa}_2\text{Cu}_3\text{O}_{6.85}$, HF-DOPED $\text{YBa}_2\text{Cu}_3\text{O}_{7-\delta}$ AND $\text{Tl}_2\text{Ba}_2\text{CaCu}_2\text{O}_{8+\delta}$

Abstract

DLFDMA in $\text{YBa}_2\text{Cu}_3\text{O}_{7-\delta}$, Hf-doped $\text{YBa}_2\text{Cu}_3\text{O}_{7-\delta}$ and $\text{Tl}_2\text{Ba}_2\text{CaCu}_2\text{O}_{8+\delta}$ have been studied as a function of modulation field amplitude. For low modulation field amplitude the DLFDMA changes sign on the reversal of magnetic field scan. The parameters, peak height and hysteresis area, show non-linear behavior in a certain range of modulation amplitude. This range shifts towards lower value of modulation amplitude as the Hf-doping is increased. These results are explained in terms of the model proposed by Dulcic et al. Effect of microwave power on DLFDMA in these samples does not show any anomalous behavior.

Publication based on this chapter.

Md. Shahabuddin, A.G. Vedeshwar, H.D. Bist, Prem Chand, S.K. Agarwal and A.V. Narlikar, Bull. Mater. Sci. 14, 789 (1991).

5.1 INTRODUCTION

One of the many interesting features of the high T_c copper oxide based superconductors is their strongly field dependent microwave absorption at low magnetic fields below T_c . Low field dependent microwave absorption has been measured with [1-10] and without modulation field [11-16]. The field modulation and phase sensitive detection implied that the signal is the first derivative of the microwave absorption with respect to magnetic field. This method is useful over direct absorption in that it gives the rate of change of absorption as a function of magnetic field which can not be seen in the direct absorption. But by differentiating the direct microwave absorption curve with respect to the magnetic field we do not get exactly the signal of the field modulated microwave absorption especially at low modulation field amplitude [17-18]. The variation of the microwave absorption with respect to the modulation amplitude is linear for smaller values and becomes highly non-linear for larger values of the amplitude of the modulation. A similar measurement was made on the thin film of low critical temperature superconductors such as Pb and Sn [20]. For a small modulation amplitude the response was linear, and changed sign with the reversal of the d.c. field sweep. It was argued that the small modulation amplitude could not affect the flux density in the sample, so that only the boundary current was modulated. In the microscopic model for fluxon dynamics, pinning was neglected as inefficient at microwave frequencies [21]. In contrast, in a recently proposed model by Portis et al. [13,22-23], the restoring force was neglected while pinning was considered as an essential factor. The variation of microwave absorption under modulation field was interpreted as a consequence of partial pinning and depinning of fluxon during modulation cycle [22,24].

Rakvin et al. [6] have related this to the model of damped motion of free fluxon and calculated the line shape introducing the modulation field of small amplitude. Introducing negative sign to the one factor which depends on fluxoid viscosity and fraction of free fluxons for the reverse sweeps they got the line shape identical to that of the signal observed. They argued that either fluxoid viscosity or the fraction of fluxon changes sign on the reversal of the field sweep.

Flux analysis by Pozek et al. [5] shows that the flux modulation takes place even at very low modulation field amplitude and there is modulation of boundary current whose sign depends on the direction of the field sweep. They argued that lock-in detected signal contain two distinct components; one of them is the derivative of the microwave absorption. The model proposed by Dulcic et al. [11-19] supports the observation of Pozek et al. [5].

The effect of the modulation field and microwave power on the derivative of the low field dependent microwave absorption (DLFDMA) is very complicated and needs careful investigation. To have a better understanding of the nature of these effects, we need more experimental data on the subject. We have studied the effect of modulation field on DLFDMA on pure $\text{YBa}_2\text{Cu}_3\text{O}_{6.85}$, Hf-doped $\text{YBa}_2\text{Cu}_3\text{O}_{7-\delta}$ [7] and $\text{Tl}_2\text{Ba}_2\text{CaCu}_2\text{O}_{8+\delta}$ using a phase sensitive lock-in detection technique. Also, we present the effect of microwave power on DLFDMA of these materials.

5.2 EXPERIMENT

Samples were prepared by ceramic method i.e. solid state decomposition method as described in Chapter 3. Hf-doped $\text{YBa}_2\text{Cu}_3\text{O}_{7-\delta}$ and $\text{Tl}_2\text{Ba}_2\text{CaCu}_2\text{O}_{8+\delta}$ were obtained from A.V.Narlikar's group in National Physical Laboratory. The samples were

characterized by resistance measurement, X-ray powder diffraction SEM and EPR spectroscopy. The details of the characterization are described in Chapter IV. The sample $\text{YBa}_2\text{Cu}_3\text{O}_{6.85}$ is the same sample C which was studied in Chapters IV and V. The low field dependent microwave absorption of these samples were recorded in standard EPR geometry using Varian E109 EPR spectrometer at X-band. Samples were sealed in quartz capillary tube to protect it from humidity and recording was done at liquid nitrogen temperature by dipping the sealed quartz tube directly into the liquid nitrogen. The magnetic field scan was done outside the large electromagnet using home made Helmholtz coil described in Chapter III, to ensure that the scan started from zero magnetic field. For comparison, samples with different percentage of Hf-doping were taken in equal amount. In recording the low field dependent microwave absorption the samples were cooled in zero field for each value of modulation field amplitude. During the entire recording process the microwave power and modulation frequency were kept constant, and the amplitude and receiver gain only were changed.

5.3 RESULTS

Low field dependent microwave absorption in pure $\text{YBa}_2\text{Cu}_3\text{O}_{6.85}$, Hf-doped $\text{YBa}_2\text{Cu}_3\text{O}_{7-\delta}$ and $\text{Tl}_2\text{Ba}_2\text{CaCu}_2\text{O}_{8+\delta}$ were studied as a function of modulation amplitude. A typical actual recorded spectra of pure $\text{YBa}_2\text{Cu}_3\text{O}_{6.85}$ for different values of modulation amplitude are shown in Fig. 5.1. For lower modulation field the signal for reverse sweep changes sign i.e. its phase changes by 180° . But for higher modulation field it does not change sign but shows hysteresis. This type of behavior was observed in all high T_c superconductors. Only the modulation amplitude upto which the signal changes sign, vary from sample to sample. It is observed

that peak position (H_m), peak height (h_p) and hysteresis area (ΔA) of low field dependent microwave absorption are sensitive to the modulation amplitude A_m . The variation of h_p , H_m and ΔA of both the samples, $\text{YBa}_2\text{Cu}_3\text{O}_{6.85}$ and $\text{Tl}_2\text{Ba}_2\text{CaCu}_2\text{O}_{8+\delta}$, as a function of modulation amplitude A_m are shown in Figs. 5.2, 5.3 and 5.4 respectively. It is clear from Fig. 5.2 that the peak height h_p shows a linear behavior for the lower and higher A_m while it shows a non-linear behavior in the range 0.05G to 0.2G for $\text{YBa}_2\text{Cu}_3\text{O}_{6.85}$ and in the range 0.07G to 1.0G for $\text{Tl}_2\text{Ba}_2\text{CaCu}_2\text{O}_{8+\delta}$. The peak position H_m remains constant almost in the lower range of A_m , then it shows a broad minima as it is clear from Fig. 5.3. This type of behavior is not observed in Hf-doped $\text{YBa}_2\text{Cu}_3\text{O}_{6.85}$. The variation of hysteresis area (ΔA) as a function of A_m are shown in Fig. 5.4. It also shows similar of behavior as the peak height h_p , i.e. it shows two regions of linear dependence separated by a non-linear region. The range of the nonlinear region is from approximately 0.05G to 0.5G in $\text{YBa}_2\text{Cu}_3\text{O}_{6.85}$ and 0.05 to 1G in $\text{Tl}_2\text{Ba}_2\text{CaCu}_2\text{O}_{8+\delta}$. The variations in the peak height, peak position and hysteresis area in 0.5%, 1% and 2% Hf-doping as a function of A_m are shown in Figs. 5.5, 5.6 and 5.7 respectively. The peak heights h_p of 0.5%, 1% and 2% Hf-doped samples also show two regions of linear dependence separated by non-linear region. The starting of the non-linear region for h_p shifts towards lower amplitude of modulation A_m with increasing the percentage of Hf-doping. The peak position H_m shifts towards higher field with increasing A_m .

The variation in hysteresis area (ΔA) with A_m is quite interesting. The variation of ΔA for samples with different Hf-percentage as a function of A_m are shown in Fig. 5.7. Initially ΔA increases with increasing A_m except in certain range of A_m in

which ΔA decreases with increasing A_m . The value of A_m at which ΔA starts to decrease shifts towards lower value as doping percentage of Hf is increased. The range of A_m in which ΔA decreases with increasing A_m also decreases with increasing percentage of Hf doping.

Low field dependent microwave absorption of $\text{YBa}_2\text{Cu}_3\text{O}_{6.85}$ and $\text{Tl}_2\text{Ba}_2\text{CaCu}_2\text{O}_{8+\delta}$ as a function of microwave power were studied. The peak height (h_p) and hysteresis area (ΔA) do not show any anomaly. The variations in h_p , H_m , and ΔA are shown in Figs. 5.8, 5.9 and 5.10 respectively. The peak height h_p and hysteresis area ΔA vary as the square root of the microwave power as in other EPR signal and the signal does not show saturation upto 10 mW of the microwave power.

5.4 DISCUSSION

The main features of the effect of modulation field amplitude on the low field dependent microwave absorption can be summarized as follows. It shows non-linear behavior in a certain range of A_m . On either side of this non-linear region, h_p and ΔA show a linear dependence on A_m . For small value of the modulation amplitude the signal changes sign on reversing the sweep direction of the external dc field. Our observation fully supports the model of the Dulcic et al. [18] which is described in detail in Chapter IV. According to this model the microwave absorption in granular superconductors can be treated by considering the microwave response of the single representative junction. Low field dependent resistivity near transition temperature has also been explained using the model of single representative junction [25]. If the sample is exposed to dc field H_0 and microwave field

$H_1 \cos \omega t$, it induces the boundary current I_o to be superimposed by small microwave current $I_1 \cos \omega t$. These current acts as transport current for the Josephson junction. In the absence of microwave field, the phase of the current would adjust to an equilibrium value ϕ_o defined by

$$I_c \sin \phi_o = I_o \quad (5.1)$$

where I_c is the critical current of the representative junction. For small values of microwave current the phase will oscillate around ϕ_o . In the limit of $I_o < I_c$ the power absorbed in junction is given by

$$P = P_n \frac{1}{1+\eta} \quad (5.2)$$

where $P_n = \frac{1}{2} I_1^2 R$, R is the normal resistance, and

$$\eta = \frac{I_c^2 \cos^2 \phi_o}{\left(\frac{\hbar \omega}{2eR}\right)^2} \quad (5.3)$$

Superimposing modulation field $A_m \cos \omega_m t$ of small amplitude A_m with dc field one obtains the modulated signal

$$S_M \approx \frac{I_c}{(1+\eta)^{3/2}} \left[-\frac{dI_c}{dH} A_m + I_m \sin \phi_o \right] \cos \omega_m t \quad (5.4)$$

where I_m is the induced current due to modulation field. This expression has been obtained in the limit of $I_m \ll I_o$. From equation (5.4) it is clear that the modulated signal contains two parts; one part is field-sweep independent and the other is sweep-dependent, because on reversing the sweep direction, ϕ_o changes sign.

For small values of A_m the dominating term in equation

(5.4) is $I_m \sin \phi_o$ which changes sign on reversing the sweep direction of the field. Thus, for low A_m , the signal shows phase reversal. For lower values of A_m signal grows linearly as it is clear from equation 5.4. The second term in equation (5.4) was derived in the limit $I_m \ll I_o$. However for I_m comparable or larger than I_o , the phase oscillates between negative and positive values, and therefore, the signal response becomes non-linear. Thus, the non-linear response of the first harmonic of the sweep-dependent component which is lock-in detected, gets saturated and then decreases even at higher modulation field. Therefore, at higher modulation amplitudes the sweep-independent term dominates and the signal looks like the derivative signal and grows linearly with respect to A_m .

From Figs. 5.2 and 5.4 it is also clear that the nonlinear behavior in $Tl_2Ba_2CaCu_2O_{8+\delta}$ are not as pronounced as in case of $YBa_2Cu_3O_{6.85}$. This is due to the reason that $Tl_2Ba_2CaCu_2O_{8+\delta}$ is far from transition temperature and hence I_c of $Tl_2Ba_2CaCu_2O_{8+\delta}$ is large compared to that of $YBa_2Cu_3O_{6.85}$. $I_o \ll I_m$ is satisfied even at higher modulation field, and therefore, it shows linear behavior.

The value of A_m at which non-linear behavior starts, shifts towards lower A_m as we increase the Hf-doping. The increase in the percentage of Hf, increases the formation of impurity phase at grain boundary and hence increases the normal resistance of the junction [1,26]. Due to the increase of the junction resistance the critical current decreases and hence I_o decreases. Thus, due to decrease in I_o the condition for non-linearity, i.e., $I_o \approx I_m$ is satisfied at lower A_m . Thus the increase of Hf-percentage shifts the range of non-linear behavior towards lower A_m .

REFERENCE

1. A.G. Vedeshwar, Md. Shahabuddin, Prem Chand, H.D. Bist, S.K. Agarwal, V.N. Moorthy, C.V.N. Rao, and A.V. Narlikar, Physica C **158**, 385 (1989).
2. S.V. Bhat, P. Ganguly, T.V. Ramakrishnan, and C.N.R. Rao, J. Phys. C **20**, L559 (1987).
3. K. Kachaturyan, E.R. Weber, P. Tejedor, A.M. Stacy, and A.M. Portis, Phys. Rev. B **36**, 8309 (1987).
4. K.W. Blazey, K.A. Müller, J.G. Bednorz, W. Berlinger, G. Amoretti, R. Buluggiu, A. Vera, and F.C. Matacotta, Phys. Rev. B **36**, 7241 (1987).
5. M. Pozek, A. Dulcic and B. Rakvin, Solid State Commun. **70**, 889 (1989).
6. B. Rakvin, M. Pozek, M. Paljevic and N. Brnicevic, Solid State Commun. **70**, 729 (1989).
7. Md. Shahabuddin, A.G. Vedeshwar, H.D. Bist, Prem Chand, S.K. Agarwal and A.V. Narlikar, Bull. Mater. Sci. **14**, 789 (1991).
8. J. Stankowski, P.K. Kahol, N.S. Dalal, and J.S. Moodera, Phys. Rev. B **36**, 7126 (1987).
9. S.H. Glarum, J.H. Marshall and L.F. Schneemeyer, Phys. Rev. B **37**, 7491 (1988).
10. A. Dulcic, R.H. Crepe and J.H. Freed, Phys. Rev. B **38**, 5002 (1988).
11. A. Dulcic, B. Leontic, M. Peric and B. Rakvin, Europhys. Lett. **4**, 1403 (1987).
12. M. Peric, B. Rakvin, M. Prester, N. Brnicevic and A. Dulcic, Phys. Rev. B **37**, 522 (1988).
13. A.M. Portis, K.W. Blazey, K.A. Müller and J.G. Bednorz, Europhys. Lett. **5**, 467 (1988).
14. E.J. Pakulis and T. Osada, Phys. Rev. B **37**, 5940 (1988).

15. M. Giura, R. Marcon and R. Fastampa, Phys. Rev. B 40, 4437 (1989).
16. A. Gould, E.M. Jack, R. Renouard, R. Crittenden, S.M. Bhagat, N.D. Spencer, L.L. Dolhert and R.F. Wormsbecher, Physica C 156, 555 (1988).
17. S.M. Bhagat in the Proceeding of the Winter School on Superconductivity, Dec. 26th, 1989 to Jan. 6, 1990, TIFR, Bombay, India.
18. A. Dulcic, B. Rakvin and M. Pozek, Europhys. Lett. 10, 593 (1989).
19. A. Dulcic, R.H. Crepeau, J.H. Freed, L.F. Schneemeyer and J.V. Waszczak, Phys. Rev. B 42, 2155 (1990).
20. Y.W. Kim, A.M. De Graaf, J.T. Chen, E.J. Friedman, S.H. Kim, Phys. Rev. B 6, 887 (1972).
21. J.I. Gittleman and B. Rosenblum, Phys. Rev. Lett., 16, 734 (1966); J.I. Gittleman and B. Rosenblum, J. Appl. Phys. 39, 2617 (1968).
22. A.M. Portis, K.W. Blazey and F. Waldner, Physica C, 153-155, 308 (1988).
23. K.W. Blazey, A.M. Portis and J.G. Bednorz, Solid State Commun. 65, 1153 (1988).
24. M. Stalder, G. Stefaricki, M. Warden, A.M. Portis and F. Waldner, Physica C 153-155, 659 (1988).
25. A.C. Wright, K. Zhang and A. Erbil, Phys. Rev. Lett.
26. A.G. Vedeshwar, H.D. Bist, S.K. Agarwal and A.V. Narlikar, Phys. Rev. B 41, 11294 (1990).

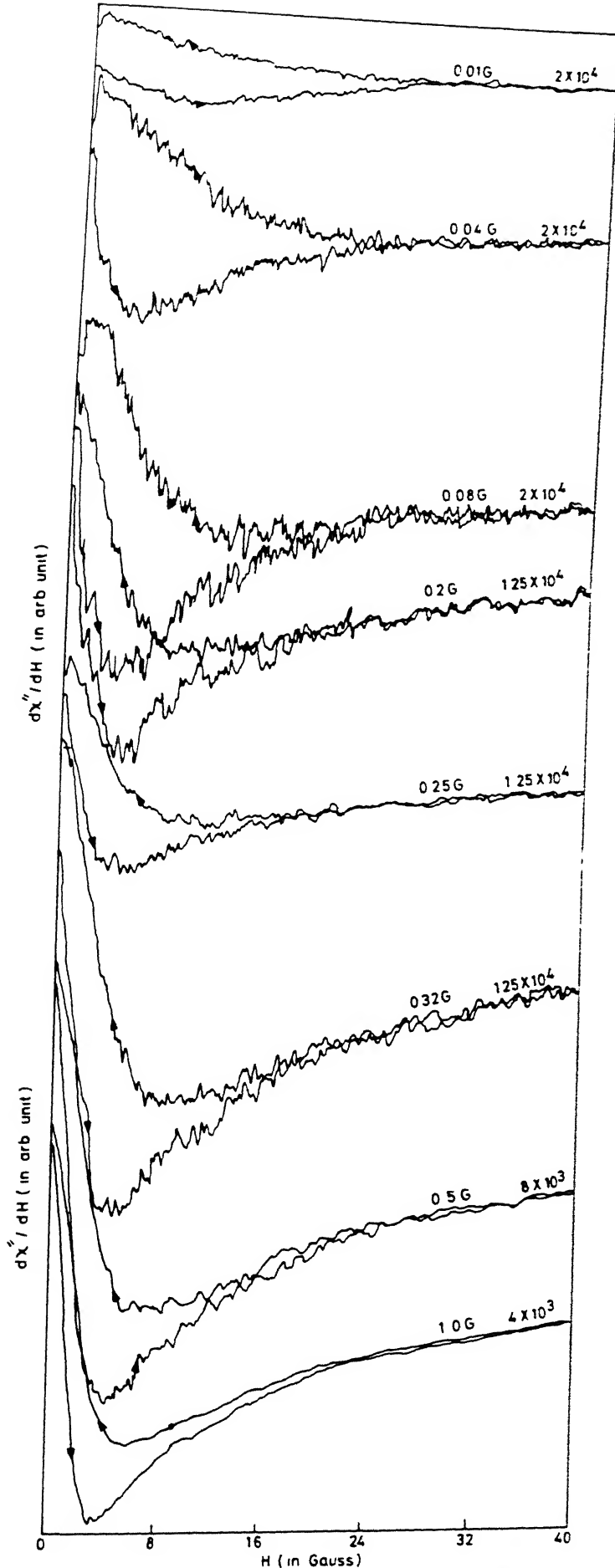


Fig. 5.1 Actual recorded spectra of DLFDMA of $\text{YBa}_2\text{Cu}_3\text{O}_{6.85}$ at different mod. ampl. Each recording was done in ZFC condition. Mod. ampl. and gain are specified at each spectrum

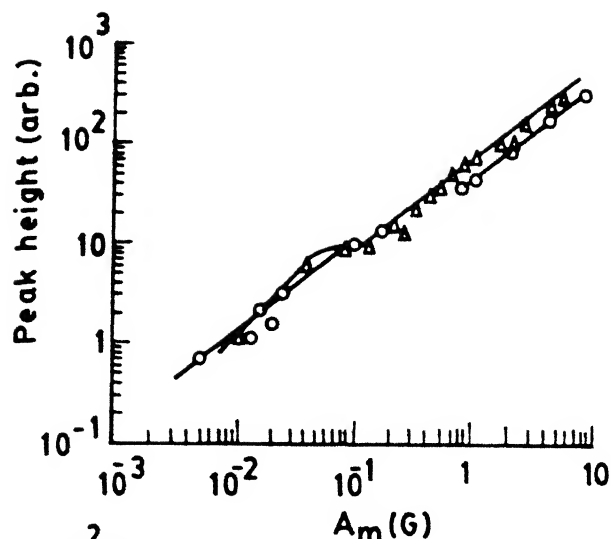


Fig. 5.2 Variation of peak height of DLFDMA of $\text{YBa}_2\text{Cu}_3\text{O}_{6.85}$ & $\text{Tl}_2\text{Ba}_2\text{CaCu}_2\text{O}_{8+\delta}$ as a function of mod. ampl. (A_m)

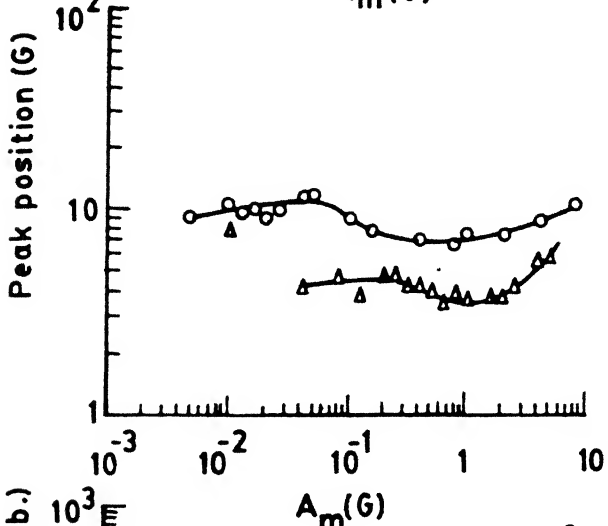


Fig. 5.3 Variation of peak position of DLFDMA of $\text{YBa}_2\text{Cu}_3\text{O}_{6.85}$ & $\text{Tl}_2\text{Ba}_2\text{CaCu}_2\text{O}_{8+\delta}$ as a function of mod. ampl. (A_m)

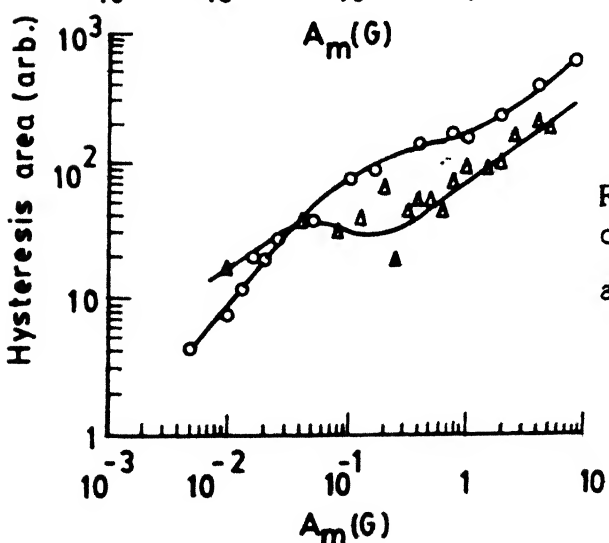


Fig. 5.4 Variation of hysteresis area of DLFDMA of $\text{YBa}_2\text{Cu}_3\text{O}_{6.85}$ & $\text{Tl}_2\text{Ba}_2\text{CaCu}_2\text{O}_{8+\delta}$ as a function of mod. ampl. (A_m)

Δ - $\text{YBa}_2\text{Cu}_3\text{O}_{6.85}$
 \circ - $\text{Tl}_2\text{Ba}_2\text{CaCu}_2\text{O}_{8+\delta}$

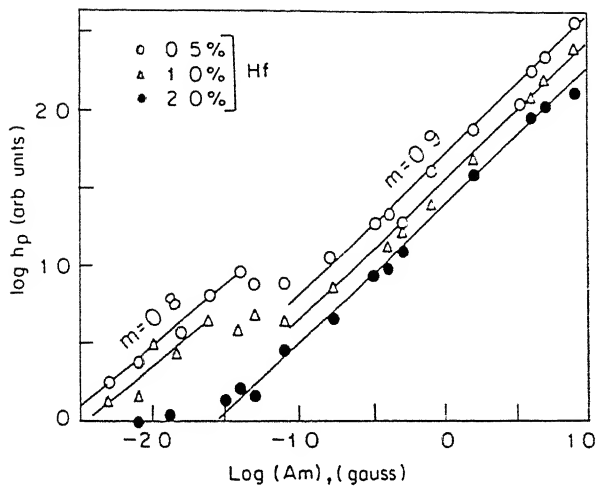


Fig.5.5 Log-log plot of h_p of DLFDMA of Hf-doped $\text{YBa}_2\text{Cu}_3\text{O}_{7-\delta}$ Vs mod. ampl.

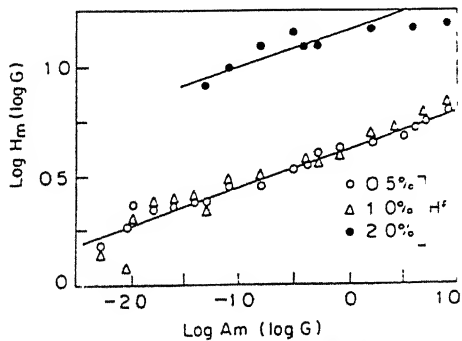


Fig.5.6 Log-log plot of H_m of DLFDMA of Hf-doped $\text{YBa}_2\text{Cu}_3\text{O}_{7-\delta}$ Vs mod. ampl.

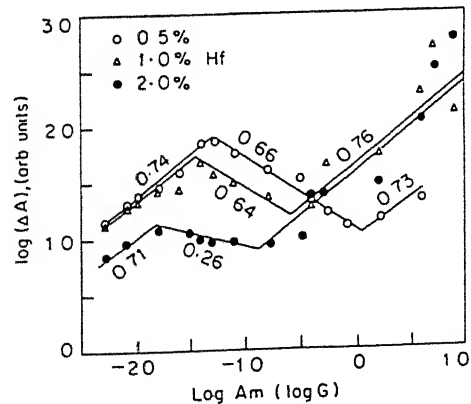
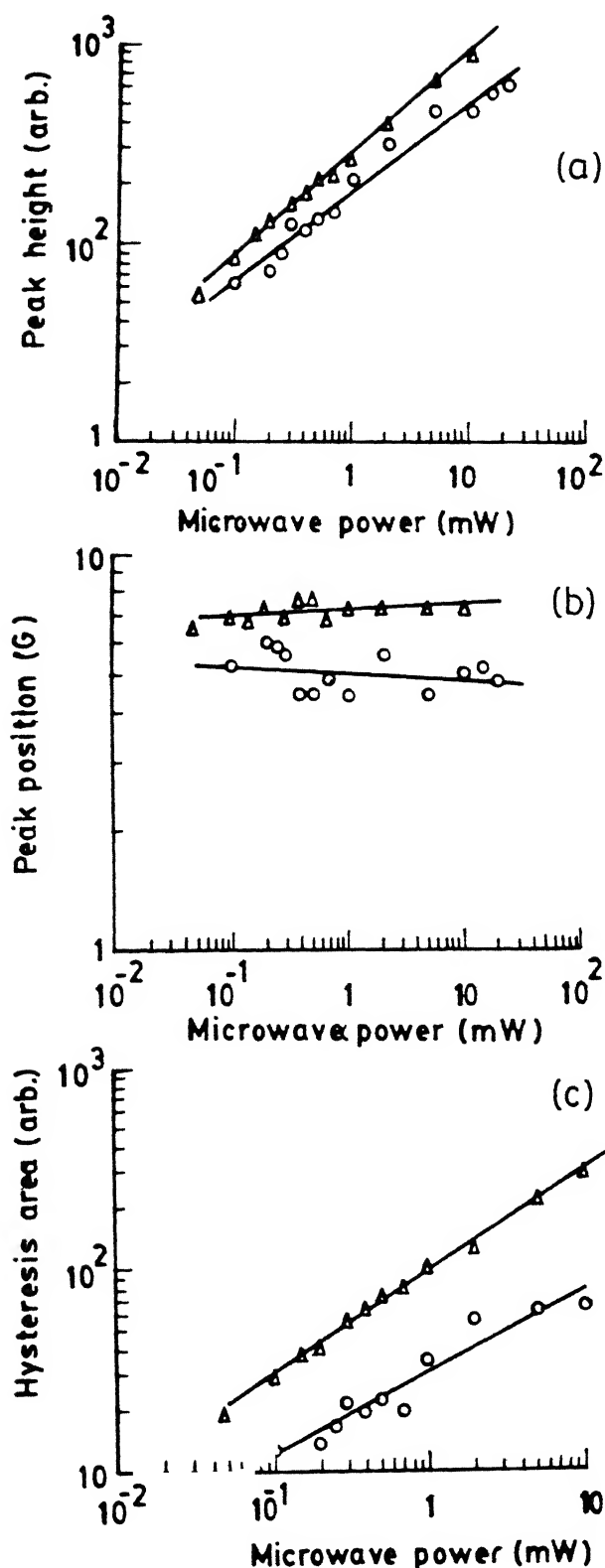


Fig.5.7 Log-log plot of ΔA of DLFDMA of Hf-doped $\text{YBa}_2\text{Cu}_3\text{O}_{7-\delta}$ Vs mod. ampl.



Δ - YBa₂Cu₃O_{6.85}
○ - Tl₂Ba₂CaCu₂O_{8+δ}

Fig.5.8 Variation of (a) peak height (b) peak position and (c) hysteresis area of DLFDMA of YBa₂Cu₃O_{7-δ} and Tl₂Ba₂CaCu₂O_{8+δ} as a function of microwave power

CHAPTER VI

EFFECT OF FIELD EXPOSURE AND FIELD COOLING ON DERIVATIVE OF LOW FIELD DEPENDENT MICROWAVE ABSORPTION (DLFDMA) IN $\text{YBa}_2\text{Cu}_3\text{O}_{6.85}$, HF-DOPED $\text{YBa}_2\text{Cu}_3\text{O}_{7-\delta}$ AND $\text{Tl}_2\text{Ba}_2\text{CaCu}_2\text{O}_{8+\delta}$ SUPERCONDUCTORS

Abstract

Effect of different field exposures (in the low field region) on DLFDMA of zero field cooled $\text{YBa}_2\text{Cu}_3\text{O}_{6.85}$ and $\text{Tl}_2\text{Ba}_2\text{CaCu}_2\text{O}_{8+\delta}$ is presented. The peak height, peak position and hysteresis area which are sensitive to the strength of the field exposure are studied. Field cooling effects on DLFDMA of $\text{YBa}_2\text{Cu}_3\text{O}_{7-\delta}$ and $\text{Tl}_2\text{Ba}_2\text{CaCu}_2\text{O}_{8+\delta}$ are also presented. The field exposure and field cooling effects show different behavior. Upto a certain low value of the exposure of magnetic field (H_{c1J}) DLFDMA does not show hysteresis. As this value is surpassed it shows hysteresis. In the field cooling case the hysteresis area increases initially and attains a maximum. The peak occurs at H_{c1J} of the samples. They decrease very fast as cooling field is surpassed. The peak height and peak position, also show interesting behavior in both the case of field exposure and field cooling. The results are explained in terms of the critical state model of random intergranular Josephson junctions which have different coupling strengths. The studies on the effect of negative field exposure on the DLFDMA of the field exposed and field cooled $\text{YBa}_2\text{Cu}_3\text{O}_{7-\delta}$ and $\text{Tl}_2\text{Ba}_2\text{CaCu}_2\text{O}_{8+\delta}$ show that the pinning strength in $\text{Tl}_2\text{Ba}_2\text{CaCu}_2\text{O}_{8+\delta}$ is less than that in $\text{YBa}_2\text{Cu}_3\text{O}_{6.85}$.

Publication based on this chapter :

A.G. Vedeshwar, Md. Shahabuddin, H.D. Bist, S.K. Agarwal and A.V. Narlikar, Bull. Mater. Sci. 14, 777 (1991).

6.1 INTRODUCTION

High T_c superconductors exhibit unusual magnetic properties especially in very low field region. The diamagnetism of the low field cooled samples (Meissner effect) is a fraction of that observed in the zero field cooled (Shielding effect) samples [1], indicating a strong flux trapping [2] in the former case. The ac and dc magnetic susceptibilities are not the same [3]. Even very low fields have a large effect on the diamagnetic susceptibility [4,5], resistivity [6] and critical current density [7-9]. Also, there is a slow relaxation of the magnetic moment to an equilibrium value after magnetic field is suddenly changed [10-13]. Explanation of the most of these properties have been tried in terms of clusters of superconducting grains weakly coupled through Josephson junctions [14-16]. The exposure of the magnetic field decouples the grains [5] and on removing the magnetic field, the flux remains trapped in intergranular Josephson junctions.

Measurement of the microwave properties of high T_c oxide superconductors has fundamental physical and technological relevance. Huge absorption signal as a function of the magnetic field in the low field region has been observed in all high T_c ceramics with [17-20] and without [21-22] modulation field. This has been a very sensitive tool to detect the superconducting transition [17], grain size [22-23], ageing effect [23], and impurity phases [23] in the samples. Its origin is attributed to the fluxon pinning and depinning in the critical state model [24-25]. However, there are very few studies on low field microwave absorption in field cooled (FC) and field exposed (FE) samples. A large difference has been observed in ZFC and FC studies by other measurements [2,11,26] and is interpreted in terms of glass model [2,13] or a flux creep model [11,12]. Therefore, we

have studied microwave absorption in the FE and FC pure $\text{YBa}_2\text{Cu}_3\text{O}_{6.85}$ and $\text{Tl}_2\text{Ba}_2\text{CaCu}_2\text{O}_{8+\delta}$ samples in standard EPR geometry to have better understanding of the low field magnetic properties of the ceramic samples.

6.2 EXPERIMENT

Pure $\text{YBa}_2\text{Cu}_3\text{O}_{6.85}$ is the same sample C described in Chapter III which has been characterized by resistivity, X-ray, SEM and EPR measurements. $\text{Tl}_2\text{Ba}_2\text{CaCu}_2\text{O}_{8+\delta}$ came from Narlikar's group and its characterization is described in Chapter III.

Derivatives of low field microwave absorption were recorded using an EPR spectrometer Varian E109 described in Chapter II. All the spectra were recorded at liquid nitrogen temperature using home made quartz Dewar. Magnetic field scan was done outside the electromagnet using Helmholtz coils. Recording of the spectra of field exposed (FE) and field cooled (FC) samples were done as follows.

Field exposed

- (i) Samples were cooled in the zero field to liquid nitrogen temperature.
- (ii) Scan of field was done upto field H_{EF} in forward direction and then scanned back to zero field.
- (iii) Second scan was also done upto field H_{EF} in exactly the same way as in step (ii).
- (iv) The memory effect was destroyed i.e. samples were heated above T_c .
- (v) And steps (i) to (iv) were repeated for different field scan.

Field Cooled :

- (i) Samples were cooled in the field H_{FC} from normal state to liquid nitrogen temperature (LNT) (superconducting state).
- (ii) When equilibrium temperature was reached the field was brought back to zero and spectra were recorded scanning the magnetic field from zero to 60G and then back to zero.
- (iii) Second scan was done just after the first scan without destroying the magnetic memory.
- (iv) Samples were heated above T_c to destroy the previous memory effect and again the samples were cooled in a different field H_{FC} and steps (ii), (iii) and (iv) were repeated.

To study the negative field exposure effect on DLFDMA of the positive field exposed sample the spectra were recorded as follows:

- (i) Samples were cooled in zero field to LNT and spectra were recorded by scanning the magnetic field from zero to some fixed value and then scanning back to zero.
- (ii) Second scan was done just after step (i) to the same field as in (i) followed by a reverse scan from fixed maximum magnetic field to zero.
- (iii) A sudden negative field H was applied to the sample and then the field was reduced to zero after equilibrium is reached.
- (iv) Spectra were recorded by scanning the field from zero to the maximum field as in step (i) and then back to zero by reverse sweep.
- (v) Steps (iii) and (iv) were repeated for different values of negative field H .

Negative field exposure effect on the positive field cooled DLFDMA were studied and the spectra were recorded as follows :

- (i) Samples were cooled in the constant positive field H_c to LNT.
- (ii) The negative field H was applied to the sample.
- (iii) Spectra were recorded in both forward and backward scan starting from zero.
- (iv) Now sample was heated to room temperature and the above three steps were repeated by changing the negative field H and keeping the cooling field fixed.

6.3 RESULTS

6.3.1 Field Exposure Effect on DLFDMA of $\text{YBa}_2\text{Cu}_3\text{O}_{6.85}$ and $\text{Tl}_2\text{Ba}_2\text{CaCu}_2\text{O}_{8+\delta}$

The effect of field exposure on the DLFDMA of pure $\text{YBa}_2\text{Cu}_3\text{O}_{6.85}$ and $\text{Tl}_2\text{Ba}_2\text{CaCu}_2\text{O}_{8+\delta}$ was studied. The way in which the spectra were recorded is described in Section 6.2. The spectra for different field scan (i.e. for different field exposure) of the zero field cooled samples $\text{YBa}_2\text{Cu}_3\text{O}_{6.85}$ and $\text{Tl}_2\text{Ba}_2\text{CaCu}_2\text{O}_{8+\delta}$ are shown in Figs. 6.1 and 6.2 respectively. It is clear from these figures that upto a certain scan field there is no hysteresis and above it the signal starts to show the effect of hysteresis. In case of $\text{YBa}_2\text{Cu}_3\text{O}_{6.85}$ and $\text{Tl}_2\text{Ba}_2\text{CaCu}_2\text{O}_{8+\delta}$ the minimum fields at which the hysteresis effect appears are approximately 4G and 1G respectively. The hysteresis area of the field exposed samples increases throughout the range of exposed field, except in certain range of field in which it shows plateau behavior. There is a difference between the hysteresis area of the first scan and second scan of the DLFDMA for the equal exposed field. The hysteresis area of the second scan of DLFDMA is less than that of the first scan. The hysteresis area of the first and second scans of DLFDMA

of $\text{YBa}_2\text{Cu}_3\text{O}_{6.85}$ as a function of the field exposed, are shown in Fig. 6.3. The plateau range of hysteresis area for the first scan (ZFC) of DLFDMA for Sample $\text{YBa}_2\text{Cu}_3\text{O}_{6.85}$ is from 10G to 30G, while in case of $\text{Tl}_2\text{Ba}_2\text{Ca}_1\text{Cu}_2\text{O}_{8+\delta}$ the plateau range is from 30G to 45G. The hysteresis area of the second scan of the DLFDMA of sample $\text{YBa}_2\text{Cu}_3\text{O}_{7-\delta}$ shows different behavior from that of the first scan as shown in Fig. 6.3. The hysteresis area of second scan increases linearly at a slow rate. The hysteresis area of first and second scans of DLFDMA of $\text{Tl}_2\text{Ba}_2\text{CaCu}_2\text{O}_{8+\delta}$ as a function of exposed field are shown in Fig. 6.4.

In case of sample $\text{Tl}_2\text{Ba}_2\text{CaCu}_2\text{O}_{8+\delta}$ there is a difference in the variation of the hysteresis area of the DLFDMA of first and second scans as a function of exposed field. But the difference is not as much pronounced as in case of sample $\text{YBa}_2\text{Cu}_3\text{O}_{7-\delta}$. The second scan hysteresis area of $\text{Tl}_2\text{Ba}_2\text{CaCu}_2\text{O}_{8+\delta}$ shows a linear behavior throughout the range of the exposed field except around 20G where it shows a nonlinear behavior.

Two more important parameters of the DLFDMA are peak height and peak position. The peak height (h_p) and peak position (H_m) are also sensitive to the field exposed. The peak height and peak position of the first scan of the DLFDMA for different field exposure remain constant as is clear from Figs. 6.1 and 6.2 because in all the cases the virgin sample is cooled in zero field (i.e. condition are the same). But the peak height and peak position of the second scan of DLFDMA vary as function of exposed field. The variations in the peak position of the DLFDMA for $\text{YBa}_2\text{Cu}_3\text{O}_{7-\delta}$ and $\text{Tl}_2\text{Ba}_2\text{CaCu}_2\text{O}_{8+\delta}$ as a function of the field exposed to the samples are shown in Figs. 6.5 and 6.6 respectively. In both the samples the peak position shifts towards the higher field as the strength of the field exposed to the samples increases. But the variation in

peak position of the DLFDMA of $\text{YBa}_2\text{Cu}_3\text{O}_{6.85}$ is large compared to that in $\text{Tl}_2\text{Ba}_2\text{CaCu}_2\text{O}_{2.8+\delta}$. The variation in peak height (h_p) of DLFDMA for $\text{YBa}_2\text{Cu}_3\text{O}_{6.85}$ and $\text{Tl}_2\text{Ba}_2\text{CaCu}_2\text{O}_{2.8+\delta}$ as a function of exposed field are shown in Figs. 6.7 and 6.8 respectively. In case of $\text{YBa}_2\text{Cu}_3\text{O}_{7-\delta}$ the peak height h_p increases initially and then decreases with increasing exposed field and it shows a maximum around 14G of the exposed field which is much larger than the ZFC peak position which is at 4.5G. However, in case of $\text{Tl}_2\text{Ba}_2\text{CaCu}_2\text{O}_{2.8+\delta}$ the peak height is not very much sensitive to the exposed field. The trend of the variation in peak height is exactly the same as in $\text{YBa}_2\text{Cu}_3\text{O}_{7-\delta}$ but the maximum occurs at a higher field, i.e., around 30G which is much higher than the peak position of DLFDMA of ZFC $\text{Tl}_2\text{Ba}_2\text{CaCu}_2\text{O}_{2.8+\delta}$ which is at 8G. The signal height of DLFDMA of the field exposed sample is always greater than the signal height of ZFC sample upto a certain strength of the field exposed to the sample. This value is 80G in case of $\text{Tl}_2\text{Ba}_2\text{CaCu}_2\text{O}_{2.8+\delta}$ and 30G in case of $\text{YBa}_2\text{Cu}_3\text{O}_{6.85}$.

6.3.2 Field Cooling Effect on DLFDMA of $\text{YBa}_2\text{Cu}_3\text{O}_{6.85}$, 1% Hf Doped $\text{YBa}_2\text{Cu}_3\text{O}_{7-\delta}$ and $\text{Tl}_2\text{Ba}_2\text{CaCu}_2\text{O}_{2.8+\delta}$.

The field cooling effect on DLFDMA of pure $\text{YBa}_2\text{Cu}_3\text{O}_{6.85}$, Hf-doped $\text{YBa}_2\text{Cu}_3\text{O}_{7-\delta}$ and $\text{Tl}_2\text{Ba}_2\text{CaCu}_2\text{O}_{2.8+\delta}$ was studied. The actual recorded spectra of DLFDMA of pure $\text{YBa}_2\text{Cu}_3\text{O}_{7-\delta}$ and $\text{Tl}_2\text{Ba}_2\text{CaCu}_2\text{O}_{2.8+\delta}$ for different field cooling are shown in Figs. 6.9 and 6.10 respectively. The field in which sample was cooled for each recording are written on each spectra. The parameters of these spectra, such as the hysteresis area (ΔA) peak position (H_m) and peak height (h_p) are very sensitive to the field in which the sample was cooled. The variation in the hysteresis area of $\text{YBa}_2\text{Cu}_3\text{O}_{6.85}$, $\text{Tl}_2\text{Ba}_2\text{CaCu}_2\text{O}_{2.8+\delta}$ and 1% Hf-doped $\text{YBa}_2\text{Cu}_3\text{O}_{7-\delta}$ as a

function of field in which they were cooled, are shown in Figs. 6.3, 6.4 and 6.11 respectively. Hysteresis area increases, attains a maximum value and then decreases very fast and then saturates as the cooling field increases in case of $\text{YBa}_2\text{Cu}_3\text{O}_{6.85-\delta}$. The range of the cooling field in which hysteresis area increases is very small. The peak occurs at 4G at which the hysteresis effect in DLFDMA appears in case of the field exposer to the ZFC samples $\text{YBa}_2\text{Cu}_3\text{O}_{6.85}$. It is shown by an arrow in Fig. 6.3, while in case of $\text{Tl}_2\text{Ba}_2\text{CaCu}_2\text{O}_{2.8+\delta}$ the hysteresis area does not show peak, rather it shows a slight decrease and then saturation as the cooling field is increased. If peak should occur, in this case, then it should be at a field less than 1G, because the hysteresis effect in $\text{Tl}_2\text{Ba}_2\text{CaCu}_2\text{O}_{2.8+\delta}$ appears for a field exposure case around 0.8G. Since the range of the field (0 to 0.8G) is very small, it is very difficult to observe the increase in the hysteresis area. The decrease of the hysteresis saturates at the cooling field 45G and 10G in $\text{YBa}_2\text{Cu}_3\text{O}_{6.85}$ and $\text{Tl}_2\text{Ba}_2\text{CaCu}_2\text{O}_{2.8+\delta}$ respectively. The hysteresis area of the second scan of DLFDMA of $\text{YBa}_2\text{Cu}_3\text{O}_{6.85}$ decreases and saturates with increasing cooling field. However, the fall is not as sharp as in case of the first scan. The hysteresis area in case of Hf-doped $\text{YBa}_2\text{Cu}_3\text{O}_{7-\delta}$ also decreases and gets saturated with increasing cooling field as is clear from Fig. 6.11 [27].

The peak height (h_p) also shows a maximum in $\text{YBa}_2\text{Cu}_3\text{O}_{6.85}$ when plotted against the field in which the sample was cooled. The maximum occurs at the same cooling field at which hysteresis area shows the maximum. The variation in h_p as a function of cooling field for $\text{YBa}_2\text{Cu}_3\text{O}_{6.85}$, $\text{Tl}_2\text{Ba}_2\text{CaCu}_2\text{O}_{2.8+\delta}$ and 1% Hf-doped are shown in Figs. 6.7, 6.8 and 6.12 respectively. The variation of h_p as a function of cooling field in $\text{Tl}_2\text{Ba}_2\text{CaCu}_2\text{O}_{2.8+\delta}$ is not very large.

Its variation as a function of cooling field is maximum around 0.8G which was not clearly observed in the variation of hysteresis area. The decrease in the peak height gets saturated at a cooling field around 50G in $\text{YBa}_2\text{Cu}_3\text{O}_{6.85}$ and 20G in $\text{Tl}_2\text{Ba}_2\text{CaCu}_2\text{O}_{2.8+\delta}$. However, in case of 1% Hf-doped $\text{YBa}_2\text{Cu}_3\text{O}_{7-\delta}$, all these parameters h_p , H_m and ΔA get saturated around 60G [27].

Peak positions (H_m) are very sensitive to the cooling field in all the samples. The variation of peak position as a function of cooling field in $\text{YBa}_2\text{Cu}_3\text{O}_{6.85}$, 1% Hf-doped $\text{YBa}_2\text{Cu}_3\text{O}_{7-\delta}$ and $\text{Tl}_2\text{Ba}_2\text{CaCu}_2\text{O}_{2.8+\delta}$ are shown in Figs. 6.5, 6.12 and 6.6 respectively. Peak position increases very fast initially and then gets saturated as cooling field increases. The saturating cooling fields in $\text{YBa}_2\text{Cu}_3\text{O}_{6.85}$, 1% Hf-doped $\text{YBa}_2\text{Cu}_3\text{O}_{7-\delta}$ and $\text{Tl}_2\text{Ba}_2\text{CaCu}_2\text{O}_{2.8+\delta}$ are 50G, 60G and 40G respectively.

6.3.3 Negative Field Exposure Effects on DLFDMA of Field Exposed and Field Cooled Samples $\text{YBa}_2\text{Cu}_3\text{O}_{6.85}$ and $\text{Tl}_2\text{Ba}_2\text{CaCu}_2\text{O}_{2.8+\delta}$

(a) Field exposed

The effect of negative field exposure on DLFDMA of the positive field exposed and field cooled samples were studied. The actual recorded spectra of DLFDMA showing the negative field exposure effect on positive field exposed $\text{YBa}_2\text{Cu}_3\text{O}_{6.85}$ and $\text{Tl}_2\text{Ba}_2\text{CaCu}_2\text{O}_{2.8+\delta}$ are shown in Figs. 6.13 and 6.14 respectively. The parameters hysteresis area (ΔA), peak position (H_m) and peak height (h_p) of DLFDMA of FE samples are sensitive to the negative field exposure. The samples $\text{YBa}_2\text{Cu}_3\text{O}_{6.85}$ and $\text{Tl}_2\text{Ba}_2\text{CaCu}_2\text{O}_{2.8+\delta}$ were exposed to the positive field of strengths 126G and 82G respectively before exposing to different negative fields. The variation of hysteresis

area of $\text{YBa}_2\text{Cu}_3\text{O}_{6.85}$ and $\text{Tl}_2\text{Ba}_2\text{CaCu}_2\text{O}_{2.8+\delta}$ as a function of the negative field exposure are shown in the Fig. 6.15. It is clear from the figure that the hysteresis areas of the DLFDMA of both the FE samples $\text{YBa}_2\text{Cu}_3\text{O}_{6.85}$ and $\text{Tl}_2\text{Ba}_2\text{CaCu}_2\text{O}_{2.8+\delta}$ show maxima when plotted against the negative field. The maximum occurs around 15G in $\text{Tl}_2\text{Ba}_2\text{CaCu}_2\text{O}_{2.8+\delta}$ and 70G in $\text{YBa}_2\text{Cu}_3\text{O}_{6.85}$.

The variations in the peak height and peak position of the DLFDMA of FE samples $\text{YBa}_2\text{Cu}_3\text{O}_{6.85}$ and $\text{Tl}_2\text{Ba}_2\text{CaCu}_2\text{O}_{2.8+\delta}$ as a function of negative field exposure are shown in Figs. 6.16 and 6.17 respectively. Fig. 6.16 shows that the peak height of $\text{YBa}_2\text{Cu}_3\text{O}_{6.85}$ decreases with increasing negative field exposure throughout the range, except in the region of 10G to 50G, in which it shows no variation. Whereas in case of $\text{Tl}_2\text{Ba}_2\text{CaCu}_2\text{O}_{2.8+\delta}$, the peak height decreases and then gets saturated as the negative field exposure increases. The field at which saturation occurs is around 20G.

From Fig. 6.17 we observe that the peak positions of DLFDMA of both the samples decrease with increasing negative field exposure and attain minima, and on further increasing the negative field, H_m increases but the rate of increment is slow in comparison to the rate of decreasing at the lower field. The minima of the peak position occurs at 15G and 80G of the negative field exposure in $\text{Tl}_2\text{Ba}_2\text{CaCu}_2\text{O}_{2.8+\delta}$ and $\text{YBa}_2\text{Cu}_3\text{O}_{6.85}$ respectively.

(b) Field cooled

Effect of negative field exposure on the DLFDMA of positive field cooled samples $\text{YBa}_2\text{Cu}_3\text{O}_{6.85}$ and $\text{Tl}_2\text{Ba}_2\text{CaCu}_2\text{O}_{2.8+\delta}$ was studied. Typical actual recorded spectra showing the negative field exposure effect on the positive (11.7G) field cooled $\text{YBa}_2\text{Cu}_3\text{O}_{6.85}$ are shown in Fig. 6.18. The variations in the

hysteresis area, peak height and peak position of DLFDMA of both the samples as a function of negative field exposure are shown in the Fig. 6.19, 6.20 and 6.21 respectively. It is clear from Fig. 6.19 that hysteresis area shows a broad maxima. The maxima depends on the samples and the positive cooling field.

It is clear from the Figs. 6.20 and 6.21 that the peak heights and peak positions of DLFDMA of positive FC samples $\text{YBa}_2\text{Cu}_3\text{O}_{6.85}$ and $\text{Tl}_2\text{Ba}_2\text{CaCu}_2\text{O}_{8+\delta}$ decrease linearly with increasing negative field-exposure, except in the peak position of $\text{Tl}_2\text{Ba}_2\text{CaCu}_2\text{O}_{8+\delta}$ in which the rate of decreasing of the peak position is higher at lower negative field exposure than that at the higher negative field exposure. In $\text{YBa}_2\text{Cu}_3\text{O}_{6.85}$ the rate of decrease of peak height decreases with increasing the positive cooling field while the rate of shift of peak position towards lower field with respect to the negative field exposure increases with increasing the cooling field. But this increase is very small.

6.4 DISCUSSION

Most workers now agree that DLFDMA is related to the large number of Josephson junctions connecting the grains of the ceramic, which allows flux to enter at very low effective H_{c1} . Like type-II superconductors the granular superconductors have critical fields H_{c1j} . At H_{c1j} the field starts to penetrate into the junction. The values of H_{c1j} are very small compared to H_{c1} of the grain. The low field dependent microwave loss in high T_c ceramics is mainly into the intergrain Josephson junction.

Blazey et al. [24] attributed the microwave loss to the fluxon pinning and depinning by critical currents. This phenomenon is similar to the magnetic field hysteresis observed above H_{c1} in

the microwave surface resistance of type-II hard superconductors as seen in $Pb_{1-x}In_x$, PbTl and Nb_3Sn [28]. A fraction of the fluxons are free for both increasing and decreasing fields. Changing field direction, however, first decreases the number of free fluxons which are pinned. Further reduction of the field establishes the reverse pressure gradient that depins fluxon which may again contribute to the microwave absorption. During each cycle some fluxons are pinned and signal shows hysteresis. Thus hysteresis area is proportional to the trapped flux. The hysteresis effect will appear above the lowest H_{c1j} when the fluxon enters into the intergrain Josephson junction and gets pinned. This is clearly seen in Fig. 6.3 that the hysteresis area of the DLFDMA of ZFC $YBa_2Cu_3O_{6.85}$ as a function of the field (scan or exposed, upto H_{c1j} around 4G from zero) there is no hysteresis and above it the hysteresis area increases very fast upto the field around 8G of the scan field and gets saturated above it to field 30G from where it again starts growing linearly. The field 30G, at which the hysteresis area again increases linearly with scan field is the H_{c1g}^* (lower critical field of the grain) at 77K. The exposed field $H_j^*(8G)$ in case of $YBa_2Cu_3O_{6.85}$, at which the hysteresis area gets saturated is the field at which the Josephson junctions are in the critical state. In case of $Tl_2Ba_2CaCu_2O_{8+\delta}$ the hysteresis appears at very low field (around 0.8G), increases linearly and gets saturated around 30G. In case of $Tl_2Ba_2CaCu_2O_{8+\delta}$ ($Tl2212$) H_j^* is around 30G and H_{c1g}^* (where again hysteresis starts growing) is 45G at 77K. This value of H_{c1g}^* matches with the other measurements [29]. The assignment of H_{c1j} and H_j^* are done according to the Bean's critical state model. According to this model there would be no hysteresis effect upto H_{c1}^* and above it the hysteresis will increase upto the field H^* where all samples are in the critical

state and after that the hysteresis will remain constant because the sample can no more pin the vortices. The increase of hysteresis above H_{c1g} is due to the pinning of the vortices inside the grains (which have higher pinning strength).

The high T_c superconductors contain random network of Josephson junctions, each junction having different coupling strength. Therefore we expect a distribution of H_{c1j} . In the samples, which have broad distribution of H_{c1j} , hysteresis effect should appear at a very low field and the increase in the hysteresis area should continue upto a higher field. In the samples, which have sharp distribution of H_{c1j} , the hysteresis should appear at higher field and in the vicinity of the peak of H_{c1j} distribution curve. The peak position (H_m) in the DLFDMA correspond to that H_{c1j} where the maxima occurs in the distribution of H_{c1j} i.e., where large number of junctions having same H_{c1j} are taking part in microwave absorption. In case of $\text{YBa}_2\text{Cu}_3\text{O}_{6.85}$ the distribution of H_{c1j} is sharp so we see the hysteresis effect at 4G near the H_m (4.5G) which gets saturated at a relatively lower field (around 8G). While in case of Tl2212 the hysteresis effect appears at a very low field of scan (around 0.8G), the lowest H_{c1j} in the distribution, which is much smaller than H_m (8G) and gets saturated at 30G. Also the increase of the hysteresis area as a function of exposed field is not sharp in comparison to that in $\text{YBa}_2\text{Cu}_3\text{O}_{6.85}$. We observe the hysteresis area in the second scan for the same scan field as in the case of the first scan of the ZFC samples. But the hysteresis area of the second scan is less than that of the first scan. The fact that there is hysteresis in the second scan as well, indicates that the pinning of the flux is not the sole cause of hysteresis. Because the maximum flux which is pinned during the first scan, would remain pinned and for the same

scan field in the second scan there would be no further pinning of the vortices and therefore, there would be no hysteresis in the second scan. The hysteresis in second scan is either due to the creeping of the flux or due to the sweep scan dependent signal in the model of Dulcic et al. described in section 4.5.

The junctions with H_{c1j} less than the exposed field will not take part in the DLFDMA; only those junctions with H_{c1j} greater than the exposed field will take part. Thus, we expect the shift of H_m of DLFDMA of exposed field which is clear from Figs. 6.5 and 6.6, which show the peak position versus exposed field in $\text{YBa}_2\text{Cu}_3\text{O}_{6.85}$ and $\text{Tl}_2\text{Ba}_2\text{CaCu}_2\text{O}_{2.8+\delta}$ respectively. The range in which we expect H_m to shift towards the higher field and get saturated will depend on the sharpness of the distribution of H_{c1j} . We should observe a shift in the peak position in the range of exposed field in which hysteresis area increases, which is 4G to 8G in $\text{YBa}_2\text{Cu}_3\text{O}_{6.85}$ and 1G to 30G in $\text{Tl}_2\text{Ba}_2\text{CaCu}_2\text{O}_{2.8+\delta}$. For $\text{YBa}_2\text{Cu}_3\text{O}_{6.85}$, the range is small, so we do not have data for FE case in that range. This would be very much clear in FC case. The shift of the peak position to above 30G of exposed field in $\text{YBa}_2\text{Cu}_3\text{O}_{6.85}$ and 45G in $\text{Tl}_2\text{Ba}_2\text{CaCu}_2\text{O}_{2.8+\delta}$ is due to the absorption in the grain. The peak height (h_p) is the measure of the amount of the change in the slope of the absorption versus field curve at certain characteristic field H_m . Thus, we expect the increase of the peak height to occur in the region in which hysteresis area increases, because the junctions with H_{c1j} less than the exposed field are not taking part. So the maximum in the h_p versus exposed field is observed at the field upto which hysteresis area increases, which is 8G in $\text{YBa}_2\text{Cu}_3\text{O}_{6.85}$ and 30G in $\text{Tl}_2\text{Ba}_2\text{CaCu}_2\text{O}_{2.8+\delta}$ as shown in Figs. 6.7 and 6.8 respectively.

The hysteresis area, peak position and peak height of the FC samples show different behavior than the FE effect on the ZFC samples. We see in Figs. 6.3 and 6.7 that the hysteresis area and peak height of the FC $\text{YBa}_2\text{Cu}_3\text{O}_{6.85}$ samples as a function of cooling field increases as the cooling field is increased from zero to the lowest H_{c1j} (at which hysteresis appears in the FE case). Upto this field the samples behave exactly in the same way as in the case of exposed field in the range of H_{c1j} to H_j^* . The origin of this behavior is not clear. However, Vedeshwar et al. [30] have reported that there is no change in the hysteresis area upto H_m , where as they have observed an increase in the peak height upto H_m in FC samples. They correlated the peak position H_m of DLFDMA to the cooling field at which the maxima in the plot of peak height as function of cooling field occurs. But our observation is that the maxima in the plot of the peak height as a function of cooling field occur at the field at which hysteresis appears in the FE case. We do not observe any maximum in the hysteresis area of DLFDMA of T12212 as a function of cooling field because the lowest H_{c1j} for that sample is around 0.8G. If the maximum would have been at H_m , then it should appear at 8G, but we observe that the hysteresis area starts decreasing from zero itself. In the range zero to 1G of cooling field the maximum in the plot of peak height versus cooling field is seen at 0.8G which is H_{c1j} of T12212. In $\text{YBa}_2\text{Cu}_3\text{O}_{6.85}$ the peak height and the hysteresis area decrease very fast as function of cooling field above the lowest H_{c1j} which is clear from Figs. 6.3 and 6.7 and get saturated around 30G. However, in case of T12212 the fall is not so sharp as in case of $\text{YBa}_2\text{Cu}_3\text{O}_{6.85}$. This is due to the broad distribution of H_{c1j} of the intergranular Josephson junction in case of T12212. The decrease in the hysteresis area of the DLFDMA above the lowest H_{c1j} is due

to the increase in the trapped flux because of cooling the sample in stronger and stronger field. Microwave losses can be decreased by pinning the vortices. Therefore, as we increase the cooling field we are pinning more and more vortices and hence the peak height h_p decreases with increasing cooling field. The peak position of the DLFDMA of samples $\text{YBa}_2\text{Cu}_3\text{O}_{6.85}$ and $\text{Tl}_2\text{Ba}_2\text{CaCu}_2\text{O}_{8+\delta}$ as a function of cooling field are shown in Figs. 6.5 and 6.6 respectively. In case of $\text{YBa}_2\text{Cu}_3\text{O}_{6.85}$ the peak position H_m remains constant upto the cooling field equal to the lowest H_{c1j} (around 4G) and shifts towards higher field at a very fast rate, as the cooling field is increased above the lowest H_{c1j} and gets saturated at higher cooling field. The same behavior is seen in case of $\text{Tl}_2\text{Ba}_2\text{CaCu}_2\text{O}_{8+\delta}$. However the rate of shift of the peak position as a function of cooling field is not as fast as in case of $\text{YBa}_2\text{Cu}_3\text{O}_{6.85}$. This behavior shows that the distribution of H_{c1j} of the intergranular Josephson junctions are sharp in $\text{YBa}_2\text{Cu}_3\text{O}_{6.85}$ and broad in $\text{Tl}_2\text{Ba}_2\text{CaCu}_2\text{O}_{8+\delta}$. Vedeshwar et al. [30] tried to explain this behavior in terms of Ebner and Stroud model [16] and assumed H_m to be equal to H_c^* where the ac and dc susceptibilities differ. H_c^* is related to the area of the superconducting loop normal to the magnetic field by the relation $S = \phi_0 / 2H_c^*$. The trapped flux decouple the weakly coupled grain and the effective area of the superconducting loop is decreased, and hence, H_c^* increases and thus H_m [30]. Difference in the DLFDMA of ZFC and FC samples is attributed to the glassy behavior of the sample above H_m .

The exposure of the negative field to the positive field exposed sample depinns the flux which were trapped in the sample and hence the DLFDMA of the sample recover towards ZFC signal. This is evident from Figs. 6.13 and 6.14. The peak position shifts towards the lower field as the negative exposure field increases

due to depinning of the flux and this is clear from Fig. 6.16. However, we see a small decrease in peak height h_p in $\text{YBa}_2\text{Cu}_3\text{O}_{6.85}$ for the negative field exposure range 0 to 8G in which range the hysteresis area in the FE case increases (Fig. 6.3). The range of the negative field exposure in which the peak height increases, though very slowly, and decreases above it, is the range of exposed field in which the hysteresis area shows no change. But in case of $\text{Tl}_2\text{Ba}_2\text{CaCu}_2\text{O}_{8+\delta}$ the peak height decreases very fast for the negative field exposure and then gets saturated. The hysteresis area increases with increasing negative field exposure because some of the flux pinned in the positive exposed field are depinned. This is shown in Fig. 6.15. For higher negative field exposure, the hysteresis area again starts decreasing which indicates that the flux are again pinned in the opposite direction. In case of $\text{Tl}_2\text{Ba}_2\text{CaCu}_2\text{O}_{8+\delta}$ the increase in the hysteresis area and decrease in peak height is very sharp, indicating a lower pinning force in $\text{Tl}_2\text{Ba}_2\text{CaCu}_2\text{O}_{8+\delta}$. The effect of negative field exposure on the DLFDMA of the different positive field cooled $\text{YBa}_2\text{Cu}_3\text{O}_{6.85}$ and $\text{Tl}_2\text{Ba}_2\text{CaCu}_2\text{O}_{8+\delta}$ shows a systematic behavior. From Fig. 6.19 it is clear that hysteresis area of the DLFDMA of the positive field cooled $\text{YBa}_2\text{Cu}_3\text{O}_{6.85}$ as a function of the negative field exposure shows a maximum. The maxima shifts towards the higher negative field as the cooling field increases. This is obvious because cooling the sample in a higher field traps more flux and so to depin these large amount of flux, a large negative field is required. The parameter peak height h_p decreases linearly with negative field exposure. As the cooling field is increased, the rate of decrease of peak height decreases. This is obvious because increasing the cooling field means that the flux remain trapped in larger potential well and to depin the flux the larger value of

negative field is required. Similar is the behavior of the peak position.

In summary, we have tried to explain qualitatively, the FC and FE effects on the DLFDMA of $\text{YBa}_2\text{Cu}_3\text{O}_{6.85}$ and $\text{Tl}_2\text{Ba}_2\text{CaCu}_2\text{O}_{8+\delta}$ in the light of the critical state model of the random intergranular Josephson junctions assuming a distribution of the coupling strengths of the grains. The model proposed by Dulcic et al. which we have used to explain the temperature dependence of the DLFDMA, can also be used to explain the FC and FE effects. But for this, we require the data of the critical current of random Josephson junctions as a function of FC and FE in very low field region.

REFERENCES

1. J.B. Boyce, F. Bridges, T. Claeson, T.H. Geballe, C.W. Chu, and J.M. Tarascon, Phys. Rev. **35**, 7203 (1987).
2. K.A. Müller, M. Takashige and G. Bednorz, Phys. Rev. Lett. **58**, 1143 (1987).
3. F.S. Razavi, F.P. Koffyberg and B. Mitrovic, Phys. Rev. B **35**, 5323 (1987).
4. A.G. Emelchenko, P.A. Kohonovich, V.V. Rjazanov, M.V.K. Arzovnik, and I.F. Shegolev, in Proceeding of the International Workshop on Novel Mechanisms of Superconductivity, Berkeley, June 1987, Edited by V.Z. Kresin and S.A. Wolf (Plenum, New York, 1987).
5. J.F. Kwak, E.L. Venturini, D.S. Ginley and W. Fu in ref. 4.
6. A.C. Wright, K. Zhang and A. Erbil, Phys. Rev. Lett. (Preprint).
7. R.L. Peterson, and J.W. Ekin, Phys. Rev. B **37**, 9848 (1988).
8. J.F. Kwak, E.L. Venturini, P.J. Nigrey and D.S. Ginley, Phys. Rev. B **37**, 9749 (1988).
9. Y. Zhao, S.F. Sun, Z.P. Su, H. Zhang, Z.Y. Chen and Q.R. Zhang, Z. Phys. B - Condensed Matter **71**, 53 (1988).
10. M. Tuominen, A.M. Goldman, M.L. McCartney, Phys. Rev. B **37**, 548 (1988).
11. Y. Yeshurun, A.P. Malozemoff, Phys. Rev. Lett. **60**, 2202 (1988).
12. C.W. Hagen and R. Griessen in Studies of High Temperature Superconductors, 3, Ed. Anant Narlikar (NOVA Science Publisher 1989).
13. C. Rosseel, Y. Maeno and I. Morgenstern, Phys. Rev. Lett. **62**, 681 (1989).
14. P.G. deGennes, C.R. Acad. Sci. Ser. B **292**, 9 (1981).
15. P.G. de Gennes, C.R. Acad. Sci. Ser. B **292**, 279 (1981).

16. C. Ebner and D. Stroud, Phys. Rev. B, 165 (1985).
17. K. Kachaturyan, E.R. Weber, P. Tejedor, A.M. Stacy and A.M. Portis, Phys. Rev. B 36, 8309 (1987).
18. K.W. Blazy, K.A. Müller, J.G. Bednorz, W. Berlinger, G. Amoretti, R. Bluluggiu, A. Vera and F.C. Matacotta, Phys. Rev. B 36, 7241 (1987).
19. S.V. Bhat, P. Ganguly, T.V. Ramkrishnan and C.N.R. Rao, J. Phys. C 20, L559 (1987).
20. R.S. Rubins, J.E. Drumheller, S.L. Hutton, S.V. Rubanecker, B.Y. Jeong and T.D. Black, J. Appl. Phys. 64, 1312 (1988) and references therein.
21. E.J. Pakulis and T. Osada, Phys. Rev. B 37, 5940 (1988).
22. A. Gould, E.M. Jackson, R. Renoward, R. Crittenden, S.M. Bhagat, N.D. Spencer, L.L. Dolhert and R.F. Wormsbecher, Physica C 156, 555 (1988).
23. A.G. Vedeshwar, Md. Shahabuddin, Prem Chand, H.D. Bist, S.K. Agarwal, V.N. Moorthy, C.V.N. Rao, and A.V. Narlikar, Physica C, 158, 385 (1989).
24. K.W. Blazey, A.M. Portis and J.G. Bednorz, Solid State Commun. 65, 1153 (1988) and references therein.
25. M. Warden, M. Stalder, G. Stafanicki, A.M. Portis and F. Waldner, J. Appl. Phys. 64, 5800 (1988) and references therein.
26. E.V. Bilnov et al. JETP Letter 48, 159 (1988).
27. A.G. Vedeshwar, Md. Shahabuddin, H.D. Bist, S.K. Agarwal and A.V. Narlikar, Bull. Mater. Sci. 14, 777 (1991).
28. M. Cardona, J. Gittleman and B. Rosenblum, Phys. Lett. 17, 92 (1965).
29. M.D. Sastry, Studies of High Temperature Superconductors, Ed. A.Narlikar, Vol.2, P.260 (NOVA Science Publisher 1989).
30. A.G. Vedeshwar, H.D. Bist, S.K. Agarwal and A.V.Narlikar, Phys. Rev. B 41, 11294 (1990).

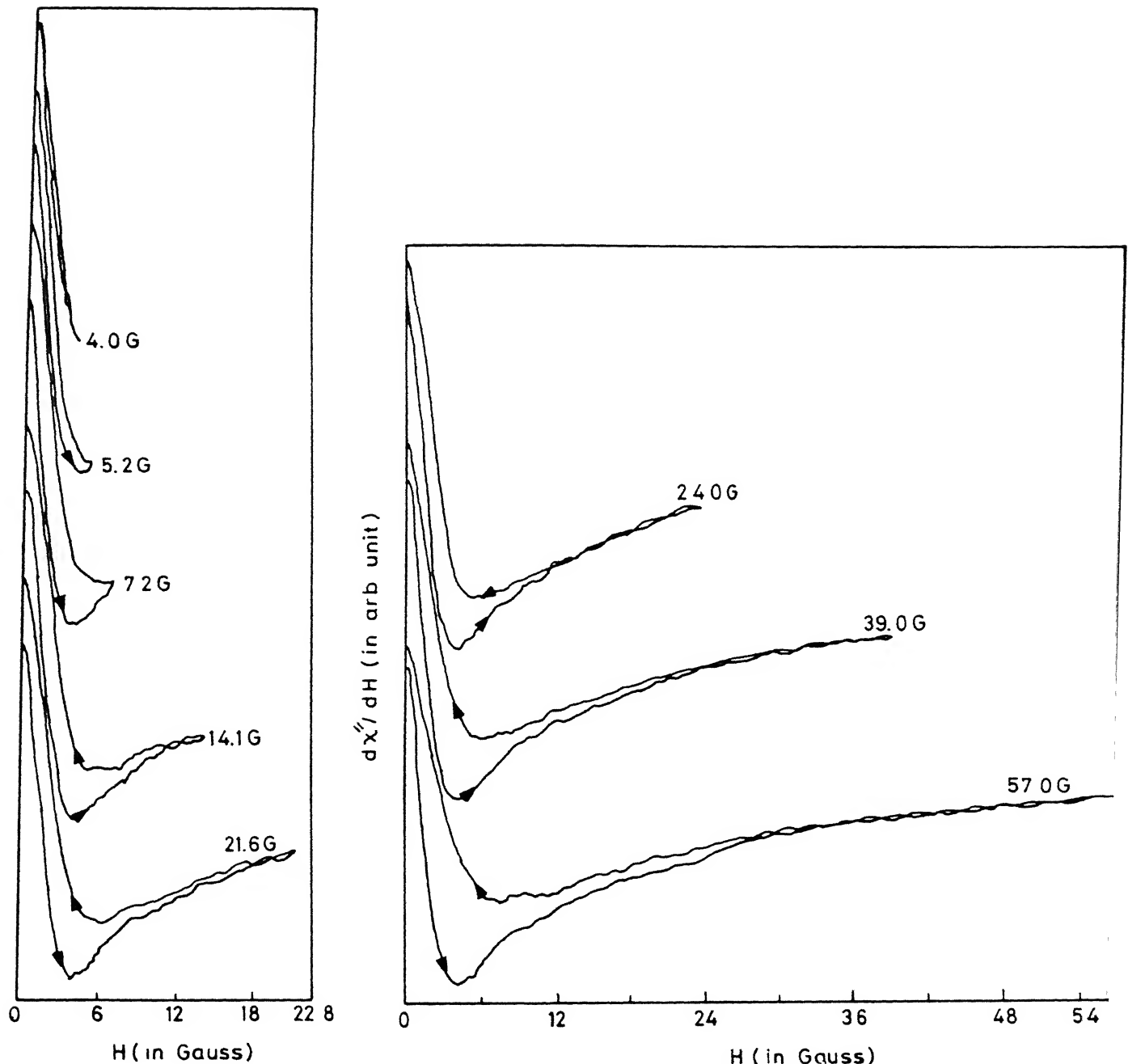


Fig. 6.1 Actual recorded spectra of zero field cooled $\text{YBa}_2\text{Cu}_3\text{O}_{6.85}$ for different field scan. The scan field is written on each spectrum. Sample was cooled in zero field every time for each recording.

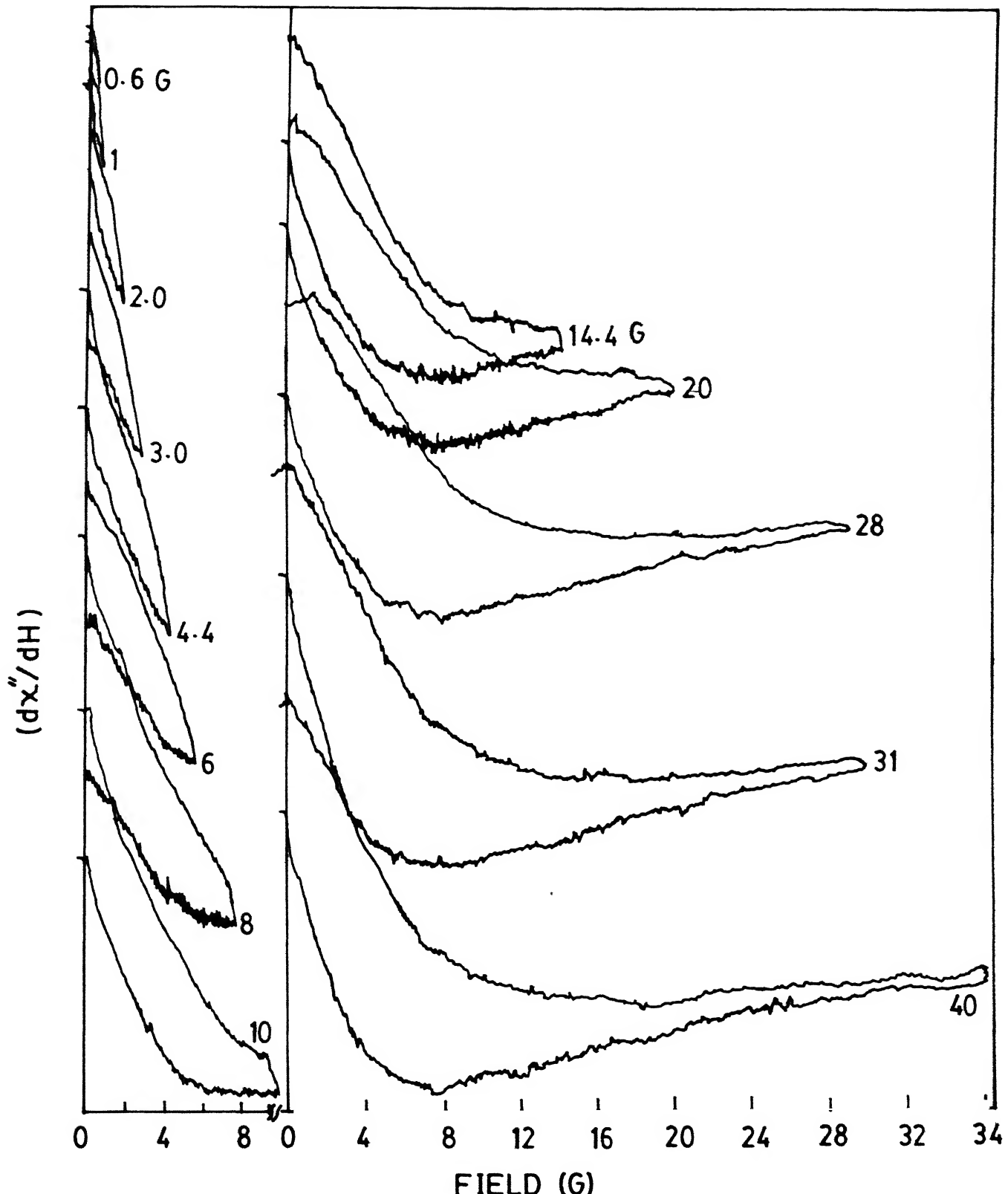


Fig. 6.2 Actual recorded spectra of zero field cooled $Tl_2Ba_2CaCu_2O_{8+\delta}$ for different field scan. The scan field is written on each spectrum. Sample was cooled in zero field every time for each recording.

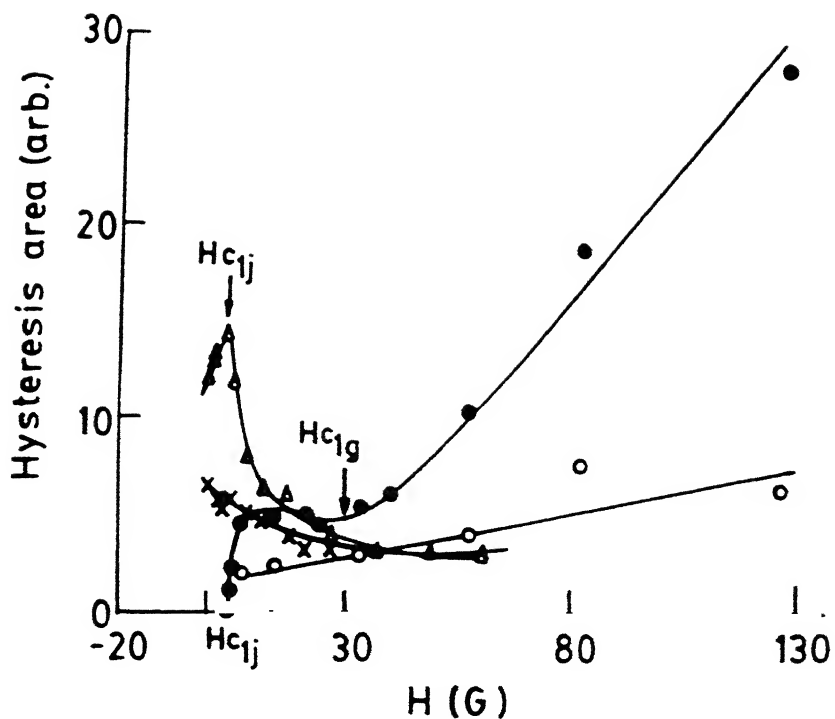


Fig. 6.3 Hysteresis area of the first scan of DLFDMA of $\text{YBa}_2\text{Cu}_3\text{O}_{6.85}$ as function of exposed field (●), cooling field (○) and that of the second scan of $\text{YBa}_2\text{Cu}_3\text{O}_{6.85}$ as a function of exposed field (○) and cooling field (x)

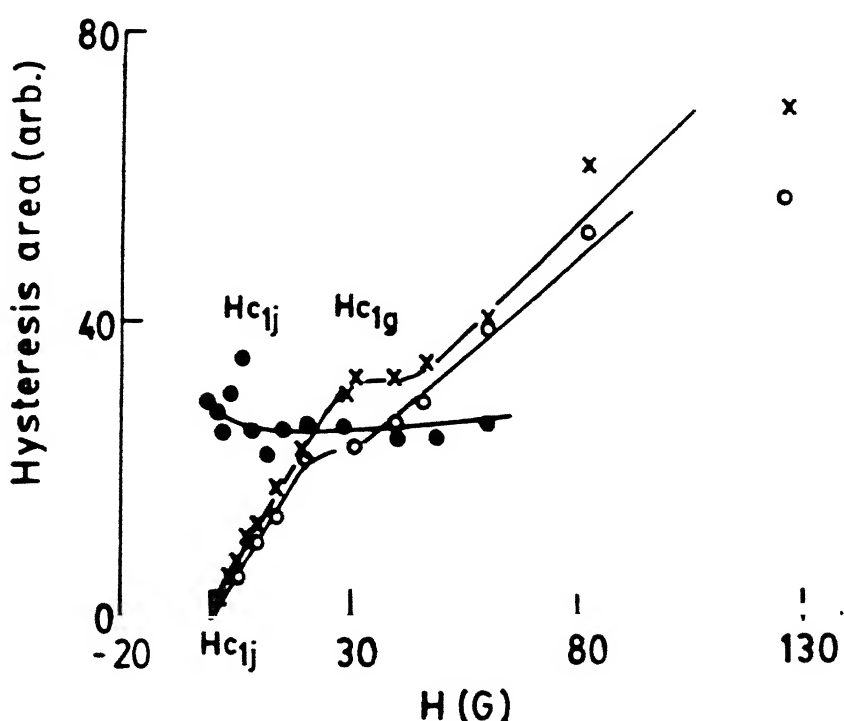


Fig. 6.4 Hysteresis area of the first scan of DLFDMA of $\text{Tl}_2\text{Ba}_2\text{CaCu}_2\text{O}_{8+\delta}$ as a function of exposed field (x) and cooling field (o), (o) represents the hysteresis area of second scan of DLFDMA of $\text{Tl}_2\text{Ba}_2\text{CaCu}_2\text{O}_{8+\delta}$ as a function of

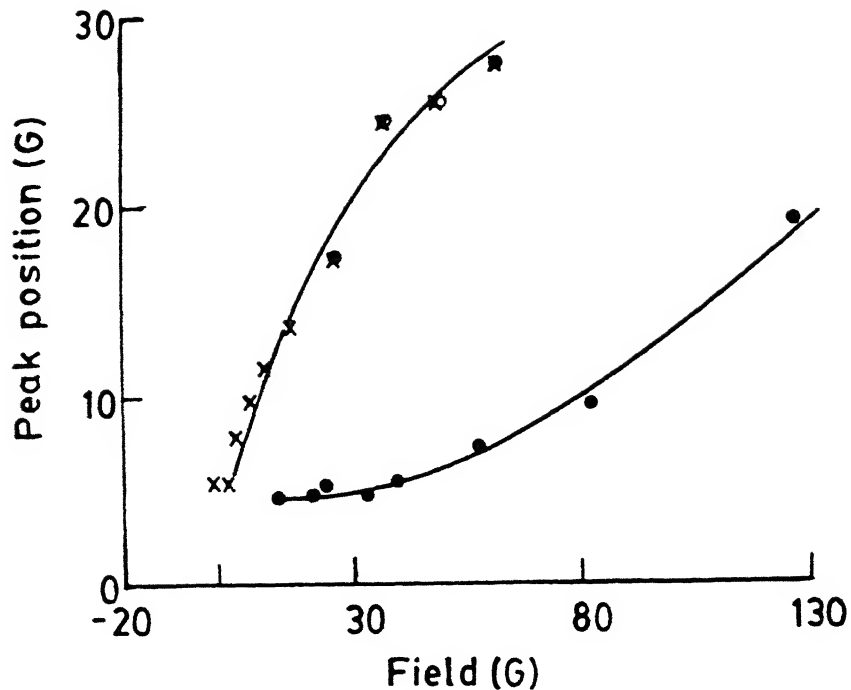


Fig. 6.5 Variation of peak position (H_m) of DLFDMA of $\text{YBa}_2\text{Cu}_3\text{O}_{6.85}$ as a function of field exposure (●) and field cooling (x).

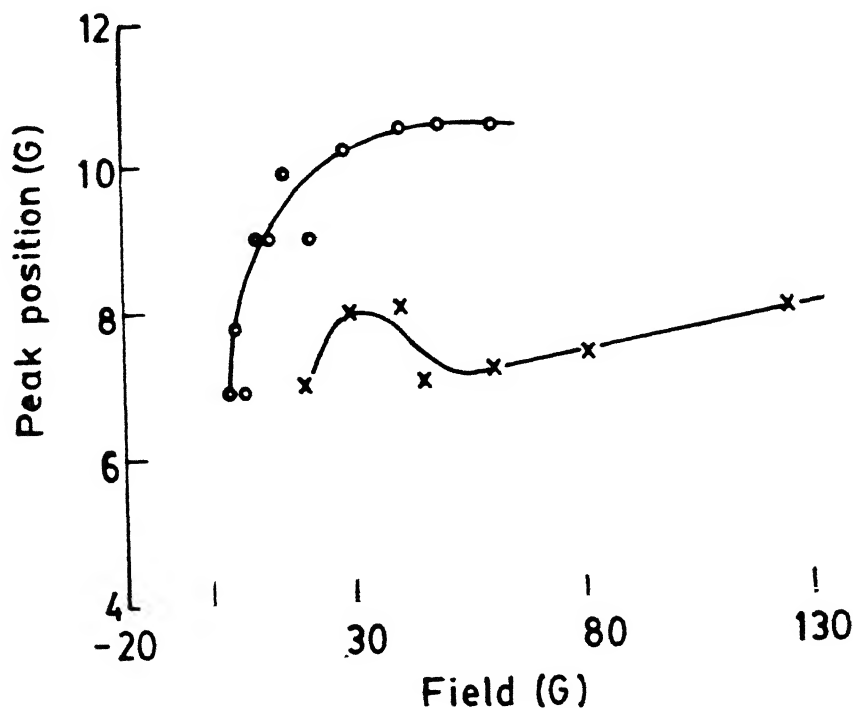


Fig. 6.6 Variation of peak position (H_m) of DLFDMA of $\text{Tl}_2\text{Ba}_2\text{CaCu}_2\text{O}_{8+\delta}$ as a function of field exposure (x) and field cooling (○).

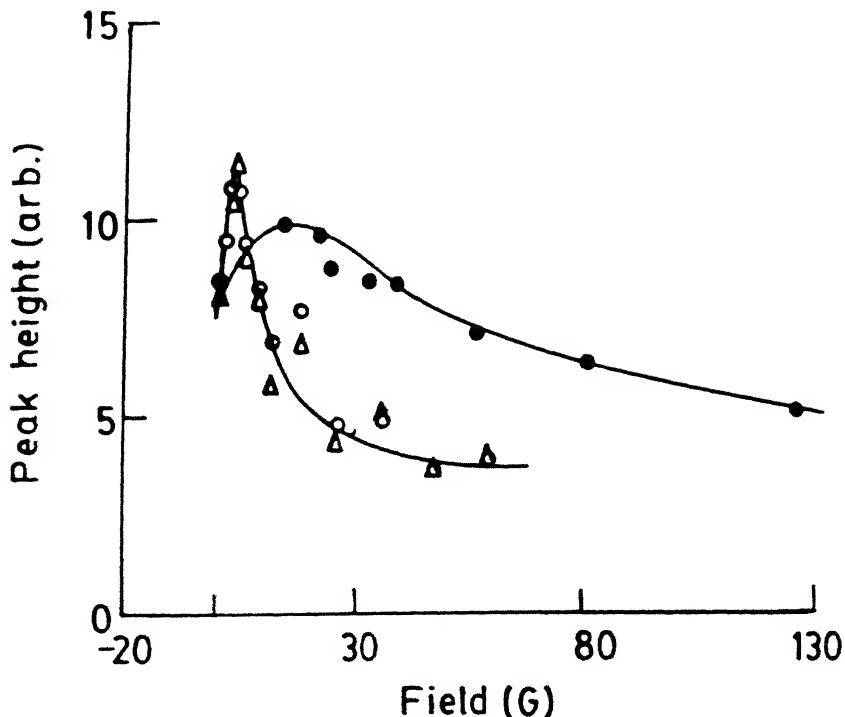


Fig. 6.7 Variation of peak height (h_p) of DLFDMA of $\text{YBa}_2\text{Cu}_3\text{O}_{6.85}$ as a function of field exposure (●) and field cooling (○).

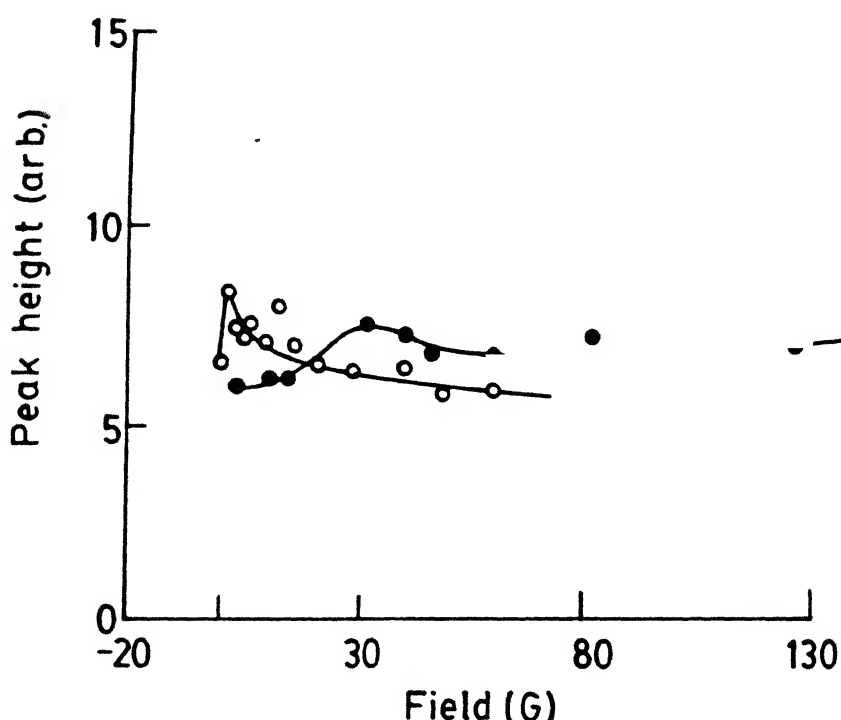


Fig. 6.8 Variation of peak height (h_p) of DLFDMA of $\text{Tl}_2\text{Ba}_2\text{CaCu}_2\text{O}_{8+\delta}$ as a function of field exposure (●) and field cooling (○).

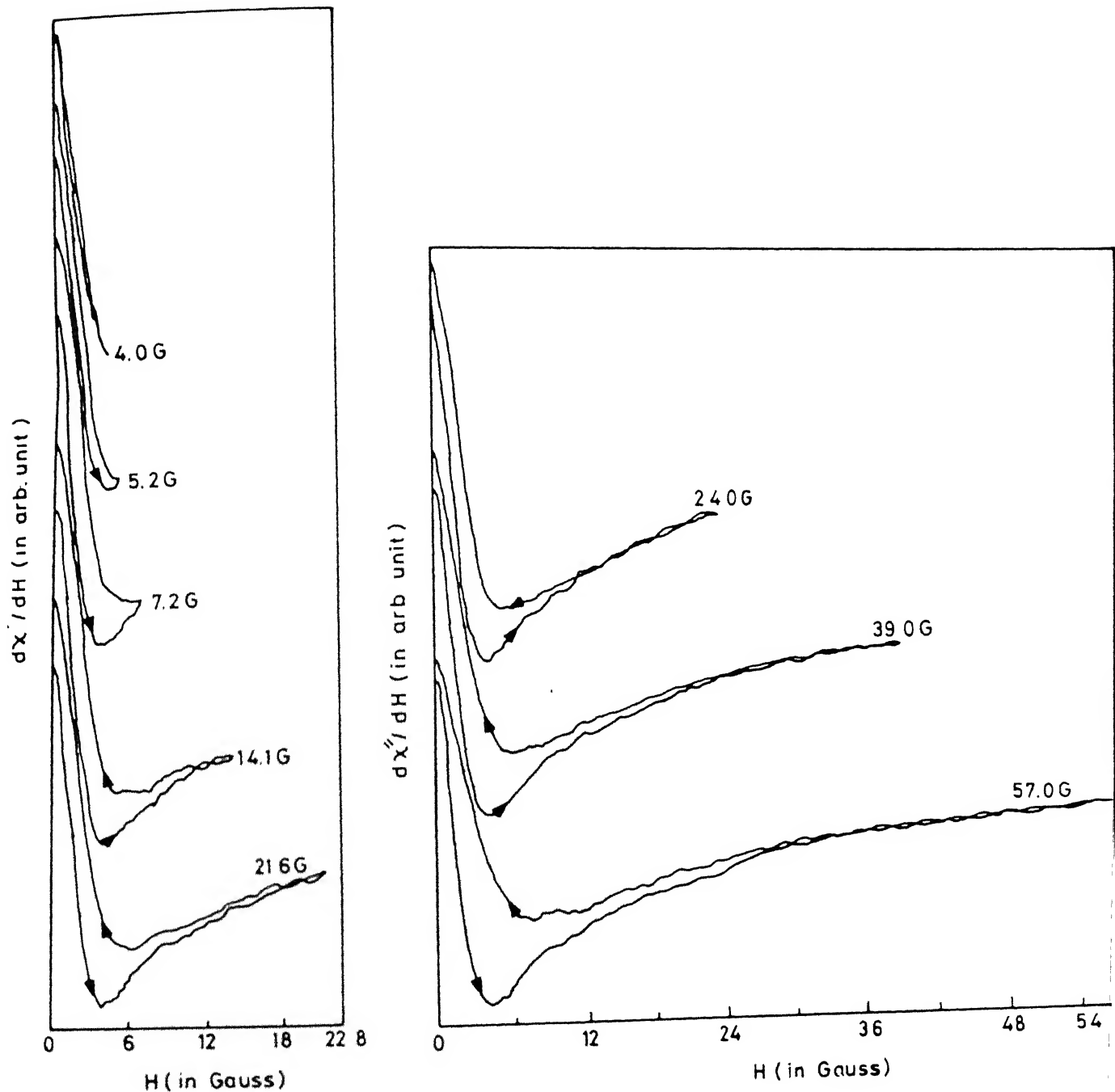


Fig. 6.9 Recorded spectra of DLFDMA of $\text{YBa}_2\text{Cu}_3\text{O}_{6.85}$ at different cooling field. Each recording was done after removing the earlier magnetic memory (i.e by heating above T_c). The fields in which sample was cooled are specified at each spectrum.

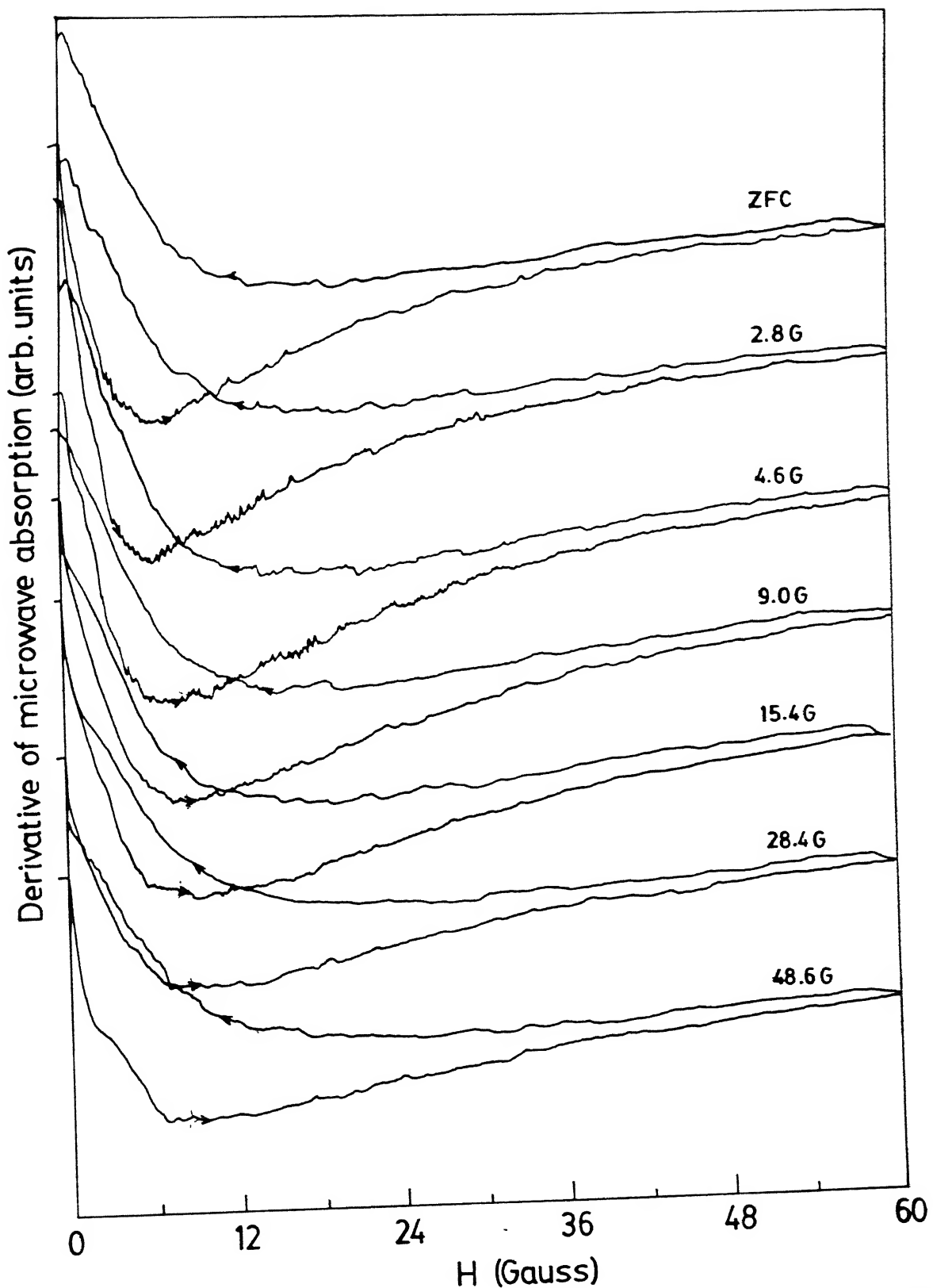


Fig. 6.10 Recorded spectra of DLFDMA of $Tl_2Ba_2CaCu_2O_{8+\delta}$ at different cooling field. Each recording was done after removing the earlier magnetic memory (i.e. by heating above T_c). The fields in which sample was cooled are specified at each spectrum. Starting of each spectrum is shown by horizontal bar.

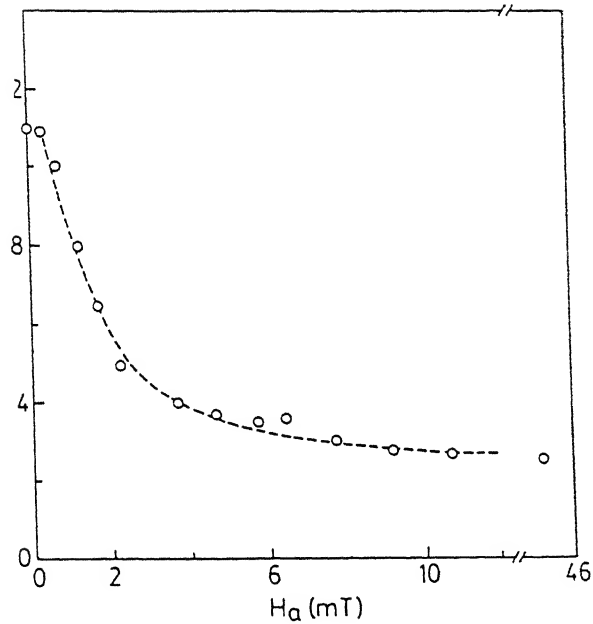


Fig. 6.11 Hysteresis area (ΔA) of DLFDMA of 1% Hf-doped $YBa_2Cu_3O_{7-\delta}$ as a function of cooling field.

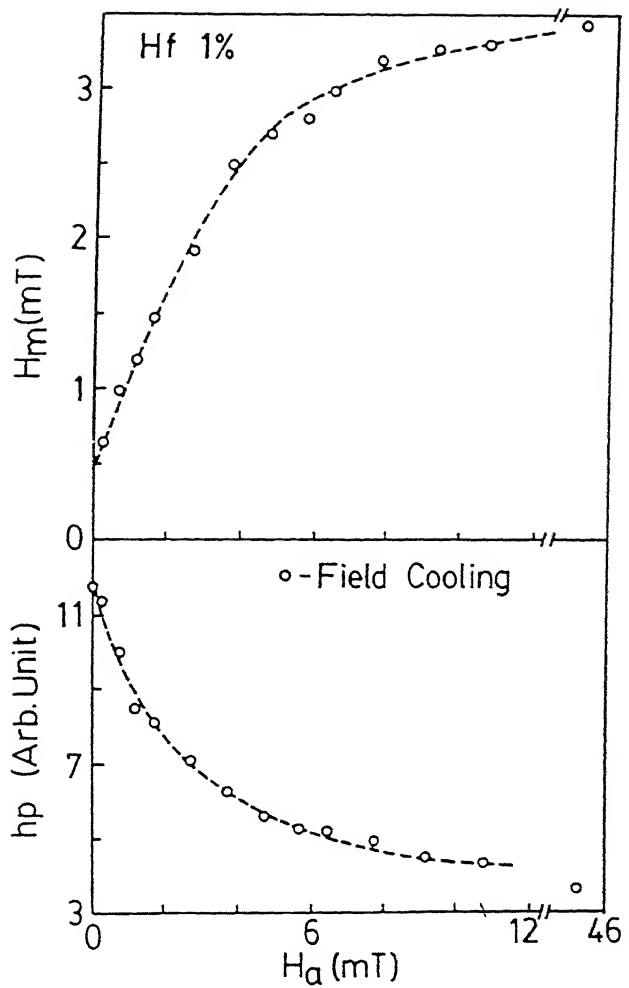


Fig. 6.12 Variation of peak height (h_p) and peak position (H_m) of DLFDMA of 1% Hf-doped $YBa_2Cu_3O_{7-\delta}$ as a function of cooling field.

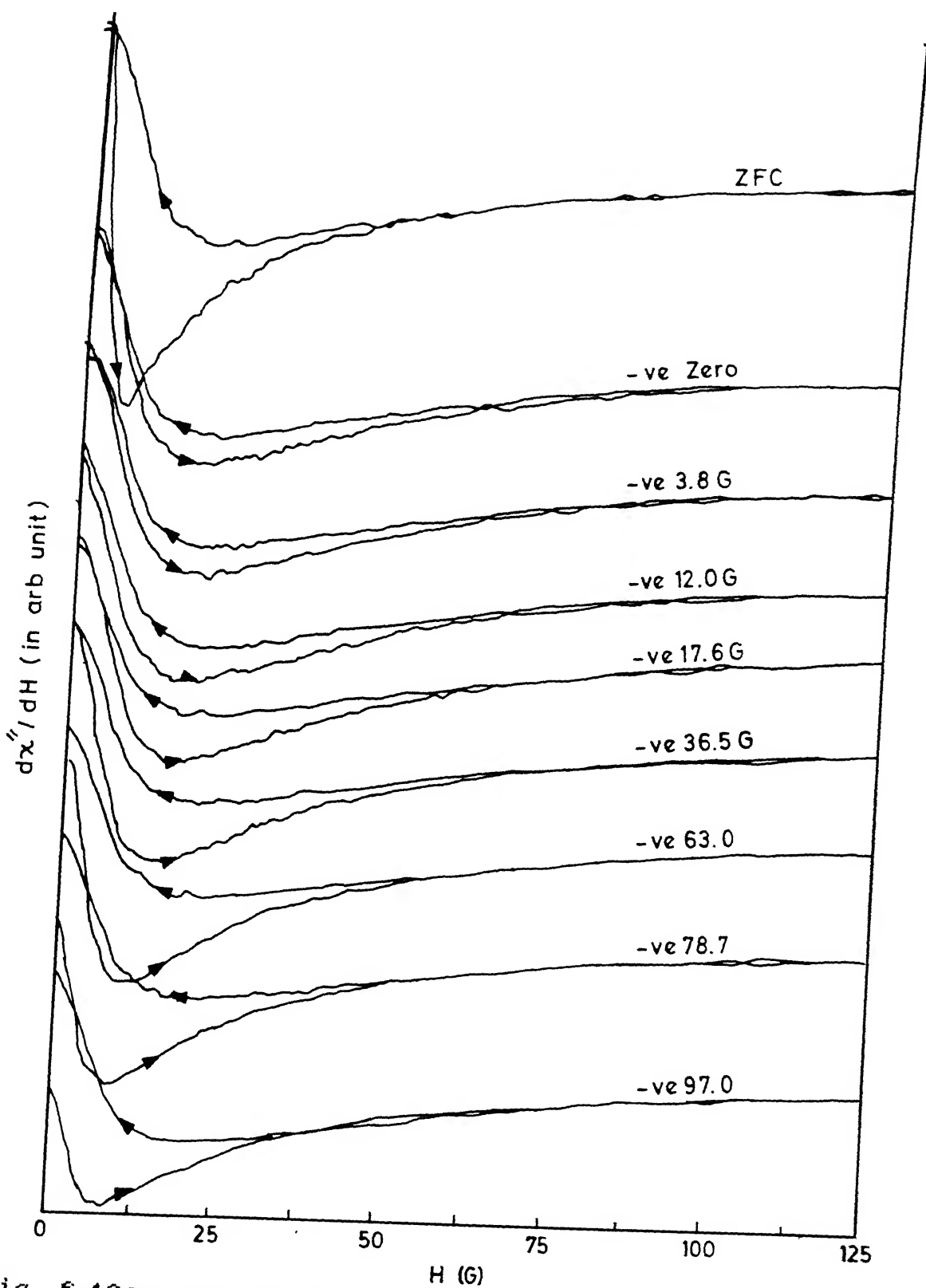


Fig. 6.13 Recorded spectra of DLFDMA of $\text{YBa}_2\text{Cu}_3\text{O}_{6.85}$ at different negative field exposure on the positive exposed field 126G. The negative field exposed to the sample is specified at each spectrum.

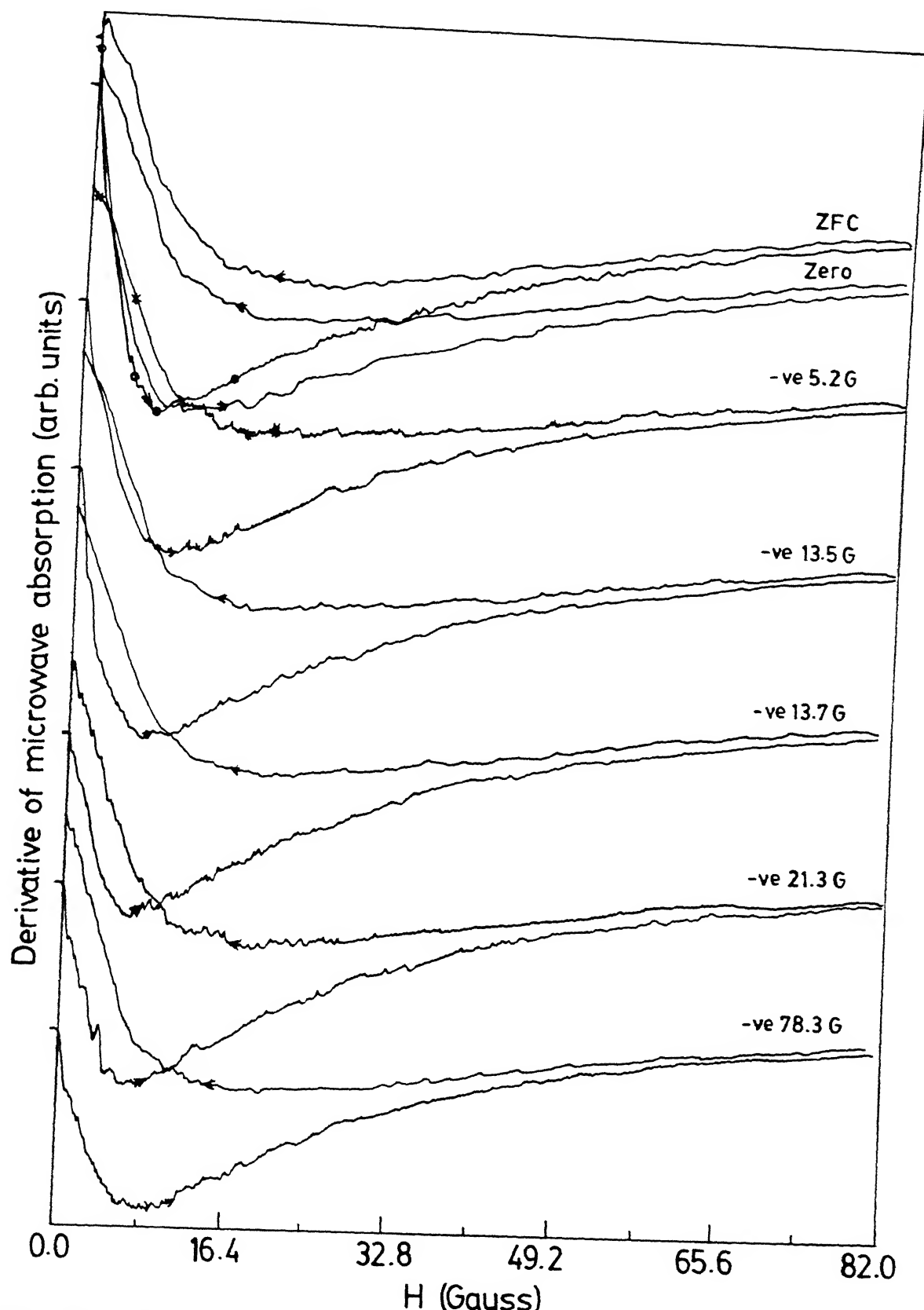


Fig. 6.14 Recorded spectra of DLFDMA of $Tl_2Ba_2CaCu_2O_{8+\delta}$ at different negative field exposure on the positive exposed field 82G. The negative field exposed to the sample is specified at each spectrum.

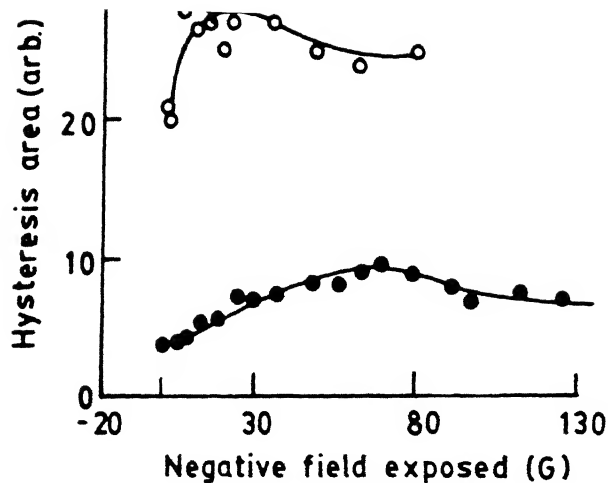


Fig. 6.15 Variation of hysteresis area of DLFDMA of positive exposed field $\text{YBa}_2\text{Cu}_3\text{O}_{6.85}$ & $\text{Tl}_2\text{Ba}_2\text{CaCu}_2\text{O}_{8+\delta}$ as a function of negative field exposure.

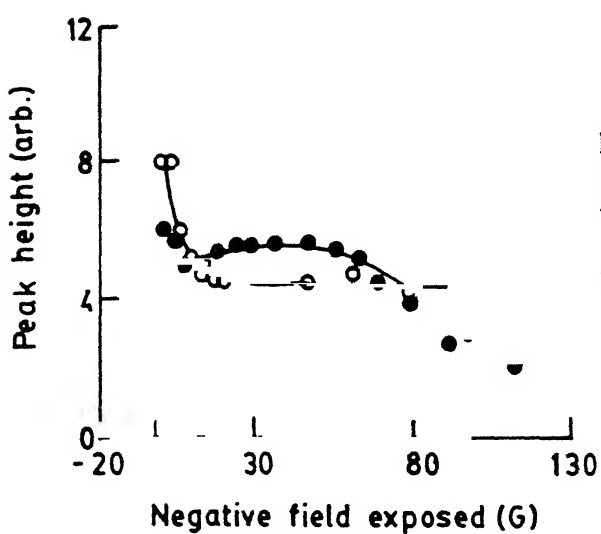


Fig. 6.16 Variation of peak height of DLFDMA of positive exposed field $\text{YBa}_2\text{Cu}_3\text{O}_{6.85}$ & $\text{Tl}_2\text{Ba}_2\text{CaCu}_2\text{O}_{8+\delta}$ as a function of negative field exposure.

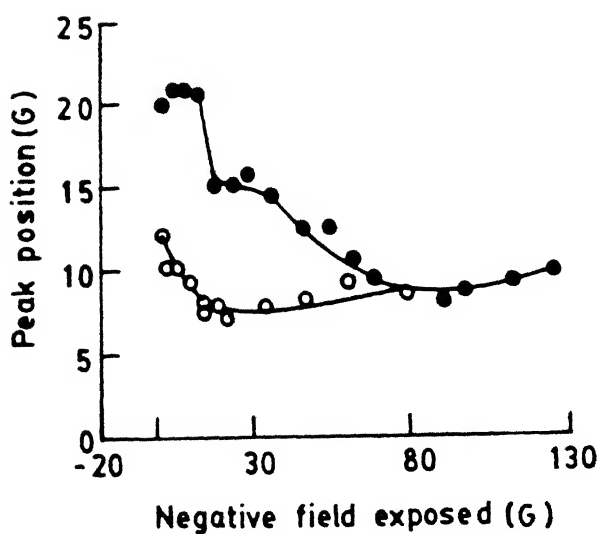


Fig. 6.17 Variation of peak position of DLFDMA of positive exposed field $\text{YBa}_2\text{Cu}_3\text{O}_{6.85}$ & $\text{Tl}_2\text{Ba}_2\text{CaCu}_2\text{O}_{8+\delta}$ as a function of negative field exposure.

● - $\text{YBa}_2\text{Cu}_3\text{O}_{6.85}$
 ○ - $\text{Tl}_2\text{Ba}_2\text{CaCu}_2\text{O}_{8+\delta}$

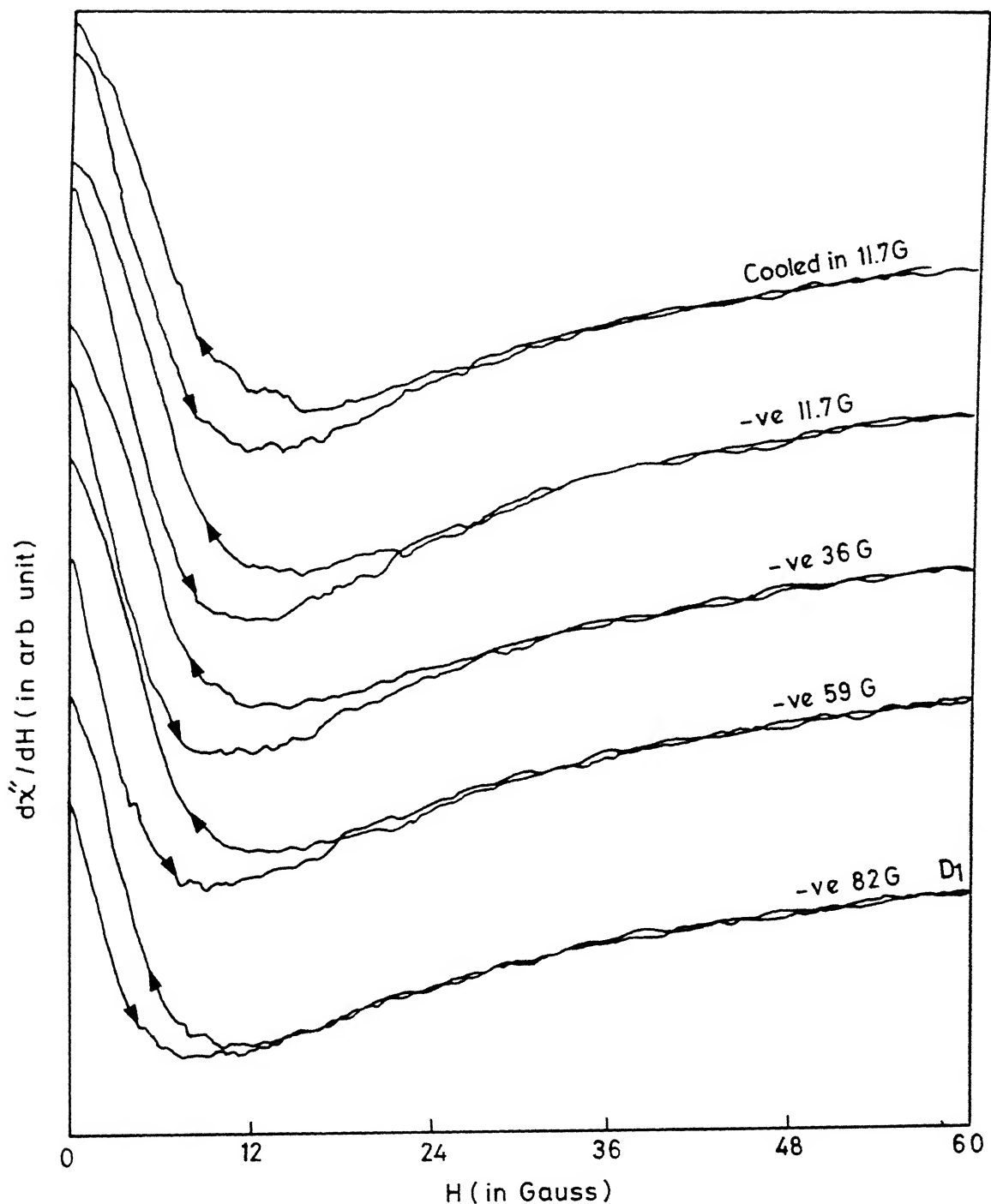


Fig. 6.18 Recorded spectra of DLFDMA of positive field cooled $\text{YBa}_2\text{Cu}_3\text{O}_{6.85}$ at different negative field exposure. The negative field exposed to the sample is specified at each spectrum. Fixed positive field in which sample was cooled was 11.7G.

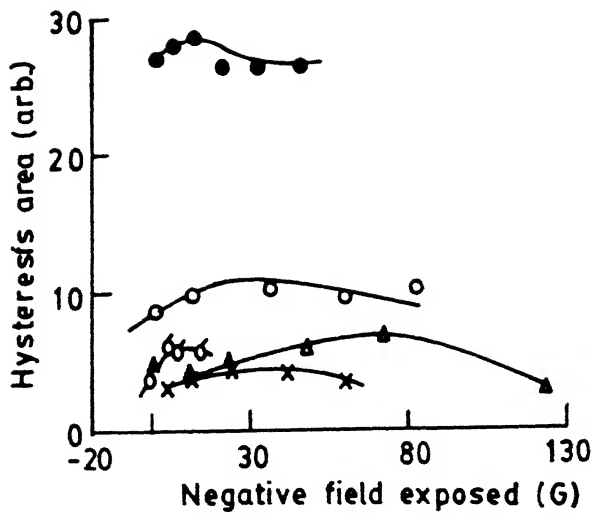


Fig. 6.19 Variation of hysteresis area of DLFDMA of field cooled $\text{YBa}_2\text{Cu}_3\text{O}_{6.85}$ & $\text{Tl}_2\text{Ba}_2\text{CaCu}_2\text{O}_{8+\delta}$ as a function of negative field exposure.

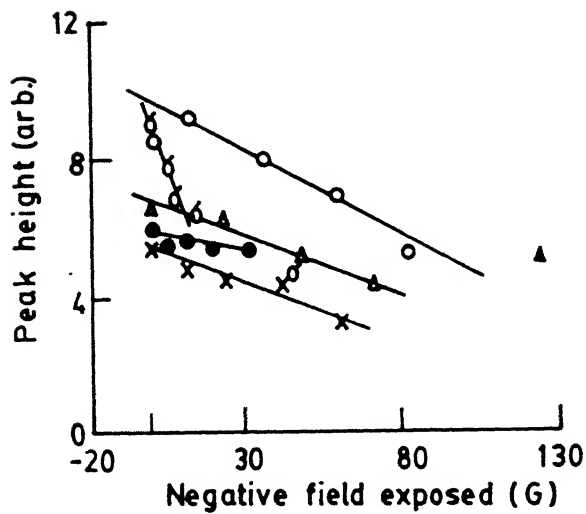


Fig. 6.20 Variation of peak height of DLFDMA of field cooled $\text{YBa}_2\text{Cu}_3\text{O}_{6.85}$ & $\text{Tl}_2\text{Ba}_2\text{CaCu}_2\text{O}_{8+\delta}$ as a function of negative field exposure.

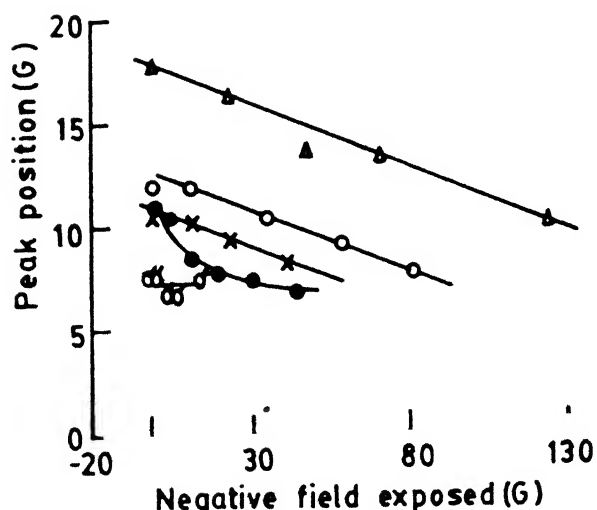


Fig. 6.21 Variation of peak position of DLFDMA of field cooled $\text{YBa}_2\text{Cu}_3\text{O}_{6.85}$ & $\text{Tl}_2\text{Ba}_2\text{CaCu}_2\text{O}_{8+\delta}$ as a function of negative field exposure.

- - $\text{Tl}_2\text{Ba}_2\text{CaCu}_2\text{O}_{8+\delta}$ cooling field - 59G
- - $\text{YBa}_2\text{Cu}_3\text{O}_{6.85}$ cooling field - 6.6G
- × - $\text{YBa}_2\text{Cu}_3\text{O}_{6.85}$ cooling field - 11.4G
- - $\text{YBa}_2\text{Cu}_3\text{O}_{6.85}$ cooling field - 11.7G
- ▲ - $\text{YBa}_2\text{Cu}_3\text{O}_{6.85}$ cooling field - 24G

CHAPTER VII

CONCLUSIONS

In this thesis we presented a detailed study of derivative of low field dependent microwave absorption (DLFDMA) in ceramic pure $\text{YBa}_2\text{Cu}_3\text{O}_{7-\delta}$, Hf-doped $\text{YBa}_2\text{Cu}_3\text{O}_{7-\delta}$ and $\text{Tl}_2\text{Ba}_2\text{CaCu}_2\text{O}_{8+\delta}$. Also we have studied the EPR spectra of these materials at room temperature. The results of DLFDMA were explained in terms of the model proposed by Dulcic et al. Field exposed and field cooling effects were discussed in terms of the critical state model of random granular Josephson junctions.

High T_c superconductors are EPR silent at all temperatures. However, we have observed some weak signals which we have attributed to the presence of impurity phases in the samples. Various possible reasons, in terms of metallic nature of the sample, antiferromagnetic ordering and formation of $(\text{Cu}-\text{O}-\text{Cu})^{2+}$ molecules having singlet ground state and very remote triplet state, have been discussed. All high T_c superconductors exhibit large low field dependent microwave absorption below T_c . Its derivative signal shows a peak. We have studied the DLFDMA in $\text{YBa}_2\text{Cu}_3\text{O}_{7-\delta}$ as a function of grain size. We observed that, the peak position shifts towards lower field as the grain size of the sample increases. Peak height h_p of DLFDMA in all the samples varies as $(T_c - T)^{\alpha}$ near T_c where α varies from sample to sample. Hysteresis area also shows a similar behavior. The peak position remains constant when the temperature of the sample is varied around T_c . Observations have been explained satisfactorily in terms of model proposed by Dulcic et al. The DLFDMA in high T_c superconductors takes place in the random intergranular Josephson junctions. This

model assumes that the field dependent microwave absorption in high T_c superconductors can be explained in terms of the response of a single representative Josephson junction in the presence of dc and microwave fields. Also, this model explains our results of the effect of modulation field amplitude qualitatively. To explain the field exposure and field cooling effects, the Dulcic model requires some more experimental data, such as the critical current as a function of field exposure and field cooling in the low field region. For better understanding of this complicated behavior of DLFDMA as a function of modulation amplitude more theoretical efforts and more generalized models are required.

The effects of field exposure (shielding effect) and field cooling (Meissner effect) on DLFDMA are different. The measurements for field exposure case show that the field penetrates in the intergranular junction of the sample at very low field (H_{c1J}) and gets trapped. This trapped flux is proportional to the hysteresis area of the DLFDMA. The hysteresis area increases as a function of exposure field above H_{c1J} and gets saturated. On further increasing the exposure field, hysteresis area increases. The range of field exposure in which hysteresis area shows a saturation, vary from sample to sample. The increase in hysteresis area as a function of exposure field at higher values shows that the field penetrates into the grain and gets trapped. Thus the measurement of hysteresis area of DLFDMA as a function of exposure field gives the value of H_{c1J} and H_{c1g} of the sample. In field cooling case, hysteresis area of DLFDMA increases with increase in the cooling field and attains maxima at H_{c1J} . On further increasing the cooling field the hysteresis area decreases rapidly. Peak height of DLFDMA increases initially as the cooling field or exposure field is increased and attains maximum. On further

increasing the cooling field or exposure field the peak height decreases and gets saturated at higher value of cooling field or exposure field. The maxima in the peak height versus cooling field occurs at H_{c1J} . The peak position of DLFDMA shifts towards the higher field as the exposure field or cooling field is increased. All these observations have been explained qualitatively in terms of the critical state model of the random intergranular Josephson junction having a distribution of coupling strengths. For better understanding of the field cooling and field exposure effect on DLFDMA, more experimental data at different temperatures and in different high T_c superconductors are required.

Thus to understand the complicated behavior of low field dependent microwave absorption as a function of modulation amplitude, field cooling and field exposure, more generalized model and theoretical efforts are required.